ASSISTIVE
INTELLIGENT
ROBOTICS

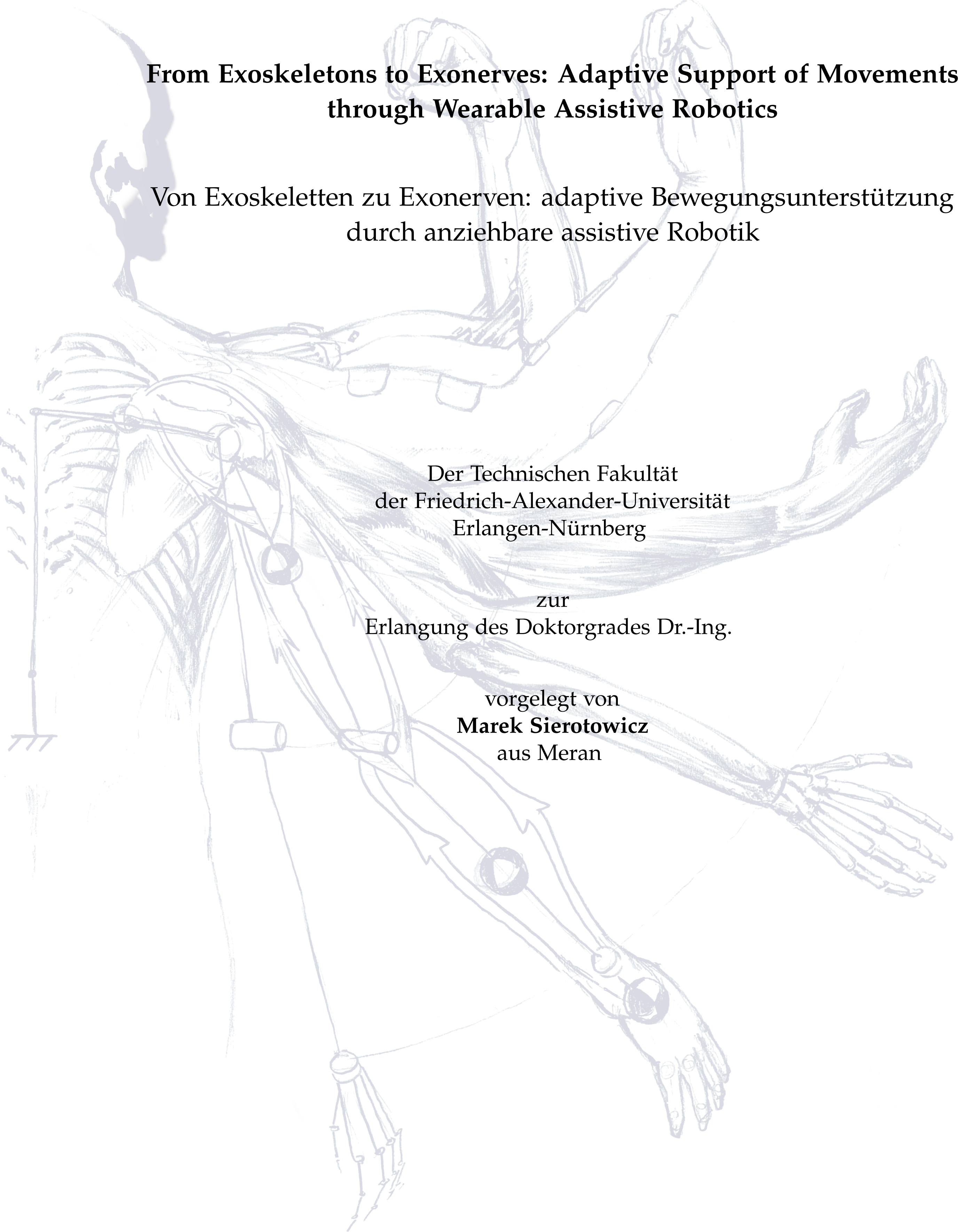

From Exoskeletons to Exonerves: Adaptive Support of Movements through Wearable Assistive Robotics

Von Exoskeletten zu Exonerven: adaptive Bewegungsunterstützung durch anziehbare assistive Robotik

Der Technischen Fakultät
der Friedrich-Alexander-Universität
Erlangen-Nürnberg

zur
Erlangung des Doktorgrades Dr.-Ing.

vorgelegt von
Marek Sierotowicz
aus Meran

Als Dissertation genehmigt
von der Technischen Fakultät
der Friedrich-Alexander-Universität Erlangen-Nürnberg

Tag der mündlichen Prüfung:	15.7.2024
Gutachter/in:	Prof. Dr. Claudio Castellini Prof. Dr. Thomas Seel

I confirm that this doctorate is my own work and I have documented all sources and material used.

Erlangen, Marek Sierotowicz

Acknowledgments

If I'm being honest, from where I stand now it feels like all of the work that went into this thesis simply happened. Nevertheless, this is the result of something that started quite a while ago, in the scope of my life, and I will certainly forget many of the people whom I was fortunate to meet during this long journey. I will start with the easy ones.

First I want to thank my supervisor, Prof. Claudio Castellini. I will be the first student he brings to a doctorate, together with my esteemed colleague Andrea Gigli, so I can't but wish Claudio better luck for next time. I would also like to thank my second reviewer Prof. Thomas Seel, who I think was the author of the first ever publication to cite my work. Seems appropriate.

Now onto throwing the wider net. The work presented in this thesis was realized with mainly three teams. The current one is the AIROB lab, which I have contributed to set up, together with Fabio Egle, Marc-Anton Scheidl and Sabine Thürauf, who helped me in writing this work with her rare attention to detail. But we all know that it was actually Benjamin the Wunderkind who helped. It would be hard to mention all people who have come and gone through our lab in these last few years, but I hope Silvana Montenegro and Hannah Braun can join our group soon. I would probably be remiss if I didn't mention some of the wider group who resides and resided in our building, some of whom are sadly not with us any more. I would like to mention Basti, Silvana (the other), Frank, Brian, and the whole of the Werner-von-Siemens staff.

Secondly, I have to thank our collaborators in Heidelberg. Mainly Prof. Lorenzo Masia, who somehow could stand me long enough to host me for a whole month when COVID made it hard to travel, and Prof. Rüdiger Rupp, together with their teams. I should thank at least those with whom I have directly worked: Nicola Lotti, Francesco Missiroli, Ryan Alicea, Laura Nell, and Xiaohui Zhang.

The last main team, with whom I have spent some of the best years of my professional life (which admittedly isn't saying much yet), is the Robotics and Mechatronics Center of the German Aerospace Center, west of Munich. I will start with the now defunct adaptive bio-interfaces group, where I got my start. There, I met the aforementioned Andrea Gigli and my master's supervisor Mathilde Connan. There, I also made the acquaintance of my esteemed co-author Donato Brusamento, who together with Markus Nowak, elected to transition to the private sector. I suppose Academia is a harsh mistress. Still, what a loss. Many colleagues from other departments also helped me greatly: Michael Panzirsch, Harsimran Singh, Bernhard Weber, Jean-Pascal Lutze, Ribin Balachandran, Neal Lii, Bernd Henze, Maximo Roa-Garzon.

I should also at least briefly mention the good people at Ottobock. Benjamin Schirrmeister, Jose Gonzalez-Vargas, Jonas Bornmann.

Now onto the personal ones. It is uncanny to think how many things changed for my family from the start of this doctorate until now. Here too, some are no longer with us, and some have changed quite radically. I thank all of my family for supporting me and not cutting me off entirely, in spite of my not being as present as I should have been. Same goes for my friends Claudio (the other), Samuel, Ana, Alejandra, Mariangela, Dario, the Lasagnas, and many others. I started this with Leticia by my side. It was nice while it lasted.

Finally I thank Flaminia, for coaching me to the end. I am glad we got to converse between dissertations.

Per aspera ad astra.

Abstract

In human-machine interfaces, the neuromuscular system can be monitored through a variety of sensor modalities in order to infer and transmit the intended movement and force output from a user to a machine. Likewise, the neuromuscular system can be stimulated through many mechanisms to relay somatosensory feedback from a sensing system to the user or to provide support. Over the last decades, wearable robotics has focused on aiding human users in executing arduous tasks and in enhancing their force output by encasing them in fully rigid robotic exoskeletons. More recently, there was a transition towards lighter structures, finally converging on continuum-based soft exosuits which rely on the user's own skeleton as a load-bearing structure. Currently, a new paradigm is being investigated, which relies increasingly on the user's own musculature. Through functional electrical stimulation, it is possible to implement movement and force control by injecting electrical currents directly into the user's motoneurons, effectively acting in parallel to the peripheral nervous system. The possible applications have not yet been fully investigated. This work presents the sensor modalities, the control architectures, and the hardware necessary to drive human limb movements through functional electrical stimulation. Firstly, a self-developed upper body tracker based on inertial measurement units is introduced. Secondly, the focus shifts onto theoretical and experimental assessments of various approaches to measure and estimate human force output, as well as to provide assistance through exosuits and lightweight exoskeletons. Finally, a self-produced, wearable functional electrical stimulation system is introduced, which can enforce impedance control of human limbs. This system is shown to be capable of producing multi-joint movements, and of driving the user's limb to arbitrary poses in the peri-personal space. The combination of external muscles and nerves opens many possible research venues in the field of human-machine interfaces, blurring the boundary of the human's and machine's agency and capabilities.

Zusammenfassung

Bei Mensch-Maschine-Schnittstellen kann das neuromuskuläre System durch eine Vielzahl von Sensormodalitäten überwacht werden, um die beabsichtigte Bewegung und Kraftabgabe eines Nutzers an eine Maschine zu ermitteln und zu übertragen. Ebenso kann das neuromuskuläre System durch viele Mechanismen stimuliert werden, um somatosensorisches Feedback von einem Sensorsystem an den Nutzer weiterzugeben oder externe Unterstützung zu bieten. In den letzten Jahrzehnten konzentrierte sich die Forschung im Bereich der tragbaren Robotik auf die Unterstützung menschlicher Nutzer bei der Ausführung körperlich fordernder Aufgaben und bei der Ausübung einer erhöhten Kraft, indem sie in vollständig starre robotische Exoskelette gehüllt wurden. In jüngerer Zeit ging man zu leichteren Strukturen über und kam schließlich zu kontinuumsbasierten weichen Exosuits, die sich auf das eigene Skelett des Nutzers als tragende Struktur stützen. Derzeit wird ein neues Paradigma erforscht, das sich zunehmend auf die Muskulatur des Nutzers selbst stützt. Durch funktionelle elektrische Stimulation ist es möglich, Bewegungs- und Kraftsteuerung zu implementieren, indem elektrische Ströme, parallel zum peripheren Nervensystem, direkt in die Motoneuronen des Nutzers eingespeist werden. Die möglichen Anwendungen in der rehabilitativen und assistiven Robotik wurden noch nicht vollständig untersucht. Diese Arbeit stellt die Sensormodalitäten, die Steuerungsarchitekturen und Hardware vor, die erforderlich sind, um die Bewegungen der menschlichen Gliedmaßen durch funktionelle elektrische Stimulation zu steuern. Zunächst wird ein selbst entwickeltes Oberkörpertracker vorgestellt, das ausschließlich aus Inertialmessgeräten besteht. Zweitens fokussiert man sich auf der theoretischen und experimentellen Bewertung verschiedener Ansätze zur Messung und Schätzung der menschlichen Kraftleistung sowie zur Unterstützung durch Exosuits und leichte Exoskelette. Schließlich wird ein eigens für diesen Zweck konstruiertes, tragbares funktionelles elektrisches Stimulationssystem vorgestellt, das eine Impedanzsteuerung der menschlichen Gliedmaßen ermöglicht. Es wird gezeigt, dass dieses System in der Lage ist, mehrgelenkige Bewegungen zu erzeugen und die Gliedmaßen des Nutzers in beliebige Posen im peri-personalen Raum zu bringen. Die Kombination von externen Muskeln und Nerven eröffnet viele Möglichkeiten für die Forschung auf dem Gebiet der Mensch-Maschine-Schnittstellen und verwischt die Grenze zwischen den Handlungsmöglichkeiten und Fähigkeiten von Mensch und Maschine.

Contents

List of Publications

Core publications

This dissertation is comprised of and written around the findings from the following peer-reviewed core publications. Quoted names are utilized throughout the text for ease of reference and exposition.

Peer-reviewed journal articles

Publication 1: "Human-in-the-loop assessment of an ultralight, low-cost body posture tracking device" reported in Chapter A.1

[1] **Marek Sierotowicz**, Mathilde Connan, and Claudio Castellini. "Human-in-the-loop assessment of an ultralight, low-cost body posture tracking device" In *Sensors* 20(3), 2020, p. 890, DOI: 10.3390/s20030890

Publication 2: "EMG-driven machine learning control of a soft glove for grasping assistance and rehabilitation", reported in Chapter A.2

[2] **Marek Sierotowicz**, Nicola Lotti, Laura Nell, Francesco Missiroli, Ryan Alicea, Xiaohui Zhang, Michele Xiloyannis, Rüdiger Rupp, Emese Papp, Jens Krzywinski, Claudio Castellini, and Lorenzo Masia. "EMG-driven machine learning control of a soft glove for grasping assistance and rehabilitation" In *IEEE Robotics and Automation Letters* 7(2), 2022, pp. 1566-1573, DOI: 10.1109/LRA.2021.3140055

Publication 3: "Unobtrusive, natural support control of an adaptive industrial exoskeleton using force myography", reported in Chapter A.3

[3] **Marek Sierotowicz**, Donato Brusamento, Benjamin Schirrmeister, Mathilde Connan, Jonas Bornmann, Jose Gonzalez-Vargas, and Claudio Castellini. "Unobtrusive, natural support control of an adaptive industrial exoskeleton using force myography" In *Frontiers in Robotics and AI* 9, 2022, p. 919370, DOI: 10.3389/frobt.2022.919370

Publication 4: "Omnidirectional endpoint force control through Functional Electrical Stimulation", reported in Chapter A.4

[4] **Marek Sierotowicz**, and Claudio Castellini. "Omnidirectional endpoint force control through Functional Electrical Stimulation" In *Biomedical Physics & Engineering Express* 9(6), 2023, p. 065008, DOI: 10.1088/2057-1976/acf04b

Peer-reviewed Conference Publications

Publication 5: "A Comprehensive Framework for the Modelling of Cartesian Force Output in Human Limbs", reported in Chapter A.5

[5] **Marek Sierotowicz**, Nicola Lotti, Rüdiger Rupp, Lorenzo Masia, and Claudio Castellini. IEEE. "A Comprehensive Framework for the Modelling of Cartesian Force Output in Human Limbs" In *2022 International Conference on Rehabilitation Robotics*, 2022, pp. 1-6, DOI: 10.1109/ICORR55369.2022.9896547

Publication 6: "Robot-inspired human impedance control through functional electrical stimulation", reported in Chapter A.6

[6] **Marek Sierotowicz**, and Claudio Castellini. "Robot-inspired human impedance control through functional electrical stimulation" In *2023 International Conference on Rehabilitation Robotics*, 2023, pp. 1-6, DOI: 10.1109/ICORR58425.2023.10304750

Related publications

The author also contributed to additional works that further support the research discussed in this dissertation.

Peer-reviewed Journal articles

[7] **Marek Sierotowicz**, Bernhard Weber, Rico Belder, Kristin Bussmann, Harsimran Singh, and Michael Panzirsch. “Investigating the influence of haptic feedback in rover navigation with communication delay” In *Haptics: Science, Technology, Applications: 12th International Conference, EuroHaptics* 2020, pp. 527-535.

[8] Mathilde Connan, **Marek Sierotowicz**, Bernd Henze, Oliver Porges, Alin Albu-Schäffer, Maximum Alejandro Roa, and Claudio Castellini. Learning teleoperation of an assistive humanoid platform by intact and upper-limb disabled users. In *Converging Clinical and Engineering Research on Neurorehabilitation IV: Proceedings of the 5th International Conference on Neurorehabilitation*, 2020, pp. 165-169.

Peer-reviewed Conference publications

[9] Mathilde Connan, **Marek Sierotowicz**, Bernd Henze, Oliver Porges, Alin Albu-Schäffer, Maximum Alejandro Roa, and Claudio Castellini. "Learning to teleoperate an upper-limb assistive humanoid robot for bimanual daily-living tasks" In *Biomedical Physics & Engineering Express*, 8(1), 2021, p. 015022.

[10] Michael Panzirsch, **Marek Sierotowicz**, Revanth Prakash, Harsimran Singh, and Christian Ott, "Deflection-Domain Passivity Control of Variable Stiffnesses Based on Potential Energy Reference" In *IEEE Robotics and Automation Letters*, 7(2), 2022, pp. 4440-4447.

[11] **Marek Sierotowicz**, and Claudio Castellini "A surface neuromuscular electrical stimulation device for universal Cartesian force control in humans", In *Journal of Artificial Organs*, 46.11, 2022, pp. e323-e327.

[12] **Marek Sierotowicz**, Marc-Anton Scheidl, Claudio Castellini, "Adaptive filter for biosignal-driven force controls preserves predictive powers of sEMG" In *Proceedings of 7th International Conference on Rehabilitation Robotics*, 2023, pp. 1-6.

Master’s thesis

[13] **Marek Sierotowicz**, "Fusion of IMU and Muscular Information in Order to Solve the Limb Position Effect", Technical University of Munich, 2019.

Patent

[14] **Marek Sierotowicz**, Jean-Pascal Lutze, "Verfahren zur Rückkopplung von exogenen Kräften an einen Nutzer mittels elektrischer Muskelstimulation, Steuereinheit zur Steuerung einer Kraftrückkopplungsvorrichtung, Kraftrückkopplungsvorrichtung und Verwendung einer Steuereinheit oder einer Kraftrückkopplungsvorrichtung", DE Patent No. 102020122551A1 2022.03.03, *Pending*

List of Figures

List of Tables

Acronyms and abbreviations

ADL Activities of Daily Living

AIROB Assistive Intelligent ROBotics

AR Augmented Reality

ARV Average Rectified Value

BJT Bipolar Junction Transistor

DoA Degree of Actuation

DoF Degree of Freedom

e.g. *exempli gratia* (for example)

EE End Effector

EEG Electroencephalography

EMG Electromyography

EMS Electrical Muscular Stimulation

Eq. Equation

et al. *et alia* (and others)

FDA Food and Drug Administration

FES Functional Electrical Stimulation

FFLS Fingertip Force Linear Sensor

Fig. Figure

FK Forward Kinematics

FMG Force Myography

FSR Force Sensing Resistor

GMM Gaussian Mixture Model

hdFES high density Functional Electrical Stimulation

HMI Human-Machine Interface

HRI Human-Robot Interaction

i.e. *id est* (that is)

IED Inter-Electrode Distance

IK Inverse Kinematics

IMU Inertial Measurement Unit

MEMS Micro Electro-Mechanical Systems

ML Machine Learning

NMES Neuro-Muscular Electrical Stimulation

NN Nearest Neighbour

nRMSe normalized Root Mean Square error

PCA Principal Component Analysis

PCB Printed Circuit Board

pHRI physical Human-Robot Interaction

PID Proportional Integrative Derivative

RBF Radial Basis Function

RFF Random Fourier Features

RMSe Root Mean Square error

RQ Research Question

RR Ridge Regression

s.t. such that

SCI Spinal Cord Injury

sEMG surface Electromyography

SI *Système Internationals d’unités* (international system of units)

SR Success Rate

STA Soft Tissue Artefacts

Tab. Table

TAC Target Achievement Control

TBI Traumatic Brain Injury

TCT Task Completion Time

TDPA Time Domain Passivity Approach

TENS Transcutaneous Electrical Neuro-Muscular Stimulation

VR Virtual Reality

vs. *versus* (against)

w.r.t. with respect to

WLOG Without Loss Of Generality

WRMSD Work-Related Musculoskeletal Disorder

Nomenclature

a	A scalar. Scalars are non-bold, both upper and lower case.
$\boldsymbol{a}$	A vector, e.g. $\boldsymbol{a} \in \mathbb{R}^{m}$. Vectors are noted in bold lower case. The i-th individual component of a vector $\boldsymbol{a}$ is denoted as a_i. In expressions, vectors can behave like matrices of dimensionality $\mathbb{R}^{m\times 1}$.
$\{c\}$	This notation indicates a Cartesian coordinate frame.
$\boldsymbol{a}^{\{c\}}$	This notation indicates a vector $\boldsymbol{a}$ expressed in a coordinate frame $\{c\}$.
$\boldsymbol{A}$	A matrix, e.g. $\boldsymbol{A} \in \mathbb{R}^{m\times n}$. Matrices are noted in upper case and bold script. The element of a matrix belonging to the i-th row and the j-th column is denoted as $A_{i,j}$. Occasionally, vectors might be presented as column matrices of the form $\boldsymbol{A} \in \mathbb{R}^{m\times 1}$. In such cases, the vector and matrix notation is interchangeable.
$\boldsymbol{I}$	This indicates a square unit matrix of unspecified dimensionality. For all the matrix elements on the diagonal we have $I_{i,i} = 1$, while all other elements are 0.
$\boldsymbol{I}_{a\times b}$	This indicates a unit matrix of a columns and b rows, s.t. its elements $I_{i,j} = 1$ if $i = j$ and $I_{i,j} = 0$ if $i \neq j$.
$\boldsymbol{A}^{T}$	This indicates the transpose of a matrix $\boldsymbol{A} \in \mathbb{R}^{m\times n}$, s.t. $\boldsymbol{A}^{T} \in \mathbb{R}^{n\times m}$. Each element $T_{i,j}$ of the transposed matrix is equal to the element $A_{j,i}$ of the original matrix $\boldsymbol{A}$. If applied to a vector $\boldsymbol{a} \in \mathbb{R}^{l}$, the transpose operator turns it into a row vector of the form $\boldsymbol{a}^{T} \in \mathbb{R}^{1\times l}$.
$\boldsymbol{A}^{-1}$	This indicates the inverse of a matrix $\boldsymbol{A} \in \mathbb{R}^{n\times n}$, so that $\boldsymbol{A}^{-1}\boldsymbol{A} = \boldsymbol{A}\boldsymbol{A}^{-1} = \boldsymbol{I}_{n\times n}$.
$\boldsymbol{A}^{\#}$	This indicates the left Moore-Penrose pseudo inverse of a matrix $\boldsymbol{A} \in \mathbb{R}^{m\times n}$, which is defined as $\left(\boldsymbol{A}^{T}\boldsymbol{A}\right)^{-1}\boldsymbol{A}^{T} \in \mathbb{R}^{n\times m}$. If such a matrix can be calculated, which is contingent on $\boldsymbol{A}^{T}\boldsymbol{A}$ being full rank, we have that $\boldsymbol{A}^{\#}\boldsymbol{A} = I_{n\times n}$, but unlike the proper inverse of a square matrix, $\boldsymbol{A}\boldsymbol{A}^{\#}$ is not defined, and would require a right pseudo inverse.
$\boldsymbol{A}^{-T}$	This indicates the inverse of the transpose of a matrix $\boldsymbol{A}$, s.t. $\boldsymbol{A}^{-T} = \left(\boldsymbol{A}^{T}\right)^{-1} = \left(\boldsymbol{A}^{-1}\right)^{T}$.
$\boldsymbol{a} \times \boldsymbol{b}$	Vectorial cross product. Both $\boldsymbol{a}$ and $\boldsymbol{b}$ have to be 3-dimensional vectors.
$\lfloor \boldsymbol{a} \rfloor_{\times}$	The skew symmetric matrix derived from $\boldsymbol{a}$, s.t. $\lfloor \boldsymbol{a} \rfloor_{\times}\boldsymbol{b} = \boldsymbol{a} \times \boldsymbol{b}$, with $\boldsymbol{a}, \boldsymbol{b} \in \mathbb{R}^{3}$ and $\lfloor \boldsymbol{a} \rfloor_{\times} \in \mathbb{R}^{3\times 3}$.

$\boldsymbol{a} \cdot \boldsymbol{b}$	Scalar product of two vectors of same dimensionality $\boldsymbol{a}, \boldsymbol{b} \in \mathbb{R}^m$. This notation is distinct from matric product, which has no symbol. If vectors are converted to matrices $\boldsymbol{A}, \boldsymbol{B} \in \mathbb{R}^{m \times 1}$, s.t. $A_{i,1} = a_i$ and $B_{i,1} = b_i$, the scalar product can be expressed as $\boldsymbol{A}^T \boldsymbol{B} \in \mathbb{R}$.
Δ	This notation indicates a variation in a scalar, vector or matrix.
$\boldsymbol{e}$	This notation indicates a unit vector or direction of arbitrary dimensionality, i.e. a vector whose Euclidean norm is 1.
δ	This notation indicates a small, but not differential, variation in a scalar, vector or matrix.
$\nabla_{\boldsymbol{a}}$	This notation indicates a vectorial partial derivative operator over a vector $\boldsymbol{a} \in \mathbb{R}^m$ of the form $[\frac{\partial}{\partial a_1}, ..., \frac{\partial}{\partial a_m}]^T$. This operator is applied on either scalars or vectors.
$\dot{a}$	This notation indicates the first order derivative over time $t \in \mathbb{R}$, and is equivalend to $\frac{d}{dt}$.
$\ddot{a}$	This notation indicates the second order derivative over time $t \in \mathbb{R}$, and is equivalend to $\frac{d}{dt}\left(\frac{d}{dt}\right)$.
$Null(\boldsymbol{A})$	This notation indicates the null space of a matrix $\boldsymbol{A} \in \mathbb{R}^{m \times n}$, which is the subset of $\mathbb{R}^n$ comprising all non-zero vectors $a \in \mathbb{R}^n$ s.t. $\forall \boldsymbol{a} \in Null(\boldsymbol{A})\ \boldsymbol{A}\boldsymbol{a} = \boldsymbol{0}$
$[u]$	This notation indicates a measurement unit. Unless otherwise specified, SI standard units are used everywhere. On plots, if no unit is specified, or if the notation [] or $[*]$ is used, the indicated property is normed, and has no physical dimension. In these cases, the plots are meant to convey qualitative properties.
$\approx$	Approximately equal.
$\mathcal{N}(\mu, \sigma^2)$	Normal (or Gaussian) probability density distribution with mean μ and standard deviation σ.
$\mathcal{O}$	Asymptotic upper complexity bound.
$\mathcal{U}_{[a,b]}$	Continuous uniform probability density distribution defined over an interval $[a, b] \subset \mathbb{R}$.
$\overset{!}{=}$	Must be equal, usually based on previous considerations.

1 Introduction

Assistive robotics as a branch of medical robotics studies solutions that have the main goal of aiding the functioning of a patient, ideally enabling them to perform as well as an able-bodied individual, or to augment the physical capabilities of an able-bodied user [15, 16]. While the ultimate goal of assistive robotics is to facilitate and assist movement, these systems can be seen as having the fundamental goal of amplifying the voluntary force output of their user, so as to improve their mobility or enable them to perform tasks in their surroundings or even remotely [15].

In the context of assistive robotics, one of the most common device classes used to aid the movement of motion-impaired patients is that of exoskeletons [17]. These consist of segmented robotic mechanisms connected to individual body segments of the user. Exoskeletons are, in general, robotic devices built in accordance with the traditional design philosophy of rigid components and joint-link chains. These features offer many advantages, most crucially exact observability of the system's state and ease of control. However, the stiffness and rigidity of traditional exoskeletons can lead to uncomfortable and potentially unsafe interactions with the user [18].

In recent years, with the improvement of computational power and the progress in machine learning techniques, alternative solutions have emerged, with the potential to improve Human-Robot Interaction (HRI) and potentially open new possibilities in regard to rehabilitation. First and foremost, many passive or semi-passive exoskeletons are now commercially available and have been demonstrated to reduce fatigue and strain on the user during several types of activities, such as overhead work using heavy tools, as well as to lower the incidence of Work-Related Musculoskeletal Disorders (WRMSDs), at least in the short term [19, 20, 21]. These commercial devices can typically be seen as lighter, under-actuated versions of conventional robotic exoskeletons, which still rely on a rigid structure, but offer transparent, often passive support. This capillary diffusion has nonetheless sparked renewed interest in research seeking to improve on these concepts. An example is adaptive assistance capable of regulating the support forces provided by these lighter exoskeletons based on the user's posture and lifted mass [21, 22]. This integration of active elements should still make good use of the developments in ergonomics that these commercial devices have brought over recent years.

Besides these lightweight passive or semi-passive support devices, compliant versions of traditional exoskeletons, called exosuits [23], have seen a rise in popularity. These devices propose to aid the actuation of movements by exerting forces and pressures on the user, but do not usually feature load-bearing structures in the traditional sense, as opposed to typical exoskeletons. Some exceptions exist in particular devices that can arguably bear weight thanks to inflatable elements [24, 25, 26], as opposed to tendon-driven exosuits, which can only pull on the user through a harness. For this reason, exosuits, and especially tendon-driven exosuits, are sometimes called *exomuscles* [27]. These devices pose several challenges from the point of view of system observability, actuation and control, but they do lead to generally safer human-machine interactions, as well as increased comfort for the wearer [18]. Because of the absence of the load-bearing structure, exosuits are also typically lighter and more promising for the purpose of active assistance, which would require complete portability in the ideal case.

Functional Electrical Stimulation (FES) is a technique by which, through the injection of electrical currents, motor neurons are caused to fire, therefore causing muscular contractions [28], thereby exploiting the user's existing anatomy to assist movements even further. FES could be seen as going one step beyond exosuits, not even applying support forces through artificial muscles, but merely providing a control signal of sorts that activates the user's own muscles, thus causing the desired motion. If exoskeletons can be seen as operating in parallel to the user's muscular-skeletal system and exosuits as operating in parallel to the user's muscles only, FES systems could be seen as operating parallel to the nervous system. If exosuits are sometimes called exomuscles, by the same token FES systems could be designated as *exonerves*. Figure 1.1 shows an artistic rendition of the progression from kinematics modeling to assistance through exonerves and wearable robotics.

FES has gained traction in the last few decades as a way to both assist movement and facilitate rehabilitation of patients affected by a variety of ailments, first and foremost Spinal Cord Injury (SCI) [29, 30] and stroke [31, 32, 33], as well as Traumatic Brain Injury (TBI) [34, 35]. FES presents some advantages compared to functional assistance of movement through external aids such as exoskeletons and exosuits, mainly because, under stimulation, the work is provided by the user's own muscles. This has potential benefits in terms of rehabilitation and neurological recovery [36], and can avoid various secondary ill-effects of inactivity such as atrophy. Unfortunately, FES poses more challenges from a control standpoint than even exosuits, which themselves are typically more difficult to drive than exoskeletons. Because of this, many hybrid solutions have been proposed that integrate FES and traditional wearable as well as endpoint-coupled robotics [32, 37], i.e. robotic mechanisms only connected to the user's extremities, and not to any other body segment, as well as exosuits [38].

1.1 General scope

The core publications presented in this dissertation deal with some of the main issues pertaining to the assistance of movement through FES. These are subdivided into posture tracking [1, 5], the monitoring and estimation of force output [2, 3], assistance through compliant wearable exosuits [2] and lightweight exoskeletons [3], and general-purpose multi-joint force control through FES [4, 6]. Other discussed topics comprise the role of force feedback as well as force output estimation in telerobotics and assistive robotics.

When attempting to assist movements through electrical stimulation currents, it quickly becomes clear that the human musculoskeletal system presents more technical challenges from a control science standpoint compared to traditional robot systems. For most intents and purposes pertaining to functional movements, the skeletal system can be modeled as a series of quasi-rigid links connected by rotational joints, as opposed to prismatic ones. Even with these approximations, it is not trivial to implement a practical and sufficiently precise method to monitor the configuration of this kinematic chain. The reason for this is that, even though the quasi-rigid structure of the skeleton would make it easy to compute forward kinematics on it, it is challenging to accurately measure its joint positions. This is due to the compliance of the superficial soft tissues, which would cause any sensor worn on top of them to shift relative to the skeletal structure during movement, leading to so-called Soft Tissue Artefacts (STA) [39]. Furthermore, if we are interested in computing the force output in joint or Cartesian space, we have to consider that the muscular system is inherently compliant, with geometrical characteristics that can vary greatly across different postures [40, 41]. Additionally, muscles exhibit hysteretic and time-variant or transient behavior [42, 43]. Consequently, the torque output of a given muscle group at the joint level can be hard to predict. The same applies, in some respects, to certain assistive devices such as tendon-driven exosuits, with the difference that such devices can be more easily fit with sensors suitable to monitor their full dynamic state, i.e. both in terms of positional coordinates as well as in terms of endogenous and exogenous forces. FES presents an additional complication; namely, the dependency between muscular force output and electrical stimulation is less predictable than the response of an actuator which might be employed in an exosuit or an exoskeleton, adding an ulterior layer of non-linear behavior to the system [44].

This gap can be bridged by integrating some form of force sensing in the control loop of the FES system either online or during a calibration sequence prior to normal operation, as illustrated in Chapters A.4 and A.6. At any rate, it is an imperative requirement for stable control to provide a fitting form of feedback to the system, be it in the form of direct sensing or of an estimate. In human users, typical sensors to measure positional parameters are usually less cumbersome compared to those measuring force outputs, and they generally entail less interference with normal movements. This is exemplified in Chapters A.1 compared to, e.g., Chapters A.2, A.4, and A.6. Positional data have to be converted into generalized force outputs through body dynamics [45] or, as illustrated in Chapter A.2, by imposing a known dependency between positional and force coordinates. The latter approach still requires some interference with the user's natural movements, as imposing this dependency usually entails some form of (semi-) rigid harness. If, however, the imposed position-to-force dependency can be actively changed, for example through an impedance control, the trade-off between precision in force output measurement and interference to natural motion could be negotiated based on the task at hand. A further way to directly measure the force output of a user without constraining the limb is by making use of an actuated set of tendons fitted with longitudinal force sensors, as presented in [46], which should imitate the function of the proprioceptors detecting muscle load and tension forces, acting in parallel to the user's muscular system, as discussed in Section 2.2.

On the other hand, it is possible to estimate force output caused by muscle contractions by sensing muscular activity [47], as exemplified in Chapters A.2 and A.3. This can generally be done without interfering with movements, even though many studies in this sense present results gathered from isometric setups [12, 48]. Nevertheless, sensing muscular activity can provide an estimation of force output both at the joint level and in the task space, provided that it is possible to measure the contraction of all independently controlled muscle groups involved in the movement of interest. This topic is discussed in Sections 4.5 and 4.6.

Provided a fitting form of force output monitoring or estimation, in order to project this force output from a generalized task space onto joint space and actuator space, it is necessary to know the user's posture. Besides the use of protractors, which have the advantage of directly measuring kinematic angles as opposed to absolute body segment orientation, but can lead to large projection errors in case of misalignment, most posture trackers involve the use of stationary equipment. In recent years, wearable solutions tend to make use of Inertial Measurement Unit (IMU) devices. The core publications of the present thesis that discuss this topic are mainly concerned with this sensor modality for posture tracking [1].

1.2 Structure of the thesis

The works presented in this dissertation focus on the development of sensor modalities and actuation strategies to facilitate movement assistance through both FES as well as external aids. Each of the core publications focuses on one main aspect of the practical implementation of a transcutaneous FES-based assistive and rehabilitative device.

The main body of the dissertation presents the state of the art, discussed in Chapter 2, the aims of this thesis and the Research Questions (RQs) in Chapter 3, while Chapter 4 presents the methods employed in the core publications, as well as pertaining to some yet unpublished results. The main results are presented in Chapter 5, and their significance and contribution is also discussed therein. The conclusions and prospects for future research are presented in Chapter 6.

In Appendix A, the core publications are reported in full-text form and subdivided into chapters. The relevant information regarding citation style and copyright is reported before each full-text copy.
Chapter A.1 presents the BodyRig, a self-contained posture tracker based on IMU devices, which can provide posture data to the control loop of a FES-based system. The BodyRig was used in several of the other core publications.
Chapter A.2 presents a wearable grasp-assisting glove driven through Electromyography (EMG), which demonstrates some of the principles of using a compliant exosuit to provide assistance in movements while monitoring output forces in a non-static setup, which represents a proof of concept for an assistive device also used as a force output sensor.
Chapter A.3 presents a semi-active shoulder exoskeleton able to provide adaptive support based on Force Myography (FMG) measurements. This is a further proof of concept for a force output estimator that does not limit the user's range of motion and can successfully be used to provide adaptive assistance when lifting weights overhead, and could also be used for intent prediction in FES setups.
Chapter A.5 presents the MyoCeption, a prototype Transcutaneous Electrical Neuro-Muscular Stimulation (TENS)-based device designed to test various control and hardware concepts to

provide electrical stimulation for movement support, force output control, and force feedback. In particular, this chapter focuses on a comparison of the MyoCeption's musculoskeletal model and a third-party benchmark model.
Chapter A.4 presents the results of a user study with the aim of characterizing the quality of force output control of the MyoCeption driven by the musculoskeletal model presented in Chapter A.5.
Finally, Chapter A.6 presents an early analysis of a larger cohort testing the MyoCeption in a positional control task. In this experiment, the MyoCeption does not employ a musculoskeletal model, but rather a Ridge Regression (RR) predictor that provides an estimate of the joint torque output based on the stimulation currents injected. This model is then integrated into a loop featuring an impedance control able to drive the user's arm toward a given target.

Appendix B reports the relevant information about the related publications. Pending patents are not reported.

Appendix C contains the copyright statements relevant to the publications reported in full text and to the original images produced for this thesis.

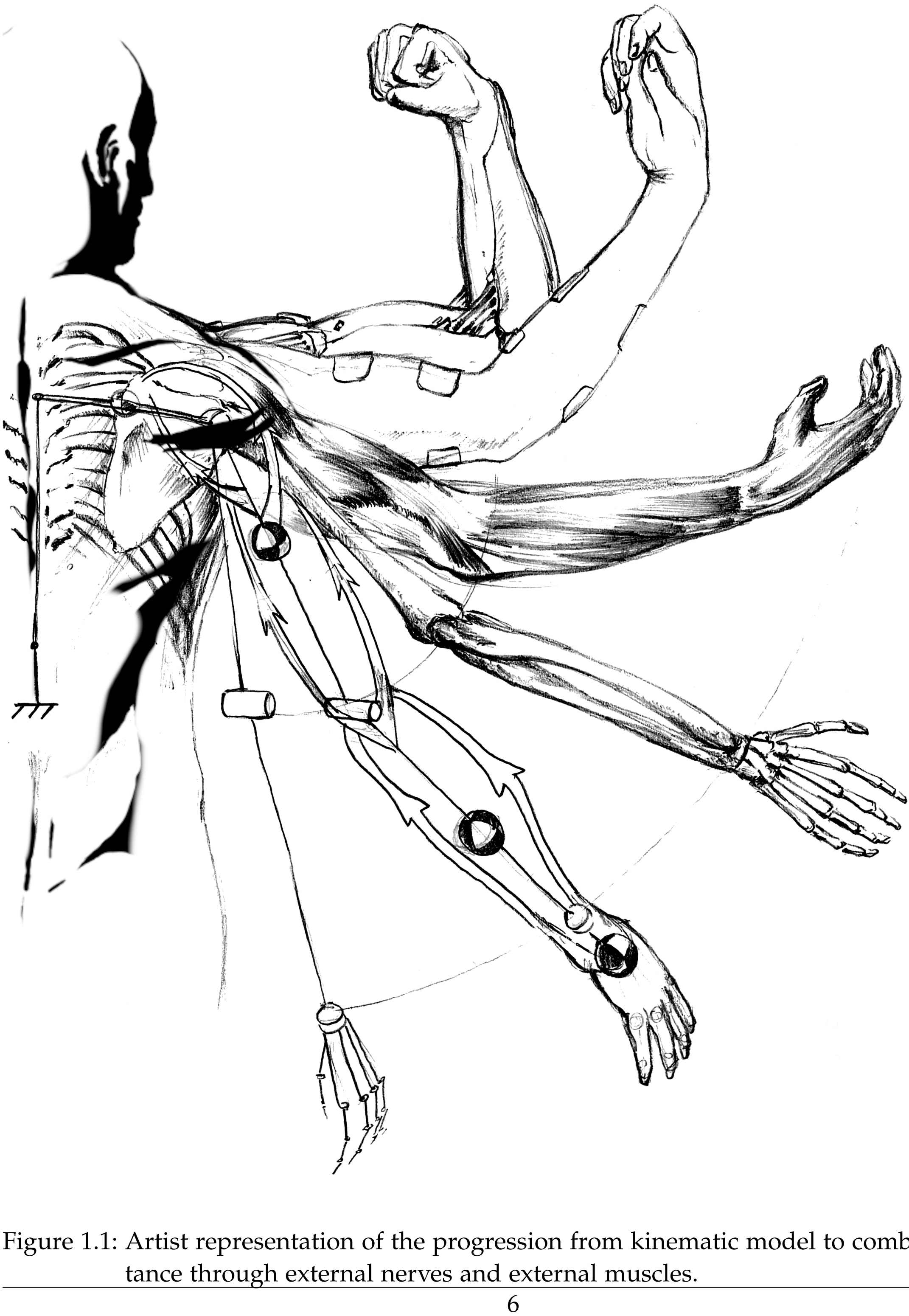

Figure 1.1: Artist representation of the progression from kinematic model to combined assistance through external nerves and external muscles.

2 State of the art

The implementation of wearable devices for the assistance of movements requires the solution of many different problems pertaining to many diverse aspects. In this chapter, the state of the art shall be discussed as it pertains to the core publications. The first topic is posture tracking through self-contained wearable sensors, as well as real-time muscle geometry estimation based on posture. Secondly, the core publications deal with force output estimation and measurement obtained through muscular activity sensors and wearable exosuits, respectively, as well as examining the role played by force output and posture measurement in the calibration and control of FES-based systems. Finally, the performance of FES-facilitated movement and force control are explored.

2.1 Body posture tracking and muscle routing

Many possibilities exist for the monitoring of human posture. Due to the compliant nature of the tissues enveloping the skeleton, it is not trivial to measure joint angles or absolute orientation of individual body segments, as any wearable sensors coupled to the user's body could experience misalignment w.r.t. the underlying skeletal structure. Therefore, the best results, in terms of precision, accuracy and bandwidth, can be achieved through absolute position monitoring by means of, e.g., optical tracking using either cameras and, in some cases, light sources mounted around the user. Commonly used devices that employ this approach are, for example, the Vicon marker-based tracking systems [49, 50] and the VIVE VR systems [51]. However, setups which rely on optical tracking through external cameras are not wearable. This does not exclude the use of this technique in rehabilitative applications, but it is a major argument against its use to provide assistance during Activities of Daily Living (ADL).

Some setups propose to use egocentric cameras mounted on the user in order to directly observe the wearer's limb pose [52, 53]. A commercially successful example in this sense is Microsoft's HoloLens [54]. These approaches have the advantage of allowing for the measurement of the complete transform from the camera or light sensor to the light source or marker, in terms of both translation and rotation. However, in the case of HoloLens, the performance can be insufficient when the marker itself is moving, as would be the case when attempting to track the position of the wearer's limbs, and the user's range of motion might be limited due to the necessity of an uninterrupted line of sight existing between the optical sensor and the target [52].

Most wearable body trackers use a different approach, namely to measure the orientation of individual body segments, either in relative or absolute terms. The positions are then computed by using Forward Kinematics (FK) and, in some cases, various kinds of sensor fusion applied to IMU-derived signals [55]. The most immediate implementation is that of fitting the user with protractors measuring the relevant joint angles [56] through goniometric techniques. This method can also be used if the user is wearing an exoskeleton. This approach, however, might lead to sizable estimation errors or cause discomfort to the user due to the possibility of misalignment between the protractors and the joints themselves [55].

IMUs are sensors that encompass several modalities. These are capable, in most cases, of detecting acceleration through a seismic mass, rotation rate through a gyroscope, and direction of the magnetic field through a magnetometer. These measurements can be used to track the sensor's orientation and, to some extent, its position. Wearing IMUs is generally more comfortable than wearing protractors, as the sensors can be worn away from joints, and while IMU-based kinematics calculations can still suffer from sensor misalignments, the sensors generally do not need to be exactly aligned to the joints and the functional axes.

The *de facto* state of the art in IMU-based body tracking setup is the Xsens motion capture suit [55]. This setup allows for high bandwidth measurements of the human movements, and can even detect different gait schemes. The system is, however, arguably ill-fitted for bespoke applications, such as those in patient assistance. The Xsens system is not sufficiently modular, and is rather designed to be a general-purpose whole-body tracking device. Furthermore, the system autonomy is arguably too limited for daily use, which would be a requirement for an assistive device.

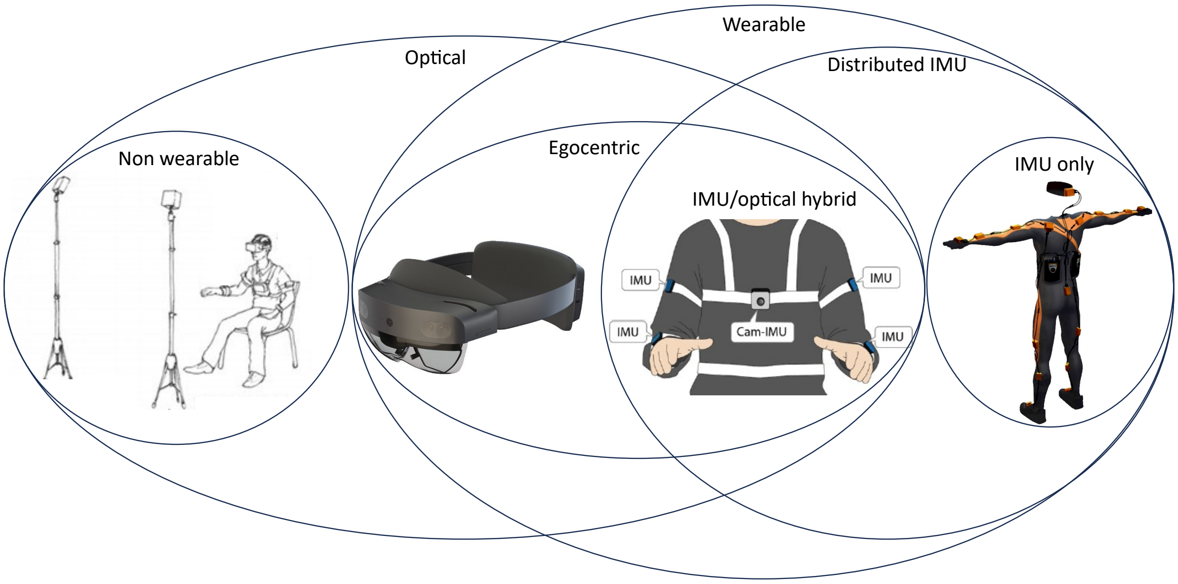

Figure 2.1: Taxonomy of various non-goniometric posture tracking techniques subdivided based on wearability and use of optical tracking as opposed to distributed IMUs. From left to right, an exemplification of a body tracking system relying on external equipment, like the Vicon tracking system or the VIVE VR setup, HoloLens 2, a hybrid IMU/egocentric camera system, and the Xsens IMU-based motion capture suit. Images from [1, 52, 55, 57]

In recent years, the advent of cheap Micro Electro-Mechanical Systems (MEMS)-based IMUs has rendered them much more cost-effective and widely used. The BNO055 integrated IMU platform has been shown to provide precision that is in some cases comparable to the mit-300 IMUs used in the Xsens suit. Overall, the mt-300 provides better performance, but the price per unit is two orders of magnitude higher compared to the BNO055, which has served as the basis for at least one further generation of MEMS.

Posture tracking is paramount for the projection of desired forces from task space or Cartesian space onto joint space, but also for the estimation of muscle geometry. In the research community, one of the most widely used software for biomechanical modeling of the human body, and for the integration of real-life posture measurements in such models, is OpenSim [45]. This is an open-source software suite that includes, among other things, a number of solvers for direct and inverse kinematics, dynamics, biophysical modeling of, e.g., muscle activation dynamics and interactions with the environment. Not all of these solvers are capable of working in real-time, although some of them can and have been used in online applications for the control of, e.g., exoskeletons and exosuits [58]. In offline analyses, OpenSim musculoskeletal models can be used as benchmarks to compare against, as illustrated in Chapter A.5.

Musculoskeletal models often rely on the concept of line of action or line of force, by which a bundle of muscle fibers is approximated by means of a series of line segments along which the muscular force is assumed to act [59]. Such models associate one or several lines of action to each simulated muscle group, as exemplified in [60]. Canonically, a model based on line of action relies on a line running through the average centroid of the physiological cross-section along the whole length of the stimulated muscle groups, as introduced in [61] and, more recently, in [41]. Many studies have demonstrated how inhomogeneities in muscle activation can lead to great effects on joint torques. In the case of the musculoskeletal model used in [4] and [5], the line of action routing is based on the observation of functional effects during muscle contraction on the musculoskeletal system in a given position, as first introduced among others in [62].

In general it can be arduous to find a ground truth for muscle routing, especially during functional movements. In [41] Hainisch and colleagues demonstrated how muscle routing can be inferred from tomographic images. This approach, however, is only practical with the user at rest or with very specific motions and poses. Ultrasound imaging could provide information with regards to both muscle routing and contractile state [63, 64, 65], but in order to be useful in a functional setup this information needs to be coupled with a posture tracking setup, in order to project the measured muscular state onto joint space and then task space.

The main role of a musculoskeletal model in, e.g., a FES system is to estimate the direction of the torque vector that would be caused on the user's joints if a stimulation current were injected across one given electrode pair, as illustrated in Chapters A.4 and A.5. A properly calibrated musculoskeletal model can provide an estimate of both the direction of the stimulation-caused torque and its magnitude given the user's posture and the injected current intensity. Musculoskeletal models can be used in various further applications that do not require real-time capabilities, such as ergonomics. In this field, musculoskeletal models may be used to

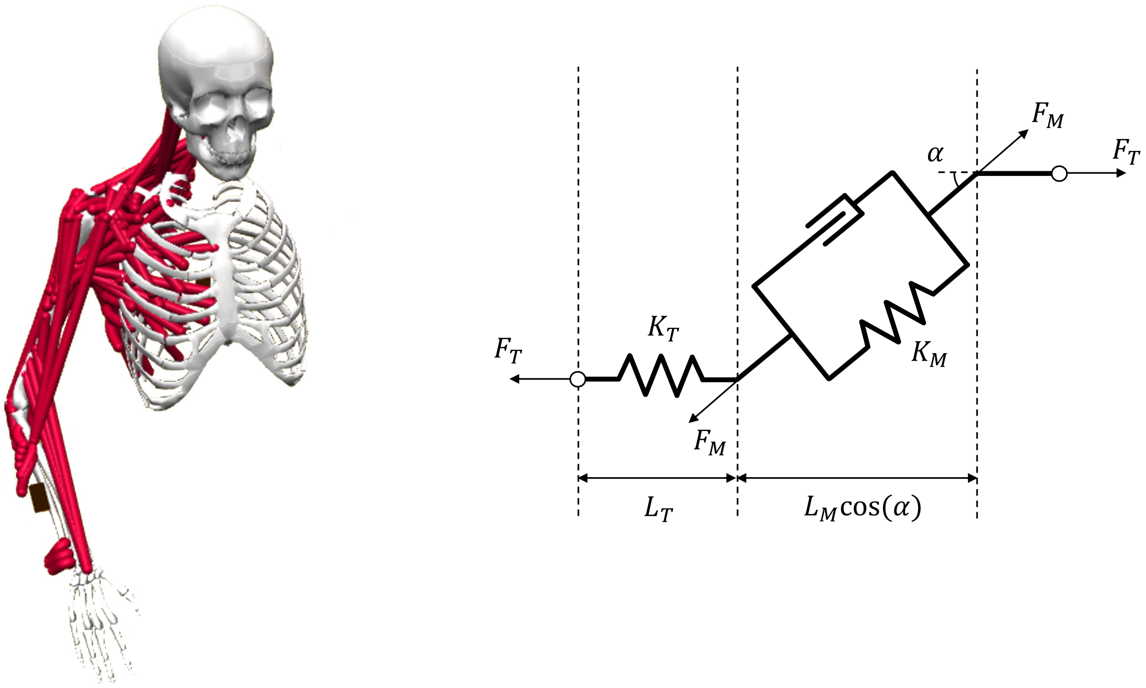

Figure 2.2: **Left:** An Opensim model including several muscle groups from the right upper limb. **Right:** Diagram of a Hill-type model including a compliant tendon of stiffness K_T and rest length L_T as well as an active muscle of resting length L_M with in-parallel arrangement of the muscle fiber stiffness K_M. The model includes the pinnation angle α. The force along the tendon is denoted as F_T, and the force along the muscle fiber's orientation is denoted as F_M.

identify the muscle groups most used during a given movement, or the foreseeable load the musculoskeletal system might be subjected to when performing a given task or activity [66, 67].

By contrast, an application requiring real-time capabilities and relying on musculoskeletal models is teleimpedance. In this case, an estimate of the joint stiffness is used to regulate robotic teleoperation controls. The intended stiffness can be inferred by calibrating a multi-muscle hill-type [68] musculoskeletal model [69], as depicted in Fig. 2.2. This provides a stiffness estimate for every muscle group, which can then be projected to joint space, provided that the muscular geometry is known. The direct observation of joint stiffness is not trivial, as stiffness is determined by muscle co-contraction which occurs in the muscular null space of net force output. In other words, muscular co-contraction, does not lead to measurable force output, which is instead determined by the net difference in contractile force. Furthermore, it is possible to demonstrate that muscular stiffness cannot be assumed to be linear w.r.t. contraction [70, 71]. Because of this, Hill-type muscle models feature a transfer function where the passive spring-like elements are typically modeled as having a contraction-dependent stiffness. It is therefore possible to increase the overall impedance of the muscle element by contraction, and by extension increase the stiffness of the joint. At any rate, if real-world stiffness measurements are used for the calibration of such models, they usually have to be acquired at the joint level [69]. Measuring the stiffness of muscles *in vivo* is however arguably possible through techniques like elastography [72], or generally by monitoring the propagation of mechanical shear waves along the muscular tissue [63, 73].

As is the case for force estimation, intended stiffness estimation can be implemented without explicit modeling of the muscle geometry and without real-world stiffness measurements. In [10], for example, a single joint example is presented. Therein, a Random Fourier Features (RFF)-based linear predictor is used to directly infer the intended rotational stiffness at the wrist based on EMG measurements acquired at the forearm. The model is calibrated on artificial labels, whereby a state of full co-contraction is associated with an arbitrary maximum joint stiffness value. The user is then relied upon in order to adjust their commands to the observed system behavior.

2.2 Exoskeletons and exosuits

Exoskeletons and exosuits both belong to the broader category of wearable robotics. Exoskeletons arguably represent the most affirmed subset of devices in wearable robotics [74], as they consist of non-compliant robots designed largely according to traditional design philosophy set up to surround the wearer and move alongside them, even though the types of controls to achieve this synergy have changed greatly over the years. More recently, other classes of devices have emerged, with different implications concerning the physical and functional interactions between the device and the wearer [75, 76]. In the following, some of the salient aspects of wearable robotics to be used to support movement in concurrence with both volitional efforts by the user and FES are examined.

2.2.1 Safety and human-device interactions

Traditional exoskeletons have gone through multiple paradigms. From early attempts, which often relied on pure position controllers [77], to more recent iterations with a higher emphasis on physical Human-Robot Interaction (pHRI), as presented in [78]. In recent times, lightweight, (semi)passive exoskeletons have emerged as the most practical solution for the general market [79, 80]. As it stands, however, these machines are rarely able to provide truly adaptable support. If they are, this support is seldom regulated based on muscular activity. Instead, usually a conscious and explicit effort by the user is required, such as shifting the center of mass in the case of lower-limb exoskeletons or giving commands through a wrist-worn input device. This is the case also for some active exoskeletons [81].

In recent years, so-called exosuits have attracted much interest in research. Exosuits are compliant, wearable devices. Various options exist for their actuation [23, 26]. For the purposes of movement assistance through FES, it is desirable that the exosuit be usable to both provide assistance against gravity in the more proximal joints, as well as to monitor the force output in real-time without limiting the user's range of motion [37, 38]. The support is necessary, as gravity compensation on proximal joints might not be possible or practical solely through electrical stimulation. This is the case e.g. in [29], where a robotic support is needed to counteract gravity.

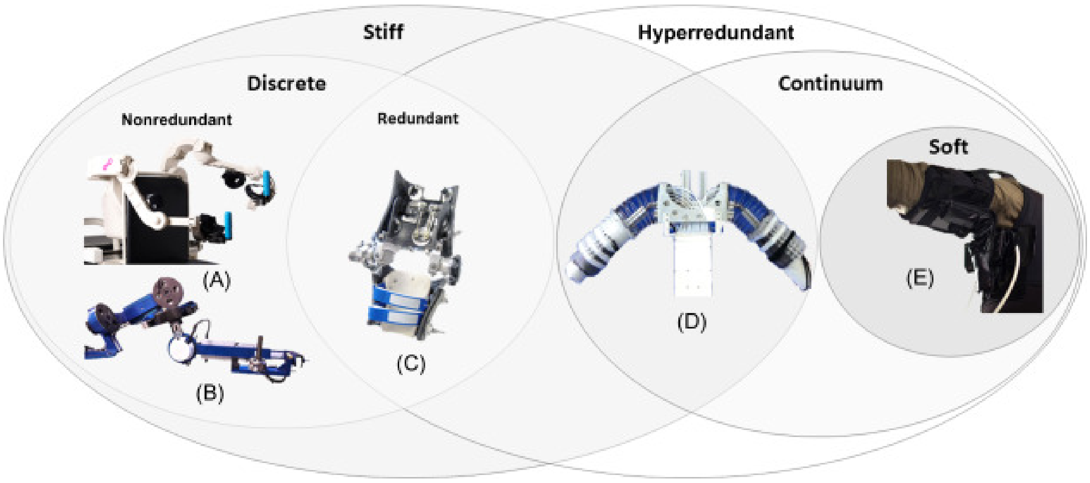

Figure 2.3: Classification of wearable robots for the upper limb based on DoF redundancy up to and including continuum-based soft robotic systems [82].

Fig. 2.3 shows a taxonomy, with examples, of wearable robotics systems based on structural redundancy and compliance. Actuated, rigid exoskeletons can largely be controlled like traditional robots, with most modern control concepts centered around the human-robot power exchange [78]. Exosuits, on the other hand, while typically featuring less complex hardware, often present more challenges from a control standpoint. For one, exosuits often present finite degrees of actuation, but potentially infinite degrees of freedom, in the case of a flexible, continuum-based wearable structure, such as is the case in [2]. Semi-active exoskeletons can be a practical compromise in that they often feature relatively simple, lightweight hardware, as they tend to offer a limited amount of actuated degrees of freedom. In the case of such devices, the most challenging aspect resides in controlling the system in a transparent and intuitive manner, without burdening the user with any excessive cognitive load. Furthermore, in order for such controllers to be viable in the industry or in the clinical field, the sensor modalities employed to provide such controllers with inputs should be practically and commercially viable.

On the topic of clinical viability, the clearance of wearable robotics as medical devices is a long and arduous one, which is largely informed by the observed potential risks entailed by human-robot interactions with conventional exoskeletons. The Food and Drug Administration (FDA), which is the agency competent for the risk assessment of exoskeletons as medical devices in the United States, released a comprehensive list of potential dangers associated with wearable robotic devices [83]. Therein, the FDA identifies numerous risks stemming from an inconvenient interaction between the user and the exoskeleton, both due to potential user error and to intrinsic properties of the materials and structures in contact with the user. While the FDA does not classify exosuits separately, many of the risks reported in [83] could be mitigated by the use of soft, bio-compatible materials and by avoiding rigid structures. The FDA does, however, make a distinction between active or powered and passive or non-powered exoskeletons, classifying the former as a class II medical device, generally requiring special controls to mitigate potential risks given by the active electro-mechanical components, and the latter as class I, thus requiring no special controls besides pre-market approval [84]. Ac-

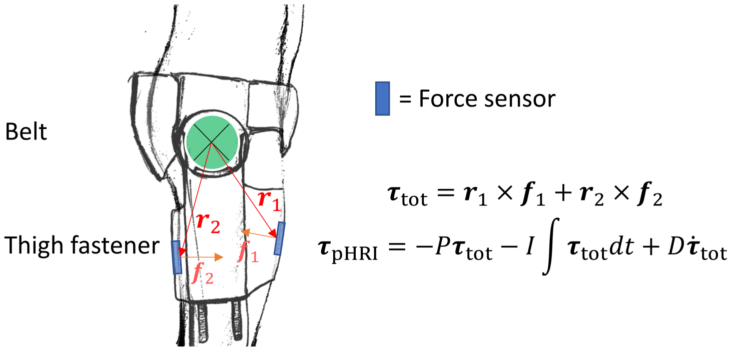

Figure 2.4: Example depiction of a hip exoskeleton controller based on minimization of net interaction forces between the user and orthosis.

cording to European regulations, exoskeletons are classified as medical devices in any case [85].

2.2.2 Control strategies

As reported in [78], the interaction forces between the user and the wearable robot can be used to control the robot's output force so as to augment the force imparted by the user onto the environment, under the condition that this interaction only happens through the robot itself. In such a setup, the control problem could be stated as trying to move the robot so as to minimize the interaction forces between the user and the robot. As depicted in Fig. 2.4, where a hip-assisting exoskeleton is depicted schematically, the interaction forces $\boldsymbol{f}_1, \boldsymbol{f}_2 \in \mathbb{R}^3$ can lead to the calculation of a net interaction torque $\boldsymbol{\tau}_{\text{tot}} \in \mathbb{R}^3$ by calculating the cross product with the positions $\boldsymbol{r}_1, \boldsymbol{r}_2 \in \mathbb{R}^3$ relative to the joint. The pHRI-controlled torque delivered to the hip motor $\boldsymbol{\tau}_{\text{pHRI}} \in \mathbb{R}^3$ is then computed by a Proportional Integrative Derivative (PID) controller with coefficients $P, I, D \in \mathbb{R}$. Besides the fact that for this control to work the user interaction with the environment has to be mediated by the exoskeleton [78], in the case that the user is not able to sustain their own weight with their own musculature, the exoskeleton would not be able to assist in this regard. This makes pHRI potentially unsuitable for assistive or rehabilitative applications, unless it is applied on top of a control with the goal of compensating for a fraction $\alpha \in [0, 1]$ of the user's own weight and the pose-dependent interaction forces $\boldsymbol{g}(\boldsymbol{q}) \in \mathbb{R}^Q$ deriving from it, as shown for example in Fig. 2.5. This would necessitate some form of dynamics model of the user's body, where $Q \in \mathbb{N}$ would be the number of Degree of Freedom (DoF) considered therein. In the case of a tendon-actuated exosuit, the controller would operate in terms of tension force $\boldsymbol{f}_{\text{mot}}$. In some cases, a system integrating both a wearable robot and FES could bypass this issue, as voluntary muscular activity could be amplified to sustain the user's own weight.

Alternatively, if the interaction between the user and the environment should not be mediated by the robot, biosignal-based control could be used [12, 47, 48]. These control paradigms can be borrowed from the larger field of prosthetic controls. Figuratively, prostheses work in series to the user, as opposed to in a parallel fashion like exoskeletons, exosuits, and exonerves. Although a prosthesis wearer can typically interact with the environment only through the prosthesis itself, self-powered prosthetic devices normally feature degrees of freedom with

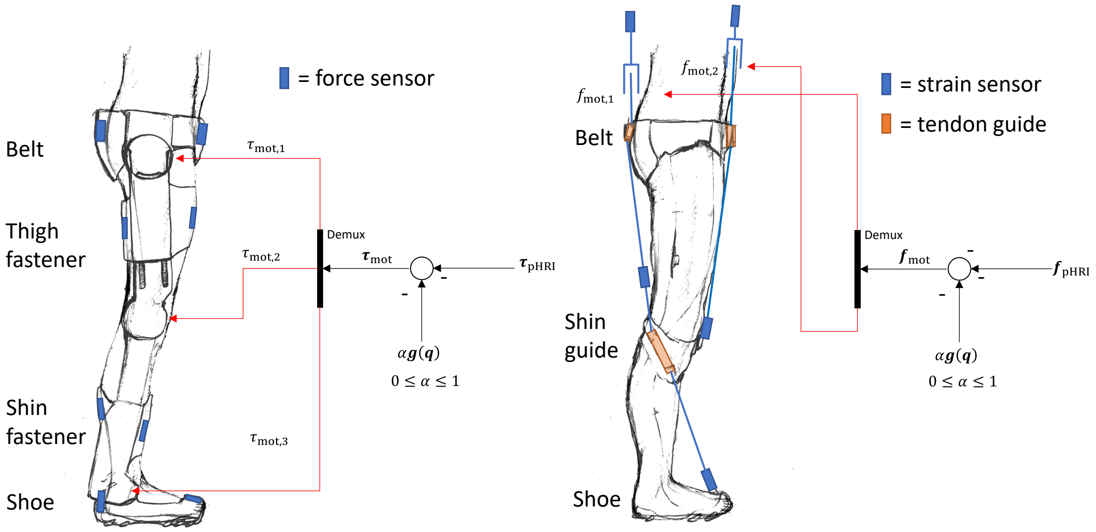

Figure 2.5: **Left:** Depiction of pHRI-based control for exoskeletons. **Right:** Depiction of pHRI-based control for exosuits. Both controls are added to a gravity compensation term.

which the user can not directly exchange mechanical power. Therefore, in the case of transparent, intent detection-based controls, the prosthetic can be driven based on some form of muscle activity measurement, which is used to infer the intended force output or movement. Although relatively rare in exoskeleton and exosuit control, this biosignal-based concept could be employed in the same manner as pHRI, substituting direct measurement of user-robot interaction forces through the inferred intended force output. Muscle activity-based inference of force output would not require the user-environment interaction to happen through the mediation of the robot, would also decrease the impairment on the user's range of motion [47].

While interaction force measurement and inferred volitional force output can be used as a control input for wearable robots, it is also true that wearable robots themselves can be used to provide various levels of precision in the measurement of force output for diagnostic purposes or real-time control. As stated in the introduction, direct force measurement entails exerting some form of resistance onto the user, which leads to a general trade-off: the more resistance is applied, the greater the range and the better the achievable force measurement precision. On the other hand, applying resistance to the user's movements obviously impairs natural motion, and can be especially counter productive for users with reduced mobility. As stated above, inference of intended force output based on muscular activity can largely sidestep this problem, as the range of motion is typically not decreased by most available sensor setups [47]. Such force output predictions are however prone to estimation errors. On the other hand, exoskeletons and, in some cases, exosuits, can tune their compliance, and could therefore be set to operate at any desired operational point is needed given the current force measurement requirements.

Similar considerations can be made for the measurement of limb stiffness, as the trade-off, in this case, is determined by the necessity of measuring the deflection caused by an interference of known force and direction in order to calculate the stiffness itself.

2.3 Functional electrical stimulation

Functional Electrical Stimulation (FES) represents an integral part of the rehabilitation of certain neurological patients. As stated previously, FES causes the firing of peripheral motor neurons through the injection of electrical currents [28]. This can be useful in rehabilitation, which, at its root, has the purpose of re-forming damaged neural connections, typically between the central and the peripheral nervous systems. FES offers many advantages with respect to rehabilitation facilitated through external aids, chief among them the fact that the user employs their own muscles in order to complete the movements, thus avoiding secondary complications such as muscle atrophy. In the early phase of rehabilitation, FES is an effective tool in a task-specific, restorative therapy program to foster neurological recovery [36, 86]. In the chronic phase after a neurological disease or trauma, FES may be used as a neuroprosthesis for compensation of completely lost or very weak motor functions. Particularly in individuals affected by SCI and the associated impairments of the reaching and grasping function, FES has been successfully employed for assistance in ADLs, both using transcutaneous [30] and intramuscular electrodes [29]. FES has also been used to aid patients affected by stroke [31, 32, 33], as well as TBI [34, 35]. Besides rehabilitation and assistance, FES, or more in general Electrical Muscular Stimulation (EMS) techniques, are also becoming an accepted clinical practice for diagnostic purposes to assess certain aspects of patient functionality [87, 88].

In the following, the salient aspects of both the physical and the software implementation of FES concepts are discussed.

2.3.1 Intramuscular vs. transcutaneous FES

Transcutaneous FES relies on adhesive electrodes kept in constant contact with the user's skin. The currents are injected into the motor nerves through the tissue lying between it and the electrode. This leads to an inherently harder-to-predict current distribution, as represented in Fig. 2.6, with additional difficulties caused by the fact that muscles will shift under the skin across different positions. Furthermore, transcutaneous FES generally does not allow the selective stimulation of deeper muscle groups while leaving superficial ones inactive, as the current distribution within the muscular tissue is likely to show higher current densities closer to the skin, as depicted in Fig. 2.6.

This leads to increased difficulties in predicting the direction and magnitude of the force output caused by injecting a given current through the electrode pair, in a similar fashion as what occurs in EMG-controlled prostheses due to the limb position effect [89]. Due to these factors, the non-linear superposition of the effect of injected currents in transcutaneous FES has been identified in some experiments as a significant source of error [90]. Transcutaneous FES is however much less invasive than intramuscular FES, and therefore it is also used in applications outside of the medical field, e.g. Virtual Reality (VR) and Augmented Reality (AR) [91, 92]. Besides the rendering of force vectors, it is possible to provide different forms of haptic cuing through electrical stimulation: for instance, virtual barriers or force fields can be rendered, which could potentially be employed to train specific movements. FES has also been used to inform users about affordances that can be applied to objects in a scene [93].

Intramuscular or nerve-cuff electrodes, as opposed to transcutaneous electrodes, allow for selective and precise stimulation of the muscle group in which they are implanted, but they entail invasive interventions. The increased spatial and time resolution they can afford, however, leads to great precision in force control applications [94]. Furthermore, many studies report that stimulation delivered through this type of electrodes is linear in the produced force output. [44, 95].

In all kinds of FES techniques, the force as a function of stimulation current can be approximately represented as a sigmoid [44, 90], which leads to further non-linearities being introduced in the system.

2.3.2 Control science considerations

The context of rehabilitation can offer some advantages, as the repetitive, task-specific nature of the movements typically performed during a therapy session makes it possible to implement iterative learning, which allows to calibrate inertial parameters and to differentiate the user's own volitional efforts from electrical stimulation [96, 97]. However, many of these setups rely heavily on the assumption of repeated movements, and might be ill-fitted to aid motions that are not periodic. Furthermore, currently available FES systems, both in the medical field and beyond, tend to use static stimulation schemes in order to generate predefined multi-joint movements. Most setups available can successfully induce task-specific movements requiring the stimulation of muscle groups directly associated with them in a bijective fashion (that is to say that one specific functional movement, such as elbow flexion, is associated, usually by experts, with the stimulation of a specific anatomical muscle group) [32].

There is a fair amount of literature regarding single joint motions involving few or only one DoF. Within these confines, many trends have emerged proposing possible solutions for the control of FES systems. Finite-state controllers, which transition between different (usually

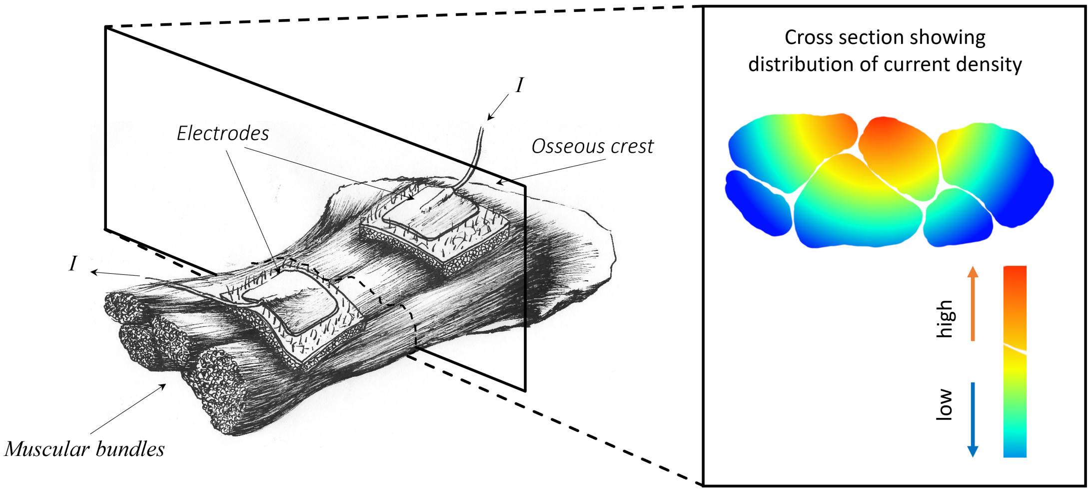

Figure 2.6: Depiction of transcutaneous electrodes injecting currents into a group of skeletal muscles and the associated distribution of current density.

feed-forward) control modes based on the measured state of the system, have been proposed [98]. Continuous controllers, such as PID [99, 100] and sliding-mode [101, 102], have also emerged, and have been used together with exoskeleton systems in a closed-loop fashion. Artificial neural networks have also been employed to this end [103, 104], as well as non-linear predictive controllers [105, 106].

On the other hand, examples of general-purpose frameworks capable of associating arbitrary movements or force outputs to more than a few stimulated muscle groups, in particular without relying on the assumption of repeated actions, are fairly rare. The applicability of the single-DoF control systems mentioned above to more degrees of freedom has mainly been reported in simulations [99, 100]. FES presents many difficulties from the point of view of movement control in multi-joint systems, as determining the forces and torques exerted by a muscle group stimulated through surface electrodes can prove to be difficult. Some examples of setups that are able to enforce a general-purpose movement control of multiple joints are presented in [44, 94, 107, 108]. Schearer and colleagues, in their works, present the results of experiments performed on an SCI patient with implanted electrodes, which, as stated in the previous section, are in many ways less challenging from a control perspective. In [44], in particular, the authors show evidence that force output components due to stimulation currents seem to combine linearly. This finding is corroborated by other similar studies, such as [95] and [109]. In [94], Schearer and colleagues report the performance of a force controller introduced in [44] for movement control, and the force output predictor is only calibrated in one arm position. The upper limb's dynamics, however, have to be calibrated by moving the arm across different postures. Razavian and colleagues, on the other hand, present a setup featuring transcutaneous FES and a controller formulated in task space, as opposed to joint space [108]. As such, the control system has to be calibrated in various postures across the task space, which in this case is planar.

2.3.3 Model-mediation

As can be inferred from the above-mentioned considerations, designing a multi-joint FES system that can be easily adapted to any individual user is still very much an open topic. Besides considerations about the physical delivery of stimulation currents, some space should be dedicated to the discussion of the practicality and convenience of the control concepts upon which FES setups are based. For the purposes of this discussion, some distinctions have to be drawn based on which kind of model is used to control the FES setup.

In this regard, two main paradigms can be identified in the design of FES control systems. On the one hand, musculoskeletal systems can be employed to infer the general routing of the muscles, and consequently of the force that they would exert if stimulated [110]. Besides the model proposed by Chadwick and colleagues, a further real-time model that includes muscular as well as arm dynamics, and that is capable of real-time functionality, was proposed by Sartori and colleagues in [111]. While these latter models are mainly concerned with predicting movements given the EMG measurements sampled from the user, the two problems are inherently linked, so much so that certain setups from the literature use EMG measurements associated with gestures to perform spatial calibration of the FES injection pattern associated with those same gestures [112]. In [113], on the other hand, surface Electromyography (sEMG) is used to detect the electrophysiological response to sub-threshold EMS injections, as opposed to measuring stimulation-caused twitches or force outputs. The models presented in [110] and [111] are both based on the *OpenSim* modeling framework. Such musculoskeletal models require some anatomical expertise to be set up, as they usually call for manual routing, at least to some degree, of the muscle groups. Adjusting such a model to an individual user's anatomy can require the use of costly and time-consuming imaging techniques, as exemplified in [41]. However, because they rely on an anatomically informed muscle placement, musculoskeletal models can inherently account for variation in muscle routing due to changes in posture. They might require some level of functional calibration in order to compute the transfer function from stimulation to force output, but once there is an indication of which muscle groups are going to contract under a given electrode pair, an educated guess can already be made as for the force output direction caused by single-channel FES pulses.

On the other hand, black-box Machine Learning (ML)-based controllers are directly trained based on real-world measurements of force output caused by the injection of stimulation currents. ML models need to be trained specifically for any given electrode placement and need samples at various current intensities in order to compensate for the stimulation to force output sigmoid transfer function [44]. The thus obtained force output prediction can be used also to provide a solution in terms of stimulation that would elicit a desired force output, if necessary by considering additional constraints, such as keeping the overall current to a minimum. Unlike musculoskeletal models, such an approach can not inherently generalize well over different postures, and the predictor would need to be trained on data sampled in different limb poses in order to do so, as is the case for example in [107] and [108]. The advantage of ML-models is that they do not require particular anatomical expertise in order to be set up, and can inherently adapt to individual users.

3 Aim of the thesis

The main aim of the works presented here is to characterize and explain the key aspects of the design and implementation of a FES-based, wearable device usable for assistance, rehabilitation, and other applications. Each presented work focuses mainly on one aspect or subsystem that can be used in a FES assistive or rehabilitative setup. As the translation from laboratory to clinics is a major focus of the research presented here, certain aspects of these concepts aim at providing a self-contained, easy-to-use, practical solution that could be deployed in a clinical or even domestic setting.

The BodyRig posture tracking system is an example of this philosophy, as it can be donned in seconds, and is extremely versatile and low-cost. While an optical system would almost certainly provide more precise and accurate posture tracking, most such systems require non-portable equipment and are susceptible to non-ideal lighting problems or line-of-sight interruptions.

The BodyRig proposes to be a cheaper, more specialized alternative to the Xsens. This is achieved by employing recent integrated IMU modules, namely the BNO055 from Bosch [114], which provide comparatively good performance, relative to the cost [115]. The system is presented in the publication in Chapter A.1 and was prominently featured in [8, 9].

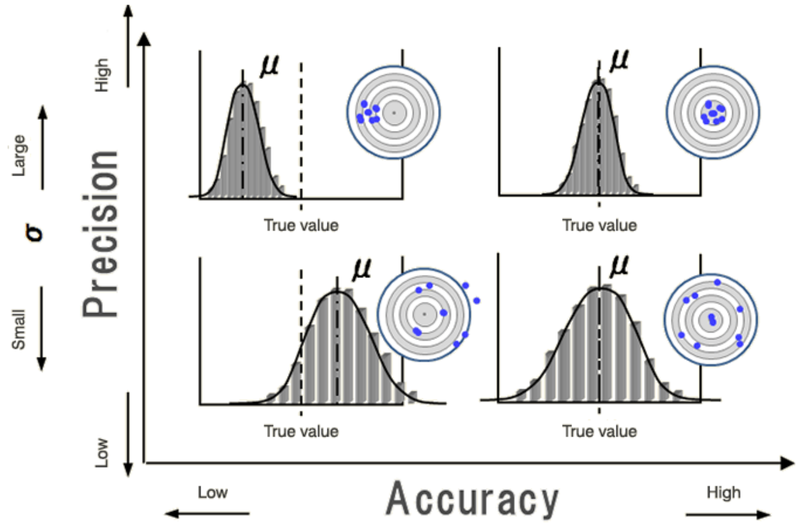

Figure 3.1: Explanatory depiction of accuracy and precision. The former is the vicinity of an estimate or an experimental outcome to a reference (true) value, while the latter refers to the consistency or repeatability of the experimental outcome [116].

Both the featured exosuit and semi-active exoskeleton are also designed to provide the user with force support while featuring extremely lightweight structures. Furthermore, the presented experiments introduce setups where these devices are used to indirectly monitor force output in non-static tasks.

Finally, the main goal of the MyoCeption FES system is to provide a model usable in movement control that can be easily adapted to an arbitrary user, as well as to test various options to provide electrical stimulation with the best possible trade-off between fitting and calibration time and precision.

In the core publications in Chapters A.4 and A.6, two main concepts are presented, one based on a musculoskeletal model and one on an RR-based predictor of the stimulation-induced force output. Both models feature a specific calibration procedure the advantages and disadvantages of which will be analyzed in greater detail in the following chapters.

3.1 BodyRig and posture monitoring

The BodyRig is designed to be a versatile and easy-to-use body tracking system. IMUs are particularly well suited from a practical standpoint, as they can be worn above clothing without the need for any rigid structure, as a mechanical joint protractor would require, for example. IMU-based body tracking can be very practical in certain applications, provided that the requirements for precision and especially accuracy are met, as IMUs can guarantee good repeatability, but accuracy in posture tracking can be lacking. Fig. 3.1 depicts the salient attributes of a precise and of an accurate measurement.

The BodyRig system was originally designed to integrate data pertaining to body posture in intent predictors for prosthesis control [13]. However, it was mainly used in experiments involving teleoperation, as shown in [8, 9]. In either case, the posture tracking was to put more emphasis on precision or repeatability, rather than on accuracy. This is to say that the forward kinematics estimate of the user's End Effector (EE) position should not necessarily be close to the real pose of the user, as long as the estimate is consistent every time the user assumes a given posture. The actual pose of the user's body segments in space is not as important as repeatability and transparency in most applications involving teleoperation or prosthesis control. In such scenarios, the users can easily adjust to any bias errors between their actual hand pose and that transmitted to the robotic avatar's end effector. Furthermore, most ML algorithms for prosthesis control only need qualitative measurements in order to provide a prediction of movement intention. In [9], for example, offsets in the inferred position of the user's hands could be added in order to make it more practical for the study participants to teleoperate the humanoid platform TORO without self-colliding during bimanual tasks. This does lead the body tracking measurement away from the real posture of the user but does not influence the precision of the measurement. The participants of that study were able to press keys on a telephone keypad through the humanoid robot with only visual feedback, collocating the attainable precision of the setup in the sub-centimeter range.

For the purposes of FES, on the other hand, the accuracy of the body tracking measurements does play a bigger role, as these measurements are then used to align a musculoskeletal model to be as close as possible to the real position of the user, and to then compute the stimulation needed to induce a desired force output or movement. The BodyRig can be used to perform this alignment in real-time, provided that the length of the body segments has been measured with sufficient accuracy and that the angular offsets between each sensor and the respective body segment are also well assessed, and that the sensor fixture ensure that this offset does not change too much during movement. The identification of functional joint axes is also of relevance for the use of musculoskeletal models in FES applications. In Chapter 4, a few strategies for the computation of such axes that were used in experiments involving the BodyRig are discussed.

While the skeletal segments can be more easily aligned, it is less trivial to provide a reasonably good inference of the muscle geometry as a function of body posture. Nonetheless, with a few assumptions on how the muscle should be routed, it is possible to infer the geometry of a given muscle group's line of action, as shown for instance in [110] and confirmed for the MyoCeption's controller in [5]. The present work also aims at comparing the performance of an expert model, i.e. a musculoskeletal model designed with some anatomical expertise, and a more general ML-based model. The BodyRig plays a role even in the latter case, as it is employed to infer the position and orientation of the joints. This is in turn used to compute the joint torques needed to achieve a given force output in Cartesian space to be matched by FES-caused muscle contractions.

This leads to RQ1, which regards the performance attainable using a portable, self-contained body tracking system.

Research Question 1: what is the realistic precision and accuracy attainable by using a self-contained IMU-based body tracking system to monitor both skeletal kinematics as well as muscular geometry? What degree of precision is required in order to control a FES system?

3.2 Wearable robotics and force output measurement

The main roles of wearable robotics in FES setups are to provide additional support when stimulation-induced joint torques are not sufficient to perform the desired movement, as well as to monitor force output. As stated in previous sections, such wearable devices can be used to measure interaction forces with the user in real-time, ideally with negligible limitations to the user's range of motion.

With regards to force output measurements, the relation between this and injected stimulation currents in a quasi-static setup is explored in Chapter A.4. The intent is to assess the possibility of integrating force output measurements in a calibration procedure for a FES-based assistive device prior to online operation. Concretely, force output measurements in this sense can be performed by locking the user's forearm in a cuff, which is itself connected to a load cell. This can be used to monitor force and torque output as well as to project these onto joint space. This technique, however, entails locking the user's arm and preventing it from moving. Such a calibration procedure was used in A.6.

Chapters A.2 and A.3 investigate two separate solutions with the goal of assessing force output without limiting the user's range of motion while providing adaptive support. In Chapter A.2, the force measurement is obtained by imposing a known compliance to infer interaction forces by measuring displacements. The compliance is enforced by an admittance-controlled handle, which the users had to grasp during the experiment. The admittance was used to project an sEMG-based estimation of the grasping force onto positional coordinates of the hand closing movement, which for the purposes of this experiment was reduced to one single DoF. The control loop was tasked with minimizing the error between the estimate of the desired hand grasp angle and the actually measured angle.

In a further proof of concept presented in Chapter A.3, FMG is used to estimate the torque at the shoulder caused by lifting various weights. This technique does not entail a closed loop like the solution presented in A.2, but it does not require the imposition of a known compliance and therefore decreases the limits on the user's range of motion.

In both cases, the assistive device provides support forces and torques tuned on the basis of the desired output force. In the concepts presented in A.2 and A.3, the support force provided by the wearable robot is based on the momentary volitional muscular activity, with the intent of decreasing the slope of the volitional effort over the force output curve.

Chapters A.3 and A.2 are conducive to RQ2, which relates to alternatives to rigid exoskeletons and static force and torque sensing setups for the purposes of force output measurements.

Research Question 2: what alternatives exist to traditional rigid exoskeletons to provide assistance to functional movements while monitoring intended as well as actual force output without constraining the user? What benefits would such modalities offer in terms of performance and efficiency?

3.3 Functional electrical stimulation

While posture tracking and force output estimation are all paramount aspects of multi-joint Functional Electrical Stimulation systems, FES entails an entirely separate series of control problems, and therefore deserves its own sub-topic.

As can be surmised from the State of the Art, implementing an easily adaptable multi-joint FES system is still very much an open topic. Regarding the method of delivering the stimulation currents to the peripheral nerves, intramuscular or otherwise implanted electrodes would automatically make the system more adapted to the recipient, as such implantation interventions are inherently highly individualized. On the other hand, surgeries have well-known potential complications and do require a remarkable commitment from the recipient.

It is therefore fair to assume that ease of use and adoption by a general population is not the main focus of such systems as those proposed by Schearer et al. [94], which are all based on implanted electrodes. Assuming that an ideally versatile system should rely on surface electrodes to provide FES, the placement of these should be easy to rearrange. Furthermore, the model upon which the system's controller relies should be easily modifiable to better fit each individual, ideally without the need for much anatomical expertise, and if possible even automatically.

With regard to FES, various concepts are presented and reported in this dissertation. The main benchmark to test these is the MyoCeption. The MyoCeption prototype is a surface FES device featuring a wearable Velcro-lined jacket. The MyoCeption framework's development led to the filing of a patent [14]. While FES applied through surface electrodes has been used in many previous publications for both assistive and rehabilitative purposes, the concepts described therein usually stimulate single joints in order to achieve specific movements. A general-purpose framework to apply FES to any given body segment is, however, still missing. Furthermore, few of the setups presented in the literature are self-contained.

As far as the MyoCeption setup is concerned, the aims of the experiments presented in this dissertation are to investigate the benefits of integrating posture tracking, muscle activity, and force/torque output sensor modalities in the control loop in order to improve the effectiveness of the electrical stimulation in aiding movements. This includes the investigation of approaches that allow for a short calibration allowing the system to adjust to individual users.

The MyoCeption prototype has been assessed in the achievable precision and functional performance in both [4] and [6]. In the modeling of the human musculoskeletal system, the skeleton can be approximated like a series of effectively rigid links connected by revolute (that is to say, rotational) joints.

Based on these assumptions, a musculoskeletal model is introduced and described in Chapter A.5. In Chapter A.4 the performance of a FES force control relying upon such a musculoskeletal model is assessed. In particular, the performance of the non-calibrated model was compared to that of the same model calibrated through a procedure that automatically adjusts the line of force routing. The results demonstrate the advantages of musculoskeletal models, namely that they can perform to some degree even with no calibration performed. The force control is achieved through a computationally efficient Nearest Neighbour (NN) muscular recruitment strategy. This technique requires the association of every line of action in the musculoskeletal model to a given joint, and for each one, it individuates the muscle group the stimulation of which would cause the torque output closest in direction to the desired one. The experiment from A.4 also allowed for an offline analysis to assess the reliability with which it is possible to predict the wrench output at the end effector, or the torque output at the joint level given the stimulation currents injected.

Based on the offline results presented in Chapter A.4, an ML-based concept is presented in Chapter A.6, where real-world force measurements are used to calibrate a joint-space torque predictor based on the injected currents. This predictor is then integrated into a control loop and used to find an optimal stimulation vector to cause a desired output force through gradient descent.

Chapters A.4 and A.6 are concerned with RQ3, which ultimately regards the attainable performance of FES-based force controls and their use in impedance-mediated movement assisting controls.

Research Question 3: what precision and accuracy can be achieved with a FES-driven force control of the human limb? How can this be translated to movement control? How can such control systems be calibrated in a practical way?

4 Methods

In the core publications, the main aspects relating to posture tracking, muscle geometry estimation, adaptive assistance, force output prediction and FES-facilitated force control are characterized and validated. In addition to these core publications, this dissertation includes some unpublished results, mainly derived from pre-tests or relating to direct comparisons between available datasets. The results are presented in the following chapters. Here the methodological aspects are discussed, as well as some of the empirical considerations that have led to some design and experimental decisions.

The first sections in this chapter present fundamental aspects relevant to the core publications, which are reported here as a means of familiarization for readers who might be unfamiliar with some of the disciplines upon which the proposed assistive devices are based.

4.1 Fundamentals in robotics and multi-body system modeling

Traditional robotic arms are typically modeled as an arrangement of rigid links connected by joints. Joints can either be rotational, also known as revolute, which rotate by an angle $\theta \in \mathbb{R}$ around a rigidly defined axis of direction $\boldsymbol{e} \in \mathbb{R}^3$, or prismatic, which elongate or shorten by a length $l \in \mathbb{R}$ along a similarly defined axis. More complex joints, like ball-and-socket articulations for instance, can be modeled as combinations of many elementary revolute and prismatic joints. These internal system coordinates can be grouped in a vector, which we will denote $\boldsymbol{q} \in \mathbb{R}^Q$, where $Q \in \mathbb{N}$ is the number of DoFs of the robot. Fig. 4.1 depicts an example kinematic chain consisting of both prismatic and revolute joints, where all axes and joint parameters are numbered with an index indicating the joint number.

Skeletal structures can also be modeled to a good degree of approximation for most practical intents and purposes as a series of links connected by typically revolute joints [39]. For this reason, many of the aspects discussed in the following are of interest also for the direct control of human limbs through FES.

In task-oriented applications, it is usually necessary to achieve a given pose in a task space $\boldsymbol{p} \in \mathbb{R}^T$. In many cases, the task space is comprised of coordinate vectors $\boldsymbol{p} \in \mathbb{R}^6$, which define a pose in three-dimensional Euclidean space $\mathbb{E}^3$ in terms of 3 translational and 3 rotational DoFs. The group of all possible rigid isometric transformations in $\mathbb{E}^3$, i.e. the transformations which preserve the handedness of a set of points, are grouped in the so-called Special Euclidean group $SE(3)$, which is of interest in robotics as it defines all operations useful to convert a pose between different coordinate systems [117, 118]. Many options exist to formulate the coordinate vector to signify the EE's pose w.r.t. a coordinate system $\{0\}$. In the following, the pose vector $\boldsymbol{p}$ is formulated as being comprised 2 sub-vectors $\boldsymbol{h} \in \mathbb{R}^3$ and $\boldsymbol{\rho} \in [0, 2\pi[^3$ which

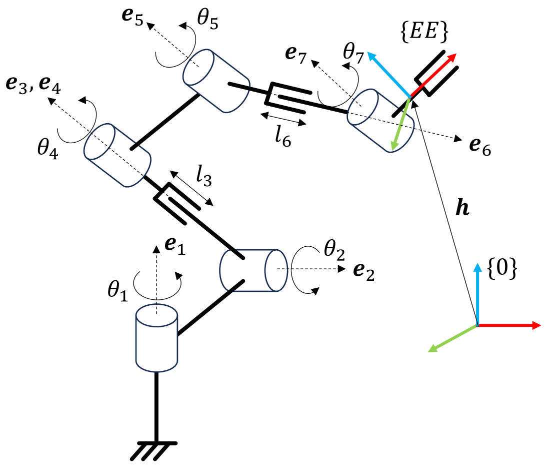

Figure 4.1: Example of a series link-joint kinematic chain consisting of both revolute and prismatic joints.

encode 3 translational and 3 rotational coordinates expressed as angles in radians, respectively, s.t. $\boldsymbol{p}$ can be defined as

$$\boldsymbol{p}^T = [\boldsymbol{h}^T, \boldsymbol{\rho}^T]. \tag{4.1}$$

Many options exist to express the orientation of an object in $\mathbb{E}^3$. For the intents and purposes of this chapter, it is sufficient to assert that the rotational coordinate vector $\boldsymbol{\rho}$ is expressed in the same frame as the Cartesian torque $\boldsymbol{\tau}_w \in \mathbb{R}^3$, which will be better defined in the following sections, so that the scalar product of $\boldsymbol{\tau}_w$ and $\dot{\boldsymbol{\rho}}$ gives the kinetic power output in the Cartesian rotational DoFs.

4.1.1 Multi-body kinematics

The problem of FK, for a robotic system or generally for any system that can be modeled in a similar fashion, consists in calculating the pose $\boldsymbol{p} \in \mathbb{R}^T$ of the system in task or Cartesian space given the system's internal coordinates $\boldsymbol{q} \in \mathbb{R}^Q$. Conversely, the problem of Inverse Kinematics (IK) consists of finding a set of internal coordinates, if at least one exists, that can put the system's EE in a given desired pose $\boldsymbol{p}_{\text{des}} \in \mathbb{R}^T$ in task space. In the case of series link-joint systems, i.e. systems where links that can be assumed to be rigid are connected by joints, such as the one depicted in Fig. 4.1, where at most two links are connected by one joint, the problem of inverse kinematics is typically of considerably harder tractability, and often no explicit general solution exists [119].

Since standardized methods exist to create the forward kinematics function $\boldsymbol{p}(\boldsymbol{q}) : \mathbb{R}^Q \rightarrow \mathbb{R}^T$ of series link-joints systems, e.g. the Denavit-Hartenberg notation and the associated geometrical projections [120], it is possible to solve the inverse kinematics problem numerically by identifying the system's Jacobian $\boldsymbol{J}(\boldsymbol{q}) \in \mathbb{R}^{T \times Q}$ as follows

$$\boldsymbol{J}(\boldsymbol{q}) = \nabla_q^T \boldsymbol{p}(\boldsymbol{q}). \tag{4.2}$$

This gives us a relation between the differential variations of $\boldsymbol{p}$ and $\boldsymbol{q}$, namely

$$d\boldsymbol{p} = \boldsymbol{J}(\boldsymbol{q})d\boldsymbol{q} \tag{4.3}$$

or, in terms of first-order time derivatives,

$$\dot{\boldsymbol{p}} = \boldsymbol{J}(\boldsymbol{q})\dot{\boldsymbol{q}} \tag{4.4}$$

and, therefore, if we can invert the Jacobian, we can solve the inverse kinematics problem to any desired precision numerically. The process of finding the solution $\boldsymbol{q}$ such that $\boldsymbol{p}(\boldsymbol{q}) = \boldsymbol{p}_{\text{des}}$ is implemented in iterative, discrete steps. Given an initial set of joint parameters $\boldsymbol{q}_0 \in \mathbb{R}^Q$, the solution $\boldsymbol{q}$ is updated by adding a small increment defined as $\delta\boldsymbol{q} = \boldsymbol{J}^{-1}(\boldsymbol{q})\delta\boldsymbol{p}$, with the error in task or Cartesian space w.r.t. a desired configuration $\boldsymbol{p}_{\text{des}} \in \mathbb{R}^T$ at every step being computed as $\delta\boldsymbol{p} = \alpha(\boldsymbol{p}_{\text{des}} - \boldsymbol{p}(\boldsymbol{q}))$. In this context, $\alpha \in \mathbb{R}$ is a small gain that should be set in such a way that a single increment is lower in module compared to the desired precision of the IK solver. Provided an initial set of joint parameters $\boldsymbol{q}_0 \in \mathbb{R}^Q$, for the k-th step, we have the following solution update

$$\boldsymbol{q}_{k+1} = \boldsymbol{q}_k + \alpha\boldsymbol{J}^{-1}(\boldsymbol{q})(\boldsymbol{p}_{\text{des}} - \boldsymbol{p}(\boldsymbol{q}_k)). \tag{4.5}$$

It is important to note that, in general, multiple solutions to the IK problem exist. Such iterative solvers, if all parameters are suitably set, should converge towards whatever solution is closest in $\mathbb{R}^Q$ to the initial joint parameter vector $\boldsymbol{q}_0$.

It can however be that the Jacobian is not invertible, i.e. when it does not have full rank, which is the case if, for example, the system has a degree of redundancy, which is to say that it has more internal coordinates than the ones presented in task or Cartesian space and we therefore have $Q > T$. Furthermore, even if $\boldsymbol{J}(\boldsymbol{q})$ can generally be inverted, it can happen that, in the vicinity of certain configurations $\boldsymbol{q}_s \in \mathbb{R}^Q$, called singularities, the increment defined in Eq. 4.5 would assume very large values, which could lead to non-converging behavior of the algorithm, and if the solver is controlling an actual physical system, to unsafely fast movements.

In the case of redundancies, it is possible to use a form of pseudo-inverse of the Jacobian, such as the left-hand Moore-Penrose pseudo inverse $\boldsymbol{J}^{\#}$ [121] instead of the Jacobian inverse $\boldsymbol{J}^{-1}(\boldsymbol{q})$ in Eq. 4.5. In order to avoid singularities $\boldsymbol{q}_s$, safety checks have to be put in place. This form of IK solver has quadratic convergence rate for $\boldsymbol{p}(\boldsymbol{q})$ in the neighborhood of $\boldsymbol{p}_{\text{des}}$ [122].

An alternative IK solver which is inherently more stable in the vicinity of singularities comes from a generalization of Newton's method for the identification of function roots. The solver minimizes the error function $H(\boldsymbol{q}) : \mathbb{R}^Q \to \mathbb{R}$ defined as

$$H(\boldsymbol{q}) = \frac{1}{2}\|\boldsymbol{p}_{\text{des}} - \boldsymbol{p}(\boldsymbol{q})\|^2 = \frac{1}{2}(\boldsymbol{p}_{\text{des}} - \boldsymbol{p}(\boldsymbol{q}))^T(\boldsymbol{p}_{\text{des}} - \boldsymbol{p}(\boldsymbol{q})) \tag{4.6}$$

by gradient descent, which leads to the following update rule

$$\boldsymbol{q}_{k+1} = \boldsymbol{q}_k - \beta\nabla_{\boldsymbol{q}}H(\boldsymbol{q}_k) = \boldsymbol{q}_k + \beta\boldsymbol{J}^T(\boldsymbol{q}_k)(\boldsymbol{p}_{\text{des}} - \boldsymbol{p}(\boldsymbol{q}_k)), \tag{4.7}$$

with $\beta \in \mathbb{R}$ again being a gain that influences the update step's magnitude, and therefore the solver's resolution. A commonly used thumb rule is setting $\beta < \frac{1}{\lambda_{\text{max}}}$, with $\lambda_{\text{max}} \in \mathbb{R}$ being the greatest eigenvalue of the matrix $\boldsymbol{J}^T\boldsymbol{J}$. The gradient descent method is inherently more stable in that, unlike inverse Jacobian solvers, its increment tends to $\mathbf{0}$ when in the vicinity of a singularity. The implementation is furthermore simpler and more computationally efficient, as it does not require a matrix inversion. The convergence rate is however slower [123], and the algorithm is prone to the possibility of not converging if it ends on a joint parameter vector $\boldsymbol{q}_k$ for which the gradient $\nabla_{\boldsymbol{q}} H(\boldsymbol{q}_k)$ is $\mathbf{0}$. However, it never diverges, which can be the case when using inverse Jacobian solvers in the vicinity of singularities.

4.1.2 Multi-body robot dynamics

In parallel to positional coordinate vectors, generalized force vectors can be defined in any coordinate system. Generalized force vectors are defined in such a way that their scalar product with the first-order time derivative of the corresponding positional coordinate vectors result in a measure of the system's power output. For instance given a joint parameter vector $\boldsymbol{q} \in \mathbb{R}^Q$ consisting of both revolute and prismatic joint coordinates, its associated generalized force vector $\boldsymbol{\tau} \in \mathbb{R}^Q$ should consist of components τ_i that are torques if q_i is the angle of a revolute joint θ_i, and conversely τ_i should be a force if q_i is the state of a prismatic joint l_i, using the notation shown in Fig. 4.1. The same is true for any coordinate system, e.g. in the case of EE pose coordinate vectors $\boldsymbol{p} \in \mathbb{R}^6$ in $\mathbb{E}^3$, as defined in Eq. 4.1, the corresponding generalized force vector, or wrench, $\boldsymbol{w} \in \mathbb{R}^6$ is defined as $\boldsymbol{w}^T = \left[\boldsymbol{f}_w^T, \boldsymbol{\tau}_w^T\right]$, with $\boldsymbol{f}_w \in \mathbb{R}^3$ and $\boldsymbol{\tau}_w \in \mathbb{R}^3$ being the force and the torque applied to the EE, respectively. Given these definitions, $\boldsymbol{w} \cdot \dot{\boldsymbol{p}}$ has the physical dimension of power.

Multi-body dynamics are functions associating a generalized force to a given dynamic state of the system, i.e. a given set of values for the system's internal coordinates and their time derivatives. Various methods of identifying system dynamics exist, such as the Euler-Lagrange formalism [124], usually starting from considerations about kinetic and potential energy of the system.

In general, the dynamics of a multi-body, rigid link-joint system in a gravitational field can be represented in joint space in the form

$$\boldsymbol{\tau} = \boldsymbol{M}\ddot{\boldsymbol{q}} + \boldsymbol{C}(\boldsymbol{q}, \dot{\boldsymbol{q}})\dot{\boldsymbol{q}} + \boldsymbol{g}(\boldsymbol{q}) + \boldsymbol{n}(\boldsymbol{q}, \dot{\boldsymbol{q}}) + \boldsymbol{\tau}_{\text{ext}}, \tag{4.8}$$

where $\boldsymbol{M} \in \mathbb{R}^{Q \times Q}$ represents the generalized inertia of the system, $\boldsymbol{C}(\boldsymbol{q}, \dot{\boldsymbol{q}}) \in \mathbb{R}^{Q \times Q}$ is the so-called Coriolis term and includes all gyroscopic effects that are a direct result of spinning masses. $\boldsymbol{g}(\boldsymbol{q}) \in \mathbb{R}^Q$ is the effect of gravity, $\boldsymbol{n}(\boldsymbol{q}, \dot{\boldsymbol{q}}) \in \mathbb{R}^Q$ is the effect of frictions, and $\boldsymbol{\tau}_{\text{ext}} \in \mathbb{R}^Q$ is a term that includes the total external forces [125, 126]. It is important to note that the system dynamics can be represented in any set of coordinates, and the conversions from one coordinate space to another can be identified by applying the principle of energy conservation. This same principle allows for a further important consideration, namely that forces can easily be projected onto joint torques in a series links and joints system, in a dual fashion w.r.t. the kinematics, for which a projection from joint space to Cartesian or task space is easier, in that it does not require to identify the Jacobian's inverse, which is a computationally expensive step. Under the assumption of constant force, Without Loss Of Generality (WLOG), at any given time, power can be represented in task space as

$$P = \boldsymbol{w}^T \dot{\boldsymbol{p}} = \dot{\boldsymbol{p}}^T \boldsymbol{w}, \tag{4.9}$$

and in joint space as

$$P = \boldsymbol{\tau}^T \dot{\boldsymbol{q}} = \dot{\boldsymbol{q}}^T \boldsymbol{\tau}. \tag{4.10}$$

Due to energy conservation, the two formulations should give the same result at any given time, and therefore we have

$$\boldsymbol{w}^T \dot{\boldsymbol{p}} = \boldsymbol{\tau}^T \dot{\boldsymbol{q}}, \tag{4.11}$$

and, by plugging in Eq. 4.4

$$\boldsymbol{w}^T \boldsymbol{J} \dot{\boldsymbol{q}} = \boldsymbol{\tau}^T \dot{\boldsymbol{q}}. \tag{4.12}$$

Since the equation holds for arbitrary $\dot{\boldsymbol{q}}$, we can say $\boldsymbol{\tau}^T = \boldsymbol{w}^T \boldsymbol{J}$, and, by transposing both sides of the equation,

$$\boldsymbol{\tau} = \boldsymbol{J}^T \boldsymbol{w}. \tag{4.13}$$

As stated above, the importance of this result lies mainly in the fact that it is possible to easily project forces from Cartesian or task space onto joint space in systems constituted by links and joints arranged in series, without the need to identify the Jacobian's inverse. This is one great advantage of force controllers in robotics, as opposed to positional controllers.

4.1.3 Impedance and admittance

Impedance controls were first formalized by Hogan and colleagues in [127, 128]. As a concept, impedance is borrowed from electrical engineering. In its original definition, impedance (often denoted by the letter Z) is defined as a function defined in a space of arbitrary dimensionality $T \in \mathbb{N}$ associating a force or wrench $\boldsymbol{w} \in \mathbb{R}^T$ to a positional error $\Delta \boldsymbol{p} \in \mathbb{R}^T$ and its time derivatives in an analogous way as a spring-dampener-mass system dynamics, with $\boldsymbol{Z}$, in the form

$$\boldsymbol{w}(\boldsymbol{\Delta p}) = \boldsymbol{M} \Delta \ddot{\boldsymbol{p}} + \boldsymbol{D} \Delta \dot{\boldsymbol{p}} + \boldsymbol{K} \Delta \boldsymbol{p}, \tag{4.14}$$

with $\boldsymbol{M} \in \mathbb{R}^{T \times T}$ being a matrix gathering the inertial terms of the system, $\boldsymbol{D} \in \mathbb{R}^{T \times T}$ gathering the dampening terms, and $\boldsymbol{K} \in \mathbb{R}^{T \times T}$ the system's spring stiffnesses. The first-order time derivative $\Delta \dot{\boldsymbol{p}}$ can be seen as analogous to the current in an electrical circuit, and the spring, dampener and mass are equivalent to the circuit impedance's capacitive, resistive and inductive terms, respectively. Analogously to a mechanical impedance, an electrical impedance associates a voltage to the electrical current, charge, which is the current's first order time integral, and to the current's first order time derivative.

In a more general definition, a mechanical impedance can be seen as any function associating a force to a positional error and its time derivative or integral of any order. In manipulator control, impedance can be used to enforce positional control indirectly through force control, by setting the arm's joint torques $\boldsymbol{\tau} \in \mathbb{R}^Q$ to $\boldsymbol{J}^T \boldsymbol{w}(\Delta \boldsymbol{p})$ using Eq. 4.13. It is worth noting the parallelism between the concept of impedance and the gradient descent solver presented in equation 4.7. These two are equivalent if $\boldsymbol{w}(\Delta \boldsymbol{p})$ is given by an impedance only consisting of a scalar stiffness, which would then have the same role as the gain β in Eq. 4.7.

All these considerations also apply to the concept of admittance, often denoted as Y, which is the inverse of an impedance, and associates a positional coordinate to a generalized force. As will be discussed later, the tuning of impedance and admittance can serve the enforcement of a certain energetic behavior, for instance in Time Domain Passivity Approach (TDPA) [129], or to enforce a desired sensitivity to perturbations [10].

4.2 Regression

As a general concept, regression in ML can be defined as a continuous, as opposed to discrete, projection of an independent variable $\boldsymbol{x} \in \mathbb{R}^D$, onto a dependent variable $y \in \mathbb{R}$, which is assumed to be a scalar here WLOG, with the intent of predicting some sort of outcome. The core publications of this thesis feature examples of linear regression, ridge regression, and kernelized ridge regression.

4.2.1 Linear regression

Linear regression tunes the weights of a vector $\boldsymbol{m} \in \mathbb{R}^D$ projecting an input vector $\boldsymbol{x} \in \mathbb{R}^D$ onto a dependent variable $y \in \mathbb{R}$ [32].

In linear regression, the prediction of the dependent variable given the independent variable or input $\boldsymbol{x}$ is

$$y = \boldsymbol{m} \cdot \boldsymbol{x} = \boldsymbol{m}^T \boldsymbol{x}. \tag{4.15}$$

The tuning of $\boldsymbol{m}$ is based on a set of $N \in \mathbb{N}$ known pairs $(y_i, \boldsymbol{x}_i)$, which form a so-called training set $\mathcal{T} \subset \mathbb{R} \times \mathbb{R}^D$. These pairs can be arranged in one so-called design matrix $\boldsymbol{X} \in \mathbb{R}^{N \times D}$ and a vector $\boldsymbol{y} \in \mathbb{R}^N$, the components of which are the individual $\boldsymbol{x}_i \in \mathbb{R}^D$ and $y_i \in \mathbb{R}$ samples from the training set, respectively.

The weight matrix $\boldsymbol{m}$ is calculated by minimizing the loss function $\mathcal{L}(\boldsymbol{m}) : \mathbb{R}^D \to \mathbb{R}$

$$\mathcal{L}(\boldsymbol{m}) = \frac{1}{2} \sum_{i=1}^{N} \|\boldsymbol{m} \cdot \boldsymbol{x}_i - y_i\|^2 = \frac{1}{2} (\boldsymbol{X}\boldsymbol{m} - \boldsymbol{y})^T (\boldsymbol{X}\boldsymbol{m} - \boldsymbol{y}). \tag{4.16}$$

A closed-form solution exists to this minimization problem, and it can be demonstrated that the weight matrix $\boldsymbol{w}$ that minimizes the loss function $\mathcal{L}(\boldsymbol{m})$ is

$$\boldsymbol{m} = (\boldsymbol{X}^T \boldsymbol{X})^{-1} \boldsymbol{X}^T \boldsymbol{y} = \boldsymbol{X}^{\#} \boldsymbol{y}. \tag{4.17}$$

The solution has computational costs $\mathcal{O}(D^3 + ND^2)$ [2]. Through incremental machine learning, it is possible to reduce the computational costs of the training procedure to $\mathcal{O}(ND^2)$ [2, 130]. As the name suggests, in incremental ML a training step of time complexity $\mathcal{O}(D^2)$ is executed incrementally for every new sample. In all cases, the complexity of the prediction step is $\mathcal{O}(D)$.

4.2.2 Ridge regression

First introduced in [131], RR is a form linear regression. RR includes soft constraints on the magnitude of the individual weights in the $\boldsymbol{m}$ vector. Here, the constraint is enforced by formulating the loss function in the form

$$\mathcal{L}(\boldsymbol{m}) = \frac{1}{2}\sum_{i=1}^{N} \|\boldsymbol{m} \cdot \boldsymbol{x}_i - y_i\|^2 + \|\lambda \boldsymbol{m}\|^2, \tag{4.18}$$

where the regularization term $\lambda \in \mathbb{R}$ can be seen as the precision with which the weights in $\boldsymbol{m}$ are to be selected, or as the inverse of the standard deviation they should fall within. The higher the value of λ, the narrower is the range within which the elements of W have to fall. The closed-form solution that minimizes the loss function in 4.18 is

$$\boldsymbol{m} = (\boldsymbol{X}^T\boldsymbol{X} + \lambda \boldsymbol{I}_{D\times D})^{-1}\boldsymbol{X}^T\boldsymbol{y}. \tag{4.19}$$

4.2.3 Regression kernels

A kernel function $k(\boldsymbol{x_i}, \boldsymbol{x_j}) : \mathbb{R}^D \times \mathbb{R}^D \to \mathbb{R}$, in the context of regression, is based on the scalar product of a mapping function $\boldsymbol{\phi}(\boldsymbol{x}) : \mathbb{R}^D \to \mathbb{R}^K$ that has the intent of providing a regression machine with a vector that makes the outcome prediction easier to match to the training examples. Kernel functions should therefore circumvent the linearity of the RR method. For the purposes of the kernel function, the mapping function $\boldsymbol{\phi}(\boldsymbol{x})$ does not strictly have to be tractable, and could for example have infinite dimensionality ($K = \infty$), as is the case e.g. for the Radial Basis Function (RBF) kernel [132]. In order for the kernel function to be defined, only the internal product of two mapped vectors $\boldsymbol{\phi}(\boldsymbol{x_i})$ and $\boldsymbol{\phi}(\boldsymbol{x_j})$ has to be defined, so that the kernel function is

$$k(\boldsymbol{x}_i, \boldsymbol{x}_j) = \boldsymbol{\phi}(\boldsymbol{x_i})^T\boldsymbol{\phi}(\boldsymbol{x}_j). \tag{4.20}$$

For the purposes of ridge regression, it is possible to reformulate the prediction from Eq. 4.15 by plugging in Eq. 4.19 substituting the samples $\boldsymbol{x}$ with their mapping $\boldsymbol{\phi}(\boldsymbol{x})$, and the prediction can be formulated as

$$y = \boldsymbol{y}^T(\boldsymbol{K} + \lambda \boldsymbol{I}_{D\times D})^{-1}\boldsymbol{k}(\boldsymbol{x}). \tag{4.21}$$

Here, the square and symmetric kernel matrix $\boldsymbol{K} \in \mathbb{R}^{N\times N}$ has elements $K_{i,j}$ defined as the kernel function $k(\boldsymbol{x}_i, \boldsymbol{x}_j)$, and the vector $\boldsymbol{k} \in \mathbb{R}^N$ has components $k_i|_{1\leq i\leq N}$ defined as the kernel function $k(\boldsymbol{x}_i, \boldsymbol{x})$, where $\boldsymbol{x}_i|_{1\leq i\leq N}$ is a sample among the ones forming the training set $\mathcal{T}$, and $\boldsymbol{x}$ is the vector for which the label is to be predicted [133]. Notice that the mapping function $\boldsymbol{\phi}(\boldsymbol{x})$ does not appear anywhere in 4.21, and does not need an explicit formulation for the purposes of the prediction step. This is known as the kernel trick [134]. If $\boldsymbol{\phi}(\boldsymbol{x})$ is not known, however, the Sherman Morrison formula [130] cannot be applied, and incremental learning is likewise not possible. The training step then has complexity $\mathcal{O}(N^3)$, and the prediction step has complexity $\mathcal{O}(N)$.

4.2.4 Random Fourier features

In order to use the Sherman-Morrison formula and use incremental learning, assuming that the kernel function of choice is the RBF, various approximations of the underlying mapping function $\boldsymbol{\phi}(\boldsymbol{x}) : \mathbb{R}^D \to \mathbb{R}^\infty$ exist. Introduced in [135] and demonstrated in [136] for their utility in Human-Machine Interface (HMI) applications, the RFF kernel approximates a radial basis function by means of coefficients randomly drawn from two specific distributions. The approximated mapping function $\hat{\boldsymbol{\phi}}(\boldsymbol{x}) : \mathbb{R}^D \to \mathbb{R}^K$ is defined as having single components $\phi_i|_{1<i<K}$ of the form

$$\phi_i(\boldsymbol{x}) = \sqrt{2}\cos(\boldsymbol{\Omega}^T \boldsymbol{x} + b), \boldsymbol{\Omega} \sim \mathcal{N}(0, \sigma^2), b \sim \mathcal{U}_{[0,2\pi[}, \tag{4.22}$$

where $b \in \mathbb{R}$ is sampled from a continuous uniform distribution defined over the $[0, 2\pi[$ interval, and $\boldsymbol{\Omega} \in \mathbb{R}^D$ is sampled from a Gaussian distribution with 0 mean and standard deviation $\sigma \in \mathbb{R}$, which is one of the hyperparameters of the RFF kernelized ridge regression, together with the mapping function's dimensionality K and the regularization term λ. This approximation renders it possible to formulate the training step and the prediction step completely separately, and furthermore to apply the Sherman-Morrison formula and incremental learning, bringing the time complexity of the training step back to $\mathcal{O}(ND^2)$ cumulatively. The closed form solution for the weight matrix is defined analogously to 4.19

$$\boldsymbol{m} = (\boldsymbol{\Phi}^T \boldsymbol{\Phi} + \lambda \boldsymbol{I})^{-1} \boldsymbol{\Phi}^T \boldsymbol{y}. \tag{4.23}$$

by substituting $\boldsymbol{X}$ for $\boldsymbol{\Phi} \in \mathbb{R}^{N \times K}$, the rows $\boldsymbol{\phi}_i \in \mathbb{R}^K$ of which are defined as the mapping $\boldsymbol{\phi}(\boldsymbol{x}_i)$ of the i-th sample comprised in the training set $\mathcal{T}$.

This kernel allows to compensate for non-linearities, and was used in A.4 in an offline analysis to assess the precision with which it is possible to predict force output given the stimulation currents. Because RFF can compensate for non-linearities, a comparison with RR served to assess the error contribution due to non-linear effects.

4.3 Posture and kinematics tracking

The BodyRig, which is a wireless constellation of sensors structured as shown in Fig. 4.2, can be used with either 5 or 7 peripherals. The BodyRig was mainly evaluated as an input device in [1], reported in Chapter A.1. The attainable precision and accuracy of the system were evaluated separately. For an exemplary depiction of the difference between the two, see Fig. 3.1.

The BodyRig's precision was tested in a virtual reality simulation environment. There, the attainable performance in a target-following task was assessed. The target followed a few pre-recorded trajectories at two speed levels. Additionally, the participants were also asked during separate runs to hold the avatar's hand as close as possible to a static target. The target motions to be followed by the participants were recorded using the BodyRig as body tracking. This experiment consisting of participants following the prerecorded trajectory can therefore be considered a repeatability test across repetitions as well as across different users.

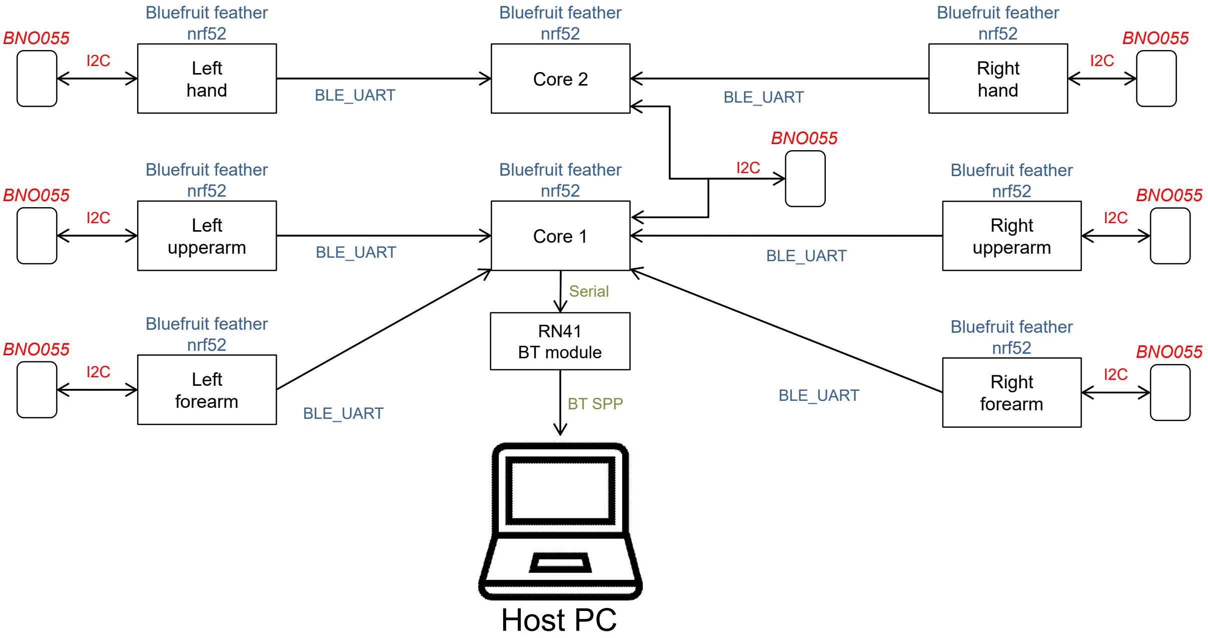

Figure 4.2: Block diagram of the sensor constellation used in the BodyRig [13].

The results presented in [1] present the main limitation that they speak to the precision of the BodyRig as a posture tracking device, but not to its accuracy. Similar proofs performance can also be inferred from the results presented in [8] and [9], where the BodyRig is used to teleoperate a humanoid robotic platform. The results from these studies mainly focus on task outcome metrics over a more extensive number of repetitions, thus allowing for some inferences about the learning curve in teleoperation tasks with the BodyRig as an input device.

An assessment of the BodyRig's accuracy as a posture tracking device for the user's upper limbs was conducted by comparing the BodyRig's prediction of the hand's pose with the hand pose as measured by an optical system, namely the VIVE VR setup from High Tech Computer (HTC) Corporation. These results are reported in [13], which is available on request. The more relevant results from all the aforementioned studies are also reported in Chapter 5.

The BodyRig is used for posture tracking in the works from Chapters A.4, A.5 and A.6, and is instrumental in computing both the arm and the muscular Jacobians (see equations 4.24-4.27 and 4.41-4.43, respectively), which are important for FES-facilitated control of movements, as shown in 4.5.

The arm Jacobian can be computed starting from the BodyRig's posture measurements as shown in Fig. 4.3. There, the vectors $\boldsymbol{j} \in \mathbb{R}^3$, $\boldsymbol{h} \in \mathbb{R}^3$ and $\boldsymbol{e} \in \mathbb{R}^3$ represent the position of a given joint, the position of the end-effector or, generally, the point of attack of a generalized force, and the direction of the axis around which the joint rotates, respectively. Following the definition from Section 4.1, the EE wrench $\boldsymbol{w} \in \mathbb{R}^6$ is assumed to be comprised of both translational force components $\boldsymbol{f}_w \in \mathbb{R}^3$ and torques $\boldsymbol{\tau}_w \in \mathbb{R}^3$. Depending on the joint, more than one rotational axis can be associated with it. In the case depicted in Fig. 4.3, the example of the elbow is shown, with $\boldsymbol{e}$ indicating the elbow flexion/extension axis' direction. With these

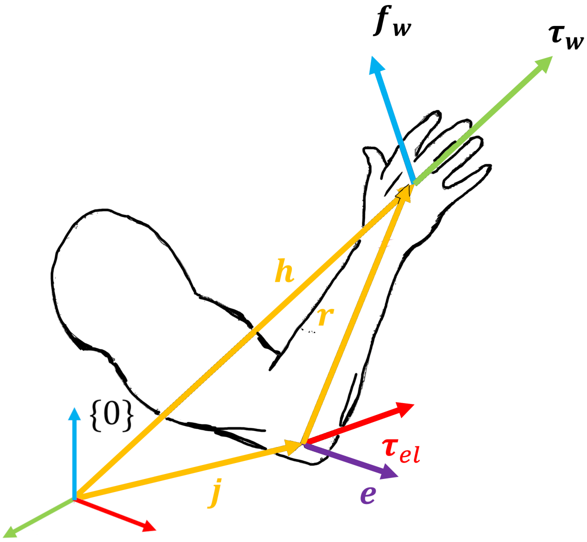

Figure 4.3: Representation of the wrench projection from Cartesian space onto the flexion/extension axis of the elbow.

elements, we can calculate individual column vectors $J_{\text{el}} \in \mathbb{R}^{6\times 1}$, which form the full arm Jacobian $J_{\text{arm}} \in \mathbb{R}^{6\times Q}$, $Q \in \mathbb{N}$ being the total number of revolute joint axes considered in the skeletal model. The arm Jacobian projects the elbow movement velocity to the corresponding Cartesian velocity as follows

$$r = h - j \tag{4.24}$$

$$\tau_{\text{el}} = r \times f_w + \tau_w = \lfloor r \rfloor_\times f_w + \tau_w = \left[\lfloor r \rfloor_\times, I_{3\times 3} \right] w \tag{4.25}$$

$$\tau_{\text{el}} = e^T \tau_{\text{el}} = \tau_{\text{el}}^T e = \left(w^T \begin{bmatrix} \lfloor r \rfloor_\times^T \\ I_{3\times 3} \end{bmatrix} \right) e \overset{!}{=} w^T J_{\text{el}} \tag{4.26}$$

$$J_{\text{el}} = \begin{bmatrix} \lfloor r \rfloor_\times^T \\ I_{3\times 3} \end{bmatrix} e \tag{4.27}$$

The sub-matrices $J_i \in \mathbb{R}^{6\times 1}$ corresponding the i-th DoF can be found analogously, and the full arm Jacobian $J_{\text{arm}} \in \mathbb{R}^{6\times Q}$ features these sub-matrices as columns, so that

$$J_{\text{arm}} = [J_1, \ldots, J_Q] \tag{4.28}$$

The right side of equation 4.26 is obtained by plugging in equation 4.13.

For specific joints, such as hinge joints, of which the elbow is an example, it might be of interest to find a robust way to pinpoint the anatomically correct direction of the functional axis in space. Such rotational axes can be identified in various ways. OpenSim, for example, usually starts from a kinematic chain created based on anatomical expertise, where all functional axes and joints are based on realistic bone geometries. OpenSim then finds the joint parameters which minimize the squared difference between the orientations and/or positions which it receives from real-life measurements and the orientations and positions of the kinematic chain of the model, effectively adopting a gradient descent IK solver on a link-per-link basis [45]. Because the model is based on bone geometry, the joint axes are always rigidly defined with respect to the involved skeletal segment. Because of the linear convergence rate, this type of solution can have high time costs, and can also lead to undesired results if the loss function is not properly weighed, where for example the solution involves bones that may not be directly monitored by a sensor ending up in wholly unnatural configurations, and the error propagates in the calculation of muscular geometry.

In [5, 8, 9], the joint axes are determined on a purely functional basis, without considering the geometry of the bones in an anatomical sense, but rather by directly performing vector computations on the orientations of the IMUs. This approach takes some liberties, as it starts with a kinematic chain where all joints, including hinge joints, are assumed to be ball-socket, 3-DoF joints, and then the functional axis of the hinge joint is identified, if needed, *a posteriori*, based on the observed movements. Specifically, in the experiment presented in [8] and [9], for instance, a few joint angles had to be inferred in order for amputees to be able to use the control interface for the humanoid platform TORO [137]. In order to do so, using the notation shown in Fig. 4.4, the axis $\boldsymbol{e}_\times \in \mathbb{R}^3$ of the elbow flexion-extension movement is identified by calculating the cross product between the z axis of the humeral and forearm IMU's coordinate frame, i.e. $\boldsymbol{e}_{H,z} \in \mathbb{R}^3$ and $\boldsymbol{e}_{H,z} \in \mathbb{R}^3$ respectively. These directions are expressed in a common coordinate frame, but importantly the translation $\boldsymbol{h}$ between the sensor's frame and the common frame are not considered. The functional axis is then formulated as

$$\boldsymbol{e}_\times = \frac{\boldsymbol{e}_{H,z} \times \boldsymbol{e}_{F,z}}{||\boldsymbol{e}_{H,z} \times \boldsymbol{e}_{F,z}||}. \tag{4.29}$$

This gives a direction $\boldsymbol{e}_\times$ perpendicular to both the humerus' and the forearm's longitudinal axis, which both provides the direction of the elbow flexion-extension axis, as well as a reference for the pronation-supination movement, the angle of which can be calculated as the one between the elbow flexion-extension axis and the z axis of the forearm's IMU. In [8] and [9], the pronation-supination angle can be offset by an angle $\theta_{\text{offset}} \in [-\pi, \pi[$ and multiplied by a gain $\gamma \in \mathbb{R}$ as needed, in the case where a trans-radial amputee is using the BodyRig, so that the pronation-supination angle expressed in radians $\theta_{\text{pron-sup}} \in [0, 2\pi[$ transmitted to the avatar is

$$\theta_{\text{pron-sup}} = \gamma \cos^{-1}\left(\boldsymbol{e}_\times \cdot \boldsymbol{e}_{F,y}\right) + \theta_{\text{offset}}. \tag{4.30}$$

This method is robust if the elbow flexion is clearly detectable, which is the case if the elbow is flexed beyond 10°-20°. If the elbow flexion angle $\theta_{\text{elbow}} \in \mathbb{R}$ falls below this threshold, a possible option is to maintain the last known flexion axis in the coordinate system of the proximal body segment, which in this case is the humerus.

This type of alignment of the body's rotational axes offers some advantages w.r.t. the IK procedure used in OpenSim or similar software suites. While somewhat less versatile, as it only allows to identify the axes of hinge joints such as the elbow, it is computationally more efficient, and it does not cause mismatches in the calculated and real orientation of the limbs when the IMU peripherals slip during movement with respect to the skeletal structure, which is an effect that should be kept into consideration, as external IMUs and markers lie on top of

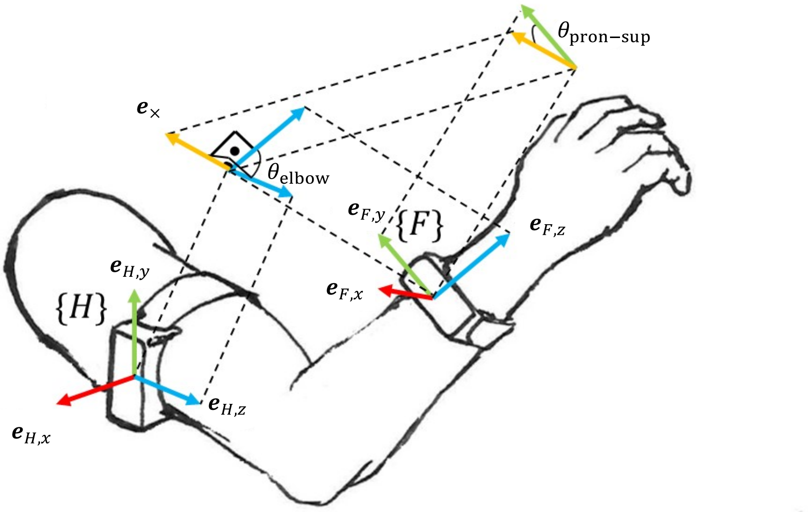

Figure 4.4: The vector calculation necessary to find the direction of the elbow flexion/extension axis and the magnitude of the pronation/supination angle [13].

soft tissues with high mechanical compliance, and are therefore subject to changes in position w.r.t. the skeletal structure. In OpenSim, markers or IMUs can be assigned to skeletal segments, and are assumed to be rigidly coupled to them. The loss function of the IK solver can be regularized in such a way that specific joint parameters have an increased influence on the loss function's value [45]. However, because of the assumption of the sensors being coupled with bones in the anatomical sense, mismatches in the angular offsets between sensors and body segments can lead to higher errors in posture estimation as opposed to a model like that proposed in [4], where all joints of the IMU-tracked skeleton are assumed to have 3 axes, and any functional axis is identified *a posteriori* based on functional movements. In the OpenSim's IK solver, on the other hand, in the case of segments separated by hinge joints, the kinematic chain has to compensate for this mismatch with a limited amount of DoFs, which can lead to unnatural poses.

4.4 External support

A wearable robotic platform can be used in order to both provide assistance to the user and in order to measure the force output without limiting the user's mobility. In order to minimize weight and maximize usability, comfort and range of motion, a lightweight platform should arguably be preferred. On the other hand, bulkier apparatuses can of course host more precise sensing equipment and more powerful actuators [17], and, if compared to soft structures, can be more easily controlled. Considering lighter robotic assistive devices, the open question which lies at the center of the experiments presented in [2] and [3] (chapters A.2 and A.3, respectively) is how to integrate appropriate sensor modalities that would provide the user with transparent and natural control of the robot's actuators, which is also the core of RQ2.

The experiments presented in [2] and [3] assess various outcome metrics attainable when driving an assistive soft glove with two degrees of actuation and a semi-passive shoulder lightweight exoskeleton, respectively, through muscular activity measurements (sEMG and FMG, respectively).

In [2], a 2-Degree of Actuation (DoA) flexible tendon-driven assistive glove is controlled by means of sEMG sensors which estimate the intended grasp force. This estimation is then used to drive the motors which drive the tendon spools, which are controlled in velocity. In order to convert the force estimation into a velocity command, an admittance is used. The finger movement is monitored in real time by way of a set of flex sensors mounted on along the glove's fingers. The experiment consisted in a series of force-reaching tasks to be performed on a handle comprised of two shell segments separated by an actuated, admittance-controlled mechanism that regulated the distance between the two segments given the applied force. Because of this setup, the characteristic admittance of this specific force reaching task was nearly constant.

In [3], a semi-passive rigid frame exoskeleton, the adaptive PAEXO by Ottobock, was driven based on an estimate of the lifted mass obtained by measuring muscular activity in the forearm by means of FMG sensors first introduced in [138]. The estimated weight of the lifted object is used to compute the torque at the shoulder level, and, conversely, the appropriate assistive torque. This is provided by shifting the attachment point of a tense rope w.r.t. the exoskeleton's shoulder joint, thus influencing the length of the lever arm at which the assistive force is applied, and therefore the resulting torque. The experiment is designed to assess the performance of the real-time lifted mass estimation by means of FMG and the muscular activity under stress with and without adaptive assistance. The participants were asked to hold three distinct weights with an outstretched arm both statically and while performing oscillatory movements at a mandated rate of approximately 1 Hz. To record muscular activity at the shoulder level, the participants were fitted with a set of three sEMG probes (Trigno AVANTI, Delsys inc.), monitoring the EMG on anterior, superior and posterior deltoid. The recorded muscular activity was used in [3] as a marker of muscular effort in order to assess the effect of adaptive support on the user physical load, as compared to non-adaptive assistance. The PAEXO's shoulder angle sensor is also used to evaluate any impact of adaptive assistance on periodic oscillatory motions.

In addition to the results reported in [3], a later analysis of correlation between low-pass filtered rectified EMG and motion as recorded by the PAEXO's internal protractors also lead to interesting results with regards to muscular recruitment in order to compensate for gravity. The results are discussed in detail in Section 5.3.2. They mainly pertain to the Pearson correlation coefficient between the low-pass filtered rectified sEMG and the band-pass filtered exoskeleton protractor measurements. Prior to the Pearson coefficient calculation, the two signals were shifted by the delay for which the cross correlation is highest. This is done because, while the protractors are measuring the momentary angle, it stands to reason that the sEMG could show higher correlation to some linear combination of the shoulder angle and its derivatives, such as angular velocity and acceleration, which in the case of a nearly sinusoidal movement is a sinusoidal signal with a phase shift. Furthermore, detectable EMG signals are known to precede measurable force output and movement by a margin of around 1 s. The identification of the lag through cross correlation should compensate for these factors. Thus, the lag-compensated signals were compared in terms of correlation coefficient, and the Pearson's R was compared across different loading conditions.

4.5 Force output monitoring

The direct and indirect measurement of force output is the basis for the calibration and, in some cases, for the online control of the assistive setups presented in the core publications. Direct measurement, here, means the monitoring of force output by some form of force-sensing sensor modality. This measurement can occur in muscle space for example through FMG, in joint space through, e.g., joint-connected load cells [17] or in Cartesian/task space, also by using load cells. As shown in Fig. 4.5, a force output can be projected to and from each of these spaces if the relevant kinematics are known.

Indirect measurement implies the use of a sensor modality that does not directly measure force. EMG is of course a proxy for muscular activity and therefore force. In [3], FMG is used to estimate the mass lifted by the user. The type of sensor employed here was presented originally in [138] and [139], and was demonstrated to provide an output that correlates well with applied force and is clearly separable across different hand gestures when the sensors are applied in bracelet-like arrangement. Sensor placement and mounting is of the utmost importance in FMG setups, as external forces can directly influence the output signals of these sensors, and it might not be possible to distinguish signals caused by muscle bulging and collisions. In [3], force output monitoring is achieved by placing FMG sensors both on the arm as well as on the forearm of the user. The sensors on the forearm especially offer the advantage of mainly monitoring muscle groups that are not aided by the exoskeleton device used in the experiment. The adaptive assistance provided by it does not therefore influence the measurements of this sensor group. The estimation of the lifted mass is then converted into an estimate of the torque at the shoulder by projecting the corresponding force downwards by the estimated lever arm.

In [4] and [6], a 6-DoF force/torque sensor is used to directly measure the wrench at the cuff holding the user's arm in place. The arm is constrained, and the wrench measurements are only used during calibration in [6], as it is not possible to move the arm when it is cuffed.

In all cases, the force measurement in muscle space and Cartesian space is projected onto joint space (see Fig. 4.5 for reference). In [3], muscle force is first projected into Cartesian space via a ridge regression predictor, and then onto joint space via a simplified arm Jacobian (as the pose of the arm is assumed to be constant in that case). In [4] and [6], the measured Cartesian wrench is projected onto joint space by calculating the arm Jacobian as illustrated in eqs. 4.24-4.27.

In [2], on the other hand, grasp force is estimated based on sEMG signals gathered on the *flexor digitorum* and on the *flexor pollicis brevis*. The sensors were applied following the SENIAM guidelines [140], and the predicted grasp force was then included in the control loop of the assistive glove by means of an admittance. The idea of implementing admittance controls to translate a force measurement into a positional control input for a wearable assistive device has been implemented before, among others in [141]. Some considerations about admittance tuning for the purposes of force output measurement are however in order here. Starting from the series-system dynamics (Eq. 4.8), WLOG, we can assume a quasi static case, where $\ddot{\boldsymbol{q}} \approx \boldsymbol{0}$ and $\dot{\boldsymbol{q}} \approx \boldsymbol{0}$. Furthermore, if we imagine a setup like that in [2], we can set $\boldsymbol{\tau}_{\text{ext}} = \boldsymbol{K}\Delta\boldsymbol{q}$, as the only external force besides gravity acting on the fingers is that of the impedance controlled force measurement device. This gives us the simplified dynamics

$$\boldsymbol{\tau} = \boldsymbol{g}(\boldsymbol{q}) + \boldsymbol{n}(\boldsymbol{q}, \dot{\boldsymbol{q}}) + \boldsymbol{K}\Delta\boldsymbol{q}. \tag{4.31}$$

From this simplified dynamics equation, it is easy to see that, by setting a high gain (either as a scalar $k \in \mathbb{R}$ or as a matrix $\boldsymbol{K} \in \mathbb{R}^{Q \times Q}$), so that $\boldsymbol{K}\Delta\boldsymbol{q} \gg \boldsymbol{g}(\boldsymbol{q}) + \boldsymbol{n}(\boldsymbol{q}, \dot{\boldsymbol{q}})$, the effect of gravity and friction can be made negligible, and therefore we'd have a nearly proportional relation of the form $\boldsymbol{\tau} \approx \boldsymbol{K}\Delta\boldsymbol{q}$, or in the form of an admittance dynamic, $\Delta\boldsymbol{q} \approx \boldsymbol{K}^{-1}\boldsymbol{\tau}$. The disadvantage of this approach is that a high stiffness hinders the movements of the user. Therefore, as mentioned in previous chapters, as well as in the conclusion of [2] in Chapter A.2, it would be desirable to tune the $\boldsymbol{K}$ gain based on the real-time requirements of both force amplification, as well as force output measurement.

4.6 FES

Most details regarding the MyoCeption are explained in the works presented in Chapter A.4, A.5, and A.6. The MyoCeption itself comprises both a biomechanical model or control system, and a wearable device for the delivery of stimulation currents. The latter consists of a compressive jacket lined with Velcro, where the electrodes can be easily placed. The stimulation currents can be regulated over wireless through an independent control device.

4.6.1 Hardware

The stimulation signals consist of current-controlled monophasic pulses reaching voltage peaks in the order of magnitude of 10 V to 50 V, depending on the electrical impedance between the stimulation electrodes. The pulse width can be set at 100 µs or 200 µs, and the pulse rate can be set between 0.5 Hz and 100 Hz. The comparatively short pulse width means that the voltage gradient over time is comparatively high. This causes non-negligible parasitic inductive effects, which lead to cross-talk between different stimulation channels. For this reason, it is imperative that the control device keep the stimulation channels electrically insulated from each other.

As the control device should not electrically interfere with the EMS, the stimulation electrode circuit is galvanically insulated. The control device is able to regulate the stimulation currents through optocouplers driven by the main micro-controller through current drivers. This is mainly done to compensate for the non-linearities in the voltage to current curve of the optocouplers diode, which closely resembles an exponential curve. Fig. 4.6 shows

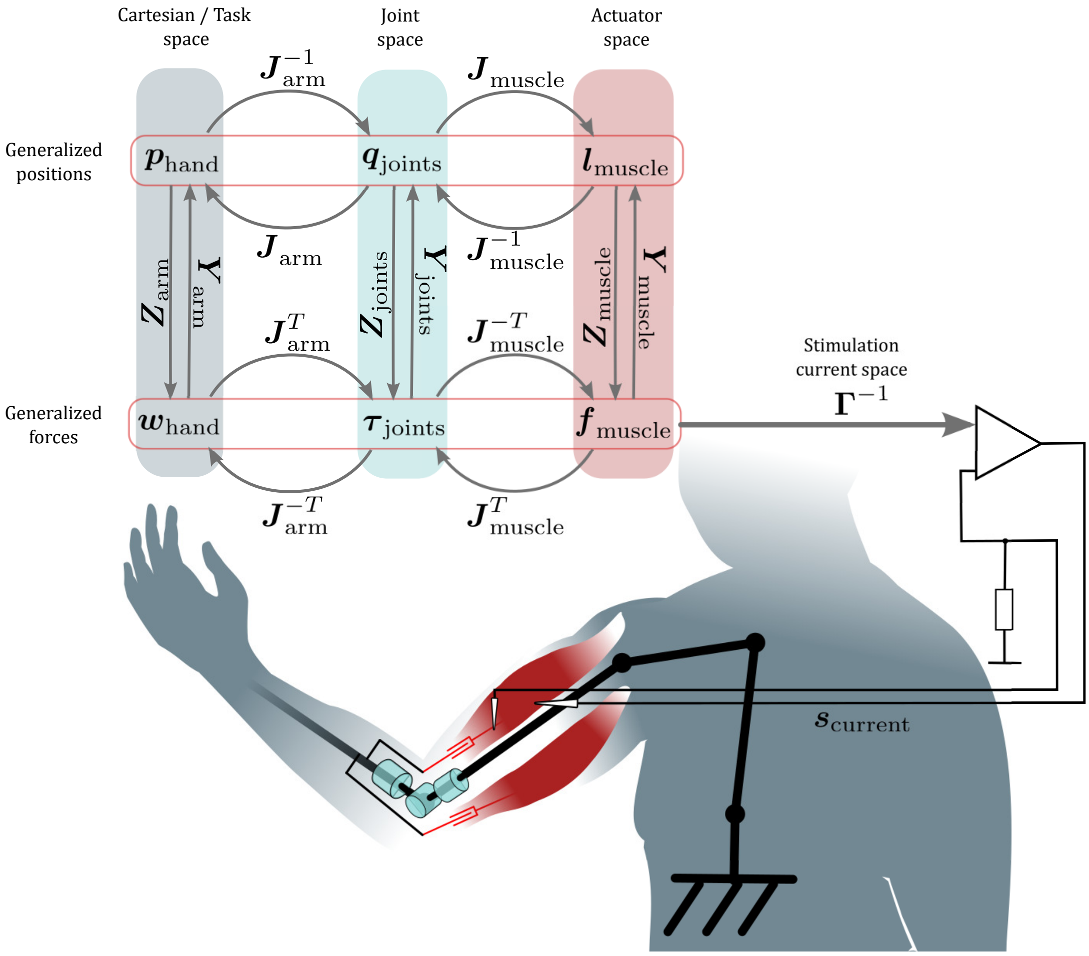

Figure 4.5: Schematic representation of the relevant positional and force coordinates necessary to control limb movements [4].

both an in-parallel and an in-series arrangement of the control electronics with respect to the stimulation channels. In both cases, as the control electronics are galvanically insulated from the stimulation lines, no current can be injected from the power source of feeding the control electronics. The wireless communication is facilitated by a micro-controller, which can output pulse-width modulated control signals with 16-bits resolution in duty cycle setting.

In later tests, which focused on high density Functional Electrical Stimulation (hdFES), the described circuit was expanded by using a demultiplexer, which allowed to connect single electrodes on a matrix to the stimulation source [142]. The possible arrangements of such high-density electrode arrays are shown in Fig. 4.7 and 4.8. The tests involving hdFES, the results of which are reported in Chapter 5, mainly focused on establishing whether different spatial stimulation injection patterns in the forearm would lead to clearly distinguishable force output patterns, both in muscular space and in terms of fingertip force output. The tests were conducted on one able-bodied participant, on the setup depicted in Fig. 4.9. The electrode matrices (depicted in Fig. 4.10) are HD10MM0804 Semi-Disposable flexible Printed Circuit Board (PCB) (OT Bioelettronica s.r.l., Turin, Italy) which has 32 electrodes with 10 mm

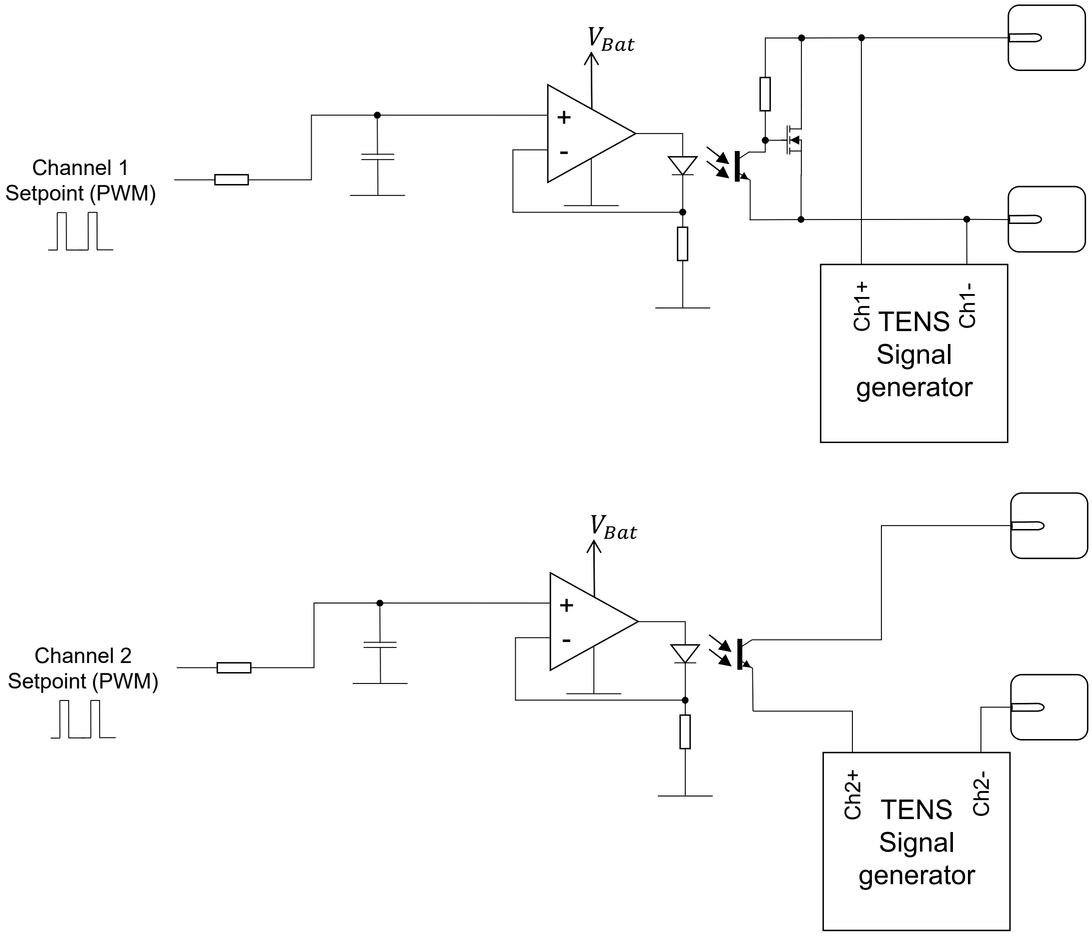

Figure 4.6: Schematic of the electrical circuits used in the MyoCeption to modulate FES pulse amplitude. **Top:** Optically driven current driver in parallel arrangement. **Bottom:** Optically driven variable resistance arrangement in series.

Inter-Electrode Distance (IED).

4.6.2 Musculoskeletal model

The model used to control the MyoCeption in [4], which is described in detail in [5], has the function of computing the force output caused by a certain stimulation, in order to compute the currents to be injected in order to induce a desired movement or force. As shown in Fig. 4.5, the model has to take into consideration both the kinematics of the arm, the geometry of the muscles, and the stimulation to contractile force transfer function. The latter is approximated trough a squared, diagonal matrix $\mathbf{\Gamma} \in \mathbb{R}^{M \times M}$, $M \in \mathbb{N}$ being the number of muscles considered in the model, and also the number of stimulation channels, with the proportionality constants between the stimulation current and the respective muscle force on the diagonal.

The musculoskeletal model of the MyoCeption can be calibrated by monitoring the twitch resulting from a sharp stimulation signal [4]. Specifically, the twitch is associated to an angular

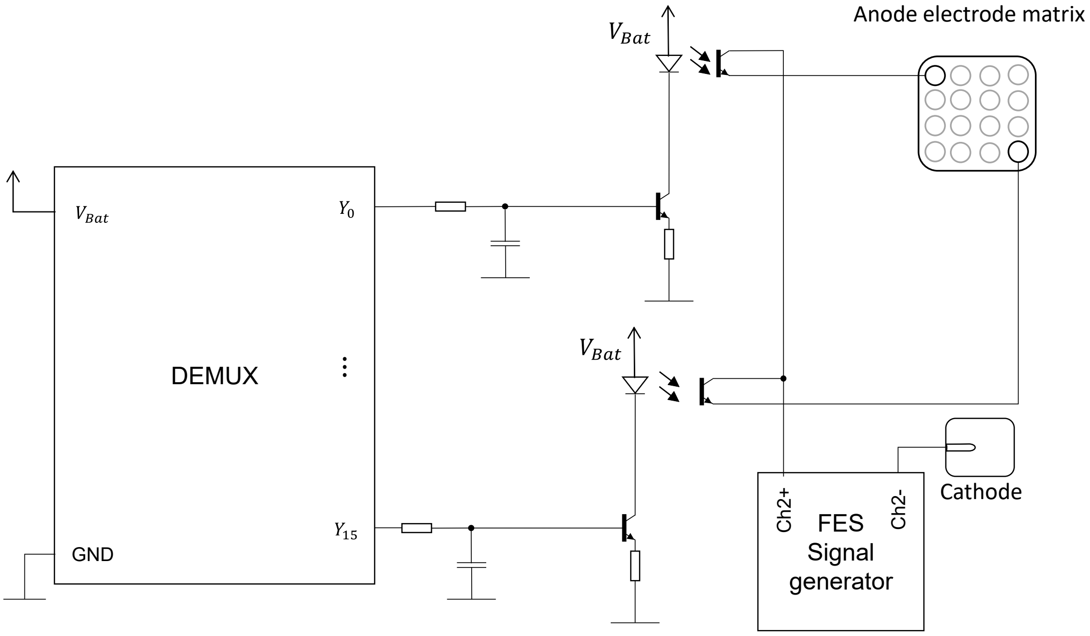

Figure 4.7: Schematic of a multiplexed FES electrode matrix where each electrode on the matrix is connected to the stimulation source anode. A cathode matrix can be built analogously.

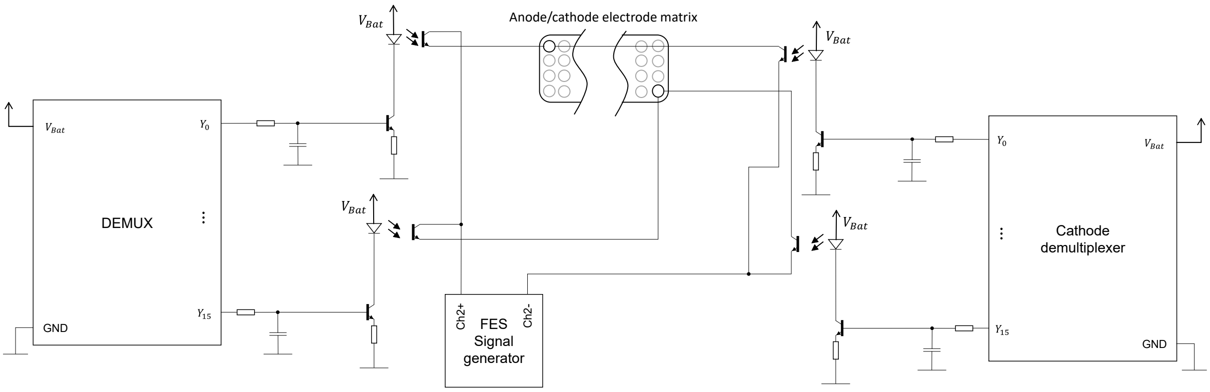

Figure 4.8: Schematic of a multiplexed FES electrode matrix where each electrode can be used both as an anode or as a cathode.

velocity vector $\boldsymbol{\omega}_{\max} \in \mathbb{R}^3$ centered on the affected joint, the location of which is $\boldsymbol{j} \in \mathbb{R}^3$. The calibration procedure assumes that the line of action corresponding to the stimulated muscle group should lie in the plan of motion in which the distal body segment moves during the twitch. As shown in Fig. 4.11, the calibration procedure adjusts the points where the line of action lies to be as close as possible to the twitch plane, which includes the joint $\boldsymbol{j}$ and has the angular velocity vector $\boldsymbol{\omega}_{\max}$ as the plane normal. This is done by finding the cylindrical coordinate $\theta_I^* \in [0, 2\pi[$ that minimize the cost function given by the distance of the routing

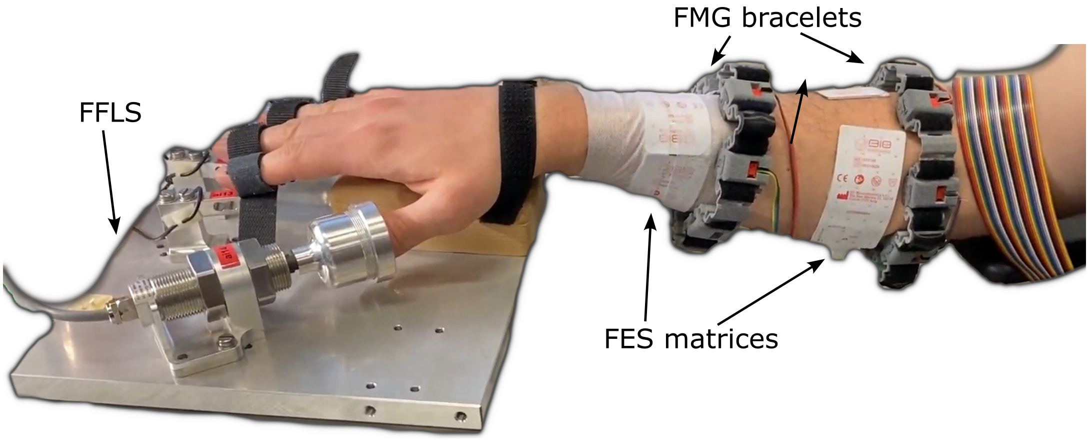

Figure 4.9: Picture of the HD-FES test setup, the FMG setup and FFLS device.

point $\boldsymbol{a_I} \in \mathbb{R}^3$ from the aforementioned plane, as per the relation

$$\theta_I^* = \arg\min_{\theta_I} \left(\sum_i \left((\boldsymbol{a_I}(\theta_I) - \boldsymbol{j}) \cdot \boldsymbol{\omega}_{\mathrm{max},i} \right)^2 \right). \tag{4.32}$$

This cost function can be minimized by gradient descent. In order to do this, we define the dependency of $\boldsymbol{a_I}$ from the cylindrical coordinate $\theta_I \in [0, 2\pi[$, using the notation shown in Fig. 4.11, as follows

$$\boldsymbol{\omega}_{\mathrm{max}}^{\{0\}} = \begin{bmatrix} \omega_x^{\{0\}} \\ \boldsymbol{\omega}_{yz}^{\{0\}} \end{bmatrix} \tag{4.33}$$

$$\boldsymbol{a}_I^{\{0\}} = \begin{bmatrix} a_x^{\{0\}} \\ \boldsymbol{a}_{yz}^{\{0\}} \end{bmatrix} = \begin{bmatrix} a_x^{\{0\}} \\ R_I \sin(\theta_I) \\ R_I \cos(\theta_I) \end{bmatrix} \tag{4.34}$$

$$\boldsymbol{a}_{yz}^{\{0\}\prime} = \frac{\delta \boldsymbol{a}_{yz}^{\{0\}}}{\delta\theta} = \begin{bmatrix} R_I \cos(\theta_I) \\ -R_I \sin(\theta_I) \end{bmatrix} \tag{4.35}$$

$$\tag{4.36}$$

Figure 4.10: Picture of one of the electrode matrices used in the initial tests about hdFES.

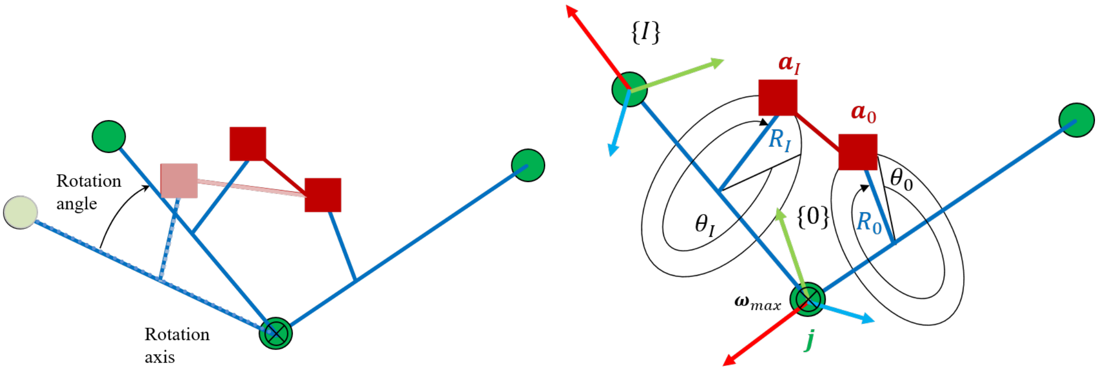

Figure 4.11: Schematic representation of a twitch occurring due to a sharp stimulation signal and the calibration of the lumped muscle origin and insertion point.

The twitch analysis can be executed based on one or more samples. In the following, it is assumed that $N \in \mathbb{N}$ samples have been gathered. Once the components of the anchor point and angular twitch velocity that are perpendicular to the body segment's length axis, $\boldsymbol{a}_{yz}^{\{0\}} \in \mathbb{R}^2$ and $\boldsymbol{\omega}_{yz}^{\{0\}} \in \mathbb{R}^2$, have been defined for every sample, the perpendicular components are arranged a matrix $\boldsymbol{\Omega} \in \mathbb{R}^{N\times 2}$ and the parallel components in a single-column matrix $\boldsymbol{R} \in \mathbb{R}^{N\times 1}$, with the individual samples as rows. The loss function $\mathcal{L}(\theta_I) : [0, 2\pi[\to \mathbb{R}$ can be formulated as a function of these matrices, and its gradient can then be computed and used to formulate the iterative update step, with a fitting scalar gain $\alpha \in \mathbb{R}$.

$$\boldsymbol{\Omega} = \begin{bmatrix} (\boldsymbol{\omega}_{yz}^{\{0\}})_1^T \\ \vdots \\ (\boldsymbol{\omega}_{yz}^{\{0\}})_N^T \end{bmatrix} ; \boldsymbol{R} = \begin{bmatrix} (\omega_x^{\{0\}})_1^T \\ \vdots \\ (\omega_x^{\{0\}})_N^T \end{bmatrix} \tag{4.37}$$

$$\mathcal{L}(\theta_I) = \frac{1}{2}\sum_i ((\boldsymbol{a_I}(\theta_I) - \boldsymbol{j}) \cdot \boldsymbol{\omega}_{\max,i}) = \frac{1}{2}\left(\Omega \boldsymbol{a}_{yz} + \boldsymbol{R} a_x\right)^T \left(\Omega \boldsymbol{a}_{yz} + \boldsymbol{R} a_x\right) \tag{4.38}$$

$$\mathcal{L}' = \frac{d\mathcal{L}(\theta_I)}{d\theta_I} = \boldsymbol{a}_{yz}^{\{0\}'} \Omega^T \Omega \boldsymbol{a}_{yz}^{\{0\}} + \boldsymbol{a}_{yz}^{\{0\}'} \Omega^T R a_x \tag{4.39}$$

$$\theta_I^{k+1} = \theta_I^k - \alpha \mathcal{L}' \tag{4.40}$$

The error function $\mathcal{L}(\theta_I)$ is minimized over the possible values of θ_I by gradient descent using the formulas presented in 4.33-4.40. In these formulas, as shown in Fig. 4.11, the origin of the coordinate system $\{0\}$ used coincides with the joint position $\boldsymbol{j}$, which leads to simplifications of the formula WLOG. Furthermore, the x-axis of the coordinate system coincides with the body link's length axis. All points along which the line of force is routed can be positioned applying the procedure in an analogous manner.

Once the muscle geometry is known, the muscular Jacobian $\boldsymbol{J}_{\text{mus}} \in R^{M\times Q}$ can be computed as exemplified in Fig. 4.12. For this purpose, the muscles can be approximated as prismatic actuators acting across one or more joints. In Fig. 4.12, a model representation of the elbow joint is shown. Lines of action are not necessarily straight lines, but are generally modeled as curves. Based on the approximated muscle displacement for small variations in joint angle, we can calculate the sub-matrix of the muscular Jacobian projecting joint angular velocity onto elbow muscle displacement as follows

$$\boldsymbol{l} = \begin{bmatrix} l_B \\ l_T \end{bmatrix} \tag{4.41}$$

$$d\boldsymbol{l} = \begin{bmatrix} 2L_1 \sin(\frac{d\theta}{2}) \\ 2R\sin(-\frac{d\theta}{2}) \end{bmatrix} \approx \begin{bmatrix} L_1 d\theta \\ -Rd\theta \end{bmatrix}\Bigg|_{d\theta \to 0} \tag{4.42}$$

$$\boldsymbol{J}_{\text{mus}} = \frac{d\boldsymbol{l}}{d\theta}\Bigg|_{d\theta \to 0} = \begin{bmatrix} L_1 \\ -R \end{bmatrix}. \tag{4.43}$$

Here as well, the complete muscular Jacobian is obtained by concatenating the sub-matrices for every joint obtained as shown in equations 4.41 - 4.43. In a more complex musculoskeletal system, where, in general, not all joints are affected by all muscles, $\boldsymbol{J}_{\text{mus}}$ is built by setting the element corresponding to the m-th muscle and j-th joint as illustrated above. If a joint's movement is not influenced by a muscle's movement, the corresponding element is 0. As illustrated in Chapter A.4, the muscular Jacobian can also be calculated based on force considerations.

The muscular Jacobian is also used to relate the muscular stiffness $\boldsymbol{K}_{\text{mus}} \in \mathbb{R}^{M\times M}$ to the joint stiffness $\boldsymbol{K}_{\text{joints}} \in \mathbb{R}^{Q\times Q}$ through a quadratic form [70] as follows

$$\boldsymbol{K}_{\text{joints}} = \boldsymbol{J}_{\text{mus}}^T \boldsymbol{K}_{\text{mus}} \boldsymbol{J}_{\text{mus}}. \tag{4.44}$$

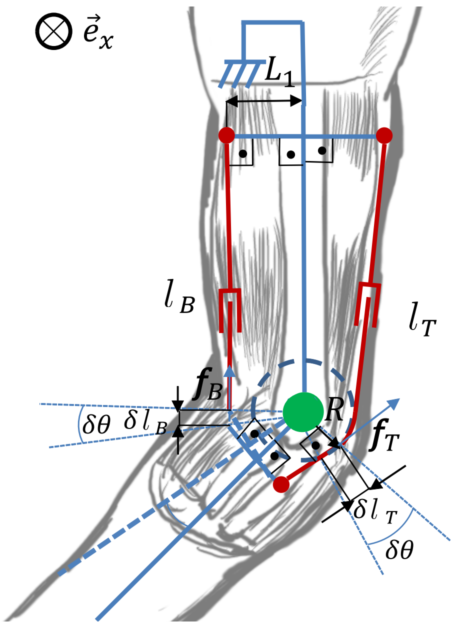

Figure 4.12: Model representation of the elbow joint, with the bicep and triceps muscular groups lumped in two prismatic joints antagonistically pulling and causing torques on the elbow joint to cause flexion and extension movements.

4.6.3 Ridge regression stimulation solver

An alternative to a musculoskeletal model to calculate the dependencies between stimulation currents and joint torques is presented in [6] and elucidated in Chapter A.6. There, a gradient descent-based solver is presented, which provides a stimulation current vector given a desired joint torque vector. The solver's update step is formulated in Eq. 4.46, which is obtained by taking the update step from Eq. 4.7 and substituting the joint parameters $\boldsymbol{q} \in \mathbb{R}^Q$ with the stimulation current vector $\boldsymbol{s} \in \mathbb{R}^M$, the pose $\boldsymbol{p} \in \mathbb{R}^T$ with the joint torque $\boldsymbol{\tau} \in \mathbb{R}^Q$, and the Jacobian transpose $\boldsymbol{J}^T \in \mathbb{R}^{T \times Q}$ with $\boldsymbol{J}_{\text{muscle}}^T \boldsymbol{\Gamma} \in \mathbb{R}^{Q \times M}$, using the notation from Fig. 4.5. As explained in Chapter A.6, the solver actually employs an approximation of $\boldsymbol{J}_{\text{muscle}}^T \boldsymbol{\Gamma}$ obtained by calibrating a RR model to predict the joint torque $\boldsymbol{\tau}$ based on the injected stimulation currents and retrieving its weight matrix $\boldsymbol{W} \in \mathbb{R}^{Q \times M}$, s.t. $\boldsymbol{W} \approx \boldsymbol{J}_{\text{muscle}}^{\boldsymbol{T}} \boldsymbol{\Gamma}$ and $\boldsymbol{\tau}(\boldsymbol{s}) \approx \boldsymbol{W}\boldsymbol{s}$. Comparing Eq. 4.46 and Eq. 4.7, one can notice an additional term. This is used to impose additional control goals on the solution update without influencing the net torque output. This is achieved by employing a null-space projection matrix $\boldsymbol{W}_{\text{null}} \in \mathbb{R}^{M \times M}$, formulated in Eq. 4.45 by using the left pseudo-inverse $\boldsymbol{W}^{\#} \in \mathbb{R}^{M \times Q}$. The additional control goals have to be formulated in the form of a scalar cost function $\hat{H}(\boldsymbol{s}) : \mathbb{R}^M \to \mathbb{R}$ to be minimized, the gradient $\nabla_{\boldsymbol{s}} \hat{H} \in \mathbb{R}^M$ of which is then projected onto the null-space by multiplication with $\boldsymbol{W}_{\text{null}}$.

$$\boldsymbol{W}_{\text{null}} = (\boldsymbol{I}_{M \times M} - \boldsymbol{W}^{\#}\boldsymbol{W}) \tag{4.45}$$

$$\boldsymbol{s}_{k+1} = \boldsymbol{s}_k + \beta \boldsymbol{W}^T (\boldsymbol{\tau}_{\text{des}} - \boldsymbol{W}\boldsymbol{s}_k) - \gamma \boldsymbol{W}_{\text{null}} \nabla_{\boldsymbol{s}} \hat{H}(\boldsymbol{s}_k) \tag{4.46}$$

Here, $\gamma \in \mathbb{R}$ is a gain designed to tune the influence of the null projection term on the update step. In Chapter A.6, the solver aims at providing as little stimulation current as possible for a desired joint torque. In that case, we have $\hat{H}(\boldsymbol{s}) = \|\boldsymbol{s}\|$ and, therefore, $\nabla_{\boldsymbol{s}} \hat{H}(\boldsymbol{s}) = \boldsymbol{s}$. Additionally, $s_i \geq 0$ is imposed for every component of $\boldsymbol{s}$, as stimulation currents can only be in the positives. With sufficient redundancy, the solver still converges to the nearest solution minimizing the difference between $\boldsymbol{\tau}_{\text{des}}$ and the stimulation-caused joint torques. It could be worth substituting the scalar γ with a matrix gain, in order to ensure homogeneous convergence across all components of the solution vector in case that $\boldsymbol{\Gamma}$ be ill-conditioned, e.g. if the different stimulation channels have much variation in how they influence the force output. The gain would have to be set based on the absolute value of the elements of the (inferred) diagonal elements of $\boldsymbol{\Gamma}$.

4.6.4 Frequency domain considerations

In order to find a sensible rate to drive the controller, a few pre-tests were conducted in order to, among other things, characterize the force output response to electrical stimulation of the human limb in the frequency domain. The setup for these pre-tests is similar to that presented in [4] in Chapter A.4. The subject sat in a chair with the forearm locked to a static robotic arm through a cuff. In this case, the robot's joint torque sensors were used to calculate the output force caused by FES.

In these pre-tests, the MyoCeption was controlled with an impedance control associating a translational force $\boldsymbol{f} \in \mathbb{R}^3$ to a positional error $\Delta\boldsymbol{p} \in \mathbb{R}^3$ calculated as the difference between the current user's hand position and a desired target position. The impedance control was comprised of proportional and integrative terms $P, I \in \mathbb{R}$ of the form

$$\boldsymbol{f} = P\Delta\boldsymbol{p} + I \int \Delta\boldsymbol{p} dt, \tag{4.47}$$

meaning that the desired force output would build up with time. Fig. 4.15 and Fig. 4.16 show a representative comparison of the commanded force and the actually measured stimulation-induced force output. The actual force output was also analyzed in terms of spectral power density in order to determine the minimal rate at which the MyoCeption's controller should be working. During these pre-tests, the user was instructed to relax as much as possible, so that no co-contraction happens. This causes the musculoskeletal structure to behave more compliantly than it would if co-contraction occurred. The power spectral density analysis of both the commanded force signal and the output force show that more than 99% of the signal power lies in the band from 0 Hz and 5 Hz. This test does not however give an estimate of what are the highest frequency components that can be successfully transmitted as force output using electrical stimulation. This can be assessed with a sweep test where the frequency of the stimulation is changed within a given range and both the muscular activity and the force output are monitored and assessed in terms of power spectral density.

Later tests show that force output measured at the fingertips has a lower power bandwidth than the muscular activity as measured in the close proximity of the stimulation electrodes through force myography. The setup for this test is shown in Fig. 4.9. The force output is monitored through a Force Sensing Resistor (FSR) sensor in Cartesian space and through FMG in muscular space. The test consists in a manual sweep of the pulse rate of the stimulation injected in proximity of the *flexor digitorum*. As shown in Fig. 4.13, the frequency of the stimulation signal was increased progressively. Above a certain frequency, the contraction of the muscle does not show a pulse, but rather a constant contraction showing an increase with rising pulse rate. During the test, the pulse rate was manually swept from 1 Hz to a maximum of ca. 30 Hz. This test shows that higher frequencies, which can be measured through FMG, are attenuated when transmitted through the full length of the muscle to the extremities, which in this case were the fingertips. The results of this tests show that the FES controller can be driven at a lower rate, as the compliance of the muscle tissue renders a higher control rate useless, as higher frequencies would be attenuated through transmission anyway. Fig. 4.14 shows the periodograms of the force output and force myography measurements. The red band shows the bandwidth in which 99 % of the total signal power falls. As is the case for the signals shown in Fig. 4.15, this bandwidth is around 5 Hz for the force output measurements. The muscular activity measurements seem to have a higher bandwidth of ca. 20 Hz. This result is in line with observations presented in [143], which presents the results of a similar test executed on animal models. While the particular transmission properties in any given musculoskeletal system depend on macroscopic factors and dimensions such as muscle length and position, besides the level of co-contraction and pre-tension, the results are qualitatively similar.

As stated above, looking at Fig. 4.13, one can see that muscles seize to show a pulsating contraction if the electrical stimulation pulses have a rate higher than a certain frequency, and beyond that threshold, force output simply shows a constant contraction which increases together with the pulse rate. The pulse rate delimiting this threshold in this test is shown to

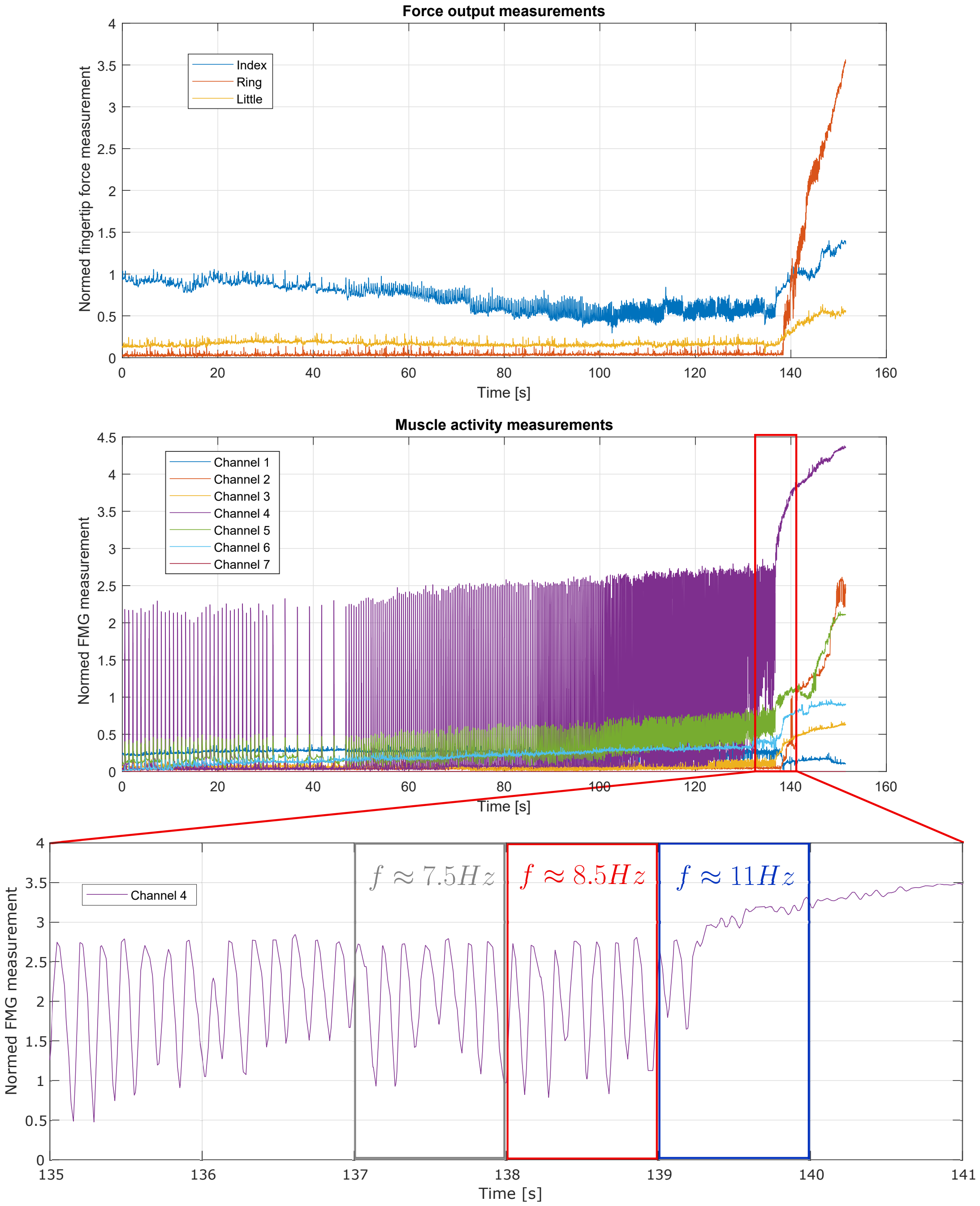

Figure 4.13: **Top:** Representative example of the fingertip force output under stimulation. **Bottom:** Representative example of the FMG-measured muscular activity under stimulation. A zoomed-in section of the transition from pulsating to sustained contraction is also depicted, with the pulse frequency f specified at 1 s intervals around the transition point.

be between 10 Hz and 15 Hz. Many factors could have an influence on the rate at which the pulsing behavior stops, such as the current amplitude, the pulse shape, electrode placement, and the electrical impedance of the tissues lying between the electrode and the motor neurons.

At any rate, this imposes a limit to the useful pulse rate that can be used to inject stimulation. This limit has repercussions also for the rate at which a current amplitude controller can be driven, as the the current amplitude can not be practically changed mid-pulse. The maximum FES pulse rate should therefore be the highest frequency at which a current amplitude FES controller makes sense. This would of course not be the case if the controller could modulate pulse frequency or pulse width, as this parameter could be tuned at any rate. There are limits given by the electrical impedance of the tissues lying between a surface electrode and the axons of the motor neurons (see Fig. 2.6).

4.6.5 Machine learning models

As elaborated in [4] and in the previous chapters, the principal categories of solvers that can be used to compute a stimulation current that would bridge the gap between a current and a desired end effector pose are on the one hand using a musculoskeletal model and on the other using a ML-model. ML-models cannot inherently account for changes in muscular geometry due to changes in posture, in most cases. In order to account for such

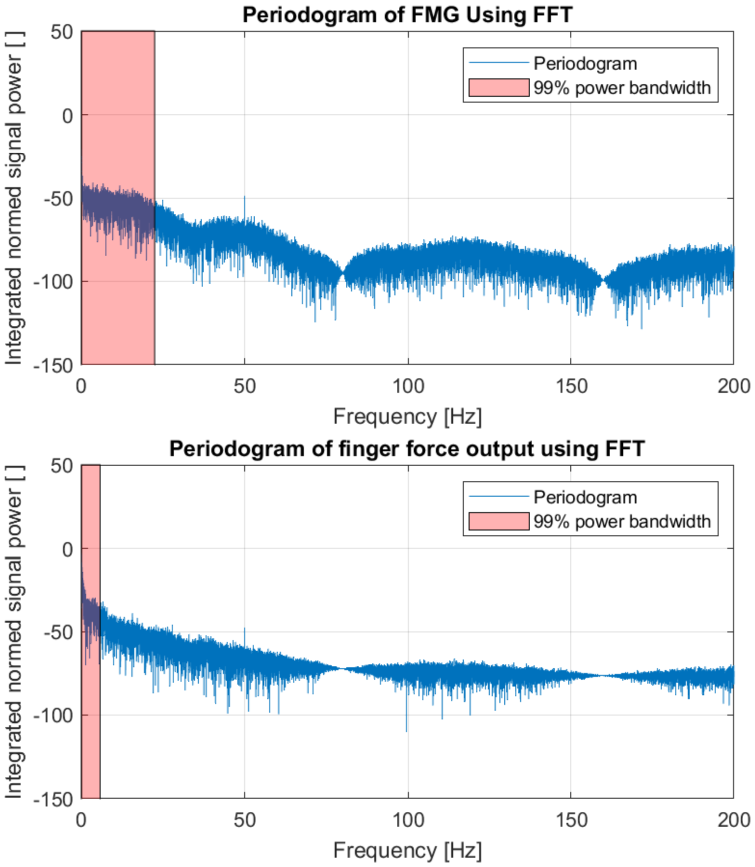

Figure 4.14: **Top:** FFT-obtained periodogram of the FMG-measured muscular activity under stimulation with 99 % power band marked in red. **Bottom**: FFT-obtained periodogram of the fingertip output force induced by stimulation with 99 % power band marked in red.

changes, most solutions presented in the literature train the ML-system over different limb postures [108]. In [94] and [107], it is the limb's dynamics that are identified in various postures.

In [4], on the other hand, the ML-model is completely based on isometric contraction measurements gathered by constraining the arm. The setup proposed in [6], which is reported in Chapter A.6, seems to perform independently of the target position, as will be discussed in Section 5.4.2, in spite of adopting a ridge regression model to predict the output force given the stimulation currents. This is due to the fact that the regression is formulated in joint space, and the predicted output torque are expressed in the coordinate system of the proximal body segment, thus minimizing the expected influence of posture changes to what is due to muscle shifting w.r.t. the body segments they span over.

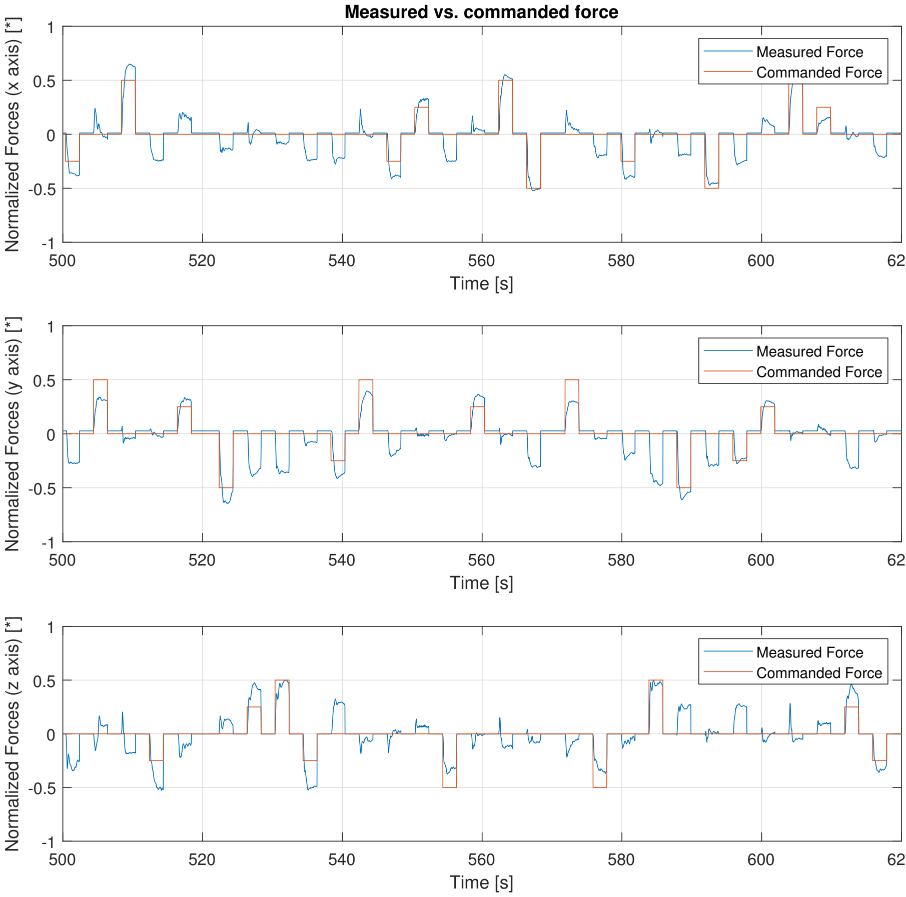

Figure 4.15: Representative comparison between the commanded force and the measured force's individual components.

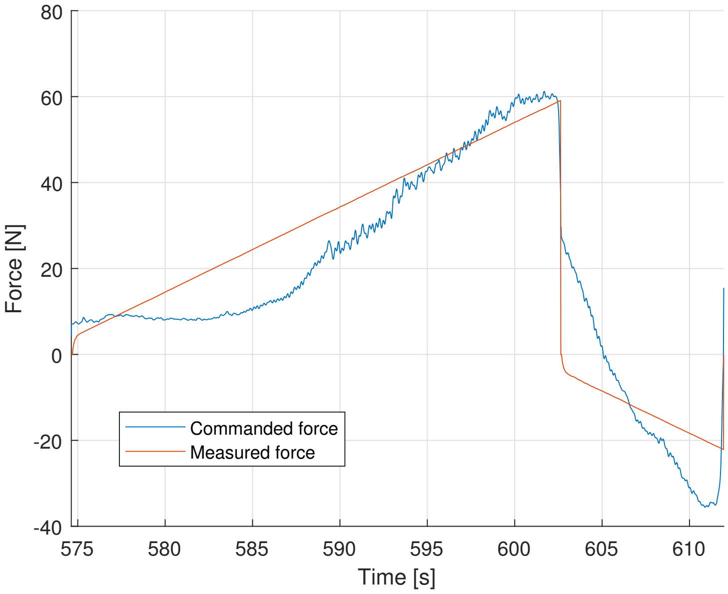

Figure 4.16: Representative plot of a commanded force ramp vs. the measured force gathered during a pre-test. This is to show the capability of the system to modulate force output through application of different current amplitudes.

4.7 Outcome metrics

This section describes some of the outcome metrics used in the experiments presented in the core and related publications of this thesis.

4.7.1 TAC test

The Target Achievement Control (TAC) test is a form of online assessment of the performance achievable when controlling a prosthetic device through myoelectric controls. In [6], this definition was extended to include the performance achievable when controlling human limbs through electrical currents. A TAC test consists in having the end effector reach a certain target configuration. The end effector is to reach a position within a range $r \in \mathbb{R}$ from the target within a certain amount of time $T_{\text{max}} \in \mathbb{R}$, and to remain within range for at least the minimal dwelling time $t_{\text{min}} \in \mathbb{R}$. Only then is the target considered reached. The main difference resides in the fact that the participants in the study from [6] were instructed to not perform any movement of their own volition, and therefore, ideally, human cognition is not part of the loop, contrary to the typical case of a prosthetic user.

It is important to note that the main parameters of a TAC test are not standardized in the literature, but vary depending on the experiment.For the target pose to be reproduced correctly, in [6], the end effector must lie within 10 cm radius of the target position. The distance from the target is calculated as the Euclidean distance. In [6], it is important to note that the range from target was not adjusted based on the total area of the reachable peri-personal space.

The TAC test allows to extract several outcome metrics [144]. The ones that are most relevant for the publications at the basis of this thesis are reported in the following:

Task Completion Time (TCT): The TCT is the time necessary for the participant to achieve the target configuration and maintain it for at least t_{min}. This metric is mainly interesting for successful tasks as it is otherwise bounded at T_{max}.

Success Rate (SR): The success rate is defined by the ratio of successful tasks to all tasks performed by the participant. The SR is usually defined for each task over all repetitions for one participant.

Number of Attempts: this metric refers to the number of times the end effector enters within range of the target and before a task is accomplished or failed. This metric can indicate the likelihood of the control overshooting, for example.

Traveled path and speed of motion: When time-free actions are performed, such as in the the evaluation of a learning curve [8, 9], possible metrics are the traveled path and speed of motion. If the hand speed over the repetitions of a task increases, this could imply better control of the device and possibly higher confidence. If an optimal path for a motion is available, the deviation of the traveled path from the cumulative minimal distance between the targets can be evaluated.

Final distance: the distance from target at the end of a task, whether successful or unsuccessful, can be used to evaluate target reachability and control precision. It is however important to consider that, because the task is considered complete after a typically small time t_{min}, after which the target is shifted, that the end effector might not be able to reach a distance from the target comparable with its actual precision after entering the minimum range r. The final distance should therefore not be considered a direct measurement of precision, but should only be considered an indirect indicator thereof.

Accuracy: Final distance as a metric can be hard to properly evaluate, as it is only measured at the point in time at which a TAC task is failed or accomplished. Furthermore, it might be useful to evaluate the system accuracy trying to exclude the influence of scenarios such as oscillatory overshooting, where the end effector oscillates around the target position. Operating on the assumption that the mean of the EE position over the oscillation is the controller's best attempt at approximating the target position, as shown in Fig. 3.1, it can be useful to average the distance from target over a moving window of a set length. The minimal dwelling time t_{min} can be seen as a sensible width for the time window [6]. The accuracy in Chapter A.6 is the minimum value of the EE distance from target averaged over a moving window during a task.

4.7.2 Predictor performance metrics

The metrics for the evaluation of the performance of a predictor, such as that used to infer the lifted mass as shown in Chapter A.3 and to predict the force output based on injected currents in Chapter A.4, vary based on whether it is a regression or a classifier that is being examined.

For regression, as the prediction is a continuous value, if a reference is available, the main performance metrics are the correlation coefficient (in most cases Pearson's $R \in [-1, 1]$) or its square R^2, and the Root Mean Square error (RMSe), or the normalized Root Mean Square error (nRMSe) [145]. Additional metrics are used in this thesis an introduced in the following.

nRMSe: The prediction accuracy, in the case of a regression algorithm, can be measured using the *nRMSe*) between the prediction $\boldsymbol{Y} \in \mathbb{R}^{N \times M}$ and the ground truth $\hat{\boldsymbol{Y}} \in \mathbb{R}^{N \times M}$ values. The individual components of these matrices $y_{k,i}|_{1 \leq k \leq N, 1 \leq i \leq M}$ and $\hat{y}_{k,i}|_{1 \leq k \leq N, 1 \leq i \leq M}$ are defined as the i-th component of the k-th sample of the predicted and ground truth, respectively. Also called a scatter index, the nRMSe is the primary offline error indicator method used to evaluate regression models. To start with, the non-normalized $\boldsymbol{RMSe} \in \mathbb{R}^M$ is to be calculated. In time-discrete signals, the i-th component of the $\boldsymbol{RMSe}$ is calculated over a horizon of N samples as

$$RMSe_i = \sqrt{\sum_{k=1}^{N} \frac{(y_{k,i} - \hat{y}_{k,i})^2}{N}}. \tag{4.48}$$

The nRMSe is derived by dividing the individual components of the RMSe by the difference between the maximum $y_{\max,i} = \max\limits_{1 \leq k \leq N} (y_{k,i})$ and the minimum $y_{\min,i} = \min\limits_{1 \leq k \leq N} (y_{k,i})$ of the i-th component

$$nRMSe_i = \frac{RMSe_i}{y_{\max,i} - y_{\min,i}}. \tag{4.49}$$

It is worth mentioning that other types of normalization are possible. Depending on the case at hand, the normalizing range might be defined differently.

Pearson's R: Pearson's correlation coefficient is the covariance between two lists of N samples $\boldsymbol{x} \in \mathbb{R}^N$ and $\boldsymbol{y} \in \mathbb{R}^N$ with average $\bar{x} \in \mathbb{R}$ and $\bar{y} \in \mathbb{R}$, respectively, normalized by the own variance of $\boldsymbol{x}$ and $\boldsymbol{y}$. As introduced in [146], Pearson's correlation coefficient R is computed as

$$R = \frac{\sum_{k=1}^{N} (x_k - \bar{x})(y_k - \bar{y})}{\sqrt{\sum_{k=1}^{N} (x_k - \bar{x})^2} \sqrt{\sum_{k=1}^{N} (y_k - \bar{y})^2}}. \tag{4.50}$$

Lag: depending on the choice of input signal $\boldsymbol{x}$, as well as on the characteristics of the regression algorithm, there might be a non-negligible lag between the prediction and the ground truth. Furthermore, if for example a muscle activity-based prediction is used to control a wearable robotic appliance, it might be of interest to measure the delay between the onset of muscle activity and measurable output of assistive force from the device. For the core publications, only a time-discrete formulation is relevant, where signals are defined over a discrete index $k \in \mathbb{N}$. The prediction and the ground truth are then denoted as $\hat{y}(k) : \mathbb{N} \to \mathbb{R}$ and $\boldsymbol{y}(k) : \mathbb{N} \to \mathbb{R}$, respectively. The two signals both have an average over k designated as $\bar{y} \in \mathbb{R}$ and $\bar{\hat{y}} \in \mathbb{R}$. A possible way to assess the lag, which was used e.g. in Chapter A.2, is the cross correlation function between the two time discrete signals of interest $\hat{\boldsymbol{R}}_{\boldsymbol{y},\hat{\boldsymbol{y}}}(j) : \mathbb{N} \to \mathbb{R}$, which is computed as the covariance between the first signal shifted by a lag $j \in \mathbb{N}$ and the second signal as follows

$$\hat{\boldsymbol{R}}_{y,\hat{y}}(j) = \sum_{k=1}^{N} (y(k-j) - \bar{y})(\hat{y}(k) - \bar{\hat{y}}). \tag{4.51}$$

Provided that the two signals are highly correlated, the value of l for which the cross correlation function $\hat{\boldsymbol{R}}_{y,\hat{y}}$ has its highest absolute value should correspond to the lag between the two signals, so that

$$lag = \arg\max_{j}(|\hat{\boldsymbol{R}}_{y,\hat{y}}(j)|). \tag{4.52}$$

Usually it is necessary to limit the search for the value of l that corresponds to the lag within a certain range, as in the case of periodic signals the cross-correlation function can have multiple maxima [147].

Principal Component Analysis (PCA): PCA is a method used for projecting a multivariate data-set onto a new coordinate system where (most of) the variation in the data can be described with fewer dimensions than the initial data [148]. Starting from a data-set of N d-dimensional samples $\boldsymbol{x} \in \mathbb{R}^D$ in matrix form $\boldsymbol{X} \in \mathbb{R}^{N \times D}$, PCA is based on the diagonal quadratic form decomposition of the covariance matrix $\boldsymbol{Q} \in \mathbb{R}^{D \times D}$

$$\boldsymbol{Q} \propto \boldsymbol{X}^T \boldsymbol{X} = \boldsymbol{W} \boldsymbol{\Lambda} \boldsymbol{W}^T, \tag{4.53}$$

where $\boldsymbol{\Lambda} \in \mathbb{R}^{D \times D}$ is a diagonal matrix gathering all the eigenvalues of $\boldsymbol{X}^T\boldsymbol{X}$ and $\boldsymbol{W} \in \mathbb{R}^{D \times D}$ gathers the corresponding eigenvectors as columns. The axes across which the data variance is highest can then be selected looking at the eigenvalue matrix $\boldsymbol{\Lambda}$, and the projected data set $\boldsymbol{Xw}$ can be then considered only in the axes along which the diagonal elements of $\boldsymbol{\Lambda}$ are highest [148]. PCA can be employed as a linear dimensionality-reduction method for the benefit of classification or regression algorithms the costs of which increase steeply with the number of dimensions of the independent variable, but can also be used for the purpose of visualization (see for example Fig. 5.9). For instance, selecting the two axes across which falls most of the variance can provide a 2D view of the data clusters, their separateness (for example through Fisher's separateness index [149]), and the path taken to reach an action. It is important to note that PCA, usually, is applied only on the independent variable data-set, and is not in any measured determined by the dependent variable or prediction value that a regression or classification algorithm might assign to a given input vector. In the example from Fig. 5.9, the color-code is assigned manually.

4.8 Effect size calculation

In the core publications, as well as in Chapter 5, various forms of tests meant to assess the influence of independent variables on various outcome metrics are used.

Pearson's R: while Pearson's R and its square are a widely used metric for the performance of regression algorithms, they are also widely use to quantify the degree to which two variables influence each other [146].

T-test : The t-test calculates a statistical probability p that two lists of data points are sampled from one normal (or Gaussian) distribution. This proposition is called the *null hypothesis*. In certain cases, the null hypothesis can be formulated in a more strict form by postulating that the mean of the data points in the first set is greater or equal than that of the second set (left-tailed), or conversely that the mean of the first set is smaller equal than the mean of the second set (right-tailed). Conventionally, the null hypothesis is considered rejected if $p < 0.05$. This threshold is arbitrary, and should not be considered the only metric of significance [150]. Two principal variants of the t-test exist, namely the paired and the unpaired t-test. The paired t-test should be used when it is possible to assume that each sample in the first set of data points can be paired to one sample in the second set. This is the case, for example, when the paired data points come from the same individual in the test population, as is the case for example in Chapters A.2 and A.3. The unpaired t-test does not assume that the samples from the first and the second set can be paired, but assumes that the two distributions have the same standard deviation [151].

ANalyis Of VAriance (ANOVA): analysis of variance (ANOVA) can be seen as an extension of the t-test to more than two sets of data [152]. Various forms of ANOVA exist, based on whether the considered variables are assumed to be dependent of each other and how the data points are grouped based on discrete values of one or more independent variables. At its core, ANOVA conveys the probability that the variance between groups outweighs the within-group variance. ANOVA merely provides an overall probability of this being the case [152], but in order to identify which group are significantly different from each other, further tests have to be conducted (e.g. pair-wise t-tests or Tukey test [153]). Like the unpaired t-test, ANOVA relies on the assumption of normal distribution of the prediction error and of the homogeneity of variance in all groups.

Wilcoxon signed-rank test: the Wilcoxon signed-rank test is an alternative to the paired t-test which does not rely on the assumption that the examined data points be sampled from a normal distribution [154]. The test works in analogous fashion to the paired Student t-test, but the null hypothesis is formulated in terms of median, instead of mean. Here as well, the null hypothesis postulate that the two medians be equal (two-sided null hypothesis), or that one be greater equal than the other (one-sided null hypothesis), as is the case in Chapter A.4.

Cohen's d: neither the t-test nor the Wilcoxon signed-rank test provide any estimate for the value of the difference, but only a probability of any difference being due to random chance. Cohen's $d \in \mathbb{R}$ is a widely used metric to assess the size of the effect [155]. In general, Cohen's d between two data sets comprised of $n_1 \in \mathbb{N}$ and $n_2 \in \mathbb{N}$ samples, respectively, with average $\bar{\mu}_1 \in \mathbb{R}$ and $\bar{\mu}_2 \in \mathbb{R}$ and standard deviation $s_1 \in \mathbb{R}$ and $s_2 \in \mathbb{R}$ is given as

$$d = \frac{\bar{\mu}_1 - \bar{\mu}_2}{s}, \tag{4.54}$$

where $s \in \mathbb{R}$ is the so-called pooled variance, which is calculated as

Table 4.1: Conventional thresholds for the effect size based on Cohen's d.

$\|d\|$ lower bound	$\|d\|$ upper bound	Effect size
0	0.2	None to very small
0.2	0.5	Small to moderate
0.5	0.8	Moderate to middle
0.8	∞	Strong

$$s = \sqrt{\frac{(n_1 - 1)s_1^2 + (n_2 - 1)s_2^2}{n_1 + n_2 - 2}}. \tag{4.55}$$

The conventional thresholds for effect sizes based on the absolute value of Cohen's d are reported in Tab. 4.1 [155]. Importantly, these thresholds are arbitrary, and should not be interpreted rigidly [150, 156].

5 Results and discussion

In the following, the main results from core publications are sorted by the aspect they relate to. In addition to the core publications, some unpublished results and additions to the discussion sections are also reported hereafter. Every section opens with the core and secondary publications the published results were originally reported in.

5.1 Posture and kinematic tracking

Primary publications:

[1] M. Sierotowicz, M. Connan, and C. Castellini. "Human-in-the-loop assessment of an ultralight, low-cost body posture tracking device." In: *Sensors* 20.3 (2020), p. 890. ISSN: 1424-8220. DOI: `10.3390/s20030890` A.1

[5] M. Sierotowicz, N. Lotti, R. Rupp, et al. "A Comprehensive Framework for the Modelling of Cartesian Force Output in Human Limbs." In: *2022 International Conference on Rehabilitation Robotics (ICORR)*. 2022, pp. 1–6. ISBN: 1-66548-829-8. DOI: `10.1109/ICORR55369.2022.9896547` A.5

Related publications:

[8] M. Connan, M. Sierotowicz, B. Henze, et al. "Learning teleoperation of an assistive humanoid platform by intact and upper-limb disabled users." In: *International Conference on NeuroRehabilitation*. Springer. 2020, pp. 165–169. DOI: `10.1007/978-3-030-70316-5_27` B.2

[9] M. Connan, M. Sierotowicz, B. Henze, et al. "Learning to teleoperate an upper-limb assistive humanoid robot for bimanual daily-living tasks." In: *Biomedical Physics & Engineering Express* 8.1 (2021), p. 015022. DOI: `10.1088/2057-1976/ac3881` B.3

[13] M. Sierotowicz. "Fusion of IMU and Muscular Information in Order to Solve the Limb Position Effect." Technical University of Munich, 2019 B.7

These results directly relate to **RQ1**, in that they pertain to the attainable precision when using a wearable IMU-based body tracker.

When describing the attainable performance of posture tracking, it is important to distinguish between precision and accuracy (see Fig. 3.1). Precision is used here as a synonym of repeatability, in that it describes how consistent is the estimation of the hand's position by the posture tracker as worn by a user. Accuracy, on the other hand, refers to how closely the estimation of the position follows a true value, usually consisting of a ground truth.

5.1.1 Attainable precision

As reported in [1], the participants could attain an average error in following a moving target around 6.33 cm and 0.66 cm in a static precision task. This performance is in line with the results published in [115]. In particular, multiplying the average error for the BNO055 reported therein by the lever arm of the avatar used in the BodyRig experiment [1], the average error is close to that observed in the static precision task.

Furthermore, analysis of the component in the error vector parallel to the target trajectory and the perpendicular component shows that the parallel component of the error shows a high correlation with the target's speed, but rather low with the target's acceleration, while the perpendicular component shows a higher correlation with the target's acceleration than with the target's velocity. This would seem to indicate a dynamic where if the target is moving fast the majority of the error is locally parallel to the target's trajectory, likely due to the user lagging behind, whereas the error component perpendicular to the trajectory is not consistently affected. On the other hand, if the target's trajectory changes abruptly, thus leading to an increased acceleration, the perpendicular component of the error vector is more directly affected than the parallel component.

5.1.2 Accuracy

The assessment of the BodyRig's absolute accuracy was not in the scope of the study presented in Chapter A.1, but was part of [13]. Therein, the BodyRig's estimate of the user's posture is compared to an optical device. The test was conducted over the course of 1 hour and 45 minutes. The ground truth is provided through the VIVE system. One marker on the hand was used to track the absolute position of the hand. Further VIVE trackers were used to monitor the orientation of the body segments of the user, as was done by the BodyRig. The ground truth in the test consists therefore of two separate measurements: one is the absolute position as measured through the VIVE marker on the user's hand, and the other is the estimation of the hand's position through forward kinematics based on the VIVE trackers orientation, which is more similar to the method used by the BodyRig. Fig. 5.1 and 5.2 show the absolute error over time, as well as a representative comparison of the estimations. The Kabsch algorithm [157] was used to find the transform that ensures the best fit between the different positional estimates, which had different coordinate systems. The median euclidean norm of the error vector was around 2.5 cm over the whole course of the experiment, which speaks to the accuracy of the BodyRig estimate. The error is comparable in the beginning and at the end of the experiment, which confirms furthermore the precision, or repeatability, of the BodyRig estimate.

The experiments presented in [8] and [9] (see Chapters B.2 and B.3) seem to show a consistent familiarization effect across different users leading to overall performance improvement over time teleoperating a humanoid robotic platform, even though the avatar is not adapted to each user's frame. Furthermore, participants who were missing one or both hands performed comparably to the normative data gathered from able-bodied participants. This would seem to indicate that users can learn to compensate for various error sources when teleoperating

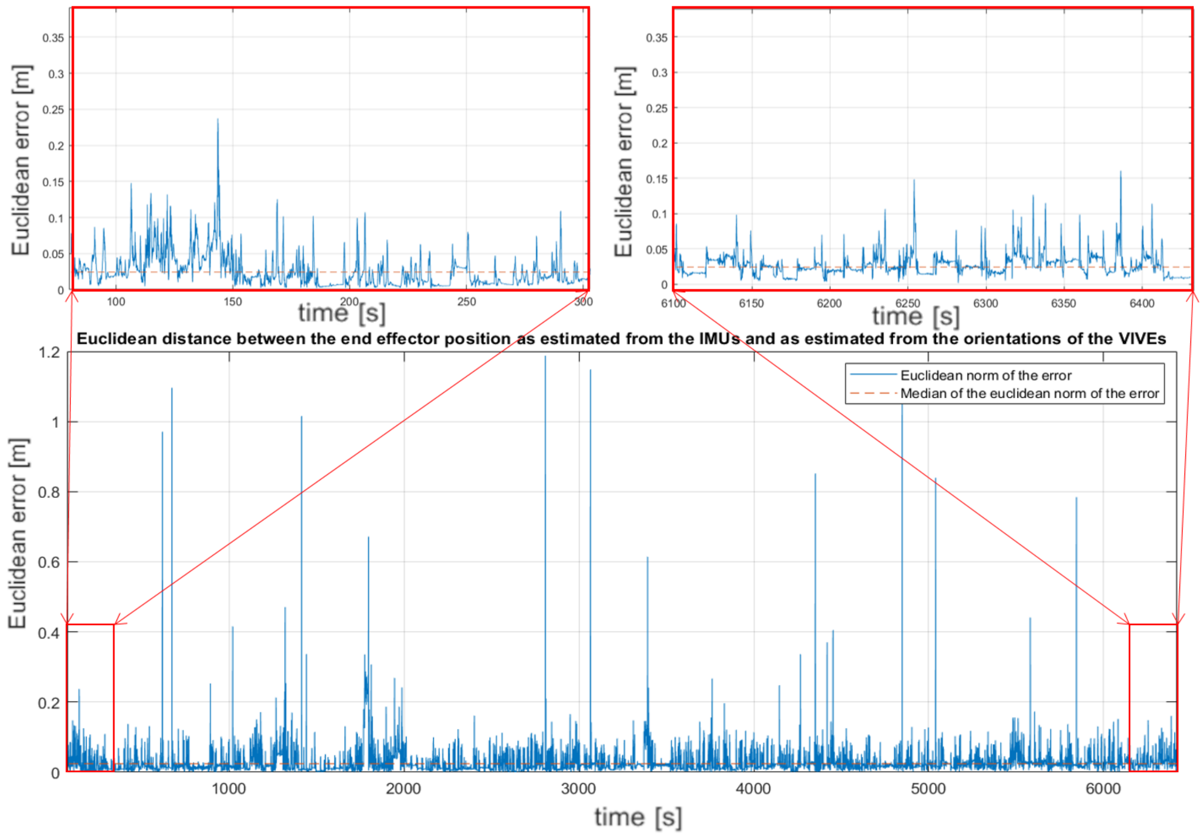

Figure 5.1: Absolute error of the BodyRig as compared to an optical forward kinematics posture tracker over time [13].

an avatar, among which apparently any discrepancy between their own body and that of the avatar. This lends credibility to the notion that, for teleoperation, and perhaps in general for applications where a user is interacting with the environment exclusively through an external support, precision and repeatability have more importance than accuracy in an absolute sense.

5.1.3 Muscle geometry estimation

These results are directly related to the second part of **RQ1**, namely the question of attainable precision when estimating muscular geometry. A ground truth of the muscular geometry can be arduous to obtain, especially during movement and *in vivo*. Therefore a proper assessment of estimation accuracy w.r.t. actual muscle routing is not practical. For this reason, the term of comparison in [5] is a third-party simulated biomechanical model of the upper limb, developed by Chadwick and colleagues in [110].

The main goal of the experiment is to show that the musculoskeletal model used in [4] and [5] (see Chapters A.4 and A.5) should be able to provide relevant properties of the muscular geometry (first and foremost moment arms). The MyoCeption's control model provides predictions of the expected torque vector for every muscle group that are qualitatively similar to those provided by an OpenSim model, while skipping many computational steps that would be required therein, such as the adjustment of the musculoskeletal model to the IMU measurements via inverse kinematics. While the results are qualitative in nature, this comparison shows that the MyoCeption's control model can predict the direction of the torque caused by a given muscle group on a given joint. The version of the MyoCeption's model used in this experiment requires the explicit assignment of an origin and insertion body segment for each muscle group, as well as a type of muscle routing. In OpenSim, each muscle group is routed from an explicitly defined origin point to similarly defined insertion point, with further possible routing points and wrap-around geometries regulating the shape of the line of action for each muscle group. Within the MyoCeption's musculoskeletal model, it would generally be desirable for less explicit definitions to be necessary. It is worth reiterating that the musculoskeletal model in [4] and [5] proposes to provide lines of force that are given by a weighed average of the action of all stimulated muscle groups, and therefore the term of comparison should not necessarily be muscles in the anatomical sense. Based on this, we would expect the geometrical properties of a line of action in the MyoCeption model to be a linear combination of those in the OpenSim model, and for this relation to be preserved across

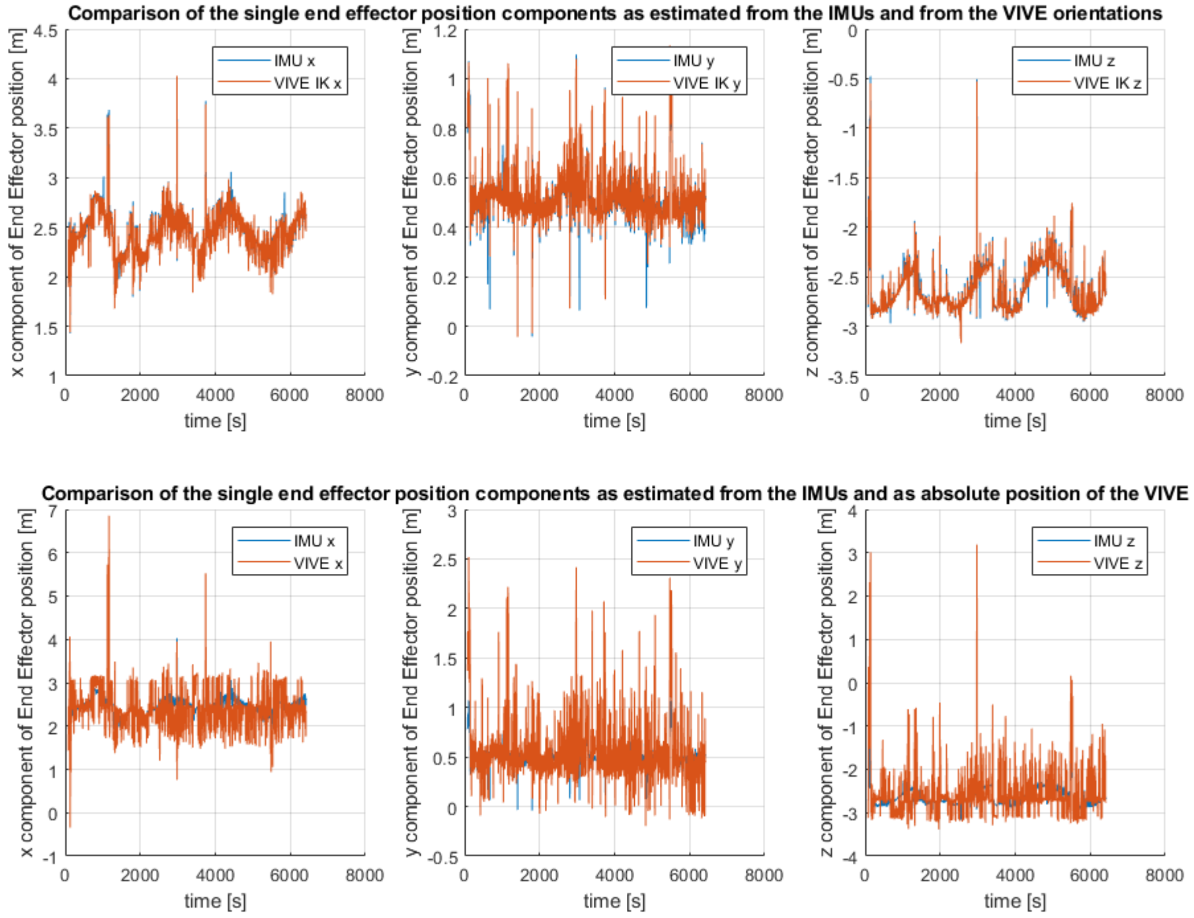

Figure 5.2: **Top:** Comparison between position tracking of the hand as computed by the BodyRig and forward kinematics with optical markers. **Bottom:** Comparison between the BodyRig direct kinematics calculation and optical trackers direct positional measurements [13].

functional movements. This seems to be the case for most muscle groups modeled examined in the MyoCeption or the benchmark model, as shown in Chapter A.5.

The musculoskeletal model used in [4] proposes to provide an estimate of muscle routing based on average force output of all stimulated muscle groups, not based on any anatomical marker. In [4] and [5], a calibration procedure is proposed which adjusts the geometry of the musculoskeletal system based on the twitch caused by a sharp stimulation current. This calibration procedure is explained in more detail in Section 4.6.2, and the results of an experiment assessing this calibration procedure are presented in Chapter A.4. As stated therein, the data gathered during the experiment indicate significant beneficial effects of the calibration procedure, but could not prove whether the benefits derive from the geometrical adjustments to the musculoskeletal model or from the adjustments to the gains by which the stimulation currents are weighed.

5.2 Force output measurement and estimation

Primary publications:

[2] M. Sierotowicz, N. Lotti, L. Nell, et al. “EMG-driven machine learning control of a soft glove for grasping assistance and rehabilitation.” In: *IEEE Robotics and Automation Letters* 7.2 (2022), pp. 1566–1573. ISSN: 2377-3766. DOI: `10.1109/LRA.2021.3140055` A.2

[3] M. Sierotowicz, D. Brusamento, B. Schirrmeister, et al. “Unobtrusive, natural support control of an adaptive industrial exoskeleton using force myography.” In: *Frontiers in Robotics and AI* 9 (2022). Publisher: Frontiers, p. 919370. ISSN: 2296-9144. DOI: `10.3389/frobt.2022.919370` A.3

[4] M. Sierotowicz and C. Castellini. “Omnidirectional endpoint force control through functional electrical stimulation.” In: *Biomedical Physics & Engineering Express* 9.6 (2023), p. 065008. DOI: `10.1088/2057-1976/acf04b` A.4

[6] M. Sierotowicz and C. Castellini. “Robot-Inspired Human Impedance Control Through Functional Electrical Stimulation.” In: *2023 International Conference on Rehabilitation Robotics (ICORR)*. 2023, pp. 1–6. DOI: `10.1109/ICORR58425.2023.10304750` A.6

Related publications:

[10] M. Panzirsch, M. Sierotowicz, R. Prakash, et al. “Deflection-Domain Passivity Control of Variable Stiffnesses Based on Potential Energy Reference.” In: *IEEE Robotics and Automation Letters* 7.2 (2022), pp. 4440–4447. ISSN: 2377-3766. DOI: `10.1109/LRA.2022.3147566` B.4

[11] M. Sierotowicz and C. Castellini. “A surface neuromuscular electrical stimulation device for universal cartesian force control in humans.” In: *JOURNAL OF ARTIFICIAL ORGANS* 46.11 (2022), e323–e327. ISSN: 1525-1594 B.5

[12] M. Sierotowicz, M.-A. Scheidl, and C. Castellini. “Adaptive Filter for Biosignal-Driven Force Controls Preserves Predictive Powers of sEMG.” in: *2023 International Conference on Rehabilitation Robotics (ICORR)*. 2023, pp. 1–6. DOI: `10.1109/ICORR58425.2023.10304772` B.6

These results directly relate to **RQ2**, as they report the attainable precision and accuracy of EMG and FMG-based force output estimation as opposed to direct measurement by using a rigid-frame exoskeleton.

In terms of force output prediction based on wearable muscle activity sensors, a comparison is present in [12]. While the focus of this publication is the development of an adaptive filter that can preserve the anticipatory edge of EMG over measurable joint torque output, it is interesting that the sensor modality showing the highest correlation with the ground truth is FMG. This does make some intuitive sense, as FMG is an inherently force-measuring sensor modality, whereas EMG measures electrophysiological muscular activity, which is bound to muscle force through several layers of non-linear dynamics, due to both the molecular machinery that comprises the muscular contractile units [158] and the inherent mechanical compliance of the muscular tissue. However, EMG is a better tool when it comes to differentiating the activity of agonistic and antagonistic muscles, and has therefore been used more often as a tool for the estimation of joint stiffness, whose estimation requires to distinguish between agonist-antagonist co-contractions, which lead to an increase in stiffness, and unilateral contraction, which rather lead to a net torque output. In the following, results from the core and related publications regarding both EMG and FMG-based force output estimation are presented.

5.2.1 EMG

The results presented in [2], included in Chapter A.2, show that surface EMG can be effectively used to assist grasping movements. Furthermore, the presented assistive glove makes use of the sEMG readings to predict the intended grasping force, which is then converted in a positional coordinate through an admittance. This is in line with the concept presented in Fig. 4.5, in this case in a mono-dimensional task space, which is spanned by the only coordinate of this force reaching task, namely the displacement between the segments of the handle to be grasped. The conversion from force to positional coordinate in this case is simple, as the handle device is controlled in impedance to generate a reaction force dependent on displacement. Because the device has a known impedance, it also has a known admittance. Therefore, the measurements of the flex sensors on the glove's fingers can be considered a proxy for force output, while not limiting the hand's range of motion. Interestingly, no statistically significant difference in prediction performance could be detected between a direct RR algorithm and one employing a RFF kernel, which can compensate for non-linearities. This could be taken as an indication that, at least in the force reaching task proposed in [2], non-linearities play a negligible role. While no statistically significant effect was found, the overall performance metric for the RFF predictor are worse. A likely explanation for this is that RFF, although able to compensate for non-linearities, exhibits unpredictable behavior for inputs that are not exactly those encountered in training. In the case of the experiment from Chapter A.2, the calibration procedure was executed with no assistance provided for the 3 force levels. During the experiment, with assistance provided by the glove, it is a demonstrated effect that the muscular activity necessary to achieve a certain level of contraction will be reduced, and therefore not coincide with the muscular activity in the training set. This could lead to a sharp decrease in assistance regulated by the RFF predictor.

In [10], EMG was used to estimate intended wrist stiffness. While in this particular experiment a precise and wide-ranging estimate was the higher priority, as opposed to a physiologically accurate stiffness estimate, the experiment showed the passivity of a 1-DoF teleimpedance system employing EMG for joint stiffness estimation. In this instance, an adaptive filter described more extensively in [12] was used to provide a stable and smooth yet high-bandwidth joint stiffness estimation.

Table 5.1: Pearson's R^2 of linear regression from FMG and sEMG ARV features to wrist torque output.

Wrist wrench output axis	Pearson's R^2 for FMG	Pearson's R^2 for sEMG
f_x	0.465	0.370
f_y	0.551	0.447
f_z	0.360	0.2570
τ_x	0.817	0.452
τ_y	0.660	0.541
τ_z	0.541	0.397

5.2.2 FMG

In [3], an FMG-mediated estimation of the shoulder torque output is used to control a semi-active exoskeleton to provide adaptive support based on the lifted weight. In this case, a predictor receiving inputs from a series of FMG sensors estimates the lifted mass. The prediction is rendered discrete and multiplied by a gain, and then used to move the attachment point of a spring to the arm orthosis, thus influencing the spring's lever arm and, by extension, the assistive torque. This controller, as shown in [3], can successfully adapt the provided assistance to the lifted mass based on FMG measurements. This is mainly shown by the fact that the muscular activity to lifted mass curve is significantly flatter if the exoskeleton provides adaptive assistance, as opposed to constant assistance. Another interesting result is that, apparently, this effect is greater in size taking into consideration the second repetition in chronological order, where fatigue is presumably affecting the user in a greater measure. This indicates that, when using adaptive assistance, fatigue leads to a lower increase in muscular activity, as compared to constant assistance. The performance of the predictor itself is also evaluated.

In this same regard, in [12], a comparison between FMG and EMG for wrist wrench estimation was conducted. In this experiment, a user was fitted with both FMG and EMG sensors, while holding a handle connected to 6-DoF force-torque strain-gauge sensor. The setup is shown in Fig. 5.3, while Tab. 5.2 shows the modality, sampling rate and number of channels for all the used sensors. While limited to a single able-bodied participant, the comparison showed that FMG lacks the leading edge of unfiltered EMG Average Rectified Value (ARV) features over measurable force output, but seems to show inherently higher correlation to the torque output reference. All correlation coefficients of a regression to wrist wrench from the FMG and from the concatenated ARV features derived from the Myo and Avanti sEMG sensors are shown in Tab. 5.1. For this comparison, ARV features from both sensors, once synchronized, were filtered through a 1st order low-pass FIR moving average filter with a cutoff frequency of 2 Hz. The results of [138] show that FMG provide clearly separable data points across different gestures. While in the experiment no direct force measurement was performed, one the gestures correspond to an isometric contraction of the forearm muscles. In [139], while the Pearson's correlation coefficient is not reported, the nRMSe suggests that FMG is a viable modality for the estimation of fingertip force output.

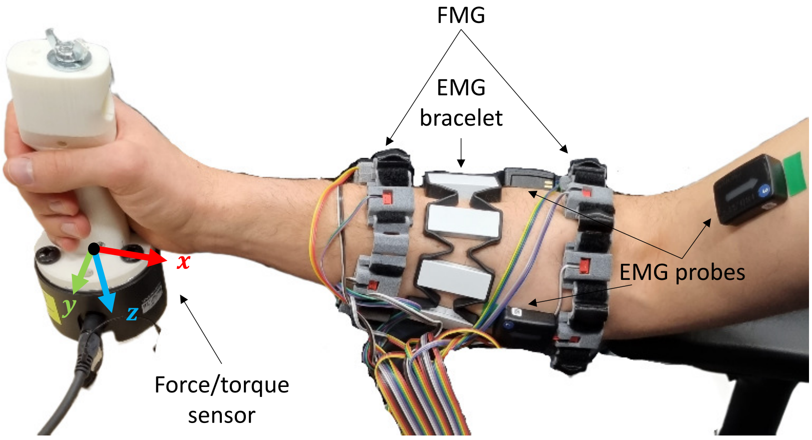

Figure 5.3: The setup used in [12] for the measurement of muscular activity underlying wrist wrench output.

Table 5.2: Sensor types, channel number and sampling rates for the setup used in [12].

Name	Sensor	Sampling Rate	Channels
Load-cell	Force/torque	200 Hz	6
FMG	Force from muscle bulging	200 Hz	13
Myo (Thalmic Labs)	sEMG	200 Hz	8
Avanti (Delsys Inc)	sEMG	2148 Hz	1 (per probe)

5.3 Adaptive assistance through external aids

Primary publications:

[2] M. Sierotowicz, N. Lotti, L. Nell, et al. “EMG-driven machine learning control of a soft glove for grasping assistance and rehabilitation.” In: *IEEE Robotics and Automation Letters* 7.2 (2022), pp. 1566–1573. ISSN: 2377-3766. DOI: `10.1109/LRA.2021.3140055` A.2

[3] M. Sierotowicz, D. Brusamento, B. Schirrmeister, et al. “Unobtrusive, natural support control of an adaptive industrial exoskeleton using force myography.” In: *Frontiers in Robotics and AI* 9 (2022). Publisher: Frontiers, p. 919370. ISSN: 2296-9144. DOI: `10.3389/frobt.2022.919370` A.3

Related publications:

[7] M. Sierotowicz, B. Weber, R. Belder, et al. “Investigating the influence of haptic feedback in rover navigation with communication delay.” In: *International Conference on Human Haptic Sensing and Touch Enabled Computer Applications*. Springer. 2020, pp. 527–535. ISBN: 3-030-58146-2. DOI: `10.1007/978-3-030-58147-3_58` B.1

[10] M. Panzirsch, M. Sierotowicz, R. Prakash, et al. “Deflection-Domain Passivity Control of Variable Stiffnesses Based on Potential Energy Reference.” In: *IEEE Robotics and Automation Letters* 7.2 (2022), pp. 4440–4447. ISSN: 2377-3766. DOI: `10.1109/LRA.2022.3147566` B.4

These results are relevant to **RQ2**, as they relate to assistance through external aids and how this can be used to reduce physical and cognitive load.

5.3.1 Fatigue reduction

The results in [2] show strong evidence that an assistive glove such as the one presented therein can successfully lower the muscular activity necessary to achieve a given grasp force, although the effect was only significant for higher grasping forces of 10 N to 15 N. This is partially due to the control gains selected for that specific user study, but in general it is expected for the effect to be more pronounced for higher grasping forces. This is in line also with the results from [3] (see Chapter A.3), where the adaptive assistance by an exoskeleton is shown to decrease the slope of the muscular activity curve as a function of load torque or lifted mass. There too, no significant effect can be detected close to the exoskeleton’s default operating point, which is the mid-range assistance level at which it was held during the non-adaptive assistance experimental condition. Analogously, the assistance provided by the glove in [2] is lower for reduced intended grasping forces, and therefore closer to the unassisted operating point.

These results underline how the influence of adaptive assistance based on the user’s inferred intention can also be thought of as an optimization of the user’s interaction with the environment, as is the approach in pHRI control [78]. The results from both [2] and [3] show that assistance from an external device modulated based on muscular activity diminishes the influence of the load imposed on the user on the muscular activity itself. This renders the interaction with the environment less straining. Force feedback-based cuing can also be used to guide the user's actions towards, for example, a safer interaction with the environment, without necessarily relieving them of any significant fatigue. The results from [7], for instance, show that force feedback can improve safety margins in rover telenavigation, with no significant effect on the user's sense of agency. In [7], the force feedback is determined purely by the rover's sensory system, whereas for the wearable robots from [2] and [3], the interaction forces were tuned using the user's musculature as an indirect instrument for measurement. Adopting this perspective underlines how many wearable robotics applications, as well as force feedback devices, are not really concerned with identifying the user's intent *per se*, but only with optimizing the robot-mediated interaction with the environment. The user is not relied upon to pilot the interaction forces, and arguably their cognition plays no role in this sense, as the interaction dynamics seem to have a tendency to emerge spontaneously. This is in contrast with, e.g., upper-limb prosthetic applications, where the robotic mechanism is working in series to the user, figuratively, and therefore the robot's movements have to be completely inferred based on the cues provided by the user voluntarily. Another exception to this are cases where the user is called upon to actively tune environmental interaction, as is the case, for instance, in teleimpedance [10]. As will be discussed in later sections, FES applications fall somewhere in between these two perspectives of intent execution and environment interaction optimization, as FES setups can be used as a form of neuroprosthesis [29], but task-level controls based on interactions with the environment could be used to integrate any lack of performance on the intent detection's side [159].

5.3.2 Influence on muscular recruitment

The analysis of muscular activity and motion of the shoulder joint that were gathered as part of the data in [3] highlighted a further effect. The correlation between motion and muscular activity after lag-compensation were compared across two different loading conditions, namely with the participants holding no weight and 2 kg in their hand, in both cases performing a circular movement at a fixed rate of 1 Hz. In this case, the anterior deltoid is the muscle responsible for compensating against gravity at the shoulder joint, while the posterior deltoid is acting antagonistically.

Interestingly, the correlation of the muscular activity of the agonistic anterior deltoid does not show significant changes across different loading conditions. The antagonistic muscle, i.e. the posterior deltoid, on the other hand, shows activity with significantly higher correlation to the shoulder angle under higher loading conditions (a signed rank test shows $p < 0.01$). A representative case is shown in Fig. 5.5. Drawing a distinction between the adaptive and non-adaptive assistance, the effect is more pronounced when only considering the non adaptive case ($p = 0.007$ vs. $p = 0.051$, Cohen's d 0.412 vs. 0.267, respectively). This indicates that most participants actively utilize the antagonistic musculature when holding a heavier object and performing a repetitive movement. The likely reason for this is that the increased weight would lead to a much higher moment of inertia of the combined arm-weight system w.r.t. the shoulder joint, and because the rate of movement was mandated at 1 Hz, the users naturally

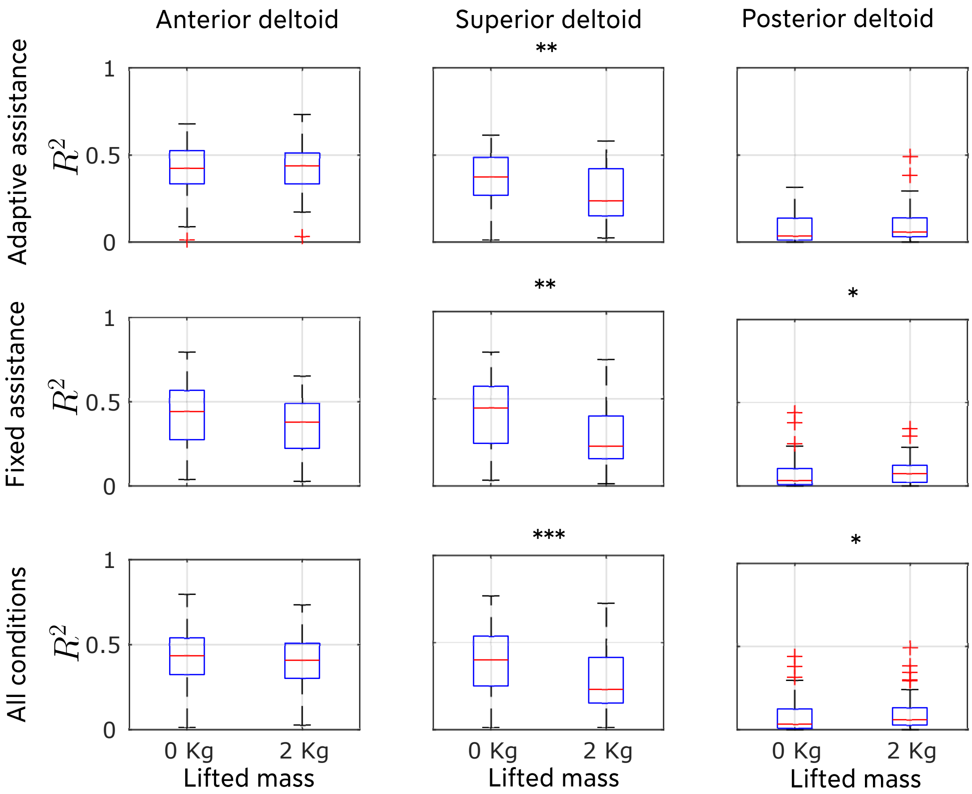

Figure 5.4: Box plots of the squared Pearson's coefficients for the three monitored muscular groups. Asterisks above individual plots indicate the effect size as determined by a signed rank test. * $p < 0.05$, ** $p < 0.01$, *** $p < 0.001$.

adopted a muscular recruitment strategy where the antagonistic muscle was used to actively accelerate the weight downwards. As for the reason why the effect is less pronounced when using adaptive assistance, that is likely due to the decreased activity of the agonistic muscle when more assistance is provided. The muscle recruitment strategy is therefore more similar to that used when moving lighter weights when using adaptive assistance, leading to the conclusion that the proposed adaptive assistance concept diminishes the influence of the lifted weight also in terms of muscular recruitment during dynamic tasks. The overall effects on the squared Pearson's R coefficients are reported in Fig. 5.4.

Furthermore, these results are indicative of the recruitment strategy adopted in this particular case, which is of interest for an assistive system integrating wearable robotics and FES. A biomimetic FES controller, when interacting with an exoskeleton, should first compute the total torque requirements by summing all control sub-goals (e.g. compensation of gravity-caused shoulder torques $g_z \in \mathbb{R}$ and trajectory tracking), and then convert it into electrical stimulation $s_{\text{sh}} \in \mathbb{R}^2$ by means of a torque-to-stim converter, driving the musculature based on the net torque resulting from this summation. Fig. 5.6 shows such a control scheme on the bottom for two cases where the commanded motion, leading to the motion-dependent torque $\tau_{\text{comm},z} \in \mathbb{R}$, is faster or slower. If the commanded motion is, e.g., slower, leading to a lower amplitude of $\tau_{\text{comm},z}$, the total torque on the shoulder joint $\tau_{\text{sh},z} \in \mathbb{R}$ remains in the positives at all times, thus only requiring a modulated stimulation of the anterior deltoid. If the motion, on the other hand, is faster, or if the inertial momenta are higher, this leads to a higher amplitude of $\tau_{\text{comm},z}$. The total torque on the shoulder $\tau_{\text{sh},z}$ could then go into the negatives, and then the antagonistic muscle would have to be stimulated in order to facilitate the movement. Fig. 5.6 at the bottom shows such the block diagram of a control system using such a recruitment strategy. The data seems to align better with this model, as opposed to one where the muscle recruitment is delivered for different control sub-goals and then superimposed, as exemplified in Fig. 5.6 at the top. In that case, the two torque components g_z and $\tau_{\text{comm},z}$ are converted into two stimulation current vectors $\boldsymbol{s}_g, \boldsymbol{s}_o \in \mathbb{R}^2$, and the net shoulder stimulation $\boldsymbol{s}_{\text{tot}} \in \mathbb{R}^2$ is the result of summing these two. As a result, both the agonist and the antagonist muscles are always under dynamic stimulation. This approach would be viable, but it would not reflect a natural recruitment strategy.

These considerations on the correlation of agonistic and antagonistic activity with movement only refer to the dynamic behavior of muscles, and not to the baseline level of contraction they might maintain during a task. Mass loading can however be demonstrated within the context of [3] to also have a significant effect on the observed mean co-contraction, defined as the product of the muscular activity of agonistic and antagonistic muscles. If the inertial load is increased, co-contraction can be shown to increase as well. Fig. 5.7 shows the main statistical effects. This is in line with the findings of [160] and [161]. As the joint stiffness increases with co-contraction, it could be argued that, in order to more precisely track a trajectory, both the agonistic and the antagonistic musculature could be contracting at the same time, leading to an increase in joint stiffness, as shown in Eq. 4.44, while modulating the net torque output to follow a given control task. As suggested in Eq. 4.31, this behavior could be seen as a strategy to lessen the influence of the system's dynamics. It would therefore be possible to consider joint stiffness a separate control goal, which does not lead to a net torque, but regulates the precision with which a trajectory is followed. Figure 5.8 shows a control concept with joint

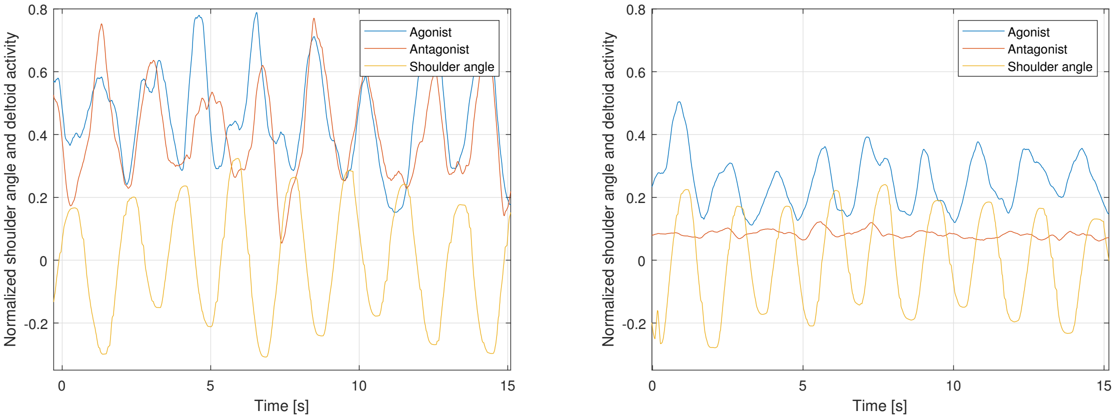

Figure 5.5: Representative examples of the EMG logs as compared to the protractor-measured shoulder angle. **Left**: Cyclical movement with the user holding a mass of 2 kg. **Right**: Cyclical movement with no additional load. All shown signals are normalized and dimensionless.

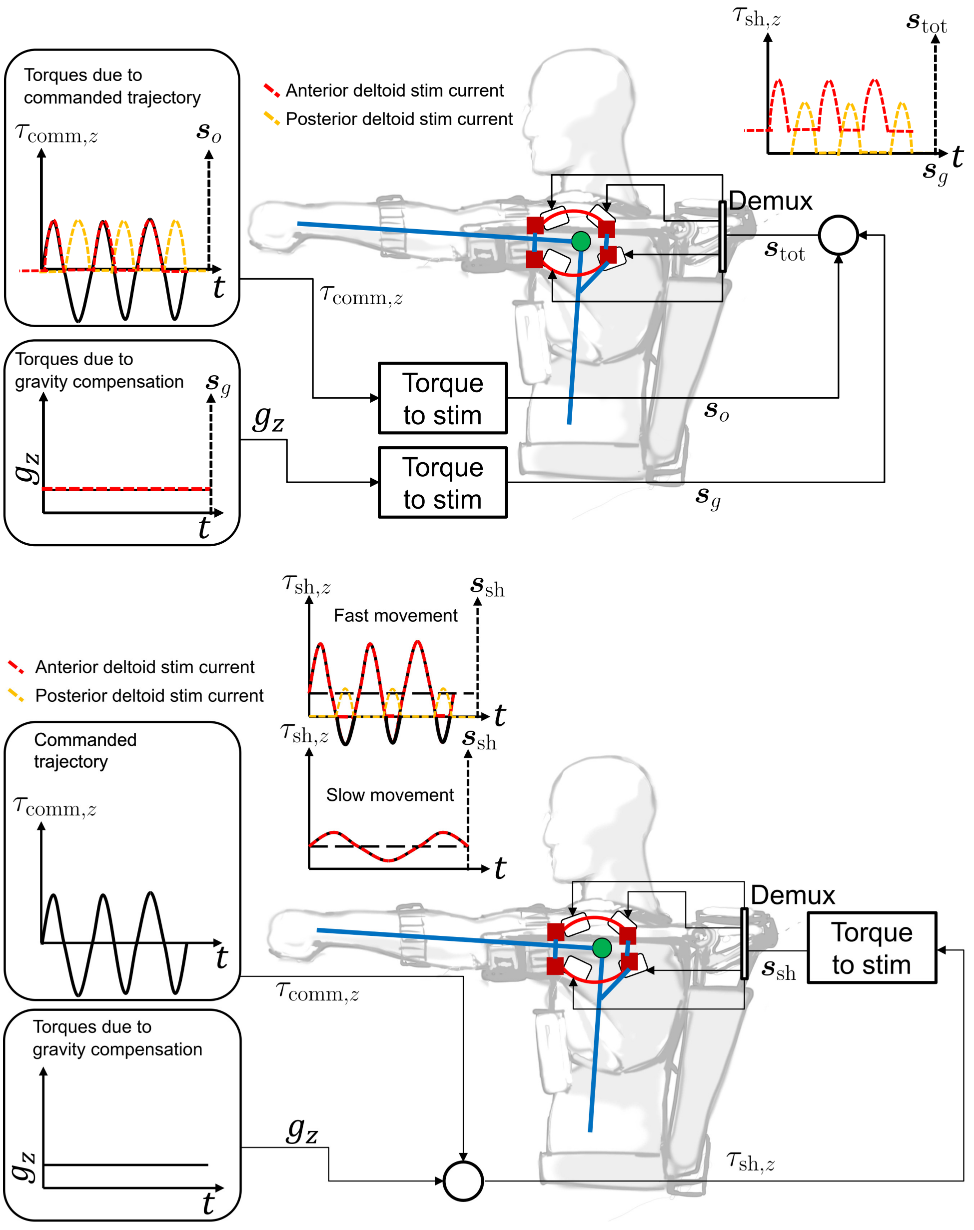

Figure 5.6: Block diagram of two possible recruitment strategies given multiple control goals. The z direction goes inside the page. **Top**: The torques necessary to achieve a given control goal are separately converted into stimulation currents, which are then summed to obtain the total stimulation for the agonist and the antagonist. **Bottom**: The torques necessary to achieve all control goals are first summed, and only then converted into stimulation.

stiffness as a separate control goal, which is converted to a muscle stimulation vector $s_p \in \mathbb{R}^2$ independently of the required net torque. The actual process of providing the controller with a proper trajectory requires awareness of the task at hand, which is a separate issue [159]. Furthermore, the attribution of agonistic or antagonistic role to any particular muscle group w.r.t. a certain movement can be a non-trivial matter, and mostly requires, in natural

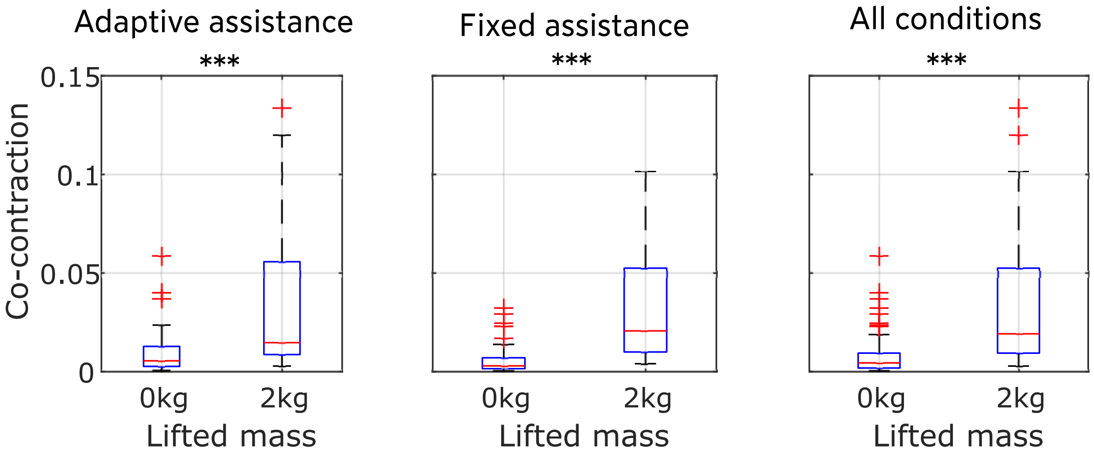

Figure 5.7: Box plots of the co-contraction, calculated as the product of the muscular activity measured on the anterior and posterior deltoid [3]. Asterisks above individual plots indicate the effect size as determined by a signed rank test. *** $p < 0.001$.

movement, the use of afferent proprioception sense organs and, generally, of feedback loops [162, 163].

In practice, the level of co-contraction could be viewed as an additional control goal only for a system with redundancies, such as can be the case for a FES system where the number of stimulation channels $M \in \mathbb{N}$ is higher than that of DoF $Q \in \mathbb{N}$ to control at the joint level. In such a case, a movement or force output goal could be achieved by providing an infinite number of stimulation vectors. For instance, going back to the example of equations 4.44 and 4.41-4.43, if the force output goal is to have zero output at the hand, technically any state of co-contraction $\boldsymbol{s}_0 \in Null(\boldsymbol{J}^T_{\text{muscle}}\boldsymbol{\Gamma})$ (using the notation from Fig. 4.5) with a net torque of zero at the joint level leads to that result. Therefore, a null-space projection as formulated in Eq. 4.46 could be used to impose the desired stiffness at the joint level as an additional control goal on top of the desired net torque output, by driving the solution towards a co-contracting stimulation vector $\boldsymbol{s}_p$ with non-zero vector length $p \in \mathbb{R}$. In order to achieve this, we could set $\hat{H}(\boldsymbol{s}) = \|\boldsymbol{s}_p - \boldsymbol{s}\|$ in Eq. 4.46, which makes the gradient $\nabla_{\boldsymbol{s}}\hat{H}(\boldsymbol{s}) = (\boldsymbol{s}_p - \boldsymbol{s})$. Finding a co-contracting stimulation current vector $\boldsymbol{s}_p$ associated with a desired joint stiffness matrix $\boldsymbol{K}_{\text{joints}} \in \mathbb{R}^{Q \times Q}$ is potentially not trivial. While muscular co-contraction can be associated with an increased joint stiffness, as shown in Eq. 4.44, an accurate model describing this association would likely necessitate a dedicated and potentially complex calibration. Conversely, if accuracy can be neglected in favor of precision, a model could be quickly calibrated by means of artificial labels, as is the case for instance in [10].

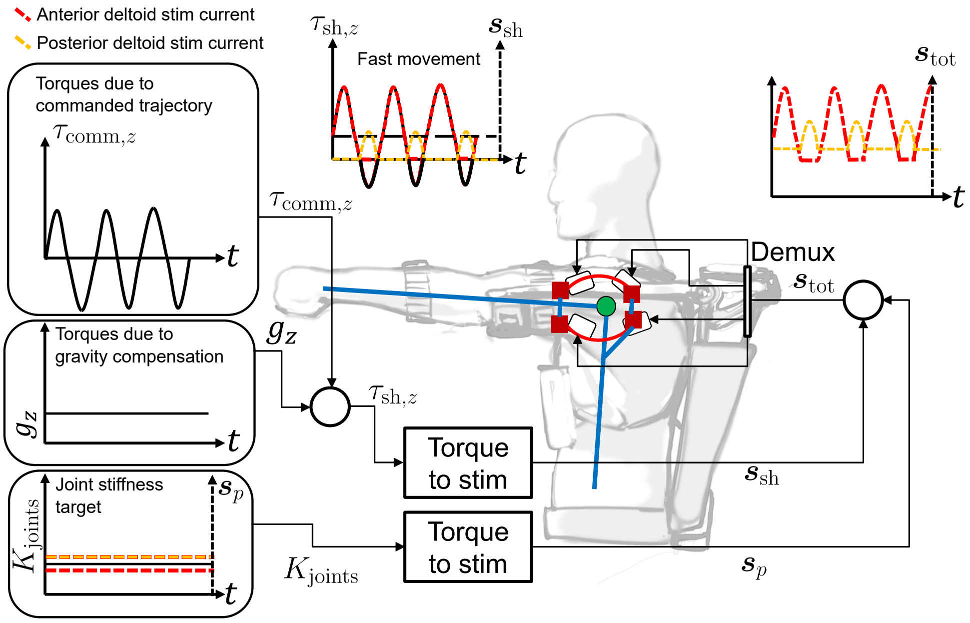

Figure 5.8: Stimulation control scheme with desired joint stiffness as an independent control goal. The z direction goes inside the page.

5.4 Functional electrical stimulation

Primary publications:

[4] M. Sierotowicz and C. Castellini. "Omnidirectional endpoint force control through functional electrical stimulation." In: *Biomedical Physics & Engineering Express* 9.6 (2023), p. 065008. DOI: `10.1088/2057-1976/acf04b` A.4

[5] M. Sierotowicz, N. Lotti, R. Rupp, et al. "A Comprehensive Framework for the Modelling of Cartesian Force Output in Human Limbs." In: *2022 International Conference on Rehabilitation Robotics (ICORR)*. 2022, pp. 1–6. ISBN: 1-66548-829-8. DOI: `10.1109/ICORR55369.2022.9896547` A.5

[6] M. Sierotowicz and C. Castellini. "Robot-Inspired Human Impedance Control Through Functional Electrical Stimulation." In: *2023 International Conference on Rehabilitation Robotics (ICORR)*. 2023, pp. 1–6. DOI: `10.1109/ICORR58425.2023.10304750` A.6

Related publications:

[7] M. Sierotowicz, B. Weber, R. Belder, et al. "Investigating the influence of haptic feedback in rover navigation with communication delay." In: *International Conference on Human Haptic Sensing and Touch Enabled Computer Applications*. Springer. 2020, pp. 527–535. ISBN: 3-030-58146-2. DOI: `10.1007/978-3-030-58147-3_58` B.1

[11] M. Sierotowicz and C. Castellini. "A surface neuromuscular electrical stimulation device for universal cartesian force control in humans." In: *JOURNAL OF ARTIFICIAL ORGANS* 46.11 (2022), e323–e327. ISSN: 1525-1594 B.5

The MyoCeption's musculoskeletal force control has been thus far characterized against a third-party model in [5] and in terms of directional force output control in [11] and [4]. The results concerning the musculoskeletal model used for force control in [4] and [11] relate to the latest part of **RQ1**, assessing the accuracy and precision attainable with the model presented in [5], in conjunction with the Nearest-Neighbor recruitment strategy described in Chapter A.4. The results quantifying the attainable precision and accuracy of the various presented force controls directly pertain to **RQ3**, and have major influences on the considerations driving the various design iterations of FES-based force control solutions presented in the core and in the related publications.

5.4.1 Nearest-Neighbor recruitment strategy

The results presented in [4] and [11] characterize the precision of the FES force control enforced through the Nearest-Neighbor recruitment strategy, and compares different stages of calibration of the underlying musculoskeletal model. The MyoCeption's musculoskeletal model provides stimulation currents that control the user's force output direction. However, the results also underline the fact that performance is highly specific to individual users. Furthermore, results indicate that the MyoCeption's twitch-based calibration leads to more consistent performance across all users. The results seem to indicate some benefit coming from the proposed twitch-based calibration process, although these benefits are highly subject-specific and hard to predict. Furthermore, the experiment did not compensate for time-dependent effects such as fatigue and familiarization, although participants were arguably given time to adjust to the sensation of FES during the initial comfort threshold setting phase.

The results presented in [4] also comprise the offline performance analysis of a predictor which is given the task of estimating the force output given the stimulation currents. The purpose of this analysis is to evaluate the potential accuracy such a prediction could achieve if calibrated with real-world force output measurements prior to normal operation where these signals are not available. A 10-fold cross validation analysis shows that a RFF algorithm can predict the force output with an average nRMSe of 0.124, and an average R^2 score of 0.857 across the prediction of Cartesian force output and joint space torque output. A result that was not published in [4] is that a non-kernelized Ridge Regression predictor can achieve nRMSe of 0.153 and R^2 of 0.836. Comparing the two predictors shows a statistically significant difference in performance in favor of the RFF estimation (with a paired t-test showing $p < 0.001$), but the effect size seems to be negligible (Cohen's d [155] is 0.202 for the nRMSe and 0.147 for the R^2 score, corresponding to a median difference of 0.014 and 0.024, respectively).

This is important, since it would indicate that non-linearities account for a comparatively small amount of the total error in force control, and that therefore, in isometric conditions at least, the assumption can be made that the stimulation currents injected through transcutaneous electrodes combine linearly into the force output space. This leads to important inferences for the design of FES-based force controls. The new approach that these inferences informed, whose performance was partially characterized in [6], represents a significant shift. The methodology used here is reminiscent of that employed by Schearer and colleagues in [44], where the authors compare the prediction of a linear model to a non-linear Gaussian Mixture Model (GMM) in a similar setup as that used in our experiments with the intent of quantifying the weight of non-linearities on the overall error in force control. The results obtained by Schearer and colleagues show an even lesser influence of non-linearities in the way stimulated muscle forces combine in the force output space. This is likely due to the face that in Schearer's case the participant is equipped with implanted FES electrodes, which as already stated grant much higher selectivity. Similar results for recipients of implanted electrodes have been reported by Friedrich and colleagues in [95], while skepticism about the assumption of linearity for transcutaneous electrodes was expressed by Westerfeld and colleagues in [90].

Table 5.3: Comparison of RR and RFF performance when predicting force output given the stimulation currents.

Force	RFF		Ridge Regression		Statistical
comp.	R^2	nRMSe	R^2	nRMSe	effects
$\|\boldsymbol{\tau}_{\text{EL}}\|$	0.846	0.133	0.833	0.137	Signed rank test shows highly significant effects $p < 0.001$. Cohen's $d \approx 0.08$ for both nRMSe and R^2.
$\|\boldsymbol{\tau}_{\text{GH}}\|$	0.837	0.130	0.829	0.135	
$\|\boldsymbol{\tau}_{\text{SC}}\|$	0.858	0.122	0.849	0.128	
$\|\boldsymbol{f}_{\text{cuff}}\|$	0.872	0.114	0.853	0.123	$p < 0.001$ on all wrench components. Cohen's $d \approx 0.12$ for R^2 and $nRMSe$.
$\|\boldsymbol{\tau}_{\text{cuff}}\|$	0.823	0.132	0.809	0.140	

Ensuring that the FES system is able to induce the desired joint torques is fundamental to the implementation of any form of higher-level controller. The results of the offline analysis provide a cursory estimate of the accuracy and precision attainable through FES. With a reliable model of joint torques deriving from a given stimulation current, it is possible to implement controllers able to achieve functionally useful goals, such as compensation for gravitational and inertial effects.

5.4.2 Ridge regression-based force control

The offline analysis conducted in [4] shows that force output both in Cartesian terms and in joint space can reliably and accurately be predicted based on the electrical stimulation. The experiment in [4] did not focus on quantifying time-dependent effects such as familiarization and fatigue. Nevertheless, the apparent accuracy of the stimulation-based force output prediction indicates that non-musculoskeletal model, which does not require the explicit definition of origin and insertion points for the individual muscle groups, nor their explicit association to individual joints, would be viable. Such a model would only require the approximate measurements of the user's skeleton, in order for the projection of the measured cuff force onto the joint space, if no direct measurement of the position of the joints is possible, i.e. through vision-based techniques.

As mentioned in the previous section, offline analysis shows that force output can be predicted almost as well through a RR linear predictor as can be done through a non-linearity compensating algorithm. Furthermore, the prediction of joint torque output is slightly better, with an average R^2 score of 0.86 as opposed to 0.855. While the difference is not consistently present, the likely sources of error for the Cartesian force prediction are small changes in arm posture which the Cartesian force output predictor cannot account for (see Fig. 4.5 for reference), unless it is also given information about the current user posture. In consideration of this, the setup presented in [6] is formulated in joint torque space, and operates by projecting all desired wrenches from task space onto it by employing the arm Jacobian $\boldsymbol{J}_{\text{arm}}$, as shown in Fig. 4.5.

The results from [6] seem to show that this approach does lead to an effective generalization over different arm poses, seen as none of the outcome metrics of the TAC seem to be significantly influenced by the arm's position, with the possible exception of the Task Completion Time (TCT), which was reported to be on the edge of significance and did later turn out to indeed be significantly affected by target position once the pool of participants was enlarged. It is of interest, however, how all other evaluated metrics (mainly Success Rate (SR), accuracy ecc.) were not affected at all. This would seem to indicate that formulating the force controller in joint space allows for better inherent generalization over different arm poses, as the posture is naturally included in the calculation seen as the desired wrench is projected onto joint space by computing the arm's Jacobian, as explained in [4]. This is in direct contrast to the position of Razavian and colleagues, who in [108] propose a controller formulated in Cartesian space. The performance reported therein is impressive, with a mean trajectory tracking accuracy in the order of magnitude of 3 cm. However, the subject pool is comparatively small and the control system requires a calibration in a large number of arm poses, rendering the calibration procedure arguably less practical than that proposed in [6]. The counterargument is that a change in posture would also lead to a change in muscular geometry, which would then lead to a change in the projection from muscle or stimulation space to joint space (by affecting the muscular Jacobian $\boldsymbol{J}_{\text{mus}}$ as shown in Fig. 4.5). Solving this would arguably still require a calibration in various arm poses, as was done also by Schearer and colleagues in [107]. The direct inclusion of limb posture in the control loop by projecting the wrench from Cartesian space to joint space would however grant continuous correction of at least part of the error that would derive from a change in position without increasing the predictor's complexity, and seems therefore the better solution.

Furthermore, it is worth mentioning that it would be possible to use the projected force output at the cuff to calculate the joint torque output, and use it in place of the twitch angular velocity vector $\boldsymbol{\omega}_{\text{max}}$ in equations 4.33-4.40. This would have the advantage of being a more explicit model, but would negate the advantage that the RR algorithm used in [4] does not require any anatomical expertise to be set up, as opposed to musculoskeletal models such as the one presented by Chadwick and colleagues in [110] and, to a lesser extent, by Sierotowicz and colleagues in [5]. It could even be thinkable to make assessment about the user's musculoskeletal system based on such a model, as it would allow to infer some characteristics about muscle geometry.

Finally, the results presented in [6] demonstrate the influence of time-dependent effects on SR. Interestingly, it would seem that familiarization plays a significantly greater role in the progression of SR over time for naive participants during their initial run, as their performance seems to initially increase to a greater degree before leveling off and then decreasing, probably due to muscle fatigue. The influence of this, incidentally, is also well evident looking at the progression of SR over time. No overall effect of user experience could be detected on any of the TAC outcome metrics.

In addition to the results published and reported in Chapters A.4 and A.6, some unpublished results were obtained during testing of hdFES setups like the ones shown in Fig. 4.7. The pre-tests these results were obtained from show the separability of the force output patterns in terms of measurable FMG and of fingertip force output as measured with the Fingertip Force Linear Sensor (FFLS) [164]. Representative PCA-reduced clusters for FMG and FFLS are shown in Fig. 5.9. The clusters come from two separate tests. The one for which the FMG clusters are reported called for 4 different patterns, while the test for which the FFLS patterns are depicted called for 12 stimulation patterns. The FFLS patterns 1, 2 and 3 show clearly distinct but internally sparse clusters. Patterns 4, 5, 6 and 12 are clearly separable from the others and non-sparse, so much so that it is possible to notice two sub-clusters (especially for pattern 6) formed due to the repetitions that were part of the experiment. Patterns 7, 8, 10 and 11 on the other hand, are not as clearly separable. Pattern 9 shows partial overlapping with pattern 10, but is otherwise distinct from the others. These results informed later iterations of the hdFES setup's design, and underline how it is possible to elicit finer force output with higher spatial resolution for the current injection, but that not all injection patterns lead to clearly discernible and distinct force outputs. All inverse dynamics solvers should keep this into account. A gradient descent-based solver analogous to the one presented in Chapter A.6

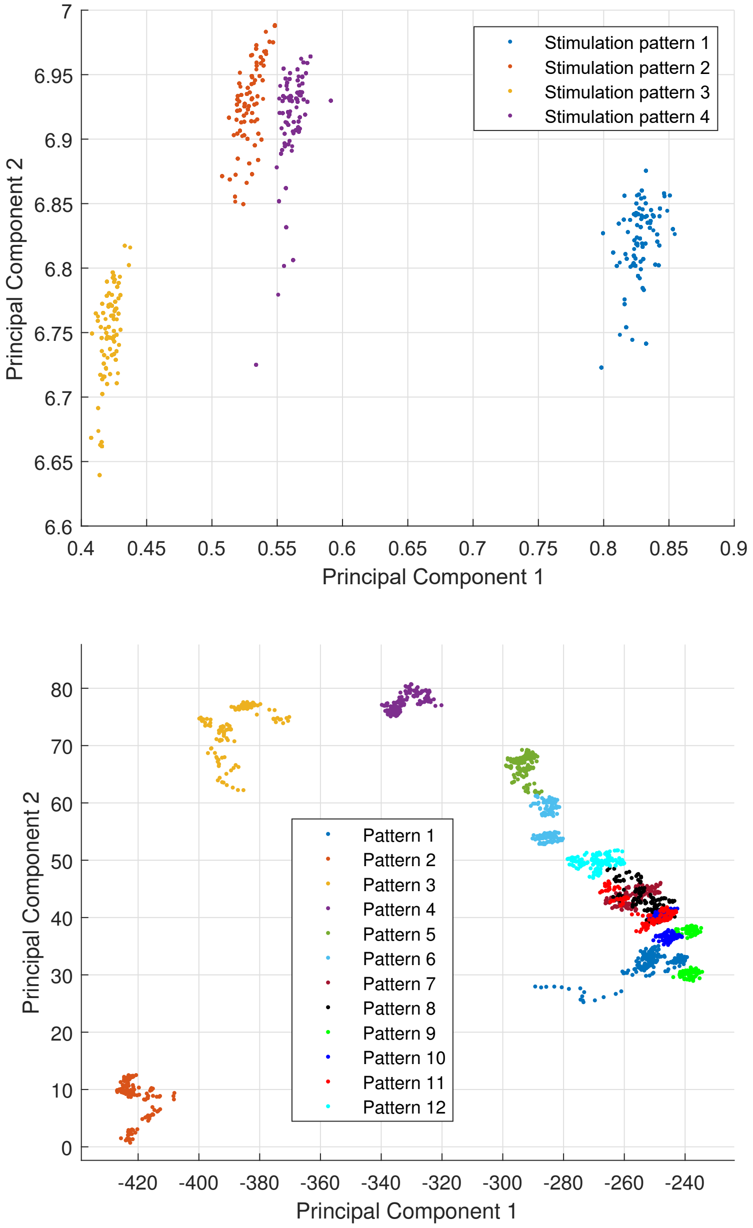

Figure 5.9: **Top:** Representative clusters of the PCA-reduced FMG sensor measurements color-coded by stimulation pattern. **Bottom:** Representative clusters of the PCA-reduced fingertip force output measurements.

was later introduced to control the hdFES setup, but results are still tentative.

5.5 Results overview

Many different technologies and devices contribute to a successful assistive solution. The results presented in this section all bear relevance to the overarching theme of assisting movement, each one informing the design of other system elements.

The BodyRig, assessed in [1] and [13], proved to provide a precise and, in the right conditions, also accurate estimation of the user's posture and of the position of their individual body segments and joint configuration. Information about body posture also allows to infer the likely muscle geometry, thus enabling a system to predict the expected torque direction and magnitude if the tension force of the muscles are known. The MyoCeption's Nearest-Neighbor recruitment control relies on a musculoskeletal model that was qualitatively verified against a third-party model in [5].

After these results confirmed that the proposed musculoskeletal model provides an estimation of muscle geometry that is qualitatively comparable to that of other standard musculoskeletal models, the Nearest-Neighbor recruitment strategy was tested in a static force control setup in [4] and [11]. The results provided an assessment of the force control performance, and demonstrated that the proposed twitch-based calibration procedure does seems to lead to a more consistent and overall better performance of the force control. The experiment could however not determine whether the benefits were due to the geometrical adjustments of the lines of action, or rather due to the adjustments to the proportionality gains.

Concurrently, the experiments illustrated in [2] and [3] characterized a way to estimate force output using FMG and EMG, respectively, and to use them in order to provide adaptive assistance to the user. Force output estimation was also demonstrated in [12]. In both cases, the experiments successfully showed that such assistive devices lead to a significant decrease in slope in the muscular activity curve as a function of force output. This indicates that exosuits and semi-active exoskeletons could effectively be used to bridge the gap between what the user's muscles can achieve and any required force output in task space. Furthermore, direct and indirect ways to measure the force output were demonstrated in these experiments and integrated in the control loop, unlike what was done in [4], where the wrench output measurement was not used for real-time force control.

Additional analyses on the data gathered in [3] allowed to make some inferences on the adopted muscle recruitment strategies under different inertial loading and external assistance. These considerations can inform the design of FES force controls, which, based on these results, should consider net torques and joint stiffness as two independent control goals. Given sufficient redundancy in the muscle stimulation space, net torque output can be enforced by any solution vector existing on a certain manifold in the stimulation current space, and a given level of co-contraction can then be enforced through null-space projection.

Finally, a FES impedance control has been tested and characterized in [6]. The experiment also quantifies the influence of fatigue and familiarization on the Success Rate over time of a positional TAC test. The proposed calibration procedure is comparatively short, requiring calibration in only one arm position. However, most of the setup time is dedicated to finding the proper placement for the electrodes and determining the comfort threshold.

In the following chapter, future venues of research are examined. These are mainly concerned with integrating FES and wearable assistive devices, as well as using wearable sensor for force output estimation and the estimate's inclusion in the control loop.

6 Conclusions and prospects

The results presented in the previous chapter depict the current state of the MyoCeption FES assistive device and the various ways that are available to control it. These results also inform various possible future venues of research, both in terms of control design and of means to provide further assistance to movement through external devices, and to measure force via direct and indirect means. The current iteration of the MyoCeption can adapt the provided stimulation to different user postures, and allows for easy manual readjustment of the electrode positioning. Currently, the control loop for the system is only closed in body posture. Force measurements could improve the system's performance, as it would hypothetically allow to adjust the electrical stimulation to the desired force output directly. However, as previously discussed, direct measurement of the force exerted by human muscles is not trivial, especially without limiting the user's range of motion.

Pursuing this aspect further could be worth the effort. Direct force output measurements could be used to differentiate the user's volitional efforts from the force exerted as a result of stimulation, thus enabling to infer the user's motion intention and to aid it by means of fitting electrical stimulation.

The following sections describe the conclusions drawn from the results presented in this dissertation and outline prospective future research directions.

6.1 External assistance

While the core publications in this thesis focus on adaptive assistance of movement and force output through external means and FES separately, future work should focus on integrating the two. The distribution of assistance between FES and external devices, in particular, warrants various considerations [165]. On the one hand, external support should step in to bridge the gap between the required torque to achieve a given goal and the torque that can be delivered through FES alone. On the other, for the purpose of rehabilitation, FES is arguably preferable to external aids, as it uses the wearer's own musculature. For these purposes, fatigue detection in real time could play an important role [38]. A progressive tuning of the assistance provided by external aids and FES, as well as of the volitional efforts asked of the user could lay the foundation to innovative forms of rehabilitative therapies.

As a way to provide external support, exosuits present their own set of challenges, as they rely on non-rigid structures. Their role as a potential way of measuring joint torques is discussed in the next section. As far as the torque output that a tendon-driven exosuit could exert, however, the problems are in many ways similar to those that a musculoskeletal model has to solve. As suggested in [5], the MyoCeption's musculoskeletal model could be used for this purpose, with the additional possibility of including longitudinal force sensors integrated in the tendons in the control loop.

6.2 Force output monitoring

While static setups can be used to monitor force output with the user being bound to a single posture, a robotic platform could be used to infer force output without limiting movement, as was done for instance in [94]. While the robot would necessarily introduce a force disturbance, the user would be able to perform motions. Many commercially available robotic manipulators could be used for this purpose.

A wearable robotic device such as an exoskeleton could also be employed to this end. Rigid exoskeletons would present similar challenges as conventional robotic manipulators. Exosuits, on the other hand, do present various advantages in terms of comfort and safety, but also come with very different challenges from a control standpoint [23]. For the purpose of force output monitoring, in the case of tendon-driven exosuits, the force output can be measured, for example, via tension load cells mounted on the tendons themselves [58]. The orientation of the tendons could likely be inferred through body tracking in a similar fashion as the MyoCeption's musculoskeletal model used in [4].

While the experiment presented in [2] proposes a control loop where surface EMG sensors are used to infer the desired force output, the predicted intended grasp force is converted into a desired velocity for the actuators of the assistive glove through an admittance. This is possible in the described setup, as the force measuring handle is an active impedance controlled device. In principle, a similar concept could be implemented in other setups as well through the application of a mechanical element of known compliance. Working under the assumption that this element would impose a certain admittance on the whole system, the force output could be inferred by monitoring the limb's position, instead of its force output, which is in many ways more practical, and would avoid completely constraining the user. As shown in Eq. 4.31, a trade-off must be still evaluated in this sense, as imposing a higher mechanical impedance on the user's joint would warrant more precision, but again hinder movements.

The results from [3] show that force myography can be effectively used to estimate the load on the human upper limb, thus enabling an exoskeleton to provide adaptive support. FMG would then be a good option to infer the force output coming from the user's muscles as well, without limiting the user's range of motion. Muscular activity sensing is in general an attractive approach for the estimation of force output, as it generally does not hinder movement. However, as discussed in the following, integration of EMG and FES is not trivial, and FMG is prone to error if the sensors come into unplanned contact with the environment, as any unplanned collision would lead to force readings that are not directly caused by muscle bulging.

6.3 Intent detection

Intent detection for a user of FES presents several challenges. The main problem is to differentiate the user's volitional force output and the force exerted as a result of FES. Additionally, FES can interfere with some sensor modalities, such as EMG, which is why, typically, other techniques are used for the purposes of intent prediction. One of the most common techniques is Electroencephalography (EEG) [29, 166].

The results presented in [2] show an example of intent prediction through a regression algorithm used in order to drive an actuated glove. EMG is however difficult to integrate with functional electrical stimulation, as the electrical fields generated by surface stimulation electrodes are orders of magnitude higher than those generated by muscular activity. Some concepts have been proposed where the same surface electrodes are alternately connected to an EMG sensor and to a FES stimulator. For instance, in [112] sEMG is used to determine the optimal injection sites for stimulation currents to achieve a certain gesture. However, if the stimulated muscles can not be directly observed, the problem remains to estimate the volitional user intent and to differentiate it from the muscle contractions caused by electrical stimulation.

A possible way to differentiate volitional efforts and FES-caused force outputs is to implement the intention-based control in phases. In this case, the injection of stimulation currents is paused during a set time window, during which the user's intention is computed by means of various sensor modalities. The intended movement is then aided through FES during a subsequent time window. This cycle would repeat in a time-discrete fashion [166]. The width of the time windows would have a minimum bound determined by the reaction time of the muscles to the onset and interruption of stimulation currents, which is usually in the tenths of a second to a second order of magnitude. This would lead to a low overall control bandwidth, but such state-based controls have been widely used in the past. Furthermore, task-level control in humans does not operate on a high bandwidth either [159, 167], and therefore this solution could be justified. Using such an approach would also solve the problem of interference between FES and EMG. Task-level controls can be used to implement various forms of reinforcement learning, as was done for example in [168], and to monitor the onset of fatigue, as was done in [169]. Within the context of state-based controls, usage of muscle synergies has also been proposed in [170] and [171] as a possible way to implement intent prediction with FES systems for SCI patients. In these cases, the user's muscular activity is monitored by measuring the activity on muscular groups that the user is able to control through volitional efforts. The concept of muscle synergies would allow to identify correlations in the activation of the monitored muscle groups and others, at least in the case of able-bodied individuals. If the user, on the other hand, due to e.g. an SCI, is not able to voluntarily activate the muscle groups the activity of which should correlate with that of the monitored muscle groups, FES can be used to enforce contraction on the paralyzed musculature. An SCI patient would therefore reacquire the ability to control over paralyzed muscles through the synergistically coupled muscle groups that they are able to voluntarily control. This relies on the assumption that the SCI did not completely eradicate the whole of the synergy.

Time-continuous controls, on the other hand, propose to seamlessly and continuously gather the user's movement intention and thereby regulate the injection of stimulation currents. A notable example in this sense is the *Orthojacket* system [172], which makes use of a filter proposed originally in [173]. This filter is able to differentiate EMG signal frequency components deriving from volitional efforts by the user and those deriving from FES, also by applying an automatic trigger signal which pauses measurement during the application of single FES pulses [174, 173, 172].

The experiment presented in [3] arguably does not count as intent prediction *per se*, as the FMG sensors were used to estimate the lifted mass through measured muscular bulging. While FMG has a few limitations compared to FMG, it seems like a good candidate to directly monitor stimulated muscles, even as the stimulation is occurring. Furthermore, let us suppose that a model can be trained to predict the muscle bulging from a given stimulation current vector, and let us assume that muscle bulging can be practically measured during normal operation. Then, under the assumption of linearity, one could subtract the expected muscle bulging, given the current stimulation, from the measured muscle bulging, and attribute to the result of this subtraction a volitional effort from the user, or alternatively muscular fatigue. This could then be used as intent prediction in the control loop. The same could be done with force output measurements in task space, if these can be obtained without limiting the user's range of motion. A possible control loop where such models are used is depicted in Fig. 6.1.

In the control loops depicted in Fig. 6.1, there is an underlying assumption of linearity in the FMG or joint torque sensor measurements. This is to say, that the FMG or joint torque measurements as the function of two given inputs $\boldsymbol{x}_1$ and $\boldsymbol{x}_2$, which we denote as $S(\boldsymbol{x}_1 + \boldsymbol{x}_2)$ should have the following property

$$S(\boldsymbol{x}_1 + \boldsymbol{x}_2) = S(\boldsymbol{x}_1) + S(\boldsymbol{x}_2) \tag{6.1}$$

which is necessary in order to differentiate between volitional and stimulation-induced muscular activity or force output. The models predicting the muscular activity or the torque output should also generalize over different body postures. This could be achieved by performing the training step in different postures, and possibly by including posture data in the model input beside the stimulation.

Looking at the block diagram, one can see that the estimation of the volitional joint torque output only needs to be multiplied by the inverted transposed Jacobian of the arm, which can be more directly observed through posture tracking. The estimation of volitional force output starting from muscular activity, on the other hand, requires also an estimation of the muscular Jacobian, which is not easily observable, even though it can be inferred, as demonstrated for example in [4] and [5].

6.4 High density FES

While the jacket used in the MyoCeption's current iteration is designed to allow easy adjustment of the electrode positioning, it would be desirable for the system to be able to adjust the spacial distribution of the stimulation without the need for manual interventions. While some

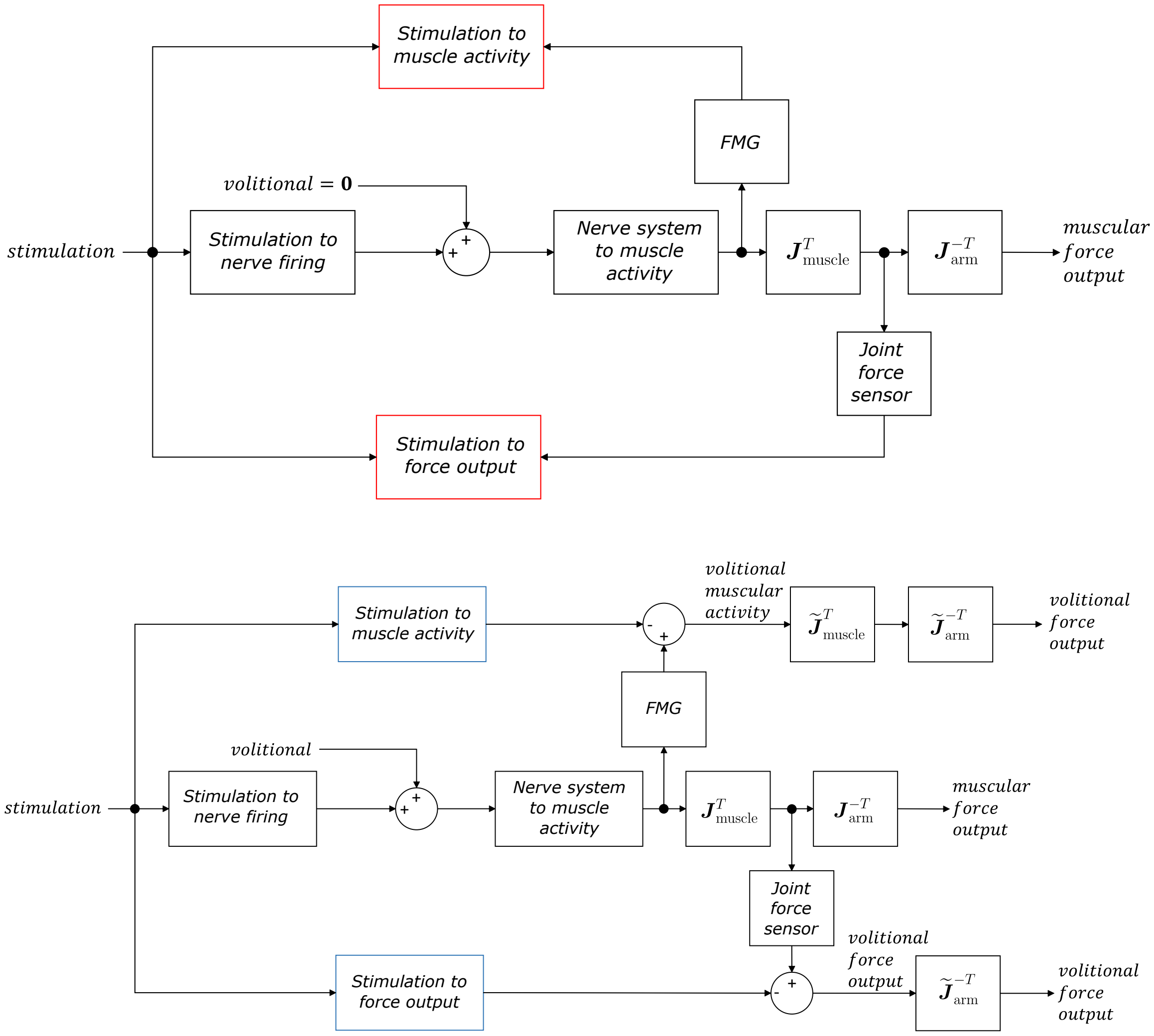

Figure 6.1: Block diagram of a possible control scheme involving muscular activity sensors and/or force output monitoring to infer the intended force output. **Top**: Supervised training of the models with stimulation as input and force output or muscular activity as target. **Bottom**: Online use of the calibrated control loop.

calibration techniques which are able to pinpoint the muscle groups responsible for exerting torques in a given direction are described in [4, 5, 6], the selection of optimal electrode pairing is not contemplated in these works. An example of a twitch-based calibration technique which does pair up electrodes is present, e.g., in [175]. A suitable way to do this would be through high-density FES, whereby some large-patch surface electrodes would be substituted with an electrode matrix, such as the one shown in Fig. 4.10. Each electrode on such a matrix would have a reduced surface, and would be connected to the main stimulation source through a suitable switch system, which would then make it possible to create a virtual electrode of the desired shape and position simply by connecting the desired electrodes on that matrix to the main stimulation source. Figures 4.7 and 4.8 show such possible arrangements.

Ideally, the wearable stimulation setup would feature dozens of stimulation electrode elements, which could then be combined to form virtual anodes and cathodes to fit individual users, postures, and force output requirements. Furthermore, this would likely make it possible to more precisely stimulate specific muscle groups, which is inherently difficult when using transcutaneous electrodes.

A few early results are reported in this dissertation. Fig. 5.9 shows the measurements of muscular activity and fingertip force output reduced in dimensionality by means of PCA labeled by stimulation pattern. The stimulation patterns refer to different stimulation currents injection sites regulated by a high density FES setup. The muscular activity measurements form clearly separate clusters. The fingertip force output measurements, on the other hand, show less differentiable clusters, although at least two pattern subsets are clearly distinguishable based on the first component of the PCA-reduced measurements.

A prototype featuring electrode matrices, as opposed to individual larger electrodes, is in development at the AIROB lab. Currently, the circuit design is similar to that shown in Fig. 4.7, but the prototype combines both high density anodes and cathodes. This makes it possible to combine any two matrix elements from the anode and the cathode, greatly increasing the number of possible combinations. Notice that the general electronic circuit is very similar to that currently used in the MyoCeption and shown in Fig. 4.6, with the noticeable difference of the demultiplexer and of a different type of current driver, which in this case is simplified to a Bipolar Junction Transistor (BJT) collector driver. The demultiplexer allows to drive potentially many electrode elements with only a few select pins from the central micro-controller. Generally speaking, multiple such demultiplexed electrodes could be controlled by a single micro-controller, and a cascaded design could also be envisioned where decentralized micro-controllers drive matrices receiving orders from centralized units running higher controls in a nested loop design.

The previously mentioned architecture still entails a distinction of every surface electrode element as belonging to either an anode or a cathode. A more versatile option is shown in Fig. 4.8, where each electrode element can be connected to both an anode and a cathode. Of course, no one element should be connected to the stimulation source anode and cathode at the same time, as this would short the stimulation source's terminals. Such a circuit, however, could be driven with anodes and cathodes as close as needed, which is not possible with the circuit shown in Fig. 4.7.

The reported preliminary results show that it is in fact possible to induce clearly distinct muscle activity patterns by stimulating different electrodes. In the future, such a setup could be used to induce finer hand gestures in individuals affected by hand paralysis [176], and adaptively adjust the current injection sites based on user posture. Preliminary experiments have already taken place and demonstrated some success, in certain subjects, in eliciting single-finger movement. The adopted control architecture is similar to the one presented in [6], with the main difference that instead of a 6-DoF force torque sensor, the Finger-Force Linear Sensor (FFLS) from [164] is used to measure the force output of individual fingers.

6.5 Further applications

The aforementioned models could also be used for other applications, such as teleimpedance. As shown in [10], muscular activity can be used to estimate joint stiffness in teleimpedance applications. The MyoCeption model can be used to project this single joint prediction onto a more complex musculoskeletal model.

Furthermore, analysis of delay occurring between muscle contraction and force output could be used to calibrate the stiffness prediction, as this delay should decrease with increasing joint stiffness. As reported in [71], most observations show that muscle stiffness tends to increase under contraction. A FES system could be used, for example, to stimulate the musculature with pulses, and the time between stimulation and force output peaks could serve as proxies to infer muscle stiffness. Inferences could even be made by analyzing the delay between muscle activity measurements taken in proximity of the stimulation electrodes and the force output. User studies could be designed to verify whether such features do correlate with physical joint or task space stiffness of the human limb. The monitoring of the peak-to-peak propagation delay can be seen as a single measurement point version of muscle elastography, which has been demonstrated to be a viable technique for the purpose of real-time sensing of muscular tissue mechanical properties [63, 72, 73, 177]. The evaluation of peak-to-peak propagation delay would employ some form of cross-correlation, which should be easy to implement and require readily available hardware.

While the publications presented in this dissertation mainly deal with the control theory aspects of FES, a comprehensive human factors analysis of force feedback through FES could reveal possible applications of this technique in haptics. Examples of such analyses can be found in [92] and [178], with a particular emphasis on VR applications.

The fact that FES can add machine-mandated impulses to the ones sent by the user's nervous system would no doubt have interesting implications on the user's own sense of agency. In [93], a Neuro-Muscular Electrical Stimulation (NMES) setup is used to communicate to the user the affordances of objects present in a scene. Potential applications of FES in neurological disorders involving the perception of one's movements could be discovered. Furthermore, FES-based force feedback systems could have interesting implications in shared autonomy teleoperation control schemes [179, 180].

Furthermore, it would be interesting to evaluate whether and how FES could be used in training specific complex movements in paralyzed patients and able-bodied individuals alike by correcting muscular activation at specific times to correct potential errors. These problems have partially been investigated in the context of rehabilitation [36, 181]. In a more general sense, it would be worth investigating how FES interacts with natural movement controls, both voluntary and involuntary. As a more concrete example, it would be interesting to evaluate whether a repeated FES-induced movement can build a central pattern generator in the peripheral nervous system, and whether this could lead to appreciable differences in the same movement performed voluntarily by the user.

As FES can use the user's own motor neurons to facilitate movements, and serve as a neuroprosthesis by potentially bridging a gap between the central nervous system and the musculoskeletal system, it could also be adopted in neurorobotics to provide an artificial model of motion control in humans or other organisms. Similarity of the measurable properties of FES-mediated movements and motions initiated by the user could be an invaluable metric to assess how voluntary movement is regulated in practice. It could be possible to investigate the role of voluntary movement initiation in proprioception, as well as the role played by the internalized model of the body's dynamics in controlling movements.

6.6 Final words

It is increasingly clear that robotic appliances can be developed that are able to surpass human performance by a large margin, and that the most challenging aspect of systems which hybridize human users and robotics is rather to facilitate optimal communication between actuating and sensing modalities on both ends. Commercial prosthetic hands with a larger number of degrees of freedom and internal sensors are often in practice barely more versatile than their body powered counterparts [182, 183]. This can be at least in part attributed to the reduced diffusion of somatosensory feedback modalities, at least in commercially available prosthetic solutions. Without a proper way to provide feedback and close the loop, the user-prosthesis system cannot improve by much, even if the user is better trained or if the prosthesis is more performing.

Exoskeletons, wearable robotics and electrical stimulation all fit in a paradigm which presents significant differences with respect to that of prostheses. If the latter can be considered as acting *in series* to the human body, the former can be considered as acting *in parallel* to it. In the case of prostheses, environmental interaction can only occur through the robotic device, while in the case of exoskeletons that is not necessarily the case. In parallel arrangements, user intention can be inferred by direct measurement of the force output, and force can be exerted on the user in order to both provide feedback and to assist in movements requiring more force than the user can provide. However, in the case of individuals where the connection between their distal body segments and the central nervous system has been compromised, such devices effectively should act as a bypass, which returning to the analogy above has more in common with the case where the machine acts *in series* to the human body.

FES, together with wearable robotics, could act in parallel to the neuromuscular loop, and could restore the capacity for movement in paralyzed individuals by bridging the points where this loop has been partially or completely severed. In order for this technique to be useful, however, the machine should be able to have access to real-time postural and force output data. This could be done by including more sensing modalities in the FES systems, such as force and torque sensing, or by monitoring the activity of afferent nerves. The inclusion of further actuators able to exert forces onto the user would further facilitate the user-machine integration, with the ideal result of the machine stepping in whenever the user is unable to perform an action on their own.

The transition from external feedback and control modalities towards direct interfacing with the nerve system could lead to HMIs with an improved space and time resolutions, whereby the connection between man and machine will increase in bandwidth and become more intimate and profound. The interfaces of the future could enable us to drive any sort of machinery as if it were a direct extension of our bodies, and they will make us able to perceive all kinds of sensation through remote sensing organs as if they were our own.

Bibliography

[1] M. Sierotowicz, M. Connan, and C. Castellini. “Human-in-the-loop assessment of an ultralight, low-cost body posture tracking device.” In: *Sensors* 20.3 (2020), p. 890. ISSN: 1424-8220. DOI: `10.3390/s20030890`.

[2] M. Sierotowicz, N. Lotti, L. Nell, F. Missiroli, R. Alicea, X. Zhang, M. Xiloyannis, R. Rupp, E. Papp, J. Krzywinski, C. Castellini, and L. Masia. “EMG-driven machine learning control of a soft glove for grasping assistance and rehabilitation.” In: *IEEE Robotics and Automation Letters* 7.2 (2022), pp. 1566–1573. ISSN: 2377-3766. DOI: `10.1109/LRA.2021.3140055`.

[3] M. Sierotowicz, D. Brusamento, B. Schirrmeister, M. Connan, J. Bornmann, J. Gonzalez-Vargas, and C. Castellini. “Unobtrusive, natural support control of an adaptive industrial exoskeleton using force myography.” In: *Frontiers in Robotics and AI* 9 (2022). Publisher: Frontiers, p. 919370. ISSN: 2296-9144. DOI: `10.3389/frobt.2022.919370`.

[4] M. Sierotowicz and C. Castellini. “Omnidirectional endpoint force control through functional electrical stimulation.” In: *Biomedical Physics & Engineering Express* 9.6 (2023), p. 065008. DOI: `10.1088/2057-1976/acf04b`.

[5] M. Sierotowicz, N. Lotti, R. Rupp, L. Masia, and C. Castellini. “A Comprehensive Framework for the Modelling of Cartesian Force Output in Human Limbs.” In: *2022 International Conference on Rehabilitation Robotics (ICORR)*. 2022, pp. 1–6. ISBN: 1-66548-829-8. DOI: `10.1109/ICORR55369.2022.9896547`.

[6] M. Sierotowicz and C. Castellini. “Robot-Inspired Human Impedance Control Through Functional Electrical Stimulation.” In: *2023 International Conference on Rehabilitation Robotics (ICORR)*. 2023, pp. 1–6. DOI: `10.1109/ICORR58425.2023.10304750`.

[7] M. Sierotowicz, B. Weber, R. Belder, K. Bussmann, H. Singh, and M. Panzirsch. “Investigating the influence of haptic feedback in rover navigation with communication delay.” In: *International Conference on Human Haptic Sensing and Touch Enabled Computer Applications*. Springer. 2020, pp. 527–535. ISBN: 3-030-58146-2. DOI: `10.1007/978-3-030-58147-3_58`.

[8] M. Connan, M. Sierotowicz, B. Henze, O. Porges, A. Albu-Schäffer, M. A. Roa, and C. Castellini. “Learning teleoperation of an assistive humanoid platform by intact and upper-limb disabled users.” In: *International Conference on NeuroRehabilitation*. Springer. 2020, pp. 165–169. DOI: `10.1007/978-3-030-70316-5_27`.

[9] M. Connan, M. Sierotowicz, B. Henze, O. Porges, A. Albu-Schäffer, M. A. Roa, and C. Castellini. “Learning to teleoperate an upper-limb assistive humanoid robot for bimanual daily-living tasks.” In: *Biomedical Physics & Engineering Express* 8.1 (2021), p. 015022. DOI: `10.1088/2057-1976/ac3881`.

[10] M. Panzirsch, M. Sierotowicz, R. Prakash, H. Singh, and C. Ott. “Deflection-Domain Passivity Control of Variable Stiffnesses Based on Potential Energy Reference.” In: *IEEE Robotics and Automation Letters* 7.2 (2022), pp. 4440–4447. ISSN: 2377-3766. DOI: `10.1109/LRA.2022.3147566`.

[11] M. Sierotowicz and C. Castellini. “A surface neuromuscular electrical stimulation device for universal cartesian force control in humans.” In: *JOURNAL OF ARTIFICIAL ORGANS* 46.11 (2022), e323–e327. ISSN: 1525-1594.

[12] M. Sierotowicz, M.-A. Scheidl, and C. Castellini. “Adaptive Filter for Biosignal-Driven Force Controls Preserves Predictive Powers of sEMG.” In: *2023 International Conference on Rehabilitation Robotics (ICORR)*. 2023, pp. 1–6. DOI: `10.1109/ICORR58425.2023.10304772`.

[13] M. Sierotowicz. “Fusion of IMU and Muscular Information in Order to Solve the Limb Position Effect.” Technical University of Munich, 2019.

[14] M. Sierotowicz and J.-P. Lutze. *Verfahren zur Rückkopplung von exogenen Kräften an einen Nutzer mittels elektrischer Muskelstimulation, Steuereinheit zur Steuerung einer Kraftrückkopplungsvorrichtung, Kraftrückkopplungsvorrichtung und Verwendung einer Steuereinheit oder einer Kraftrückkopplungsvorrichtung*. DE Patent No 10 2020 122 551 A1 2022.03.03, Pending.

[15] D. P. Miller. “Assistive robotics: an overview.” In: *Assistive Technology and Artificial Intelligence: Applications in Robotics, User Interfaces and Natural Language Processing* (2006), pp. 126–136.

[16] T. L. Chen, M. Ciocarlie, S. Cousins, P. M. Grice, K. Hawkins, K. Hsiao, C. C. Kemp, C.-H. King, D. A. Lazewatsky, A. E. Leeper, H. Nguyen, A. Paepcke, C. Pantofaru, W. D. Smart, and L. Takayama. “Robots for humanity: using assistive robotics to empower people with disabilities.” In: *IEEE Robotics & Automation Magazine* 20.1 (2013), pp. 30–39. DOI: `10.1109/MRA.2012.2229950`.

[17] Y. Zimmermann, A. Forino, R. Riener, and M. Hutter. “ANYexo: A versatile and dynamic upper-limb rehabilitation robot.” In: *IEEE Robotics and Automation Letters* 4.4 (2019), pp. 3649–3656.

[18] S. Massardi, D. Rodriguez-Cianca, D. Pinto-Fernandez, J. C. Moreno, M. Lancini, and D. Torricelli. “Characterization and evaluation of human–exoskeleton interaction dynamics: a review.” In: *Sensors* 22.11 (2022), p. 3993.

[19] P. Maurice, J. Čamernik, D. Gorjan, B. Schirrmeister, J. Bornmann, L. Tagliapietra, C. Latella, D. Pucci, L. Fritzsche, S. Ivaldi, and J. Babic. “Objective and subjective effects of a passive exoskeleton on overhead work.” In: *IEEE Transactions on Neural Systems and Rehabilitation Engineering* 28.1 (2019), pp. 152–164.

[20] A. Baldassarre, L. G. Lulli, F. Cavallo, L. Fiorini, A. Mariniello, N. Mucci, and G. Arcangeli. “Industrial exoskeletons from bench to field: Human-machine interface and user experience in occupational settings and tasks.” In: *Frontiers in Public Health* 10 (2022), p. 1039680.

[21] A. Voilqué, J. Masood, J. Fauroux, L. Sabourin, and O. Guezet. “Industrial exoskeleton technology: Classification, structural analysis, and structural complexity indicator.” In: *2019 wearable robotics association conference (wearracon)*. IEEE. 2019, pp. 13–20.

[22] T. Rahman, W. Sample, S. Jayakumar, M. M. King, J. Y. Wee, R. Seliktar, M. Alexander, M. Scavina, and A. Clark. “Passive exoskeletons for assisting limb movement.” In: *Journal of rehabilitation research and development* 43.5 (2006), p. 583.

[23] A. T. Asbeck, R. J. Dyer, A. F. Larusson, and C. J. Walsh. “Biologically-inspired soft exosuit.” In: *2013 IEEE 13th International Conference on Rehabilitation Robotics (ICORR)*. IEEE. 2013, pp. 1–8.

[24] S. Sridar, S. Poddar, Y. Tong, P. Polygerinos, and W. Zhang. “Towards untethered soft pneumatic exosuits using low-volume inflatable actuator composites and a portable pneumatic source.” In: *IEEE Robotics and Automation Letters* 5.3 (2020), pp. 4062–4069.

[25] C. Di Natali, A. Sadeghi, A. Mondini, E. Bottenberg, B. Hartigan, A. De Eyto, L. O’Sullivan, E. Rocon, K. Stadler, B. Mazzolai, D. G. Caldwell, and O. Jesús. “Pneumatic quasi-passive actuation for soft assistive lower limbs exoskeleton.” In: *Frontiers in neurorobotics* 14 (2020), p. 31.

[26] P. Polygerinos, K. C. Galloway, S. Sanan, M. Herman, and C. J. Walsh. “EMG controlled soft robotic glove for assistance during activities of daily living.” In: *2015 IEEE international conference on rehabilitation robotics (ICORR)*. IEEE. 2015, pp. 55–60.

[27] A.-M. Georgarakis, M. Xiloyannis, P. Wolf, and R. Riener. “A textile exomuscle that assists the shoulder during functional movements for everyday life.” In: *Nature Machine Intelligence* 4.6 (2022), pp. 574–582.

[28] P. H. Peckham and J. S. Knutson. “Functional electrical stimulation for neuromuscular applications.” In: *Annu. Rev. Biomed. Eng.* 7 (2005), pp. 327–360.

[29] A. B. Ajiboye, F. R. Willett, D. R. Young, W. D. Memberg, B. A. Murphy, J. P. Miller, B. L. Walter, J. A. Sweet, H. A. Hoyen, M. W. Keith, P. H. Peckham, J. D. Simeran, J. P. Donoghue, L. R. Hochberg, and R. F. Kirsch. “Restoration of reaching and grasping in a person with tetraplegia through brain-controlled muscle stimulation: a proof-of-concept demonstration.” In: *Lancet (London, England)* 389.10081 (2017), p. 1821.

[30] R. Rupp, M. Rohm, M. Schneiders, A. Kreilinger, and G. R. Müller-Putz. “Functional rehabilitation of the paralyzed upper extremity after spinal cord injury by noninvasive hybrid neuroprostheses.” In: *Proceedings of the IEEE* 103.6 (2015), pp. 954–968.

[31] O. A. Howlett, N. A. Lannin, L. Ada, and C. McKinstry. “Functional electrical stimulation improves activity after stroke: a systematic review with meta-analysis.” In: *Archives of physical medicine and rehabilitation* 96.5 (2015), pp. 934–943.

[32] C. T. Freeman, A.-M. Hughes, J. H. Burridge, P. H. Chappell, P. L. Lewin, and E. Rogers. “A model of the upper extremity using FES for stroke rehabilitation.” In: (2009).

[33] N. S. Makowski, J. S. Knutson, J. Chae, and P. Crago. “Neuromuscular electrical stimulation to augment reach and hand opening after stroke.” In: *2011 Annual International Conference of the IEEE Engineering in Medicine and Biology Society*. IEEE. 2011, pp. 3055–3058.

[34] M. Milosevic, T. Nakanishi, A. Sasaki, A. Yamaguchi, T. Nomura, M. R. Popovic, and K. Nakazawa. “Cortical re-organization after traumatic brain injury elicited using functional electrical stimulation therapy: A case report.” In: *Frontiers in Neuroscience* 15 (2021), p. 693861.

[35] B. Dang, W. Chen, W. He, and G. Chen. "Rehabilitation treatment and progress of traumatic brain injury dysfunction." In: *Neural plasticity* 2017 (2017).

[36] N. Kapadia, B. Moineau, and M. R. Popovic. "Functional electrical stimulation therapy for retraining reaching and grasping after spinal cord injury and stroke." In: *Frontiers in Neuroscience* (2020), p. 718.

[37] A. J. Del-Ama, Á. Gil-Agudo, J. L. Pons, and J. C. Moreno. "Hybrid FES-robot cooperative control of ambulatory gait rehabilitation exoskeleton." In: *Journal of neuroengineering and rehabilitation* 11.1 (2014), pp. 1–15.

[38] D. Burchielli, N. Lotti, F. Missiroli, C. Bokranz, A. Pedrocchi, E. Ambrosini, and L. Masia. "Adaptive hybrid fes-force controller for arm exosuit." In: *2022 International Conference on Rehabilitation Robotics (ICORR)*. IEEE. 2022, pp. 1–6.

[39] M. Begon, M. S. Andersen, and R. Dumas. "Multibody kinematics optimization for the estimation of upper and lower limb human joint kinematics: a systematized methodological review." In: *Journal of biomechanical engineering* 140.3 (2018), p. 030801.

[40] S. S. Blemker and S. L. Delp. "Three-dimensional representation of complex muscle architectures and geometries." In: *Annals of biomedical engineering* 33 (2005), pp. 661–673.

[41] R. Hainisch, M. Gfoehler, M. Zubayer-Ul-Karim, and M. G. Pandy. "Method for determining musculotendon parameters in subject-specific musculoskeletal models of children developed from MRI data." In: *Multibody System Dynamics* 28.1 (2012), pp. 143–156.

[42] W. Rohmert. "Determination of the recovery pause for static work of man." In: *Internationale Zeitschrift Fur Angewandte Physiologie, Einschliesslich Arbeitsphysiologie* 18 (1960), pp. 123–164.

[43] T. Xia and L. A. F. Law. "A theoretical approach for modeling peripheral muscle fatigue and recovery." In: *Journal of biomechanics* 41.14 (2008), pp. 3046–3052.

[44] E. M. Schearer, Y.-W. Liao, E. J. Perreault, M. C. Tresch, W. D. Memberg, R. F. Kirsch, and K. M. Lynch. "Multi-Muscle FES Force Control of the Human Arm for Arbitrary Goals." In: *IEEE Transactions on Neural Systems and Rehabilitation Engineering* 22.3 (2014), pp. 654–663. DOI: `10.1109/TNSRE.2013.2282903`.

[45] S. L. Delp, F. C. Anderson, A. S. Arnold, P. Loan, A. Habib, C. T. John, E. Guendelman, and D. G. Thelen. "OpenSim: open-source software to create and analyze dynamic simulations of movement." In: *IEEE transactions on biomedical engineering* 54.11 (2007), pp. 1940–1950.

[46] D. Chiaradia, M. Xiloyannis, C. W. Antuvan, A. Frisoli, and L. Masia. "Design and embedded control of a soft elbow exosuit." In: *2018 IEEE international conference on soft robotics (RoboSoft)*. IEEE. 2018, pp. 565–571.

[47] D. Staudenmann, K. Roeleveld, D. F. Stegeman, and J. H. Van Dieën. "Methodological aspects of SEMG recordings for force estimation–a tutorial and review." In: *Journal of electromyography and kinesiology* 20.3 (2010), pp. 375–387.

[48] M. Sakr and C. Menon. "On the estimation of isometric wrist/forearm torque about three axes using Force Myography." In: *2016 6th IEEE International Conference on Biomedical Robotics and Biomechatronics (BioRob)*. IEEE. 2016, pp. 827–832.

[49] P. Merriaux, Y. Dupuis, R. Boutteau, P. Vasseur, and X. Savatier. "A study of vicon system positioning performance." In: *Sensors* 17.7 (2017), p. 1591.

[50] M. Windolf, N. Götzen, and M. Morlock. "Systematic accuracy and precision analysis of video motion capturing systems—exemplified on the Vicon-460 system." In: *Journal of biomechanics* 41.12 (2008), pp. 2776–2780.

[51] V. Angelov, E. Petkov, G. Shipkovenski, and T. Kalushkov. "Modern virtual reality headsets." In: *2020 International congress on human-computer interaction, optimization and robotic applications (HORA)*. IEEE. 2020, pp. 1–5.

[52] G. Bleser, G. Hendeby, and M. Miezal. "Using egocentric vision to achieve robust inertial body tracking under magnetic disturbances." In: *2011 10th IEEE International Symposium on Mixed and Augmented Reality*. IEEE. 2011, pp. 103–109.

[53] A. Filippeschi, N. Schmitz, M. Miezal, G. Bleser, E. Ruffaldi, and D. Stricker. "Survey of motion tracking methods based on inertial sensors: A focus on upper limb human motion." In: *Sensors* 17.6 (2017), p. 1257.

[54] A. Palumbo. "Microsoft HoloLens 2 in medical and healthcare context: State of the art and future prospects." In: *Sensors* 22.20 (2022), p. 7709.

[55] D. Roetenberg, H. Luinge, and P. Slycke. "Xsens MVN: Full 6DOF human motion tracking using miniature inertial sensors." In: *Xsens Motion Technologies BV, Tech. Rep* 1 (2009), pp. 1–7.

[56] J. R. Cook, N. A. Baker, R. Cham, E. Hale, and M. S. Redfern. "Measurements of wrist and finger postures: a comparison of goniometric and motion capture techniques." In: *Journal of applied biomechanics* 23.1 (2007), pp. 70–78.

[57] *Depiction of Microsoft's HoloLens 2*. `https://www.fireware.nl/de/product/microsoft-hololens-2/`. Accessed: 12.12.2023.

[58] N. Lotti, M. Xiloyannis, F. Missiroli, C. Bokranz, D. Chiaradia, A. Frisoli, R. Riener, and L. Masia. "Myoelectric or force control? A comparative study on a soft arm exosuit." In: *IEEE Transactions on Robotics* 38.3 (2022), pp. 1363–1379.

[59] F. Scheepers, R. E. Parent, W. E. Carlson, and S. F. May. "Anatomy-based modeling of the human musculature." In: *Proceedings of the 24th annual conference on Computer graphics and interactive techniques*. 1997, pp. 163–172.

[60] W. Maurel. *3D modeling of the human upper limb including the biomechanics of joints, muscles and soft tissues*. Tech. rep. EPFL, 1999.

[61] R. H. Jensen and D. T. Davy. "An investigation of muscle lines of action about the hip: a centroid line approach vs the straight line approach." In: *Journal of biomechanics* 8.2 (1975), pp. 103–110.

[62] F. C. Van der Helm and R. Veenbaas. "Modelling the mechanical effect of muscles with large attachment sites: application to the shoulder mechanism." In: *Journal of biomechanics* 24.12 (1991), pp. 1151–1163.

[63] S. F. Eby, P. Song, S. Chen, Q. Chen, J. F. Greenleaf, and K.-N. An. "Validation of shear wave elastography in skeletal muscle." In: *Journal of biomechanics* 46.14 (2013), pp. 2381–2387.

[64] J. E. Brandenburg, S. F. Eby, P. Song, H. Zhao, J. S. Brault, S. Chen, and K.-N. An. "Ultrasound elastography: the new frontier in direct measurement of muscle stiffness." In: *Archives of physical medicine and rehabilitation* 95.11 (2014), pp. 2207–2219.

[65] F. Hug, K. Tucker, J.-L. Gennisson, M. Tanter, and A. Nordez. "Elastography for muscle biomechanics: toward the estimation of individual muscle force." In: *Exercise and sport sciences reviews* 43.3 (2015), pp. 125–133.

[66] H.-K. Kim and Y. Zhang. "Estimation of lumbar spinal loading and trunk muscle forces during asymmetric lifting tasks: application of whole-body musculoskeletal modelling in OpenSim." In: *Ergonomics* 60.4 (2017), pp. 563–576.

[67] C. R. Dickerson, D. B. Chaffin, and R. E. Hughes. "A mathematical musculoskeletal shoulder model for proactive ergonomic analysis." In: *Computer methods in biomechanics and biomedical engineering* 10.6 (2007), pp. 389–400.

[68] A. V. Hill. "The heat of shortening and the dynamic constants of muscle." In: *Proceedings of the Royal Society of London. Series B-Biological Sciences* 126.843 (1938), pp. 136–195.

[69] R. Osu and H. Gomi. "Multijoint muscle regulation mechanisms examined by measured human arm stiffness and EMG signals." In: *Journal of neurophysiology* 81.4 (1999), pp. 1458–1468.

[70] S. Pedi Artati. "Calculation of Human Arm Stiffness using a Biomechanical Model." PhD thesis. Technische Universität München, 2008.

[71] J. M. Winters and P. E. Crago. *Biomechanics and neural control of posture and movement*. Springer Science & Business Media, 2012.

[72] R. M. Sigrist, J. Liau, A. El Kaffas, M. C. Chammas, and J. K. Willmann. "Ultrasound elastography: review of techniques and clinical applications." In: *Theranostics* 7.5 (2017), p. 1303.

[73] Y. Yoshitake, Y. Takai, H. Kanehisa, and M. Shinohara. "Muscle shear modulus measured with ultrasound shear-wave elastography across a wide range of contraction intensity." In: *Muscle & nerve* 50.1 (2014), pp. 103–113.

[74] J. L. Pons, R. Ceres, and L. Calderon. "Introduction to wearable robotics." In: *Wearable Robots: Biomechatronic Exoskeletons* (2008), pp. 1–16.

[75] M. Zhu, S. Biswas, S. I. Dinulescu, N. Kastor, E. W. Hawkes, and Y. Visell. "Soft, wearable robotics and haptics: Technologies, trends, and emerging applications." In: *Proceedings of the IEEE* 110.2 (2022), pp. 246–272.

[76] A. T. Asbeck, S. M. De Rossi, I. Galiana, Y. Ding, and C. J. Walsh. "Stronger, smarter, softer: next-generation wearable robots." In: *IEEE Robotics & Automation Magazine* 21.4 (2014), pp. 22–33.

[77] R. S. Mosher. "Handyman to hardiman." In: *Sae Transactions* (1968), pp. 588–597.

[78] H. Kazerooni. "Human-robot interaction via the transfer of power and information signals." In: *IEEE Transactions on systems, Man, and Cybernetics* 20.2 (1990), pp. 450–463.

[79] P. Maurice, J. Čamernik, D. Gorjan, B. Schirrmeister, J. Bornmann, L. Tagliapietra, C. Latella, D. Pucci, L. Fritzsche, S. Ivaldi, and J. BabiČ. "Evaluation of PAEXO, a novel passive exoskeleton for overhead work." In: *Computer Methods in Biomechanics and Biomedical Engineering* 22.sup1 (2019), S448–S450.

[80] J. P. Pinho, C. Taira, P. Parik-Americano, L. O. Suplino, V. P. Bartholomeu, V. N. Hartmann, G. S. Umemura, and A. Forner-Cordero. "A comparison between three commercially available exoskeletons in the automotive industry: An electromyographic pilot study." In: *2020 8th IEEE RAS/EMBS International Conference for Biomedical Robotics and Biomechatronics (BioRob)*. IEEE. 2020, pp. 246–251.

[81] A. Esquenazi, M. Talaty, A. Packel, and M. Saulino. "The ReWalk powered exoskeleton to restore ambulatory function to individuals with thoracic-level motor-complete spinal cord injury." In: *American journal of physical medicine & rehabilitation* 91.11 (2012), pp. 911–921.

[82] D. Chiaradia, M. Xiloyannis, M. Solazzi, L. Masia, and A. Frisoli. "Rigid versus soft exoskeletons: interaction strategies for upper limb assistive technology." In: *Wearable Robotics*. Elsevier, 2020, pp. 67–90.

[83] FDA and HHS. "Medical devices; physical medicine devices; classification of the powered lower extremity exoskeleton; republication. Final order; republication." In: *Federal register* 80.85 (2015), pp. 25226–25230.

[84] G. A. Van Norman. "Drugs, devices, and the FDA: part 2: an overview of approval processes: FDA approval of medical devices." In: *JACC: Basic to Translational Science* 1.4 (2016), pp. 277–287.

[85] M. Peters and S. Wischniewski. "The impact of using exoskeletons on occupational safety and health." In: *European Agency for Safety and Health at Work* (2019), pp. 1–10.

[86] T. A. Thrasher, V. Zivanovic, W. McIlroy, and M. R. Popovic. "Rehabilitation of reaching and grasping function in severe hemiplegic patients using functional electrical stimulation therapy." In: *Neurorehabilitation and neural repair* 22.6 (2008), pp. 706–714.

[87] I. Bersch, S. Koch-Borner, and J. Fridén. "Electrical stimulation—a mapping system for hand dysfunction in tetraplegia." In: *Spinal Cord* 56.5 (2018), pp. 516–522.

[88] I. Bersch, S. Koch-Borner, and J. Fridén. "Motor point topography of fundamental grip actuators in tetraplegia: implications in nerve transfer surgery." In: *Journal of neurotrauma* 37.3 (2020), pp. 441–447.

[89] A. Fougner, E. Scheme, A. D. C. Chan, K. Englehart, and Ø. Stavdahl. "Resolving the Limb Position Effect in Myoelectric Pattern Recognition." In: *IEEE Transactions on Neural Systems and Rehabilitation Engineering* 19.6 (2011), pp. 644–651. DOI: `10.1109/TNSRE.2011.2163529`.

[90] A. J. Westerveld, A. C. Schouten, P. H. Veltink, and H. van der Kooij. "Control of thumb force using surface functional electrical stimulation and muscle load sharing." In: *Journal of neuroengineering and rehabilitation* 10 (2013), pp. 1–12.

[91] E. Galofaro, E. D'Antonio, N. Lotti, and L. Masia. "Rendering Immersive Haptic Force Feedback via Neuromuscular Electrical Stimulation." In: *Sensors* 22.14 (2022). ISSN: 1424-8220. DOI: `10.3390/s22145069`.

[92] P. Lopes, S. You, A. Ion, and P. Baudisch. "Adding force feedback to mixed reality experiences and games using electrical muscle stimulation." In: *Proceedings of the 2018 chi conference on human factors in computing systems*. 2018, pp. 1–13.

[93] P. Lopes, P. Jonell, and P. Baudisch. “Affordance++ allowing objects to communicate dynamic use.” In: *Proceedings of the 33rd annual acm conference on human factors in computing systems*. 2015, pp. 2515–2524.

[94] E. M. Schearer, Y.-W. Liao, E. J. Perreault, M. C. Tresch, W. D. Memberg, R. F. Kirsch, and K. M. Lynch. “Evaluation of a semi-parametric model for high-dimensional FES control.” In: *2015 7th International IEEE/EMBS Conference on Neural Engineering (NER)*. IEEE. 2015, pp. 304–307.

[95] A. R. Friederich, M. L. Audu, and R. J. Triolo. “Characterization of the force production capabilities of paralyzed trunk muscles activated with functional neuromuscular stimulation in individuals with spinal cord injury.” In: *IEEE Transactions on Biomedical Engineering* 68.8 (2020), pp. 2389–2399.

[96] K. L. Meadmore, A.-M. Hughes, C. T. Freeman, Z. Cai, D. Tong, J. H. Burridge, and E. Rogers. “Functional electrical stimulation mediated by iterative learning control and 3D robotics reduces motor impairment in chronic stroke.” In: *Journal of neuroengineering and rehabilitation* 9.1 (2012), pp. 1–11.

[97] C. Freeman, T. Exell, K. Meadmore, E. Hallewell, and A.-M. Hughes. “Computational models of upper-limb motion during functional reaching tasks for application in FES-based stroke rehabilitation.” In: *Biomedical Engineering/Biomedizinische Technik* 60.3 (2015), pp. 179–191.

[98] P. Crago, W. Memberg, M. Usey, M. Keith, R. Kirsch, G. Chapman, M. Katorgi, and E. Perreault. “An elbow extension neuroprosthesis for individuals with tetraplegia.” In: *IEEE transactions on rehabilitation engineering* 6.1 (1998), pp. 1–6.

[99] K. M. Jagodnik and A. J. van den Bogert. “Optimization and evaluation of a proportional derivative controller for planar arm movement.” In: *Journal of Biomechanics* 43.6 (2010), pp. 1086–1091.

[100] K. M. Jagodnik, D. Blana, A. J. van den Bogert, and R. F. Kirsch. “An optimized proportional-derivative controller for the human upper extremity with gravity.” In: *Journal of biomechanics* 48.13 (2015), pp. 3692–3700.

[101] A. Ajoudani and A. Erfanian. “A neuro-sliding-mode control with adaptive modeling of uncertainty for control of movement in paralyzed limbs using functional electrical stimulation.” In: *IEEE Transactions on Biomedical Engineering* 56.7 (2009), pp. 1771–1780.

[102] C. L. Lynch and M. R. Popovic. “A comparison of closed-loop control algorithms for regulating electrically stimulated knee movements in individuals with spinal cord injury.” In: *IEEE Transactions on Neural Systems and Rehabilitation Engineering* 20.4 (2012), pp. 539–548.

[103] J. J. Abbas and H. J. Chizeck. “Neural network control of functional neuromuscular stimulation systems: computer simulation studies.” In: *IEEE Transactions on Biomedical Engineering* 42.11 (1995), pp. 1117–1127.

[104] F. Previdi. “Identification of black-box nonlinear models for lower limb movement control using functional electrical stimulation.” In: *Control Engineering Practice* 10.1 (2002), pp. 91–99.

[105] N. Kirsch, N. Alibeji, and N. Sharma. "Nonlinear model predictive control of functional electrical stimulation." In: *Control Engineering Practice* 58 (2017), pp. 319–331.

[106] N. Mehrabi, S. Tajeddin, N. L. Azad, and J. McPhee. "Application of Newton/GMRES method to nonlinear model predictive control of functional electrical stimulation." In: *Proc. 3rd Int. Conf. Control, Dyn. Syst., Robot.(CDSR)*. 2016, pp. 3–7.

[107] E. M. Schearer, Y.-W. Liao, E. J. Perreault, M. C. Tresch, W. D. Memberg, R. F. Kirsch, and K. M. Lynch. "Semiparametric identification of human arm dynamics for flexible control of a functional electrical stimulation neuroprosthesis." In: *IEEE Transactions on Neural Systems and Rehabilitation Engineering* 24.12 (2016), pp. 1405–1415.

[108] R. S. Razavian, B. Ghannadi, N. Mehrabi, M. Charlet, and J. McPhee. "Feedback control of functional electrical stimulation for 2-D arm reaching movements." In: *IEEE Transactions on Neural Systems and Rehabilitation Engineering* 26.10 (2018), pp. 2033–2043.

[109] A. Bheemreddy, A. Friederich, L. Lombardo, R. J. Triolo, and M. L. Audu. "Estimating total maximum isometric force output of trunk and hip muscles after spinal cord injury." In: *Medical & biological engineering & computing* 58 (2020), pp. 739–751.

[110] E. K. Chadwick, D. Blana, R. F. Kirsch, and A. J. Van Den Bogert. "Real-time simulation of three-dimensional shoulder girdle and arm dynamics." In: *IEEE Transactions on Biomedical Engineering* 61.7 (2014), pp. 1947–1956.

[111] M. Sartori, D. Farina, and D. G. Lloyd. "Hybrid neuromusculoskeletal modeling to best track joint moments using a balance between muscle excitations derived from electromyograms and optimization." In: *Journal of biomechanics* 47.15 (2014), pp. 3613–3621.

[112] J. Knibbe, P. Strohmeier, S. Boring, and K. Hornbæk. "Automatic calibration of high density electric muscle stimulation." In: *Proceedings of the ACM on Interactive, Mobile, Wearable and Ubiquitous Technologies* 1.3 (2017), pp. 1–17.

[113] C. De Marchis, T. Santos Monteiro, C. Simon-Martinez, S. Conforto, and A. Gharabaghi. "Multi-contact functional electrical stimulation for hand opening: electrophysiologically driven identification of the optimal stimulation site." In: *Journal of neuroengineering and rehabilitation* 13.1 (2016), pp. 1–9.

[114] B. Sensortec. *BNO055, Data Sheets*. 2018.

[115] Z. Lin, Y. Xiong, H. Dai, and X. Xia. "An Experimental Performance Evaluation of the Orientation Accuracy of Four Nine-Axis MEMS Motion Sensors." In: *2017 5th International Conference on Enterprise Systems (ES)*. 2017, pp. 185–189. DOI: `10.1109/ES.2017.37`.

[116] *Depiction of accurate and precise measurements*. `https://www.hitachi-hightech.com/global/en/knowledge/semiconductor/room/manufacturing/accuracy-precision.html`. Accessed: 17.11.2023.

[117] W. P. H. Thurston. *Three-Dimensional Geometry and Topology, Volume 1: Volume 1*. Princeton university press, 1997.

[118] J. Cederberg. *A course in modern geometries*. Springer Science & Business Media, 2004.

[119] S. Kucuk and Z. Bingul. *Robot kinematics: Forward and inverse kinematics*. INTECH Open Access Publisher London, UK, 2006.

[120] J. Denavit and R. S. Hartenberg. “A kinematic notation for lower-pair mechanisms based on matrices.” In: (1955).

[121] R. Penrose. “A generalized inverse for matrices.” In: *Mathematical proceedings of the Cambridge philosophical society*. Vol. 51. 3. Cambridge University Press. 1955, pp. 406–413.

[122] E. Süli and D. F. Mayers. *An introduction to numerical analysis*. Cambridge university press, 2003.

[123] H. Das, J.-E. Slotine, and T. Sheridan. “Inverse kinematic algorithms for redundant systems.” In: *Proceedings. 1988 IEEE International Conference on Robotics and Automation*. 1988, 43–48 vol.1. DOI: `10.1109/ROBOT.1988.12021`.

[124] A. I. Lurie. *Analytical mechanics*. Springer Science & Business Media, 2013.

[125] R. Featherstone. “Robot dynamics algorithms.” In: *Annexe Thesis Digitisation Project 2016 Block 5* (1984).

[126] B. Siciliano, O. Khatib, and T. Kröger. *Springer handbook of robotics*. Vol. 200. Springer, 2008.

[127] N. Hogan. “Impedance Control: An Approach to Manipulation.” In: *1984 American Control Conference*. 1984, pp. 304–313. DOI: `10.23919/ACC.1984.4788393`.

[128] N. Hogan. “Impedance control: An approach to manipulation: Part II—Implementation.” In: (1985).

[129] A. Albu-Schaffer, C. Ott, and G. Hirzinger. “A passivity based cartesian impedance controller for flexible joint robots-part II: Full state feedback, impedance design and experiments.” In: *IEEE International Conference on Robotics and Automation, 2004. Proceedings. ICRA'04. 2004*. Vol. 3. IEEE. 2004, pp. 2666–2672.

[130] J. Sherman and W. J. Morrison. “Adjustment of an inverse matrix corresponding to a change in one element of a given matrix.” In: *The Annals of Mathematical Statistics* 21.1 (1950), pp. 124–127.

[131] A. E. Hoerl and R. W. Kennard. “Ridge Regression: Applications to Nonorthogonal Problems.” In: *Technometrics* 12.1 (1970), pp. 69–82. DOI: `10.1080/00401706.1970.10488635`. eprint: `https://www.tandfonline.com/doi/pdf/10.1080/00401706.1970.10488635`.

[132] B. Schölkopf, K. Tsuda, and J.-P. Vert. *Kernel methods in computational biology*. MIT press, 2004.

[133] V. Vovk. “Kernel Ridge Regression.” In: *Empirical Inference: Festschrift in Honor of Vladimir N. Vapnik*. Ed. by B. Schölkopf, Z. Luo, and V. Vovk. Berlin, Heidelberg: Springer Berlin Heidelberg, 2013, pp. 105–116. ISBN: 978-3-642-41136-6. DOI: `10.1007/978-3-642-41136-6_11`.

[134] R. Rifkin, G. Yeo, and T. Poggio. “Regularized least-squares classification.” In: *Nato Science Series Sub Series III Computer and Systems Sciences* 190 (2003), pp. 131–154.

[135] A. Rahimi and B. Recht. “Random features for large-scale kernel machines.” In: *Advances in neural information processing systems* 20 (2007).

[136] A. Gijsberts, R. Bohra, D. Sierra González, A. Werner, M. Nowak, B. Caputo, M. A. Roa, and C. Castellini. “Stable myoelectric control of a hand prosthesis using non-linear incremental learning.” In: *Frontiers in neurorobotics* 8 (2014), p. 8.

[137] J. Englsberger, A. Werner, C. Ott, B. Henze, M. A. Roa, G. Garofalo, R. Burger, A. Beyer, O. Eiberger, K. Schmid, and A. Albu-Schäffer. "Overview of the torque-controlled humanoid robot TORO." In: *2014 IEEE-RAS International Conference on Humanoid Robots*. IEEE. 2014, pp. 916–923.

[138] M. Connan, E. Ruiz Ramírez, B. Vodermayer, and C. Castellini. "Assessment of a Wearable Force- and Electromyography Device and Comparison of the Related Signals for Myocontrol." In: *Frontiers in Neurorobotics* 10 (2016). ISSN: 1662-5218. DOI: `10.3389/fnbot.2016.00017`.

[139] C. Castellini and V. Ravindra. "A wearable low-cost device based upon Force-Sensing Resistors to detect single-finger forces." In: *5th IEEE RAS/EMBS International Conference on Biomedical Robotics and Biomechatronics*. 2014, pp. 199–203. DOI: `10.1109/BIOROB.2014.6913776`.

[140] H. J. Hermens, B. Freriks, C. Disselhorst-Klug, and G. Rau. "Development of recommendations for SEMG sensors and sensor placement procedures." In: *Journal of electromyography and Kinesiology* 10.5 (2000), pp. 361–374.

[141] C. Liang and T. Hsiao. "Admittance control of powered exoskeletons based on joint torque estimation." In: *IEEE Access* 8 (2020), pp. 94404–94414.

[142] M. Eid. "A Force Output-Based Calibration of a Muscular Electrical Stimulation Array." MA thesis. Friedrich-Alexander Universität Erlangen-Nürnberg, 2023.

[143] R. Baratta, M. Solomonow, and B.-H. Zhou. "Frequency domain-based models of skeletal muscle." In: *Journal of Electromyography and Kinesiology* 8.2 (1998), pp. 79–91.

[144] A. M. Simon, L. J. Hargrove, B. A. Lock, and T. A. Kuiken. "The target achievement control test: Evaluating real-time myoelectric pattern recognition control of a multifunctional upper-limb prosthesis." In: *Journal of rehabilitation research and development* 48.6 (2011), p. 619.

[145] L. B. Sheiner and S. L. Beal. "Some suggestions for measuring predictive performance." In: *Journal of pharmacokinetics and biopharmaceutics* 9 (1981), pp. 503–512.

[146] K. Pearson. "VII. Note on regression and inheritance in the case of two parents." In: *proceedings of the royal society of London* 58.347-352 (1895), pp. 240–242.

[147] P. Stoica and R. L. Moses. *Spectral analysis of signals*. Vol. 452. Pearson Prentice Hall Upper Saddle River, NJ, 2005.

[148] I. T. Jolliffe and J. Cadima. "Principal component analysis: a review and recent developments." In: *Philosophical transactions of the royal society A: Mathematical, Physical and Engineering Sciences* 374.2065 (2016), p. 20150202.

[149] R. A. Fisher. "The use of multiple measurements in taxonomic problems." In: *Annals of eugenics* 7.2 (1936), pp. 179–188.

[150] B. Thompson. "Effect sizes, confidence intervals, and confidence intervals for effect sizes." In: *Psychology in the Schools* 44.5 (2007), pp. 423–432.

[151] Student. "The probable error of a mean." In: *Biometrika* 6.1 (1908), pp. 1–25.

[152] L. St and S. Wold. "Analysis of variance (ANOVA)." In: *Chemometrics and intelligent laboratory systems* 6.4 (1989), pp. 259–272.

[153] J. W. Tukey. “Comparing individual means in the analysis of variance.” In: *Biometrics* (1949), pp. 99–114.

[154] R. F. Woolson. “Wilcoxon signed-rank test.” In: *Wiley encyclopedia of clinical trials* (2007), pp. 1–3.

[155] J. Cohen. *Statistical power analysis for the behavioral sciences*. Academic press, 2013.

[156] D. Lakens. “Calculating and reporting effect sizes to facilitate cumulative science: a practical primer for t-tests and ANOVAs.” In: *Frontiers in psychology* 4 (2013), p. 863.

[157] W. Kabsch. “A discussion of the solution for the best rotation to relate two sets of vectors.” In: *Acta Crystallographica Section A: Crystal Physics, Diffraction, Theoretical and General Crystallography* 34.5 (1978), pp. 827–828.

[158] I. Rayment, H. M. Holden, M. Whittaker, C. B. Yohn, M. Lorenz, K. C. Holmes, and R. A. Milligan. “Structure of the actin-myosin complex and its implications for muscle contraction.” In: *Science* 261.5117 (1993), pp. 58–65.

[159] L. H. Ting, S. A. Chvatal, S. A. Safavynia, and J. Lucas McKay. “Review and perspective: neuromechanical considerations for predicting muscle activation patterns for movement.” In: *International journal for numerical methods in biomedical engineering* 28.10 (2012), pp. 1003–1014.

[160] F. Lestienne. “Effects of inertial load and velocity on the braking process of voluntary limb movements.” In: *Experimental Brain Research* 35 (1979), pp. 407–418.

[161] Z. Hasan. “Optimized movement trajectories and joint stiffness in unperturbed, inertially loaded movements.” In: *Biological cybernetics* 53 (1986), pp. 373–382.

[162] L. Grimby and J. Hannerz. “Recruitment order of motor units on voluntary contraction: changes induced by proprioceptive afferent activity.” In: *Journal of neurology, neurosurgery, and psychiatry* 31.6 (1968), p. 565.

[163] C. De Luca and J. Kline. “Influence of proprioceptive feedback on the firing rate and recruitment of motoneurons.” In: *Journal of Neural Engineering* 9.1 (2011), p. 016007.

[164] R. Koiva, B. Hilsenbeck, and C. Castellini. “FFLS: An accurate linear device for measuring synergistic finger contractions.” In: *2012 Annual International Conference of the IEEE Engineering in Medicine and Biology Society*. IEEE. 2012, pp. 531–534.

[165] N. Dunkelberger, J. Berning, E. M. Schearer, and M. K. O’Malley. “Hybrid FES-exoskeleton control: Using MPC to distribute actuation for elbow and wrist movements.” In: *Frontiers in Neurorobotics* 17 (2023), p. 1127783.

[166] G. R. Müller-Putz, R. Scherer, G. Pfurtscheller, and R. Rupp. “Brain-computer interfaces for control of neuroprostheses: from synchronous to asynchronous mode of operation/Brain-Computer Interfaces zur Steuerung von Neuroprothesen: von der synchronen zur asynchronen Funktionsweise.” In: (2006).

[167] S. A. Safavynia and L. H. Ting. “Task-level feedback can explain temporal recruitment of spatially fixed muscle synergies throughout postural perturbations.” In: *Journal of neurophysiology* 107.1 (2012), pp. 159–177.

[168] N. Wannawas, A. Shafti, and A. A. Faisal. “I am robot: Neuromuscular reinforcement learning to actuate human limbs through functional electrical stimulation.” In: *arXiv preprint arXiv:2103.05349* (2021).

[169] N. Wannawas and A. A. Faisal. "Towards AI-controlled FES-restoration of arm movements: neuromechanics-based reinforcement learning for 3-D reaching." In: *2023 11th International IEEE/EMBS Conference on Neural Engineering (NER)*. IEEE. 2023, pp. 1–4.

[170] D. Popovic and M. Popovic. "Tuning of a nonanalytical hierarchical control system for reaching with FES." In: *IEEE transactions on biomedical engineering* 45.2 (1998), pp. 203–212.

[171] M. Popovic and D. Popovic. "Cloning biological synergies improves control of elbow neuroprostheses." In: *IEEE Engineering in Medicine and Biology Magazine* 20.1 (2001), pp. 74–81.

[172] O. Schill, R. Wiegand, B. Schmitz, R. Matthies, U. Eck, C. Pylatiuk, M. Reischl, S. Schulz, and R. Rupp. "OrthoJacket: an active FES-hybrid orthosis for the paralysed upper extremity." In: (2011).

[173] R. Rupp. *Die motorische Rehabilitation von Querschnittgelähmten mittels Elektrostimulation: ein integratives Konzept für die Kontrolle von Therapie und funktioneller Restitution*. Verlag Dr. Hut, 2008.

[174] O. Schill, R. Rupp, and M. Reischl. "Signal processing concepts for optimal myoelectric sensor placement in a modular hybrid FES orthosis." In: *4th European Conference of the International Federation for Medical and Biological Engineering: ECIFMBE 2008 23–27 November 2008 Antwerp, Belgium*. Springer. 2009, pp. 1816–1819.

[175] M. Katoh, N. Nishimura, M. Yokoyama, T. Hachisu, M. Sato, S. Fukushima, and H. Kajimoto. "Optimal selection of electrodes for muscle electrical stimulation using twitching motion measurement." In: *Proceedings of the 4th Augmented Human International Conference*. 2013, pp. 237–238.

[176] E. Tamaki, T. Miyaki, and J. Rekimoto. "PossessedHand: techniques for controlling human hands using electrical muscles stimuli." In: *Proceedings of the sigchi conference on human factors in computing systems*. 2011, pp. 543–552.

[177] D. Sierra González and C. Castellini. "A realistic implementation of ultrasound imaging as a human-machine interface for upper-limb amputees." In: *Frontiers in neurorobotics* 7 (2013), p. 17.

[178] P. Lopes and P. Baudisch. "Interactive systems based on electrical muscle stimulation." In: *Computer* 50.10 (2017), pp. 28–35.

[179] S. Nikolaidis, Y. X. Zhu, D. Hsu, and S. Srinivasa. "Human-robot mutual adaptation in shared autonomy." In: *Proceedings of the 2017 ACM/IEEE International Conference on Human-Robot Interaction*. 2017, pp. 294–302.

[180] S. Javdani, S. S. Srinivasa, and J. A. Bagnell. "Shared autonomy via hindsight optimization." In: *Robotics science and systems: online proceedings* 2015 (2015).

[181] M. Rabelo, R. V. B. d. Moura Jucá, L. A. O. Lima, H. Resende-Martins, A. P. L. Bó, C. Fattal, C. Azevedo-Coste, and E. Fachin-Martins. "Overview of FES-assisted cycling approaches and their benefits on functional rehabilitation and muscle atrophy." In: *Muscle Atrophy* (2018), pp. 561–583.

[182] N. Kerver, S. van Twillert, B. Maas, and C. K. van der Sluis. “User-relevant factors determining prosthesis choice in persons with major unilateral upper limb defects: A meta-synthesis of qualitative literature and focus group results.” In: *PLoS One* 15.6 (2020), e0234342.

[183] A. W. Franzke, M. B. Kristoffersen, R. M. Bongers, A. Murgia, B. Pobatschnig, F. Unglaube, and C. K. van der Sluis. “Users’ and therapists’ perceptions of myoelectric multi-function upper limb prostheses with conventional and pattern recognition control.” In: *PloS one* 14.8 (2019), e0220899.

Appendix A Full text core publications

A.1 The BodyRig posture tracking system

Title: Human-In-The-Loop Assessment of an Ultralight, Low-Cost Body Posture Tracking Device.

Authors: Marek Sierotowicz, Mathilde Connan, and Claudio Castellini.

Journal: Sensors

Publisher: MDPI

Manuscript version: Published article

Review: Peer-reviewed

Citation: M. Sierotowicz, M. Connan, and C. Castellini. "Human-in-the-loop assessment of an ultralight, low-cost body posture tracking device." In: *Sensors* 20.3 (2020), p. 890. ISSN: 1424-8220. DOI: `10.3390/s20030890`

Abstract: In rehabilitation, assistive and space robotics, the capability to track the body posture of a user in real time is highly desirable. In more specific cases, such as teleoperated extra-vehicular activity, prosthetics and home service robotics, the ideal posture-tracking device must also be wearable, light and low-power, while still enforcing the best possible accuracy. Additionally, the device must be targeted at effective human-machine interaction. In this paper, we present and test such a device based upon commercial inertial measurement units: it weighs 575 g in total, lasts up to 10.5 h of continual operation, can be donned and doffed in under a minute and costs less than 290 EUR. We assess the attainable performance in terms of error in an online trajectory-tracking task in Virtual Reality using the device through an experiment involving 10 subjects, showing that an average user can attain a precision of 0.66 cm during a static precision task and 6.33 cm while tracking a moving trajectory, when tested in the full peri-personal space of a user.

Author contributions: Conceptualization; Software Design; Hardware Design; Test setup and user study execution; Formal analysis; Writing-original draft; Writing-review and editing.

sensors

Article

Human-In-The-Loop Assessment of an Ultralight, Low-Cost Body Posture Tracking Device

Marek Sierotowicz *, **Mathilde Connan** and **Claudio Castellini**

Institute of Robotics and Mechatronics, German Aerospace Center (DLR), 82234 Weßling, Germany; mathilde.connan@dlr.de (M.C.); claudio.castellini@dlr.de (C.C.)
* Correspondence: marek.sierotowicz@dlr.de; Tel.: +49-8153-28-3392

Received: 17 December 2019; Accepted: 4 February 2020; Published: 7 February 2020

Abstract: In rehabilitation, assistive and space robotics, the capability to track the body posture of a user in real time is highly desirable. In more specific cases, such as teleoperated extra-vehicular activity, prosthetics and home service robotics, the ideal posture-tracking device must also be wearable, light and low-power, while still enforcing the best possible accuracy. Additionally, the device must be targeted at effective human-machine interaction. In this paper, we present and test such a device based upon commercial inertial measurement units: it weighs 575 g in total, lasts up to 10.5 h of continual operation, can be donned and doffed in under a minute and costs less than 290 EUR. We assess the attainable performance in terms of error in an online trajectory-tracking task in Virtual Reality using the device through an experiment involving 10 subjects, showing that an average user can attain a precision of 0.66 cm during a static precision task and 6.33 cm while tracking a moving trajectory, when tested in the full peri-personal space of a user.

Keywords: wearable sensors; inertial measurement units; low-cost sensors; assistive robotics; rehabilitation robotics; teleoperation; space robotics

1. Introduction

Multi-modal intent detection is the problem of detecting a person's intention to move or to activate one's muscles using sensors pertaining to different modalities, for example, going beyond the traditional usage of surface electromyography (sEMG) [1,2]. Especially in (upper-limb) prosthetics, sEMG is in use since the 50s to convert muscle activation signals, detected through the tiny electrical fields generated by motor units while contracting [3,4], into control commands for a prosthetic device. Although no clear substitute for sEMG is in sight, this technique suffers from a number of drawbacks (see, e.g., Reference [5]) and alternative means are being studied [2,6] to detect muscle activation in a different way, for example, force myography through muscle bulging [7,8] and ultrasound scanning through musculoskeletal internal movement detection.

An interesting alternative to these techniques consists of using some form of motion tracking and/or body posture detection to provide information about the body kinematics of the user, rather than directly detecting their intention to activate their muscular system. Knowing, for example, that the user is drawing their arms close to each other might be useful to enforce a coordinated two-handed prosthetic grasping of a heavy basket—this idea already appears in Reference [1]. As well, such information could be extremely valuable in solving the limb-position effect [9,10], which refers to the change in muscular recruitment and activity (and, by extension, measurable muscular signals) for the same hand movement due to a change in body pose.

Body tracking could also provide useful data for day-to-day health monitoring, besides medically relevant data for patients using prosthetic devices. With the recent interest in Internet of Things (IoT) solutions in this direction, many devices have been presented as a tool to gather this sort of information. In many cases, authors propose solutions based on optical body tracking system [11].

However, optical, magnetic or laser-based motion tracking are enforced by detecting the position of body markers with respect to an external source of radiation (near-infrared cameras, magnetic field generators, etc.), implying that such systems cannot be wearable – one can definitely wear the markers but not the sources of energy. Furthermore, an optical system, even if used in a wearable configuration in association with markers, will always be prone to the issue of line of sight occlusions, which is especially problematic in real time applications and when analyzing activities entailing complex body postures. As opposed to such techniques and if the user's absolute position is not required, a potentially better alternative is represented by Inertial Measurement Units (IMUs). An IMU is in general able to detect its own acceleration and orientation with respect to the gravitational field; using a constellation of several such devices in specific spots on the human body, one can therefore reconstruct its kinematic configuration. This solution is already used, for example, in the XSens Suit (https://www.xsens.com) or in the rehabilitation device called Riablo (https://www.corehab.it/en). One well-known drawback of IMUs is that their measurements tend to drift over time, needing frequent recalibration; but with the advent of virtually drift-free IMUs-on-a-chip (e.g., Bosch's BNO055 [12]) this problem can be overcome even using off-the-shelf components and the optimized data-fusion algorithms that come with them. The BNO055 also has the advantage of being cheap, lightweight and low-power, therefore perfect to be coupled to a wireless/Bluetooth (BT) transmission system and a small battery.

Putting all these pieces together, in this paper we introduce the BodyRig a complete, ultralight, low-cost upper body posture detector based upon such commercial IMUs. The BodyRig, consisting of a constellation of up to 7 IMU/BT/battery modules, weighs in total 575 g, it lasts 10.5 h of continual operation, it is donned and doffed in less than a minute and costs less than 290 EUR. For comparison, the XSens Awinda setup, while consisting of a more complex constellation of 17 trackers and allowing for a faster update rate (1 kHz internal, 240 Hz output rate), has a battery life of around 6 h and requires a setup procedure of 10 min [13].

The BodyRig can be easily used to enforce real-time body posture tracking, teleoperation and multi-modal prosthetic control, both in Virtual Reality (VR) and in real life. We here assess the device through an experiment involving 10 users in an online trajectory-tracking task in VR, showing that it affords an average precision of 0.66 cm during a precision task and 6.33 cm while tracking a target moving along a prerecorded trajectory, when tested in the full peri-personal space of a user. These values are much larger than the absolute precision of the VR system employed in the experiment, which appears reasonable, given the pointing precision attainable by a human being [14].

Potential applications of this device, not limited to rehabilitation robotics [15] and discussed in detail at the end of this paper, are endless.

2. Materials and Methods

The BodyRig system was used, in this experiment, in a reduced configuration, which allows monitoring of user movements up to and including the forearms. In this reduced configuration, the total material cost is around 220 euros and the total weight around 540 g and can operate more than 13 h uninterruptedly. In this case, the system consists of 5 independent modules, each one fundamentally consisting of an IMU (in our case, Bosch's BNO055 sensors [12]), a BT module and a battery. The IMUs are connected via I2C to a bluefruit feather nRF52832 breakout board module from Adafruit (see References [16,17] for more details), which is capable of communicating using the Bluetooth Low Energy stack via a proprietary serial port emulation profile from Nordic Semiconductors called BLEUart (see Reference [18]). Each module acts as a peripheral within the BLEUart standard, except the one monitoring the movements of the user's core, which acts as a central unit. The data transmitted from the peripherals to the central is relayed to a host computer via conventional Bluetooth SPP using a RN41 module from Microchip Technology (see Reference [19]).

All components are off-the-shelf, except for the 3-D printed casings and the custom PCB for the RN41 module. At the current stage, the BodyRig can be considered a minimum viable product (MVP) but expansions are planned in the near future.

The HTC Vive VR visor (see Reference [20]) was used to provide the subjects with visual feedback in virtual reality. The visor uses two light sources to determine its own orientation and position, although in this experiment only the orientation of the visor was needed. The precision of the Vive system, measured using a "tracker," is sub-millimetric in a static configuration [21,22]. The position of the avatar's head was determined using forward kinematics based on the data coming in from the BodyRig system together with the orientation of the head as measured by the visor itself. The BodyRig monitored the orientation of trunk, both humeri and both forearms. Therefore, considering the measurement of the user's head's orientation with the visor, a total of 6 body segments were monitored. Figure 1 shows a diagram with the fundamental elements of the setup.

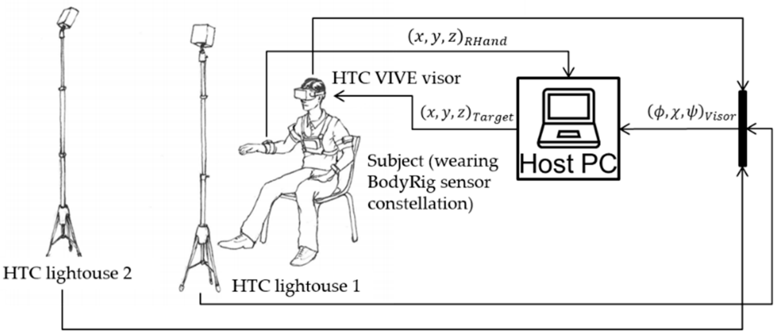

Figure 1. Block diagram and illustration of the setup.

The data from each BodyRig module is asynchronously sent to the host PC with an average frequency of about 75 Hz. Considering that the kinematic model is updated every time data from one peripheral is transmitted to the host PC, in order to handle this transmission frequency from 5 trackers, the main software acquires the incoming data at 400 Hz. The data relative to the user's posture is sent from the application managing the serial driver to the VR simulation together with the target's position. Each target movement profile is the result of a recording obtained using the BodyRig in an analogous configuration as the one used during the experiment.

Within the simulation, the position and orientation of the body segment of the avatar are represented based on the measurements of the BodyRig, according to a forward kinematic model (please refer to Reference [23] for more details). The lengths of the avatar's body segments were the same for all subjects. These lengths are important, as the position of the avatar's right hand in space is a function of these parameters. The body segment lengths are indicated in Table 1.

Table 1. Avatar body segment lengths in centimeters.

Body Segment	Length [cm]
Thorax (Pelvis to neck base)	25
Shoulder (neck base to proximal humerus, right and left)	25
Humerus (right and left)	25
Forearm (right and left)	30

Ten male, right handed subjects of age 29.1 ± 7.2 years, weight 73.7 ± 8.1 kg and height 1.82 ± 0.07 m took part in the experiment. The experimental procedure was thoroughly explained to the subjects in both oral and written form prior to the experiment and all the participants signed an informed consent form. The experiment was performed according to the World Medical Association's Declaration of Helsinki, regarding the ethical principles for medical research involving human subjects, last version, as approved at the 64th WMA General Assembly, Fortaleza, Brazil, October 2013. Data collection from subjects was formally approved by the host institution's internal board for protection of data privacy and by the work council of the German Aerospace Center. A physician is part of the council that approved the experiments.

In VR, the subjects were provided with a 3D representation of their avatar, the current position of the target and a train of spheres marking the upcoming positions of the target along its trajectory. Additionally, the subjects were provided with a textual indicator of the current distance of the target from the avatar's right hand. Furthermore, a cylinder was made visible in VR to the users, which from the center of the target pointed at the right hand of the avatar, providing a useful indication of the direction along which it was necessary to correct for the current error at each given time. Figure 2 depicts a more detailed description of each relevant element present in the VR simulation.

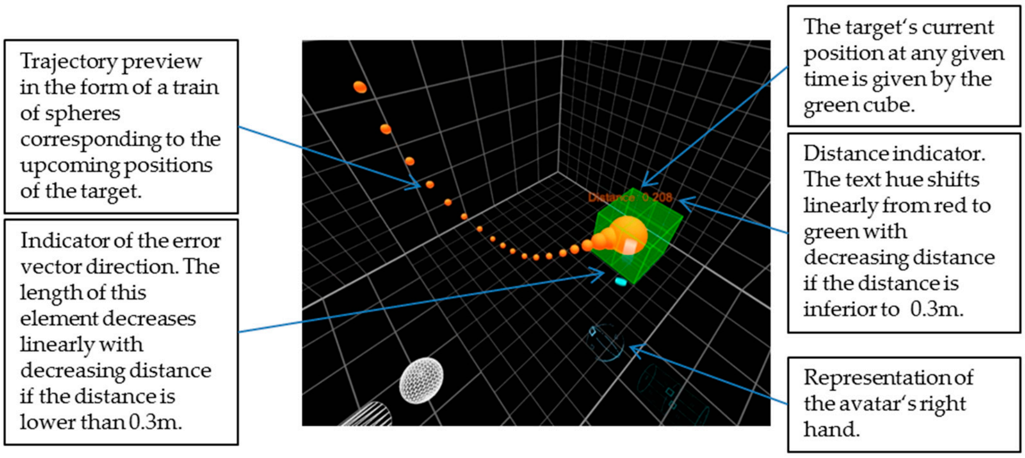

Figure 2. A representative screenshot of the Virtual Reality (VR) simulation with description of each element.

During the experiment, the data recorded included the position and orientation of each body segment monitored by the BodyRig, the position of the target and of each individual sphere from the train of spheres used in the simulation to inform the subject about the upcoming trajectory of the target. Each subject was asked to follow the target along 3 distinct trajectories, prerecorded using the BodyRig, at 2 different speeds, with 3 repetitions per speed and trajectory, for a total of 18 trials. The trajectories are hereafter respectively indicated as Infinity-shaped trajectory (IS), Constant speed Tai Chi (CT) and Variable speed Tai Chi (VT). No randomization in the order of execution of the target profiles was employed, as verifying whether better performance is achievable with a particular profile rather than another is not the goal of this experiment.

In order to familiarize themselves with the VR environment and with the equipment, the subjects were first asked to follow a separate trajectory, especially recorded to serve as a familiarization tool, at 2 different speeds with 1 repetition per speed. The familiarization target trajectory is hereafter indicated as Familiarization Profile (FP).

Between each of the 4 sets of trials with a common target trajectory (including the familiarization phase) the subjects were asked to rest at least 60 s. During this resting time, the subjects were asked to record a subjective assessment of the perceived difficulty of the previous task, as well as the perceived influence of both their current level of fatigue and the BodyRig system on their accuracy and reactivity. The assessment was to be given through a score ranging from 1 to 20. Furthermore, at the end of the experiment, the subjects were asked to fill a System Usability Scale questionnaire (see Reference [24]) in order to assess the perceived practicality of the BodyRig system in the context of the tasks at hand.

Before and after each of the 4 sets of trials with a common target trajectory, the subjects were asked, for 30 s, to keep the avatar's right hand as close as possible to a static point located in the frontal region of the peri-personal space, reachable by keeping the right arm in an almost extended pose. Figure 3 shows a flow chart of the main phases of the experiment's execution. Additional details regarding the

BodyRig system and the experiment execution can be found in the supplementary material attached to this article (see video S1 in Supplementary Materials).

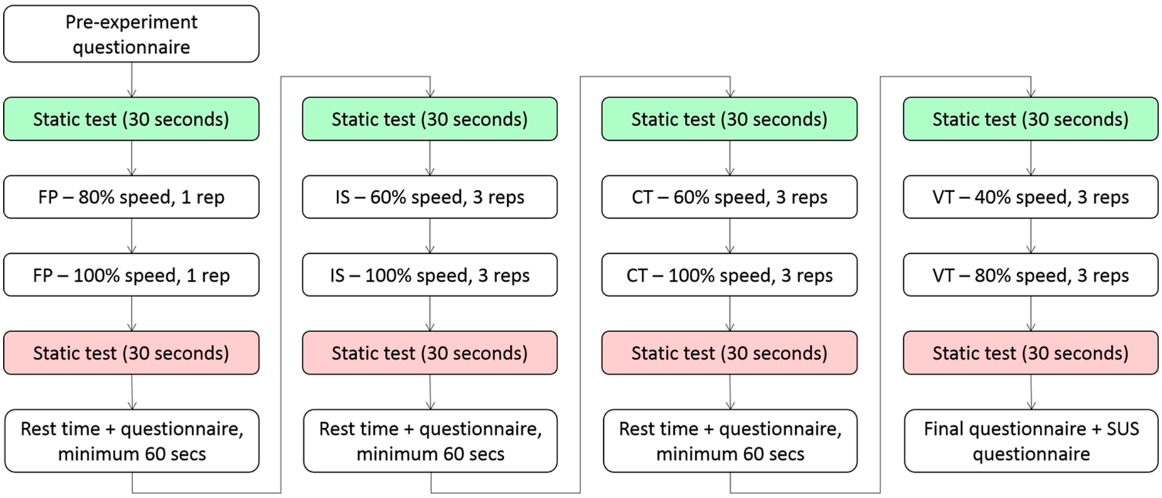

Figure 3. Flowchart illustrating the experiment's execution. The green and red color represent the static tests executed after the resting phases and after completion of a task series, respectively.

3. Results

Data analysis was based on properties measured both from the trajectories followed by the test subjects, as well as from the target trajectories themselves.

3.1. Static Tracking

During the static tests, the subjects were asked to keep the sphere representing the avatar's right hand as close as possible to a static target for 30 s. As a general measure of the subject's precision, the mean and the variance of the norm of the vector difference between the end of the avatar's right forearm and the target's position was drawn over the course of the 30 s of each trial, in an analogous way as shown in Equation (7). One of the subjects provided strongly and consistently outlying data: the mean of the error during static tests from this subject shows as the only outlier among the data from all subjects for 7 static tests out of 8, according to the generalized extreme Studentized deviate test for outliers. After qualitative analysis, it seems that this is either due to a failure, on the part of the subject, to understand the provided indications and to utilize the feedback from the VR simulation properly in order to correct the position of the right hand or possibly due to technical problems. However, no such anomaly has been observed with any other subject. For this reason, the data gathered during static tests for this subject were not considered in the analyses. Considering all remaining subjects and repetitions, the two metrics have values of 0.66 ± 0.27 cm for the mean and 0.0835 ± 0.0744 cm^2 for the variance, respectively. These metrics present a correlation coefficient of 0.63 with a $p < 0.0001$. Figure 4 shows a boxplot of the error measured during static tests over all reliable subjects sorted by test number. Figure 5 shows boxplots of the mean static error as observed specifically after a resting phase and after completion of a full task series, with the intent of showing the behavior of the error in these two specific conditions. In both cases, the data is color-coded consistently with Figure 3.

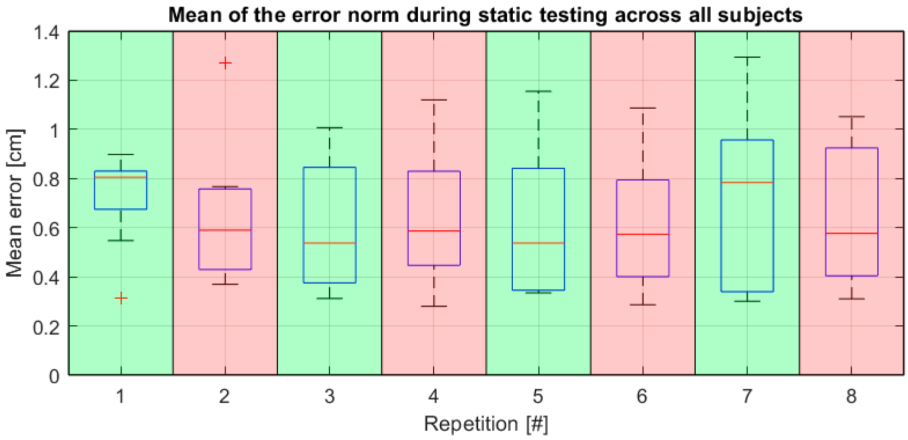

Figure 4. Boxplot over all subjects of the mean error norm measured over each static testing session.

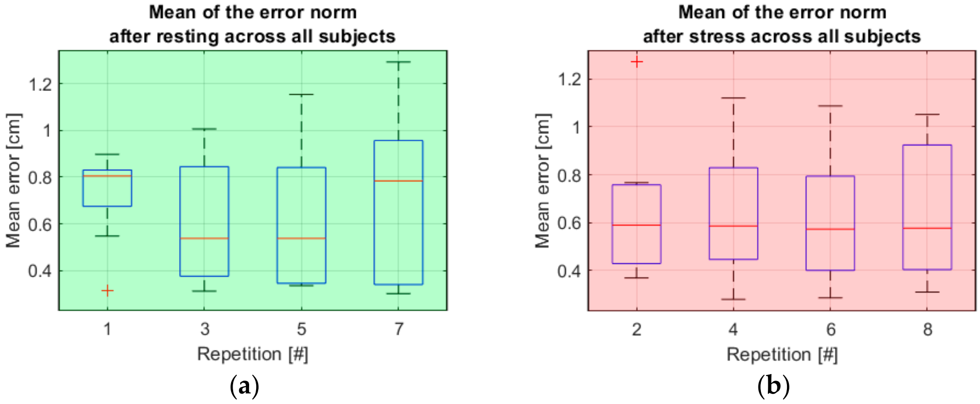

Figure 5. Boxplots of the error during static tests specifically after resting phases and after completion of one task series. (**a**) Boxplot of the mean error in static tests executed after a resting phase; (**b**) Boxplot of the mean error in static tests executed after completion of a task series, before a resting phase.

3.2. Trajectory Tracking

For the purposes of this analysis, the recorded positions of the avatar's right hand were synchronized with the respective target's position recordings and both trajectories were synchronized across subjects and repetitions using a uniform sampling time as basis for the synchronization.

Furthermore, for each trajectory point, the average difference vector between the hand's position and the target's position was divided in its parallel and orthogonal components with respect to the local tangential vector of the target's trajectory, so that the following relation applies:

$$\overline{e}(k) = \sqrt{e_{||}(k)^2 + e_{\perp}(k)^2} \tag{1}$$

where $\overline{e}(k)$ is the average norm of the error vectors $\vec{e}$ from all subjects and repetitions, whereas $e_{||}(k)$ and $e_{\perp}(k)$ are the average norms of the components of $\vec{e}$ that are respectively parallel and perpendicular to the tangent direction of the target's trajectory at the k-th sample from the start of the trial, for which the average error is computed. Furthermore, between the k-th sample of the tangent direction $\vec{t}_{trgt}(k)$ of the target's trajectory, the k-th sample of the target's speed vector $\vec{v}_{trgt}(k)$ and its norm $v_{trgt}(k)$, the following relations exist:

$$\vec{v}_{trgt}(k) = \frac{\left(\vec{p}_{trgt}(k+1) - \vec{p}_{trgt}(k)\right)}{t(k+1) - t(k)}, \tag{2}$$

$$v_{trgt}(k) = \| \vec{v}_{trgt}(k) \| \tag{3}$$

$$\vec{t}_{trgt}(k) = \vec{v}_{trgt}(k)/v_{trgt}(k), \tag{4}$$

where $\vec{p}_{trgt}(k)$ is the k-th sample of the target's position and $t(k)$ is the timestamp corresponding to the k-th sample. Furthermore, the k-th sample of the target's acceleration vector $\vec{a}_{trgt}(k)$ and its norm $a_{trgt}(k)$ are computed according to

$$\vec{a}_{trgt}(k) = \frac{\left(\vec{v}_{trgt}(k+1) - \vec{v}_{trgt}(k)\right)}{t(k+1) - t(k)}, \tag{5}$$

$$a_{trgt}(k) = \| \vec{a}_{trgt}(k) \| . \tag{6}$$

Additionally, both the velocity and the acceleration vectors were filtered through a moving average filter in order to increase the numerical stability for the purpose of statistical analysis. The width of the moving window is 0.2 s.

In all cases, the complete series of samples of a property p corresponding to a given task T is hereinafter indicated with p^T or simply p when indicating the concatenation of all samples corresponding to all tasks.

Considering the average performance over all subjects, we can observe the trend of the scalar error over each repetition. The results are shown in Figure 6. The performance, in this case, is measured by the mean scalar error over all N_{seq} samples acquired during a single sequence

$$\overline{e}_{rep} = \frac{1}{N_{seq}} \sum\nolimits_{1 \le k \le N_{seq}} e_{rep}(k), \tag{7}$$

and the properties shown in the boxplots are computed over the performance of the 10 subjects and sorted by repetition number.

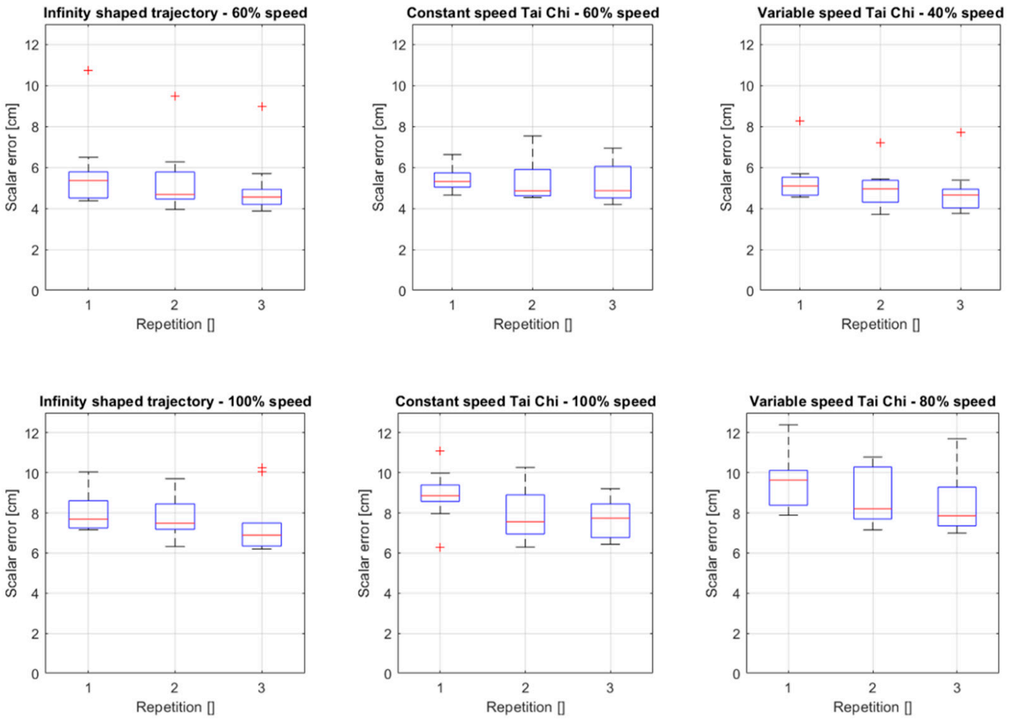

Figure 6. Boxplots of the scalar error over the repetitions for each target profile and speed.

Observing the average performance over all subjects and over all repetitions, we were able to measure general relations between the error metrics and the movements of the subjects.

The Pearson's correlation coefficients among the main properties of the target trajectory and the error metrics are reported in Table 2.

Table 2. Pearson correlation coefficients among average properties of movement over all tasks. Below the diagonal are the Pearson's cross correlation coefficients. In all cases, the coefficients are statistically significant with p far smaller than 0.0001.

p c	$e_{\|\|}$	$e_{\perp}$	v_{trgt}	a_{trgt}
$e_{\|\|}$				
$e_{\perp}$	0.516			
v_{trgt}	0.752	0.538		
a_{trgt}	0.498	0.679	0.626	
$\overline{e}$	0.948	0.751	0.750	0.619

The average trajectory followed by the test participants is computed across all repetitions and subjects and the correlation coefficients are computed for the entirety of the samples. The k-th sample of the average error is computed according to

$$\overline{e}(k) = \frac{1}{N_{rep}N_{subj}} \sum\nolimits_{1\le sub\le N_{subj}} \sum\nolimits_{1\le rep\le N_{reps}} e_{sub,rep}(k), \tag{8}$$

where $e_{sub,rep}(k)$ is the k-th sample of the scalar error measured for subject sub and repetition rep.

The means and variances of the error metrics are reported in Table A1.

Additionally, visual inspection of the error was operated. To this end, a plot with the single components of the target trajectory and the standard deviation of the error by all subjects in all repetitions was produced (see Figure A1). Furthermore, visual inspection was operated by plotting, in the form of ellipsoids, the covariance matrix corresponding to a subset of points lying on the target trajectory of each dynamic tracking task. The results are shown in Figure A2. The covariance matrix is computed according to

$$\Sigma(k) = \frac{1}{N_{rep}N_{subj} - 1} E(k)^T E(k), \tag{9}$$

where $E(k)$ is the 30×3 error observation matrix, with each row representing the k-th three dimensional error vector $\vec{e}(k)$ measured from a specific subject and repetition. The plots used for visual inspection are shown in Figures A1 and A2.

3.3. Subjective Assessment

As mentioned above, the subjects were asked to provide a subjective assessment of several relevant factors by assigning a score ranging from 1 to 20. In this context, accuracy is to be understood as the capability of maintaining the position of the right hand within the smallest possible margin of a given static target position in virtual reality and reactivity as the capability to quickly react to sudden changes in direction and speed of the target. All the subjects were provided with the aforementioned definitions.

Assuming that all subjects operated on a relative but self-consistent scale, the average of each score has been drawn across all subjects, whereas the variance of these scores was ignored. The average scores are reported in Table 3.

Table 3. Average scores across all subjects sorted by assessed factor and target trajectory profile.

Assessment	FP	IS	CT	VT
Perceived difficulty	7.3	9.5	9.8	11.6
Perceived influence of fatigue on accuracy	4.4	9.1	8.5	8.8
Perceived influence of fatigue on reactivity	5.5	8.3	9.0	8.6
Perceived influence of BodyRig on accuracy	6.1	6.7	7.4	8.4
Perceived influence of BodyRig on reactivity	6.6	6.9	7.3	7.7

Looking at the results from the System Usability Scale questionnaire [24], the subjects assigned an average score of 85 points to the system, corresponding to an A for the general usability of the device.

The subjective assessments provided by the subjects after the completion of each set of repetitions associated with a specific target trajectory profile seems to consistently bear no significant correlation to the objective error metrics. This could indicate that, independently from the subject's perception of the hardness of a task, all subjects were able to achieve it with uniformly low error.

4. Discussion

4.1. General Discussion

From the average scores assigned by the subjects, it is clear that, on average, the difficulty of the task was perceived as being consistently increasing. However, while the tasks involving the profiles IS and CT were considered at almost the same level of difficulty, the tasks involving IS were considered as more physically demanding in terms of the influence of fatigue on accuracy (see row 2 on Table 3).

The data from the static trials give a general measure of the average achievable precision in terms of average distance from the desired point. These metrics appear to be highly correlated, which seems to indicate that inaccuracy in maintaining a given position manifests itself consistently in both the inability of exactly reaching the desired position and in the instability of the hand's position. Possible sources of error in this type of trial could be fatigue, as well as non-clarity in the display of the magnitude and direction of the difference vector between the target's center and the avatar's hand. Observing the metrics over all the subjects as a function of the repetition number (see boxplots in Figure 4), no obvious influence from fatigue is evident and there is only a slight improvement visible between the very first and the following repetitions, due most likely to learning effect. The absolute precision of the Vive tracking system has been assessed as sub-millimetric in a static configuration [21,22] and, reasonably, the positioning accuracy of the target in VR was in the same range. Given this fact, the average tracking precision of 66mm obtained by the subjects seems appropriate. The human precision in pointing has actually already been determined to be about half a centimeter in Reference [14]—for further details, see also the references therein.

However, some noteworthy behavior is observable looking at the error in static tests specifically after the resting phases and after the completion of a task series (see Figure 5). Namely, one can notice, in the case of static tests executed immediately after completion of a series, that the error remains largely consistent after repetition number 2. Conversely, the error maxima seem to increase consistently in the case of static tests executed after a resting phase. This could be dictated, for the first case, by the musculature being more tonic and responsive immediately after prolonged but moderate stress and the subjects being on average more focused on the accuracy of their movements. On the other hand, right after the resting phases, during which a questionnaire was to be filled, the focus of the subjects may have been deviated from movement coordination. Fatigue is, of course, the most likely cause for the inconsistency in the mean static error observed after resting phases.

During the tracking of a dynamically moving target, the component of the error tangential to the target's trajectory presents a higher correlation with the total average error magnitude than the orthogonal component (see Table 2). However, the average magnitude of the parallel error component is not far greater than the average magnitude of the orthogonal error component (see Table A1).

Furthermore, it is worth mentioning the presence of a high correlation between the target's velocity and the error's magnitude and specifically between the target's velocity and the error's component parallel to the trajectory. This would seem to indicate that the most consistent source of error is the subjects not being able to follow the target's exact position onto its trajectory, rather than being able to maintain a short distance from the trajectory's path itself. The average orthogonal component seems to be less consistently present in the final average error norm and does not show as high a correlation with the target's speed.

There is, however, a moderate correlation between the orthogonal component of the scalar error and the target's acceleration. This is likely because, typically, most subjects find it difficult to follow the target accurately when this makes a sudden change in direction and the error in this case has a strong component perpendicular to the target's trajectory.

Lastly, Figures A1 and A2 provide a further qualitative analysis of the trajectories, showing in three dimensions the deviation from the target trajectory along the different target profiles. Figure A2, in particular, shows the error ellipsoids along the target trajectory, obtained by computing the covariance matrix from all the measured error vectors across all subjects and repetitions (see Equation (9)). The color of the depicted ellipsoids transitions from red to green over time during the target's movement. From Figure A1 one can notice an increased standard deviation when the target moves faster and when it suddenly changes direction. From Figure A2 it is apparent that the error vector components dramatically increase both as the target gets faster and as the subjects approach the points of maximum curvature of the trajectories.

Interestingly, it seems that the correlation between the perpendicular component of the error and the norm of the acceleration vector consistently increases with the successive target trajectory profiles (see Table A1). This could indicate the effect of fatigue coupled with an increasing rate of perceived difficulty (see Table 3), which renders the subjects progressively less effective at following sudden changes in direction of the target, which themselves become more pronounced during later target profiles.

The correlation coefficient between average orthogonal error component and acceleration norm corresponding to the IS tasks at 60% speed is noticeably much lower than all the following ones. A lower correlation in this case is to be expected because of the repetitiveness of this particular task. Due to this factor, it is possible that, especially after a few cycles, the subjects would start to execute the same action cyclically, rather than actively follow the target and this would lead to low correlation between the target's motion and the error's components. It is possible that central pattern generators [25] played a role in this particular task. However, this should also happen for the IS tasks at 100% speed. The most likely explanation for this is that, with the target moving faster, the subjects would naturally follow it more actively.

4.2. Limitations

It should be noted that the goal of this study is not to validate the absolute accuracy and precision of the BodyRig system, for whose task an absolute reference would be needed, for instance a VICON marker; but rather to assess the achievable performance in a range of tasks as wide as possible. In this study, the role of the ground truth is played by the target, rather than by an optical system used as reference. Any validation of the accuracy of the BodyRig in absolute terms should of course make use of a parallel body tracking setup for reference.

The BodyRig uses a kinematic model to determine the positions of the body segments and therefore it does not measure these positions directly. If the application requires exact absolute position determination, the BodyRig is prone to errors due to mismatch between the link length of the kinematic model and of the user's body.

Relevant applications which would require validation of the BodyRig in absolute terms are, for example, the measurement of anthropometric data in Cartesian space, such as the measurement of the extension of a subject's useful dexterity space. In such applications, the subject's proportions would have to be fed into the kinematic model and validation against an absolute reference would be needed to assess accuracy of the measurements. However, the BodyRig does provide useful kinematic data, such as kinematic angles, without the need for any reference or measurement of the user's body proportions. These angular measurements should have resolution and accuracy compliant with the specifications in Reference [12,26]. Such data can be used in multi-modal intent detection and makes the BodyRig a useful input device in VR and telemanipulation applications.

This experiment does show that good performance is achievable even without fitting the kinematic model to the user's actual body proportions, as the subjects of the study proved able to naturally and intuitively follow the target in VR.

5. Conclusions

In this paper, we presented the results of a user study with the main objective of evaluating the attainable precision using the BodyRig upper body tracking system in the achievement of various tasks, as well as providing a system usability score [24]. The device allows to adjust the workspace dimensions, allowing a user to be more precise at the cost of the reduction of the workspace size or vice versa. Therefore, the measurements we operated are contingent to the specific sizes chosen for the body segments of the avatar. That said, we demonstrated that an average user can achieve a precision inferior to the centimeter in static conditions and of about 6 cm when following a target, even when this is moving at fairly rapid speeds.

Additionally, we analyzed the effects of adaptation to a particular target movement profile in terms of mean error and standard deviation.

Furthermore, we were able to draw distinctions between the main error sources in following the target's movements. We were able to link statistically the error component parallel to the target's trajectory with the target's speed and the error component orthogonal to the target trajectory with the target's acceleration.

Supplementary Materials: The following are available online at http://www.mdpi.com/1424-8220/20/3/890/s1. Video S1: description of the proposed device and of the experiment.

Author Contributions: Conceptualization, M.C. and C.C.; Data curation, M.S.; Formal analysis, M.S.; Funding acquisition, C.C.; Investigation, M.S.; Methodology, M.S., M.C. and C.C.; Project administration, C.C.; Resources, M.S.; Software, M.S.; Supervision, M.C.; Visualization, M.S.; Writing—original draft, M.S., M.C. and C.C.; Writing—review & editing, M.S., M.C. and C.C. All authors have read and agreed to the published version of the manuscript.

Funding: This work was partially supported by the German Research Society project Tact-Hand—Improving control of prosthetic hands using tactile sensors and realistic machine learning, DFG Sachbeihilfe CA1389/1-1.

Conflicts of Interest: The authors declare no conflict of interest.

Appendix A

Table A1. Relevant properties of target motion and average trajectory followed by the users (± standard deviation where applicable). All correlation coefficients have p coefficients far smaller than 0.0001.

Measurement [unit]	IS-60%	IS-100%	CT-60%	CT-100%	VT-40%	VT-80%	ALL
Dynamic tests							
$\mu\left(\lVert\vec{e}\rVert\right)$ [cm]	5.365 ± 1.405	7.935 ± 2.277	5.311 ± 1.865	8.148 ± 3.315	5.061 ± 2.954	8.904 ± 5.824	6.325 ± 3.248
$\mu\left(e_{\parallel}\right)$ [cm]	4.051 ± 1.698	6.766 ± 2.490	3.547 ± 1.932	6.038 ± 3.773	3.399 ± 2.891	6.398 ± 5.630	4.684 ± 3.263
$\mu(e_{\perp})$ [cm]	3.472 ± 0.738	4.369 ± 0.954	3.842 ± 1.167	5.287 ± 1.849	3.458 ± 1.371	5.620 ± 2.852	4.066 ± 4.684
$\mu\left(\lVert\vec{v}\rVert\right)$ [cm]	23.108 ± 6.290	38.664 ± 9.101	18.666 ± 9.449	31.741 ± 14.592	15.091 ±1 1.169	30.743 ± 20.530	24.679 ± 13.957
$\mu\left(\lVert\vec{a}\rVert\right)$ [cm/s^2]	33.236 ± 15.830	76.585 ± 30.815	32.333 ± 18.495	78.750 ± 40.265	28.313 ± 28.616	87.285 ± 80.367	48.731 ± 42.854
Corr($\lVert\vec{v}\rVert$, $e_{\parallel}$) []	0.522	0.626	0.763	0.773	0.773	0.685	0.752
Corr(,$\lVert\vec{a}\rVert$ $e_{\perp}$) []	0.050	0.332	0.503	0.534	0.629	0.764	0.679

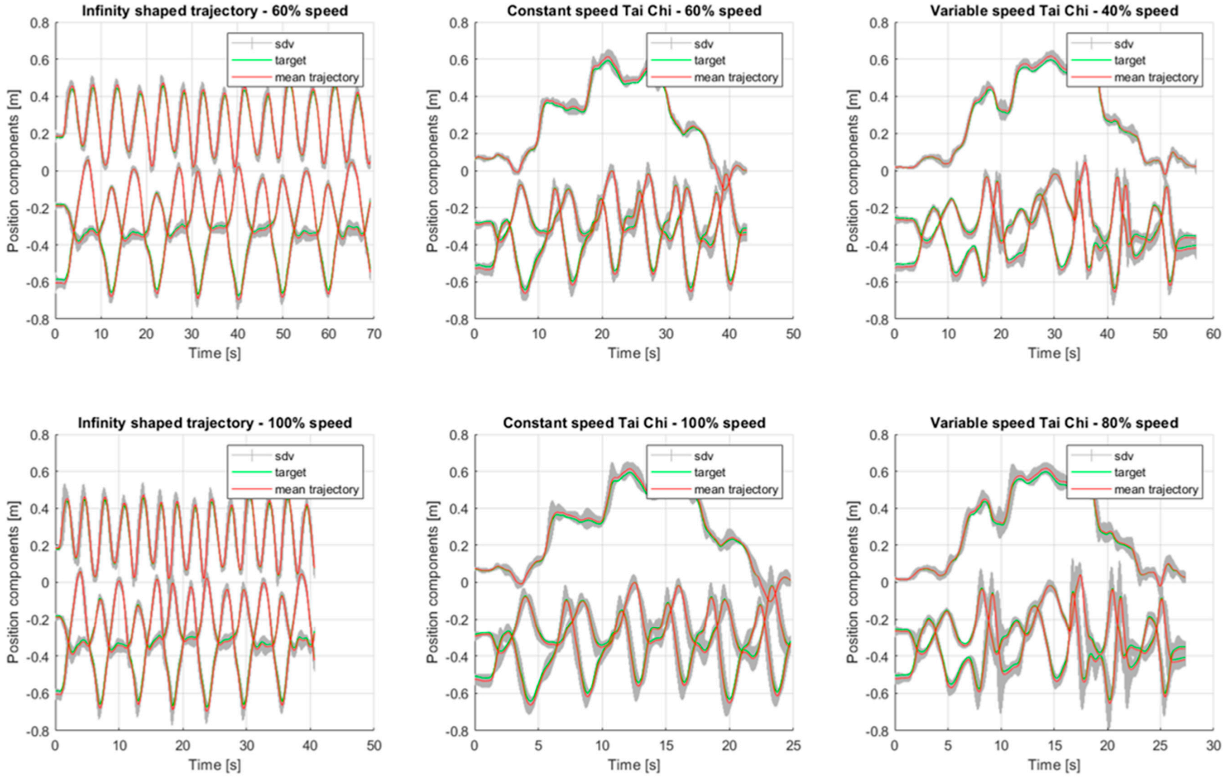

Figure A1. Average over all subjects and repetitions with standard deviation and target position.

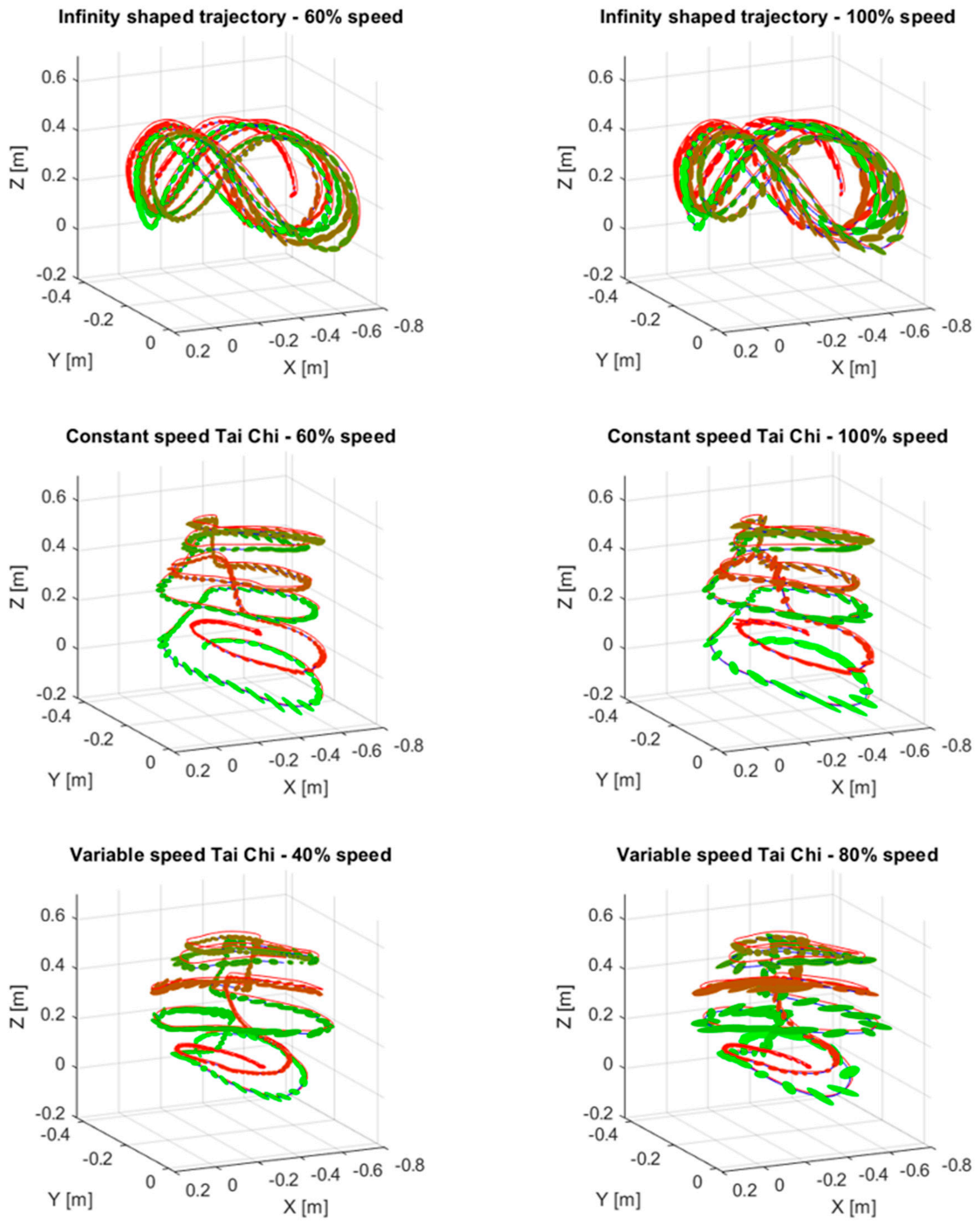

Figure A2. Trajectory with error ellipsoids. The color shifts from red to green over time during target's movement.

References

1. Fougner, A.; Stavdahl, O.; Kyberd, P.J.; Losier, Y.G.; Parker, P.A. Control of Upper Limb Prostheses: Terminology and Proportional Myoelectric Control—A Review. *IEEE Trans. Neural Syst. Rehabil. Eng.* **2012**, *20*, 663–677. [CrossRef] [PubMed]
2. Castellini, C.; Artemiadis, P.; Wininger, M.; Ajoudani, A.; Alimusaj, M.; Bicchi, A.; Caputo, B.; Craelius, W.; Došen, S.; Englehart, K.; et al. Proceedings of the first workshop on Peripheral Machine Interfaces: Going beyond traditional surface electromyography. *Front. Neurorobotics* **2014**, *8*. [CrossRef] [PubMed]

3. Merletti, R.; Parker, P.A. *Electromyography: Physiology, Engineering, and Noninvasive Applications*; John Wiley & Sons: Hoboken, NJ, USA, 2004.
4. Zecca, M.; Micera, S.; Carrozza, M.C.; Dario, P. Control of multifunctional prosthetic hands by processing the electromyographic signal. *Crit. Rev. Biomed. Eng.* **2002**, *30*, 459–485. [CrossRef] [PubMed]
5. Ison, M.; Artemiadis, P. The role of muscle synergies in myoelectric control: Trends and challenges for simultaneous multifunction control. *J. Neural Eng.* **2014**, *11*, 51001. [CrossRef] [PubMed]
6. Jiang, N.; Dosen, S.; Müller, K.-R.; Farina, D. Myoelectric Control of Artificial Limbs—Is There a Need to Change Focus? *IEEE Signal Process. Mag.* **2012**, *29*, 148–152. [CrossRef]
7. Cho, E.; Chen, R.; Merhi, L.-K.; Xiao, Z.; Pousett, B.; Menon, C. Force Myography to Control Robotic Upper Extremity Prostheses: A Feasibility Study. *Front. Bioeng. Biotechnol.* **2016**, *4*, 608. [CrossRef] [PubMed]
8. Fang, Y.; Hettiarachchi, N.; Zhou, D.; Liu, H. Multi-Modal Sensing Techniques for Interfacing Hand Prostheses: A Review. *IEEE Sens. J.* **2015**, *15*, 6065–6076. [CrossRef]
9. Fougner, A.; Scheme, E.; Chan, A.D.C.; Englehart, K.; Stavdahl, Ø. Resolving the Limb Position Effect in Myoelectric Pattern Recognition. *IEEE Trans. Neural Syst. Rehabil. Eng.* **2011**, *19*, 644–651. [CrossRef] [PubMed]
10. Jiang, N.; Vujaklija, I.; Rehbaum, H.; Graimann, B.; Farina, D. Is Accurate Mapping of EMG Signals on Kinematics Needed for Precise Online Myoelectric Control? *IEEE Trans. Neural Syst. Rehabil. Eng.* **2013**, *22*, 549–558. [CrossRef] [PubMed]
11. Miotto, R.; Danieletto, M.; Scelza, J.R.; Kidd, B.A.; Dudley, J.T. Reflecting Health: Smart Mirrors for Personalized Medicine. *NPJ Digit. Med.* **2018**, *1*, 62. [CrossRef] [PubMed]
12. Robert Bosch GmbH, BNO055 Inertial Measurement Unit by Bosch. Available online: https://www.bosch-sensortec.com/bst/products/all_products/bno055 (accessed on 14 January 2020).
13. Xsens Technologies B.V. MVN Animate. Available online: https://www.xsens.com/products/mvn-animate (accessed on 14 January 2020).
14. Liang, Z.; Xu, X.; Zhou, S. The smallest target size for a comfortable pointing in freehand space: Human pointing precision of freehand interaction. *Univers. Access Inf. Soc.* **2017**, *16*, 381–393. [CrossRef]
15. Öhberg, F.; Bäcklund, T.; Sundström, N.; Grip, H. Portable Sensors Add Reliable Kinematic Measures to the Assessment of Upper Extremity Function. *Sensors* **2019**, *19*, 1241. [CrossRef]
16. Nordic Semiconductor, nRF52832 Product Specification v1.4. Available online: https://infocenter.nordicsemi.com/pdf/nRF52832_PS_v1.4.pdf (accessed on 6 February 2020).
17. Adafruit Industries, Bluefruit nRF52 Feather Learning Guide. Available online: https://cdn-learn.adafruit.com/downloads/pdf/bluefruit-nrf52-feather-learning-guide.pdf? (accessed on 6 February 2020).
18. Nordic Semiconductor, UART/Serial Port Emulation over BLE. 2019. Available online: https://infocenter.nordicsemi.com/index.jsp?topic=%2Fcom.nordic.infocenter.sdk5.v15.0.0%2Fble_sdk_app_nus_eval.html (accessed on 6 February 2020).
19. Microchip Technology Inc., RN41 Datasheet. Available online: http://ww1.microchip.com/downloads/en/DeviceDoc/50002280A.pdf (accessed on 29 October 2019).
20. High Tech Computer Corporation, HTC VIVE User Guide. Available online: https://www.htc.com/managed-assets/shared/desktop/vive/Vive_PRE_User_Guide.pdf (accessed on 6 February 2020).
21. Niehorster, D.C.; Li, L.; Lappe, M. The accuracy and precision of position and orientation tracking in the HTC vive virtual reality system for scientific research. *i-Percept.* **2017**, *8*. [CrossRef]
22. Borges, M.; Symington, A.; Coltin, B.; Smith, T.; Ventura, R. HTC Vive: Analysis and Accuracy Improvement. In Proceedings of the IEEE/RSJ International Conference on Intelligent Robots and Systems (IROS), Madrid, Spain, 1–5 October 2018.
23. Roetenberg, D.; Luinge, H.; Slycke, P. Xsens mvn: Full 6dof Human Motion Tracking Using Miniature Inertial Sensors. 2009. Available online: https://www.researchgate.net/publication/239920367_Xsens_MVN_Full_6DOF_human_motion_tracking_using_miniature_inertial_sensors (accessed on 6 February 2020).
24. Brooke, J. SUS-A quick and dirty usability scale. In *Usability Evaluation in Industry*; CRC Press: Boca Raton, FL, USA, 1996; pp. 4–7.

25. Marder, E.; Bucher, D. Central pattern generators and the control of rhythmic movements. *Curr. Biol.* **2001**, *11*, R986–R996. [CrossRef]
26. Lin, Z.; Xiong, Y.; Dai, H.; Xia, X. An experimental performance evaluation of the orientation accuracy of four nine-axis MEMS motion sensors. In Proceedings of the 2017 5th International Conference on Enterprise Systems (ES), Beijing, China, 22–24 September 2017.

A.2 The MyoGlove grasp-assisting device

Title: EMG-driven Machine Learning Control of a Soft Glove for Grasping Assistance and Rehabilitation

Authors: Marek Sierotowicz, Nicola Lotti, Laura Nell, Francesco Missiroli, Ryan Alicea, Xiaohui Zhang, Michele Xiloyannis, Rüdiger Rupp, Emese Papp, Jens Krzywinski, Claudio Castellini and Lorenzo Masia

Journal: Robotics and Automation Letters

Publisher: IEEE

Manuscript version: Accepted article

Review: Peer-reviewed

Copyright: © 2021 by IEEE. Reprinted, with permission, from Marek Sierotowicz, Nicola Lotti, Laura Nell, Francesco Missiroli, Ryan Alicea, Xiaohui Zhang, Michele Xiloyannis, Rüdiger Rupp, Emese Papp, Jens Krzywinski, Claudio Castellini and Lorenzo Masia, EMG-driven Machine Learning Control of a Soft Glove for Grasping Assistance and Rehabilitation, IEEE Robotics and Automation Letters, 2021.

Citation: M. Sierotowicz, N. Lotti, L. Nell, et al. "EMG-driven machine learning control of a soft glove for grasping assistance and rehabilitation." In: *IEEE Robotics and Automation Letters* 7.2 (2022), pp. 1566–1573. ISSN: 2377-3766. DOI: `10.1109/LRA.2021.3140055`

Abstract: In the field of rehabilitation robotics, transparent, precise and intuitive control of hand exoskeletons still represents a substantial challenge. In particular, the use of compliant systems often leads to a trade-off between lightness and material flexibility, and control precision. In this letter, we present a compliant, actuated glove with a control scheme to detect the user's motion intent, which is estimated by a machine learning algorithm based on muscle activity. Six healthy study participants used the glove in three assistance conditions during a force reaching task. The results suggest that active assistance from the glove can aid the user, reducing the muscular activity needed to attain a medium-high grasp force, and that closed-loop control of a compliant assistive glove can successfully be implemented by means of a machine learning algorithm.

Author contributions: Conceptualization; Software Design; Formal analysis; Writing-original draft; Writing-review and editing.

EMG-driven Machine Learning Control of a Soft Glove for Grasping Assistance and Rehabilitation.

Marek Sierotowicz[1†*], Nicola Lotti[2†], Laura Nell[2], Francesco Missiroli[2], Ryan Alicea[2], Xiaohui Zhang[2], Michele Xiloyannis[3], Rüdiger Rupp[4], Emese Papp[5], Jens Krzywinski[5], Claudio Castellini[1‡] and Lorenzo Masia[2‡]

Abstract— **In the field of rehabilitation robotics, transparent, precise and intuitive control of hand exoskeletons still represents a substantial challenge. In particular, the use of compliant systems often leads to a trade-off between lightness and material flexibility, and control precision. In this paper, we present a compliant, actuated glove with a control scheme to detect the user's motion intent, which is estimated by a machine learning algorithm based on muscle activity. Six healthy study participants used the glove in three assistance conditions during a force reaching task. The results suggest that active assistance from the glove can aid the user, reducing the muscular activity needed to attain a medium-high grasp force, and that closed-loop control of a compliant assistive glove can successfully be implemented by means of a machine learning algorithm.**

I. INTRODUCTION

One of the most visionary philosophers of the current century stated that without our hands *"...we are, are we not, nothing but naked apes..."* [1]: indeed, this complex of multi-joint articulations is crucial to perform most tasks of daily living [2]. Moreover, the hands play a very important role in non-verbal communication.

Unfortunately, neuromuscular diseases and traumatic events that impair manipulation skills have significant incidence rates, and can dramatically worsen the quality of life for affected people [3]. When the technology reached a sufficient level of maturity, wearable robotics entered the stage to help people with motor impairments in restoring or compensating for lost motor functions [4]: in particular, the introduction of soft materials in these actuated devices enhanced the human-machine interaction with promising results in the rehabilitation realm [5], [6], [7].

Most of the soft actuated gloves present in literature are controlled based on intent detection algorithms, but many aspects are still challenging [8]: the most common approach is based on motor synergy analysis, which can simplify the otherwise prohibitively complex mapping of muscle activity to primary postural tasks [9]. This is done by identifying specific patterns in brain activity [10], [11] or neuromuscular signals [12], [13], [14], [15]. The latter approach has been further developed by Polygerinos and colleagues, who introduced a control based on surface electromyography (sEMG) of a pneumatic system [16]: the open-loop sEMG logic classified gross muscle contractions responsible for flexion and extension and fed the information to a low-level fluid pressure controller which regulated the pressure simultaneously in all actuators of a pre-selected group. Another example can be found in Bos et al. [17], who developed the sEMG-based control algorithm for the SymbiHand: the muscle activity was mapped into a grasping force and served as input for the actuation stage.

In prosthetic control, and generally when controlling hand-emulating robotics by means of sEMG, machine learning (ML) has been used with a good rate of success [18], [19], [20]. The main advantage of such predictive algorithms is the fact that they do not require explicit mapping of muscle activity to hand movement or posture, and that they can fit each individual user. The main disadvantage is the computational cost that these algorithms can require, especially during training, and the fact that they sometimes have unpredictable responses, especially when the user deviates from the conditions present during training. An example is the so-called limb position effect, which describes changes in muscular activity associated to a single hand posture when the upper limbs assume different postures and consequently muscle recruitment varies [21]. These downsides represent the main obstacles for the use of these control systems outside of clinical settings. Nevertheless, solutions have been proposed, which, while using very simple machine learning algorithms, still allow for robust control of prosthetic devices [22].

In our previous study [23] we demonstrated how an open-loop kinematic synergy-based control in combination with a soft assisting glove can provide assistance in the presence of grasp weakness. Starting from our previous work regarding both the topic of exosuits and ML-based prosthetic control,

---

Manuscript received: September 9th, 2021; Revised: November 29th, 2021; Accepted: December 27th, 2021. This paper was recommended for publication by Editor Jee-Hwan Ryu upon evaluation of the Associate Editor and Reviewers' comments.

† M. Sierotowicz and N. Lotti equally contributed to this work.

‡ L. Masia and C. Castellini equally contibuted to this work.

[1] M. Sierotowicz and C. Castellini are with the Institute of Robotics and Mechatronics, German Aerospace Center (DLR), 82234 Wessling, Germany and with the Department of Artificial Intelligence in Biomedical Engineering (AIBE), Friedrich-Alexander-Universität Erlangen-Nürnberg (FAU), 91052 Erlangen, Germany.

[2] N. Lotti, L. Nell, F. Missiroli, R. Alicea, X. Zhang and L. Masia are with the Institute for Technical Informatics (ZITI), Heidelberg University, 69120 Heidelberg, Germany.

[3] M. Xiloyannis is with the Institute of Robotics and Intelligent Systems, ETH Zürich, Zürich, 8092, Switzerland.

[4] R. Rupp is with the the Spinal Cord Injury Center of Heidelberg University Hospital, 69120 Heidelberg, Germany.

[5] E. Papp and J. Krzywinski are with the Chair of Industrial Design Engineering, Technical University of Dresden, 01062 Dresden, Germany.

* corresponding author, `marek.sierotowicz@dlr.de`

Digital Object Identifier (DOI): see top of this page.

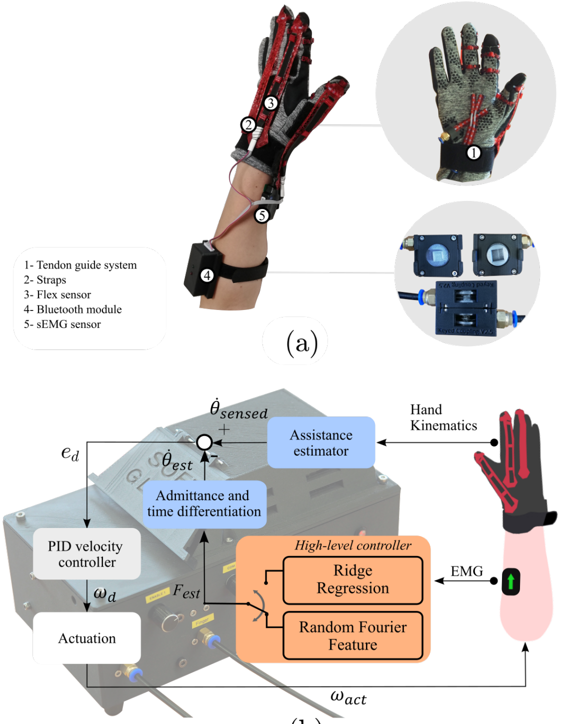

(a)

(b)

Fig. 1. *MyoGlove design and control.* **a**: the presented prototype actively assists hand grasping by means of tendon-driven actuators (1) lodged in the driver's stage. Hand opening is passively aided by three 3D printed elastic straps integrated in the glove (2). Hand movements are sensed by means of two flex sensors connected to a Bluetooth data collection module measuring overall thumb and index flexion/extension (3-4). The motion intent is estimated by means of sEMG (5). A magnetic clutch has been developed in order to allow for quick (de)coupling of the glove from the driver stage allowing for quick adjustments to the user's hand size (visible in the lower right corner of **a**). **b**: block diagram depicting the control architecture of the MyoGlove. The high-level controller aims to estimate the intended grasping force through a ridge regression or a random Fourier features algorithm. This estimate is then converted to an intended displacement through the admittance of the handle device. The first time derivative of the displacement is used as set-point and compared with the angular velocity measurement of the flex sensors in the low-level PID controller which translates the tracking error into a motor angular velocity, which is finally converted into an actuation command.

here we combine, for the first time, a soft wearable glove with a user's motion intent detection based on machine learning approaches enrolled in a closed-loop architecture. The device is characterized by means of a rehabilitative apparatus that includes a haptic handle device for grasping training. We investigate, by comparing two different machine learning algorithms, the kinematic and physiological effects of the glove in a cohort of six healthy users, in a repeated-measures study design. The machine learning algorithms used in this study had already found ample use in our previous work on the control of rigid prosthetic devices [22]. The results provide initial indicators for the usability of this apparatus in rehabilitation for task-oriented restorative training.

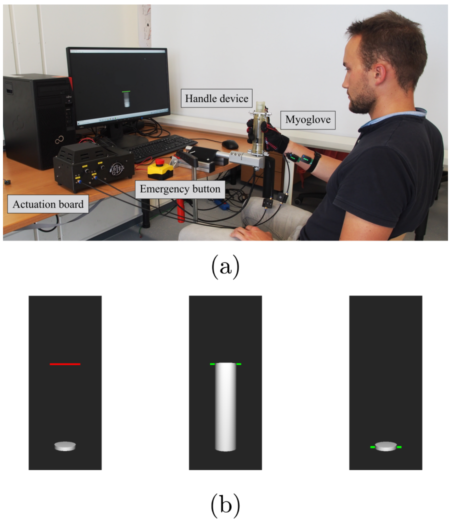

(a)

(b)

Fig. 2. *Setup and task description.* **a**: experimental setup with a participant. **b**: screenshots representing the task as shown to the user over the GUI. The red line highlights the target force to be reached. When the participant exerts a level of force within the threshold from the target, the line is highlighted in green, and subsequently reset to the starting level.

II. MYOGLOVE DESIGN

The control algorithm has been tested on a two degrees of actuation glove able to assist flexion of index and middle finger, and flexion of the thumb, respectively, by means of a tendon-driven system (Fig. 1a). The tendons are routed at the palm of the hand using a sewn-on guiding system, consisting of Teflon tubes held in place by 3D-printed parts. These lead the tendons around the fingertips of the assisted fingers in order to get a better distributed pulling force, to end up in a Bowden cable system (Shimano, SLR, $\varnothing 4\,\mathrm{mm}$, Sakai, Ōsaka, Japan), starting at the proximal end of the palm and terminating on a pulley lodged in a case which can be magnetically secured to a clutchable customized 3D-printed system (Fig. 1a). This design allows to easily connect gloves of different sizes to the actuation stage (visible in Fig 1b). Besides the active assistance of flexion movements, extension is passively aided through 3D-printed elastic straps mounted as shown in Fig. 1a. Whenever extension intent is sensed and the motors release the tendons, the straps assist the fingers in extending, acting as antagonistic muscles. Two flex sensors (Bend Labs, Salt Lake City, UT, USA) are attached to the straps at the index and thumb to detect their overall bending angle during flexion and providing position feedback to the low-level control loop. Two movements, namely flexion of the thumb and flexion of the fingers, are independently assisted by motors which pull and release the respective tendon cable. The actuation stage is placed in a custom-designed box (Fig. 1b and in Fig. 2 a), which contains the two brush-less electric motors (T-Motor 6007,Nanchang, Jiangxi, China), the motor driver unit (ODrive v3.6, ODrive robotics, San Jose, CA, USA), and the electronics needed for data processing and transmission. The communication with the motors is handled by an Arduino Mega 2560 (Arduino, Ivrea, Italy), which also receives the data from the flex sensors using Bluetooth low-energy protocol through dedicated boards (nRF52832 Bluefruit Feather, Adafruit, New York, NY, USA) and furthermore hosts the low-level control loop. The high-level control model, implemented using Matlab/Simulink environment (MathWorks, Natick, Massachusetts MA, USA), runs on a Nvidia Jetson Nano board which receives and processes the EMG data and sends back the calculated motor commands to the Arduino, which forwards them to the motor drive unit using serial protocol. Muscular activity is measured by means of two sEMG sensors (Delsys Trigno, Natick MA, USA) placed on the flexor digitorum (FD) and the abductor pollicis brevis (APB) muscles, by following the SENIAM guidelines [24].

III. REAL-TIME CONTROL ARCHITECTURE

In the present work, besides characterizing the system, we also aimed at comparing the performance of the two main intent estimators, which are both based on machine learning. For the sake of clarity, the two approaches worked in a mutually exclusive manner, being tested separately and across distinct trials, but being used by all participants.

As depicted in Fig. 1b, the architecture comprised a high-level controller, based on one of the two approaches (selected prior to test initiation), which estimated the motion intent and thus computed the set-point for the low-level admittance controller. This last layer was used in both conditions and was implemented to track the reference signal and convert it into a motor actuation command closing the loop on the flex sensors measurements (100Hz, LP filter at 10Hz).

A. High-level control layer: machine learning-based estimation

The two intent estimators consisted of a non-kernelized *ridge regression* algorithm applied directly to the filtered sEMG envelopes (sampled at 2kHz, BP filtered between 35Hz and 350Hz, rectified, LP filtered at 4Hz), and in a *random Fourier features* kernelized algorithm, respectively. Both the approaches aimed to estimate a grasping force (F_{est} in Fig. 1b). This was then converted into a finger displacement θ_{est} through an admittance consisting of a task-specific compliance determined by the the handle device. This displacement θ_{est} was fed as input to the low-level controller after first order time differentiation, as described in Sec. III-B and shown in Fig. 1b.

1) Ridge regression algorithm: ridge regression (*RR*) is among the most fundamental algorithms used in machine learning [25]. It has computational complexity of $\mathcal{O}(DC)$ (D and C being the number of observed features and the number of output channels, respectively) for the prediction step and, being a linear model, it is typically not prone to overfitting. The necessity to work with a matrix with a dimension equal to the number of observations at training time represents the main computational cost for this algorithm, which is $\mathcal{O}(D^3 + D^2N)$ at training time (N being the number of observations, and typically $N \gg D$). However, this operation can be carried out incrementally by means of the Sherman-Morrison formula [22] [26] thus reducing the overall complexity at training to $\mathcal{O}(D^2)$ for every new observed sample. This can be especially useful for higher dimensionality D, which can be necessary when applying a higher-dimensional kernel mapping. (see section III-A.2). The Sherman-Morrison formula enables an efficient implementation of incremental learning, where the predictor can efficiently integrate new data into the design matrix, thus enabling the user to adjust to changing conditions which might influence the prediction, such as varying levels of perspiration or fatigue.

2) Random Fourier Features algorithm: Random Fourier features (*RFF*) make it possible to add an approximated radial basis function kernel without losing the incremental character of non-kernelized *RR* [27], [28]. A kernel allows the model to better adapt to non-linearities and has been shown to offer better performance in prosthesis control when training a model to identify forces on multiple degrees of freedom [22]. On the other hand, it is more prone to overfitting if its hyperparameters are not suitably tuned. Furthermore, it entails an increase in feature dimensionality, meaning that D increases.

B. Low-level controller: position-velocity loop

As the low compliance from the cables made it difficult to open one's hand once a grasp was achieved, the control was closed around the error in the first time derivative of the finger flexion angle $\dot{\theta}$.

The actuation to the glove is thus controlled in a closed loop around the error between the desired set-point $\dot{\theta}_{est}$ provided by the machine learning algorithm through the known admittance of the handle device and the measurements from the flex sensors $\dot{\theta}_{sensed}$ normalized through a calibration procedure. The resulting instantaneous velocity tracking error $e_d = \dot{\theta}_{sensed} - \dot{\theta}_{est}$ is transformed into a desired angular velocity, ω_d, through a PID block of the form:

$$Y(s) = \frac{\omega_d}{e_d} = \frac{K_p + K_i \cdot s^{-1}}{1 + K_d \cdot s} \qquad (1)$$

where the K_p, K_i and K_d gains were experimentally tuned, using the Ziegler-Nichols heuristic method [29], prior to the study and then left unchanged for all participants.

As mentioned above, in order to calculate the error e_d, the grasp force estimation from the machine learning algorithm and the bending sensor feed were projected onto a common space through an admittance (or compliance) gain and a normalizing factor, respectively, as illustrated in Fig. 1 b. The normalizing factor was obtained during a calibration procedure prior to session start during which the experimenters gathered the values output by the flex sensors while the user had their hand open and closed. The admittance, on the other hand, is fixed as the inverse of the handle's impedance, as explained in Section IV-A. Both signals were then differentiated over time before being fed to the aforementioned PID motor controller.

IV. EXPERIMENTAL SETUP AND PROTOCOL

Six healthy participants were enrolled in the experiment (4 males/2 females, age 26.17 ± 1.33 years, body weight $80.33 \pm 13.29\,\mathrm{kg}$ and height $1.80 \pm 0.11\,\mathrm{m}$, mean ± sd). Inclusion criteria were based on no evidence or known history of musculoskeletal or neurological diseases, and exhibiting normal joint range of motion and muscle strength. All experimental procedures were carried out in accordance with the Declaration of Helsinki on research involving human subjects and were approved by the IRB board of Heidelberg University (Nr. S-311/2020). All subjects provided written informed consent to participate in the study.

A. Apparatus

In order to test the *MyoGlove* controllers' performance, we developed a customized setup that could be used in future studies for rehabilitation treatments: we combined the device with an actuated hand module [30] aimed to provide haptic feedback (Fig. 2a, handle device). An impedance controller was implemented in order to generate a constant-compliance force field during grasping. The handle's force F^h is related to the finger and manipulandum displacement according to the following equation,

$$F^h = K\Delta r = C^{-1}\Delta r \tag{2}$$

where $K = 1\,\mathrm{kN/m}$ is the stiffness gain and Δr is the handle displacement, obtained from the outer and inner rotors, as reported in [30], C is the compliance gain, which corresponds to the inverse of the stiffness gain. All of the gains were assumed to be constant in this experiment.

A DAQ board (Quanser QPIDe, Markham, Ontario, Canada) mounted on a dedicated desktop workstation was used to control the handle device and acquire all its signals, with a sampling frequency of $1\,\mathrm{kHz}$ (Fig. 2a). The workstation provided visual feedback to the user.

B. High-level controller calibration

Before starting the experiment, both high-level control algorithms (i.e. *ridge regression* and *random Fourier features*) were trained on a common dataset acquired during a separate round which also served for familiarization. This dataset is specific to each user and electrode placement, and therefore the acquisition round took place immediately prior to the session proper. During the acquisition, participants had to follow a visually fed back preset force profile by grasping the handle device (Fig. 2b). The force profile was then used to associate target labels $F^h \in \{0\,\mathrm{N}, 5\,\mathrm{N}, 10\,\mathrm{N}, 15\,\mathrm{N}\}$ to the acquired sEMG envelope signals in order to train the two machine learning algorithms.

The algorithms were each trained on a set of measurements from the two EMG probes (therefore each observation had 2 features) acquired at a rate of $1\,\mathrm{kHz}$ over a time of $10\,\mathrm{s}$ per label, with 5 repetitions, for a total of ca. 50000 samples per target force. The prediction was verified in terms of correlation of the estimated applied force against the target force level, and if needed, data acquisition was repeated, until the output results showed good correlation with the force profile and no apparent noise due to overfitting. The main source of errors in the prediction at this stage was bad placement of the EMG probes, which, if found, was corrected.

Both RR and RFF have a deterministic closed form solution. Furthermore, the main purpose of the implementations of RR and RFF we use is to facilitate incremental learning, which is to say that the user should be able to easily and efficiently add new samples on the fly in order to obtain better generalization. To this end, the algorithm's hyperparameters are to remain constant throughout usage [22]. These were set experimentally prior to the main experiments. Therefore, two of the experimenters tested the algorithms with different values for the hyperparameters and selected the ones which gave the better results in terms of generalization. As all hyperparameters were preset and the algorithm's optimization is deterministic, no validation round was conducted prior to the individual experimental sessions.

C. Comparison task

The main test consisted in a repeated-measure force reaching task in which participants, wearing the glove, were prompted by a GUI to reach four different isometric grasp force steps ($F^h \in \{0\,\mathrm{N}, 5\,\mathrm{N}, 10\,\mathrm{N}, 15\,\mathrm{N}\}$), grasping the handle device (Fig. 2a).

The participants' grasping force was visualized in the monitor as a white bar, which changed according to the force level. The target force step, instead, was represented via a horizontal line that changed color based on the condition (Fig. 2b): when the user was in the *rest* condition (i.e. $F^h = 0\,\mathrm{N}$), a new target force, displayed as a red line (Fig. 2b, left), appeared on a predefined level of the screen based on desired force intensity. Participants had to increase their grasp force on the handle device until the desired level was reached: once it was reached, the line changed its color from red to green (Fig. 2b, centre) and the grasp force had to be maintained for $2\,\mathrm{s}$. After this, the red line returned to the rest condition (i.e. $F^h = 0\,\mathrm{N}$) and participants were instructed to relax for $2\,\mathrm{s}$, until a new force target appeared (Fig. 2b, right). The whole sequence of force step was repeated a total of 5 times for each non-zero target force value.

The task was repeated in three different conditions: (i) without providing glove assistance (i.e. *NA* condition), (ii) with the *ridge regression* algorithm (i.e. *RR*) and (iii) with the *random Fourier feature* algorithm (i.e. *RFF*). The sequence of force steps and conditions were randomized for each participant and condition in order to account for order effects (fatigue, learning), when averaging across participants.

V. DATA ANALYSIS

Offline analysis was performed to evaluate participants performance under active assistance (RR and RFF) compared to the *NA* condition. Outcome measures included prediction accuracy, motor actuation response, and changes of muscular activities. Furthermore, the performances of the *RR* and *RFF* algorithms were directly compared in terms of R^2 score and Root Mean Square Error (RMSE). We used an external trigger to synchronize the DAQ board and the glove control unit during data processing and analysis.

A. Prediction accuracy

In order to quantify the controllers' reliability in estimating the force at the end-effector, we compared the grasping force performed during *NA* condition with the *RR* and *RFF* offline predictions using the EMG data acquired during the trial as input. We evaluated the correlation coefficient R^2 and RMSE between the measured and the predicted force levels from the early onset of the grasp movement until the end of the holding phase.

B. Motor actuation response

In order to evaluate the system's response time, we employed cross-correlation between the recorded sEMG envelope and the motor response recorded through the motor's positional encoder when the participant started applying the force necessary to reach the target grasp force.

C. Changes in muscular activity

Electromyographic signals of APB and FD were post-processed offline through a band-pass filtering (35 Hz-350 Hz) with a second-order Butterworth filter, full wave rectification, a low-pass filtering (4 Hz, second-order Butterworth filter) and normalized to the highest value of each participant during the whole experiment (i.e. MaxEMG).

We then used the root mean square (RMS) of the sEMG envelope as index of activation level across force steps (i.e. 5 N, 10 N and 15 N) and assistance conditions (i.e. *NA*, *RR*, *RFF*).

D. Statistical analysis

Data normality distribution was assessed using Shapiro-Wilk test, and sphericity condition for repeated measures analysis of variance (rmANOVA) was assessed using the Mauchly test. The rmANOVA test was used to examine the effects on the dependent variables of the assistance type, using it as within-subject factor (it can assume one out of 3 levels: *NA*, *RR*, *RFF*). A post-hoc analysis was performed using paired t-tests to evaluate the significant pairwise differences between each type of assistance for the different force steps (3 levels of F^h: $5\,\mathrm{N}, 10\,\mathrm{N}, 15\,\mathrm{N}$). For all the tests, the level of statistical significance was set at 0.05, except for post-hoc analysis, where the significance level was chosen according to the Bonferroni correction for multiple comparisons.

VI. RESULTS

A. Both controllers have a good prediction accuracy

The first outcome metrics have the purpose of evaluating the performance of the two controllers in terms of motion intent prediction: Fig. 3a shows the mean R^2 coefficients over model and target force. The R^2 scores average overall was 0.8009 ± 0.1665 for the *RR* condition and 0.7303 ± 0.2295 for the *RFF* condition, respectively.

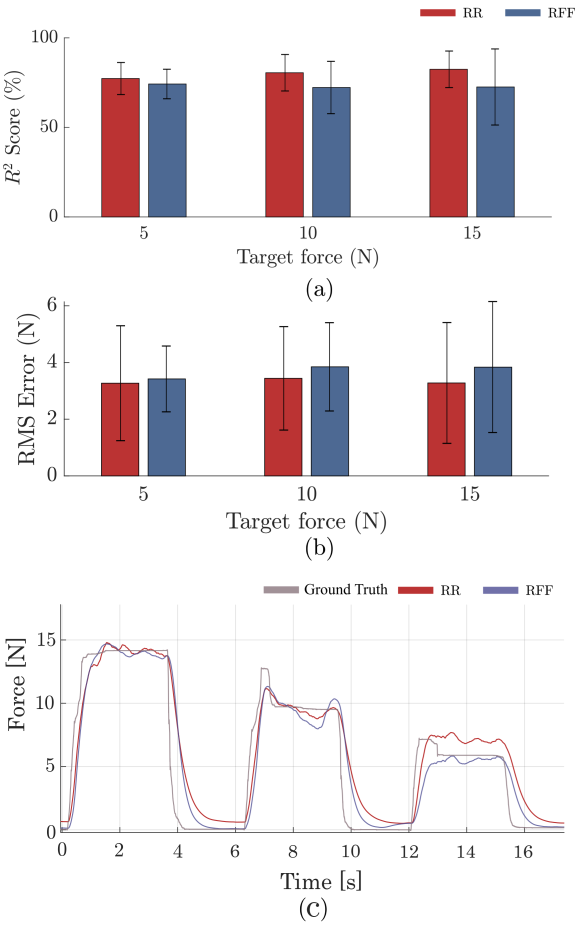

(a)
(b)
(c)

Fig. 3. **a**: R^2 values for *RR* and *RFF*. **b**: RMS Error w.r.t. the measured force. **c**: representative grasp force prediction vs. measured grasp force.

It is however worth mentioning that the R^2 score computed between the EMG envelopes and the actually produced force shows comparable values (0.7848 ± 0.1684).

The Root Mean Square Error (RMSE) was calculated over the same motion phases. Fig. 3b shows its values over model and target force. Overall, RMSE was 3.3293±1.9771 N for the *RR* condition and 3.7010±1.7328 N for the *RFF* condition.

Fig. 3c shows a representative plot of grasp prediciton vs. the actually measured force at the handle. A noteworthy effect is that, in certain portions of the plot where the measured force does not appear to change, both predictions show noticeable instability (for example between 8 s and 10 s). The most obvious explanation for this effect is the presence of static frictions in the handle device, which would cause the mechanism to remain static even if the force applied by the user's muscles changes somewhat. This is, of course, a potential source of RMS error.

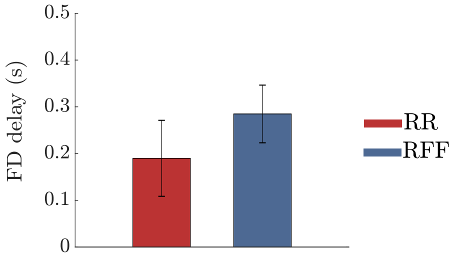

Fig. 4. Motor actuation delay across all subjects.

B. The system shows an overall small delay

The time between the neuromuscular signal and the motor actuation is an important metric related to the system's reactivity. Because the control loop does not explicitly map the APB sEMG with the thumb motor or the FD sEMG with the finger motor, cross correlation was computed for all four possible sensor-motor correlation, and only the smallest delay was considered, operating on the assumption that the motor moving was caused by the nearest increase in muscle activity. Apparently non-causal behavior was excluded from the calculation. Fig. 4 depicts the results of the cross-correlation between the muscle activities and the corresponding motor's encoder. No significant difference was found between the two controllers: during the *RR* assistance the delay between the FD and its motor we found a delay of 190±87 ms.

During the *RFF* assistance, the delay was 285±92 ms for the FD activity.

C. Both controllers reduce human muscular effort during middle-high force levels of grasping

Fig. 5a shows the reaching task time-series of a representative subject, averaged across the repetitions of each force step: by looking at the APB muscle, it is possible to notice that the muscular effort is reduced, especially during the first 25% of the movement, when the participant initiates the reaching. The *RFF* algorithm assists more than the *RR*, which seems to follow the *NA* trend, in particular during the 10 N and the 15 N force steps. The reduction results have been further confirmed by the statistical analysis ($F_{3,6} = 3.33$, $p = 0.011$) at the population level (Fig. 5b), in which we found a significant reduction between the normalized sEMG activity of the APB muscle during the *NA* condition (10 N= 20.3 ± 4.1 of % MaxEMG, mean± SE; 15 N= 19.8 ± 4.0%) and the two assistance conditions (*RR*: 10 N= 18.4 ± 3.4%, $p = 0.001$; 15 N= 18.6 ± 3.4%, $p < 0.001$. *RFF*: 10 N= 17.7 ± 3.8%, $p < 0.001$; 15 N= 17.4 ± 3.7%, $p < 0.001$.) No significant difference in measured muscle activity could be found while participants performed the 5 N force step trial, in which the APB activity was 19.4±4.0%, 18.8±3.5% and 17.5±3.7%, respectively for *NA*, *RR* and *RFF*. Furthermore, no statistical differences are presented between the two controllers in assisting the APB muscle. Similar trends can be observed by looking at the FD muscle (Fig. 5) in which we found significant difference between the no assistance condition and the two controllers ($F_{3,6} = 33.6$, $p < 0.005$) for the 10 N force step (*NA*=30.5 ± 6.2%; *RR*=23.3 ± 4.5%, $p < 0.001$; *RFF*=24.7 ± 4.6%, $p = 0.001$) and the 15 N force step (*NA*=31.0 ± 6.2%; *RR*=23.3 ± 4.3%, $p < 0.001$; *RFF*=24.9 ± 4.8%, $p < 0.001$). As in the case of the APB muscle, the two controllers provided the same assistance on the FD, and they did not show significant difference with the no assistance condition for the lowest force step (5 N), in which the FD activity was 30.2±5.8% during *NA* condition, 24.8±4.8% during the *RR* assistance and 26.3±5.1% during the *RFF*.

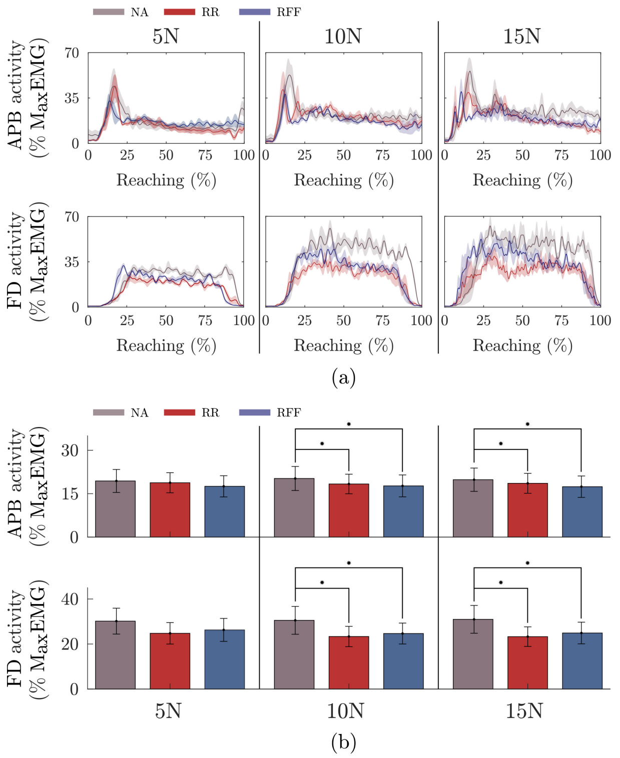

(a)

(b)

Fig. 5. *EMG analysis*. **a**: muscular activities of a typical participant during reaching task at different force steps, averaged across the five repetitions (mean ± sd): 5 N (left), 10 N (centre), and 15 N (right). Grey line represents NA condition, red and blue lines are respectively the trials performed during the assistance driven by the ridge regression (*RR*) and random Fourier feature (*RFF*) algorithms. **b** sEMG activity bar plot at the population level.

VII. DISCUSSION

Wearable technologies have always been challenged by a variety of problems which are not only related to hardware design and ergonomics but also to the difficulty in delivering assistance to replicate lost or impaired motor functions. Providing assist-as-needed during task oriented grasping training is a particularly great challenge due to both the complexity of the anatomical structures as well as the high dexterity that characterizes it and provides humans with unmatched manual abilities. Although many solutions have been proposed in terms of hardware design, state-of-the-art controllers still leave several questions unanswered. In our contribution, we specifically aimed at providing a viable option to control actuated devices for hand assistance: we propose a rehabilitation platform that combines an actuated soft glove driven by an intent detection system based upon machine learning applied to muscle activity and test it via a haptic handle device.

The work presents aspects of originality because it uses machine learning algorithms which are not merely classifying hand posture, but rather providing *a continuous estimation of the intended grasping force*, thus enabling the participant to precisely modulate the grasping interaction forces. While the mapping of EMG measurements to grasping forces through regression algorithms has been previously investigated [18][20], their use in compliant orthotic devices has never been explored in the past literature to the best of our knowledge. Our aim was to test the performance, considering two different machine learning approaches, as a first step towards assisted restorative grasping training. Both prediction algorithms show adequately accurate estimation of the exerted force, with no significant difference in their performance. This similarity is probably due to the fact that the EMG envelope shows a loose but inherent proportional relation to the grasping force. A more significant difference would likely be found if the systems were trained on more sEMG signals to operate a regression onto more assistance degrees of actuation. In such a case, the *RFF* algorithm could likely perform better, as it was shown in [22].

The two controllers did not show any significant difference in time response, with a delay between the sEMG onset and the motor actuation of about $0.2\,\mathrm{s}$: the importance of promptness in dynamic response is paramount in wearable devices in order to foster the wearer's sense of agency, which can be compromised in the presence of a delay between the user's motion intent (i.e. sEMG signals) and the device assistance. As demonstrated by Wen and colleagues [31], an action delay above $300\,\mathrm{ms}$ induces a lower sense of agency: a strong connection between the user and the robot, referred to as "embodiment", is a crucial aspect in clinical application, since it allows for more intuitive control [32] and most probably to better neuromotor recovery [33].

Both controllers reduced the activity of the two investigated muscles, APB and FD, during the middle (i.e. $10\,\mathrm{N}$) and high force steps (i.e. $15\,\mathrm{N}$): in particular, we saw higher reduction level ($\approx 50\%$) during the initial part of the task. This result further demonstrates the ability of the glove to react to the user's motion intent and to stabilize the hand in the desired force step. Should the glove's architecture remain unvaried, the ridge regression algorithm with no kernel would be preferable to RFF due to its reduced complexity and vulnerability to overfitting, and should be used in the future as the high-level controller.

Our study presents some limitations: the first one concerns the nature of the tested cohort of healthy participants, hence the performance of the two control schemes in people with upper extremity motor impairments is still an open question. Since in this preliminary work we focused on the feasibility of the platform, the next step will focus on testing such performances on patients (e.g. stroke or incomplete spinal cord injury) to clearly demonstrate that such approaches can be considered a viable option and concretely impact wearable assistive technology.

The second limitation concerns the soft glove: because the control loop takes as a setpoint the first time derivative of the machine learning-estimated desired hand closure, an overshoot of the target has often the effect of causing a release from the glove. This effect usually occurs when the muscle activity is not monotonically increasing during the reaching task, and it can thus be hard to prevent or predict. Integration of other low-level control architectures could be worth investigating. Finally, the lower reduction in muscular activity on the APB is likely due to the fact that the glove assists thumb flexion but not thumb abduction, which is normally performed when grasping a cylindrical object.

VIII. CONCLUSIONS

The human hand is a complex multi-joint system which enables the performance of a variety of tasks throughout our life: unfortunately, several diseases can affect its functionality. In the present work, we developed, for the first time, a demonstrator for a future rehabilitation platform that combines an EMG-driven machine learning soft glove with a haptic handle device aimed to restore grasping function through specific exercises. In this study we demonstrated a mostly compliant, closed-loop controlled actuated glove which can effectively use machine learning to provide assistance to a user during a force reaching task. While the effectiveness of the system was demonstrated in a scenario with a well-defined task-specific compliance matrix, its computation for an arbitrary task is a potentially nontrivial problem depending on the situation. Machine learning could provide the user with the possibility to easily switch between different levels of desired compliance by retraining the system, but an adequate integration of force or torque sensors in the glove design could bypass this problem while still allowing for closed-loop control. The training of the estimator may prove a non-trivial problem for users who are unable to achieve higher grasp forces. However, because the mapping is between muscular activity and intended forces, perhaps a recording procedure for impaired individuals could be envisioned, where the target is set to a higher level of compliance than during the testing tasks, with the assistive device bridging the gap. The main focus of the proposed intent estimators is incremental learning, rather than transfer learning. Ideally, training data should be gathered previous to all sessions from each user individually, and using another subject's data won't generally lead to good results.

REFERENCES

[1] T. R. Tallis, *Hand: A Philosophical Inquiry Into Human Being*. Edinburgh University Press, 2019.

[2] J. R. Napier, "The prehensile movements of the human hand," *The Journal of Bone and Joint Surgery. British volume*, vol. 38, no. 4, pp. 902–913, 1956.

[3] I. A. Trail and A. N. Fleming, *Disorders of the Hand*. Springer, 2015.

[4] C.-Y. Chu and R. M. Patterson, "Soft robotic devices for hand rehabilitation and assistance: a narrative review," *Journal of Neuroengineering and Rehabilitation*, vol. 15, no. 1, pp. 1–14, 2018.

[5] C. L. Jones, F. Wang, R. Morrison, N. Sarkar, and D. G. Kamper, "Design and development of the cable actuated finger exoskeleton for hand rehabilitation following stroke," *IEEE/Asme Transactions on Mechatronics*, vol. 19, no. 1, pp. 131–140, 2012.

[6] L. Cappello, J. T. Meyer, K. C. Galloway, J. D. Peisner, R. Granberry, D. A. Wagner, S. Engelhardt, S. Paganoni, and C. J. Walsh, "Assisting hand function after spinal cord injury with a fabric-based soft robotic glove," *Journal of Neuroengineering and Rehabilitation*, vol. 15, no. 1, pp. 1–10, 2018.

[7] K. Nuckols, C. J. Hohimer, C. Glover, D. S. de Lucena, W. Moyo, D. Wagner, A. Cloutier, D. J. Lin, and C. J. Walsh, "Effects of a soft robotic glove using a high repetition protocol in chronic stroke: a pilot study," in *2020 8th IEEE RAS/EMBS International Conference for Biomedical Robotics and Biomechatronics (BioRob)*. IEEE, 2020, pp. 428–433.

[8] M. Xiloyannis, R. Alicea, A.-M. Georgarakis, F. L. Haufe, P. Wolf, L. Masia, and R. Riener, "Soft robotic suits: State of the art, core technologies, and open challenges," *IEEE Transactions on Robotics*, pp. 1–20, 2021.

[9] M. Santello, M. Flanders, and J. F. Soechting, "Postural hand synergies for tool use," *Journal of Neuroscience*, vol. 18, no. 23, pp. 10 105–10 115, 1998.

[10] A. C. McConnell, M. Vallejo, R. C. Moioli, F. L. Brasil, N. Secciani, M. P. Nemitz, C. P. Riquart, D. W. Corne, P. A. Vargas, and A. A. Stokes, "SOPHIA: soft orthotic physiotherapy hand interactive aid," *Frontiers in Mechanical Engineering*, vol. 3, p. 3, 2017.

[11] N. Cheng, K. S. Phua, H. S. Lai, P. K. Tam, K. Y. Tang, K. K. Cheng, R. C.-H. Yeow, K. K. Ang, C. Guan, and J. H. Lim, "Brain-computer interface-based soft robotic glove rehabilitation for stroke," *IEEE Transactions on Biomedical Engineering*, vol. 67, no. 12, pp. 3339–3351, 2020.

[12] H. K. Yap, B. W. Ang, J. H. Lim, J. C. Goh, and C.-H. Yeow, "A fabric-regulated soft robotic glove with user intent detection using EMG and RFID for hand assistive application," in *2016 IEEE International Conference on Robotics and Automation (ICRA)*. IEEE, 2016, pp. 3537–3542.

[13] C. G. Rose and M. K. O'Malley, "Hybrid rigid-soft hand exoskeleton to assist functional dexterity," *IEEE Robotics and Automation Letters*, vol. 4, no. 1, pp. 73–80, 2018.

[14] A. Dwivedi, L. Gerez, W. Hasan, C.-H. Yang, and M. Liarokapis, "A soft exoglove equipped with a wearable muscle-machine interface based on forcemyography and electromyography," *IEEE Robotics and Automation Letters*, vol. 4, no. 4, pp. 3240–3246, 2019.

[15] S. Cheon, D. Kim, S. Kim, B. B. Kang, J. Lee, H. Gong, S. Jo, K.-J. Cho, and J. Ahn, "Single EMG sensor-driven robotic glove control for reliable augmentation of power grasping," *IEEE Transactions on Medical Robotics and Bionics*, vol. 3, no. 1, pp. 179–189, 2020.

[16] P. Polygerinos, K. C. Galloway, S. Sanan, M. Herman, and C. J. Walsh, "EMG controlled soft robotic glove for assistance during activities of daily living," in *2015 IEEE International Conference on Rehabilitation Robotics (ICORR)*. IEEE, 2015, pp. 55–60.

[17] R. A. Bos, K. Nizamis, B. F. Koopman, J. L. Herder, M. Sartori, and D. H. Plettenburg, "A case study with SymbiHand: an sEMG-controlled electrohydraulic hand orthosis for individuals with Duchenne muscular dystrophy," *IEEE Transactions on Neural Systems and Rehabilitation Engineering*, vol. 28, no. 1, pp. 258–266, 2019.

[18] D. Yang, J. Zhao, Y. Gu, L. Jiang, and H. Liu, "Estimation of hand grasp force based on forearm surface EMG," in *2009 International Conference on Mechatronics and Automation*. IEEE, 2009, pp. 1795–1799.

[19] N. Parajuli, N. Sreenivasan, P. Bifulco, M. Cesarelli, S. Savino, V. Niola, D. Esposito, T. J. Hamilton, G. R. Naik, U. Gunawardana *et al.*, "Real-time EMG based pattern recognition control for hand prostheses: a review on existing methods, challenges and future implementation," *Sensors*, vol. 19, no. 20, p. 4596, 2019.

[20] R. Ma, L. Zhang, G. Li, D. Jiang, S. Xu, and D. Chen, "Grasping force prediction based on sEMG signals," *Alexandria Engineering Journal*, vol. 59, no. 3, pp. 1135–1147, 2020.

[21] A. Fougner, E. Scheme, A. D. Chan, K. Englehart, and Ø. Stavdahl, "Resolving the limb position effect in myoelectric pattern recognition," *IEEE Transactions on Neural Systems and Rehabilitation Engineering*, vol. 19, no. 6, pp. 644–651, 2011.

[22] A. Gijsberts, R. Bohra, D. Sierra González, A. Werner, M. Nowak, B. Caputo, M. A. Roa, and C. Castellini, "Stable myoelectric control of a hand prosthesis using non-linear incremental learning," *Frontiers in Neurorobotics*, vol. 8, p. 8, 2014.

[23] R. Alicea, M. Xiloyannis, D. Chiaradia, M. Barsotti, A. Frisoli, and L. Masia, "A soft, synergy-based robotic glove for grasping assistance," *Wearable Technologies*, vol. 2, 2021.

[24] H. J. Hermens, B. Freriks, C. Disselhorst-Klug, and G. Rau, "Development of recommendations for SEMG sensors and sensor placement procedures," *Journal of Electromyography and Kinesiology*, vol. 10, no. 5, pp. 361–374, 2000.

[25] A. E. Hoerl and R. W. Kennard, "Ridge regression: Biased estimation for nonorthogonal problems," *Technometrics*, vol. 12, pp. 55–67, 1970.

[26] J. Sherman and W. J. Morrison, "Adjustment of an inverse matrix corresponding to a change in one element of a given matrix," *The Annals of Mathematical Statistics*, vol. 21, no. 1, pp. 124–127, 1950.

[27] C. Saunders, A. Gammerman, and V. Vovk, "Ridge regression learning algorithm in dual variables," *15th International Conference on Machine Learning ICML '98*, 1998.

[28] A. Rahimi and B. Recht, "Random features for large-scale kernel machines," in *Proceedings of the 20th International Conference on Neural Information Processing Systems*, 2007, pp. 1177–1184.

[29] J. G. Ziegler, N. B. Nichols *et al.*, "Optimum settings for automatic controllers," *Transactions of the American Society of Mechanical Engineers*, vol. 64, no. 11, 1942.

[30] L. Masia, H. I. Krebs, P. Cappa, and N. Hogan, "Design and characterization of hand module for whole-arm rehabilitation following stroke," *IEEE/ASME Transactions on Mechatronics*, vol. 12, no. 4, pp. 399–407, 2007.

[31] W. Wen, A. Yamashita, and H. Asama, "The influence of action-outcome delay and arousal on sense of agency and the intentional binding effect," *Consciousness and Cognition*, vol. 36, pp. 87–95, 2015.

[32] M. Tsakiris, M. R. Longo, and P. Haggard, "Having a body versus moving your body: neural signatures of agency and body-ownership," *Neuropsychologia*, vol. 48, no. 9, pp. 2740–2749, 2010.

[33] M. Pazzaglia and M. Molinari, "The embodiment of assistive devices—from wheelchair to exoskeleton," *Physics of life reviews*, vol. 16, pp. 163–175, 2016.

A.3 The adaptive PAEXO shoulder

Title: Unobtrusive, natural support control of an adaptive industrial exoskeleton using force myography

Authors: Marek Sierotowicz, Donato Brusamento, Benjamin Schirrmeister, Mathilde Connan, Jonas Bornmann, Jose Gonzales-Vargas, and Claudio Castellini

Journal: Frontiers in Robotics and AI

Publisher: Frontiers

Manuscript version: Published article

Citation: M. Sierotowicz, D. Brusamento, B. Schirrmeister, et al. "Unobtrusive, natural support control of an adaptive industrial exoskeleton using force myography." In: *Frontiers in Robotics and AI* 9 (2022). Publisher: Frontiers, p. 919370. ISSN: 2296-9144. DOI: `10.3389/frobt.2022.919370`

Abstract: Repetitive or tiring tasks and movements during manual work can lead to serious musculoskeletal disorders and, consequently, to monetary damage for both the worker and the employer. Among the most common of these tasks is overhead working while operating a heavy tool, such as drilling, painting, and decorating. In such scenarios, it is desirable to provide adaptive support in order to take some of the load off the shoulder joint as needed. However, even to this day, hardly any viable approaches have been tested, which could enable the user to control such assistive devices naturally and in real time. Here, we present and assess the adaptive Paexo Shoulder exoskeleton, an unobtrusive device explicitly designed for this kind of industrial scenario, which can provide a variable amount of support to the shoulders and arms of a user engaged in overhead work. The adaptive Paexo Shoulder exoskeleton is controlled through machine learning applied to force myography. The controller is able to determine the lifted mass and provide the required support in real time. Twelve subjects joined a user study comparing the Paexo driven through this adaptive control to the Paexo locked in a fixed level of support. The results showed that the machine learning algorithm can successfully adapt the level of assistance to the lifted mass. Specifically, adaptive assistance can sensibly reduce the muscle activity's sensitivity to the lifted mass, with an observed relative reduction of up to 31% of the muscular activity observed when lifting 2 kg normalized by the baseline when lifting no mass.

Author contributions: Conceptualization; Software Design; Formal analysis; Writing-original draft; Writing-review and editing.

frontiers | Frontiers in Robotics and AI

TYPE Original Research
PUBLISHED 12 September 2022
DOI 10.3389/frobt.2022.919370

OPEN ACCESS

EDITED BY
Leonardo Gizzi,
Fraunhofer Institute for Manufacturing Engineering and Automation, Germany

REVIEWED BY
Andrés Úbeda,
University of Alicante, Spain
Joana Figueiredo,
University of Minho, Portugal

*CORRESPONDENCE
Marek Sierotowicz,
marek.sierotowicz@fau.de

SPECIALTY SECTION
This article was submitted to Biomedical Robotics,
a section of the journal
Frontiers in Robotics and AI

RECEIVED 13 April 2022
ACCEPTED 26 July 2022
PUBLISHED 12 September 2022

CITATION
Sierotowicz M, Brusamento D, Schirrmeister B, Connan M, Bornmann J, Gonzalez-Vargas J and Castellini C (2022), Unobtrusive, natural support control of an adaptive industrial exoskeleton using force myography. *Front. Robot. AI* 9:919370.
doi: 10.3389/frobt.2022.919370

Unobtrusive, natural support control of an adaptive industrial exoskeleton using force myography

Marek Sierotowicz[1,2]*, Donato Brusamento[1], Benjamin Schirrmeister[3], Mathilde Connan[1], Jonas Bornmann[3], Jose Gonzalez-Vargas[3] and Claudio Castellini[1,2]

[1]Institute of Robotics and Mechatronics, German Aerospace Center (DLR), Erlangen, Germany, [2]Artificial Intelligence in Biomedical Engineering, Friedrich-Alexander-Universität Erlangen-Nürnberg, Erlangen, Germany, [3]Global Research, Ottobock SE and Co. KGaA, Duderstadt, Germany

Repetitive or tiring tasks and movements during manual work can lead to serious musculoskeletal disorders and, consequently, to monetary damage for both the worker and the employer. Among the most common of these tasks is overhead working while operating a heavy tool, such as drilling, painting, and decorating. In such scenarios, it is desirable to provide adaptive support in order to take some of the load off the shoulder joint as needed. However, even to this day, hardly any viable approaches have been tested, which could enable the user to control such assistive devices naturally and in real time. Here, we present and assess the adaptive Paexo Shoulder exoskeleton, an unobtrusive device explicitly designed for this kind of industrial scenario, which can provide a variable amount of support to the shoulders and arms of a user engaged in overhead work. The adaptive Paexo Shoulder exoskeleton is controlled through machine learning applied to force myography. The controller is able to determine the lifted mass and provide the required support in real time. Twelve subjects joined a user study comparing the Paexo driven through this adaptive control to the Paexo locked in a fixed level of support. The results showed that the machine learning algorithm can successfully adapt the level of assistance to the lifted mass. Specifically, adaptive assistance can sensibly reduce the muscle activity's sensitivity to the lifted mass, with an observed relative reduction of up to 31% of the muscular activity observed when lifting 2 kg normalized by the baseline when lifting no mass.

KEYWORDS

force myography, machine learning, adaptive support, exoskeletons, human–machine interaction

Introduction

An exoskeleton, as commonly defined in robotics, is a mechanism typically consisting of a series of rigid links coupled with the individual segments of the user's limbs, normally with the aim of increasing strength or facilitating movements (Yang et al., 2008; Anam and Al-Jumaily, 2012). In the industrial setting, exoskeletons can aid workers dealing with tasks which could otherwise lead to serious work-related musculoskeletal disorders (WRMSDs). (Yamamoto et al., 2002; Huysamen et al., 2018). Tasks involving manipulating or holding heavy objects overhead are linked with a variety of WRMSDs in the shoulder (Bjelle et al., 1979), especially when associated with the requirement of keeping the arm at a higher angle from the torso (Svendsen et al., 2004). Exoskeletons could be used to provide support against gravity when this sort of posture cannot be avoided. Examples of such exoskeletons which are currently available on the market include the *ShoulderX* by SuitX (SuitX, 2021), Comau's *Mate* (Comau, 2021), and the *PAEXO Shoulder Support* by Ottobock (Ottobock, 2021), all of which are designed to provide support at the shoulder joint through a passive spring mechanism. They have been shown to reduce short-term physical strain when performing tasks involving, for instance, holding a heavy tool above the head level or maintaining an awkward pose (Alabdulkarim et al., 2019; Maurice et al., 2019; Schmalz et al., 2019; Nelson et al., 2020; Fritzsche et al., 2021). Although long-term data are not yet available, these devices show promise for reducing health risks for the workers, decreasing their likelihood of incurring into shoulder WRMSDs.

However, in the aforementioned examples, the level of assistance provided by the exoskeleton can only be set manually by changing the spring stiffness parameter or the lever arms. In the literature, certain solutions are presented where the spring offset is set by a motor, but this still needs a manual input by the experimenter or the user (Grazi et al., 2020); this factor usually induces the designers to provide the support mechanism with a lower limit for the maximum force that can be exerted on the user, as the device could otherwise cause difficulties for the wearer when trying to lower their arms from a raised position. An intention-based control system, able to actively set the level of support online without the need for the user to manually input the desired level of assistance, on the other hand, could allow the designers to provide their exoskeletons with higher output torques. In Missiroli et al. (2022), a concept is presented where the level of assistance in a tendon-based system is determined based on the angle of the arm with respect to the body. Although the system presented there did not automatically change the level of assistance provided to the shoulder joint, but rather only the assistive torque exerted on the elbow, keeping the user's posture into account would definitely enable the controller to adapt the provided assistance in a natural fashion. Here, we present a solution that adapts the level of assistance based on the weight of the lifted object. This estimate is achieved by measuring muscular activity, thus providing an appropriate level of support without the need for conscious participation by the user, thus decreasing the overall mental workload as opposed to a setup where the user has to manually set the level of assistance.

The most traditional means to measure muscle activation, namely, surface electromyography (sEMG, Merletti et al. (2009)) has often been investigated in the literature as a possible mean of controlling exoskeletons (Singh et al., 2012). For example, Gopura et al. (2009) proved the effectiveness of an impedance control–based model using sEMG activity and upper-limb posture for controlling a 7DOF exoskeleton. However, this method is hardly viable in industry, as it would be unpractical to fit a worker with a set of sensors which need to be in direct and constant contact with the skin. In general, there is a lack of robust and accepted ways to let a user control an upper-limb exoskeleton, which would also be practical in an industrial setting. While pursuing this goal, in this work we turn our attention to a cheaper and easier-to-use alternative to sEMG, namely, force myography (FMG, Curcie et al. (2001), Wininger et al. (2008), Ravindra and Castellini, (2014), Radmand et al. (2016), Connan et al. (2016)). This sensor technology relies on measuring muscle bulging upon contraction, usually by means of a force sensor pressed onto the body. FMG sensors do not need to be in direct contact with the skin, and can be easily integrated in a harness worn above the clothing. A further advantage is that implementation of this kind of sensors can be extremely cheap, as force can be measured by means of a simple strain gauge, while still providing measurements so accurate that they can be used in order to control prosthetics (Cho et al., 2016).

Of course, FMG suffers from issues as well. Examples include saturation and bias of the measured signal, as well as problems of cross-talk between muscle groups depending on the harness design, for instance, bulging of one muscle could lead to an increase in pressure on sensors diametrically opposed, if the sensors are arranged in a bracelet. Still, there are already examples in the literature of FMG usage to control exoskeletons. In Islam and Bai, (2019) the authors determine three payload levels through support vector machines with FMG sensors as an input. However, in this case, the exoskeleton was not providing any support and was used passively. Ebrahimi et al. (2017) developed and tested on one participant a method for adjusting the control parameters of their exoskeleton in real time by using several measurements: joint angle, speed, force sensors on the lower and upper arms, and force-sensing gloves. In this case, the control parameters were modified based on a single calibration round, and were not changed in real time. Adopting a slightly different approach, Huang et al. (2015) and Miller and Rosen, (2010) both used force sensors to compute a trajectory that the exoskeleton would help to execute. In these cases, the experimenters used non-movable rehabilitative exoskeletons with active, non-compliant motors assisting each joint of the user.

FIGURE 1
Adaptive Paexo Shoulder as worn by a participant. 1) Textile support structure, 2) assistive structure, and 3) control electronics including power source.

The aforementioned studies have evaluated the use of FMG for exoskeleton control, but in no case, to the best of our knowledge, the approach has been fully evaluated online. The exoskeleton used is a fully portable solution employing a compliant and lightweight actuation mechanism able to provide an adaptive support via a motor changing the lever arm distance between the arm and the support bars, allowing to change the support torque at the joint.

In order to test the feasibility and the performance of the concept proposed here *in an online setting*, 12 users were recruited to perform a set of repetitive pickup–hold–carry–release tasks, while a regression-based machine learning algorithm used FMG measurements to estimate the weight lifted by the user, and appropriately adjust the level of assistance provided by an industrial exoskeleton in real time. The exoskeleton of choice was an adaptive prototype built by Ottobock, based on a modified version of the Paexo Shoulder Support (Ottobock, 2021). The modified version of the Paexo will henceforth be denoted as *Adaptive Paexo Shoulder*. Because the setup presented here is based on an assistive device which has already been tested and characterized (Maurice et al., 2019; Ottobock, 2021), the focus of this study was not to confirm the effects of exoskeleton's fixed support as compared to the unassisted condition, but rather as compared to an intent-based adaptive assistance condition. We hypothesized to observe a more constant muscular effort over different lifted masses when using adaptive assistance, as opposed to a fixed passive assistance. In other words, we expected a diminished increase in muscular activity in the shoulder muscles as a consequence of increasing the lifted mass. The results of this evaluation are extremely promising in this sense, showing furthermore that adaptive assistance increases kinematic stability of the shoulder joints enabling more precise movements. The strength of this study resides in demonstrating the feasibility of real-time control on a semi-active exoskeleton using force myography (FMG) as input. FMG sensors are potentially far more practical in real-world applications than their EMG counterparts. Furthermore, to the best of our knowledge, this is the first study showcasing the online control of a supportive exoskeleton based on the estimation of the lifted mass.

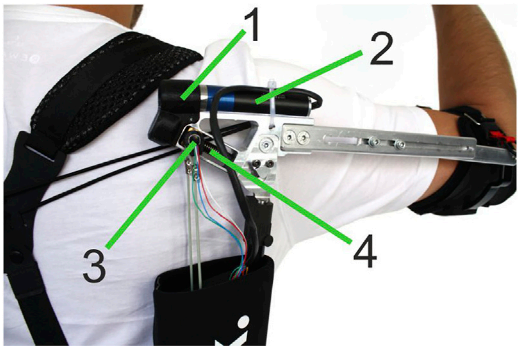

FIGURE 2
Actuated joint of the adaptive Paexo Shoulder: 1) axe compensation, 2) brushless dc servo motor, 3) nut with encoder, and 4) trapezoid leadscrew.

Materials and methods

The adaptive Paexo Shoulder

The adaptive Paexo Shoulder (Figure 1) expands upon the basic Paexo design from Ottobock (2021), as it features the possibility to automatically set the overall support provided by the passive spring-based actuator. For this purpose, a DC brushless Faulhaber 2057B motor is integrated directly at the shoulder joint (Figure 2). The motor can be used to change the length of the lever arm with which the spring element pulls the humeral orthosis. Therefore, the adaptive Paexo Shoulder still behaves like a passive device, but allows to automatically change the operating point of the of the spring mechanism, effectively increasing or decreasing the overall support provided to the user. This mechanism introduces a certain latency in the control loop, as a transition from the minimum to the maximum lever arm can last up to 2 s. However, internal testing shows that, because the system is always providing some level of support, this latency has no issue and the user still perceives the support as transparent. In the setup presented here, the level of support depends on various anthropometric measurements of the user, according to Eqs

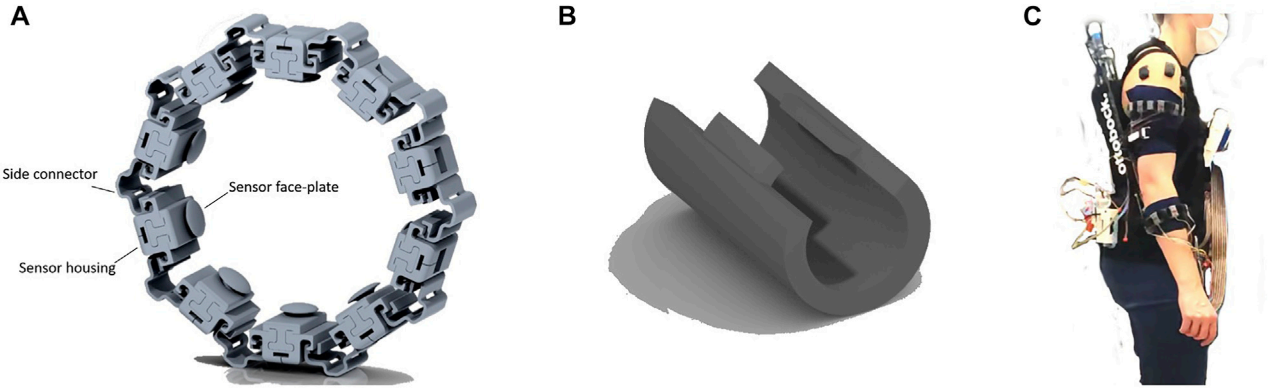

FIGURE 3
CAD view of the bracelets and bracelet elements. **(A)** Render of an assembled FMG bracelet with 10 sensing elements. **(B)** Render of one rigid clip which can be used to clamp the lateral connectors to fit the bracelet to limbs of lower circumference. **(C)** Full FMG setup as worn by a participant during the experiment. Notice also the EMG sensor probes worn on the shoulder.

3–6. The adaptive Paexo Shoulder has the same frame and structure characteristics as the Paexo: the actuator is mounted on the arm bar, which is connected to the support bar via an expander rope. This acts as a spring that generates a torque in the joint as a function of the arm anteversion. A textile stabilization harness supports donning and doffing, and keeps the structure close to the torso. The only semi-rigid structures coming into contact with the body are the belt and the two underarm cuffs. A rotational encoder is used to measure the joint angle. The entire setup weighs 3 kg and can be used with a 14.8V/1550mAh LiPo battery for 6–8 h, depending on the amount of usage.

Force myography bracelets

In the presented setup, the required support level of the adaptive Paexo Shoulder was calculated based on measurements from a set of FMG sensors. As FMG entails measuring the force from muscle bulging, the design of the harness pressing the sensors onto the body segments to be monitored is paramount. The FMG sensors were lodged in individual housings, which were in turn arranged in two modular bracelets worn by the user on the forearm and upper-arm, respectively. The FMG sensors (*FSR 400 short* by Interlink Electronics, (Electronics, 2022)) are integrated in an analog amplification circuit designed internally (see (Connan et al., 2016)). The amplification circuit board and the FSR were housed in flexible 3D-printed housings, as shown in Figure 3. The armbands (as shown in Figure 3) consisted of four elements:

- Sensor housing main body, which holds the sensor and binds the shell assembly to the lateral connectors.
- Sensor face-plate, which conveys and directs the pressure from muscle bulging directly on the sensor strain gauge. The two sub-elements are connected by means of snap-on appendages on the face-plate.
- Side connectors, designed to be easily extendable, thus providing flexibility over a range of arm sizes, with the possibility of being fitted with a rigid clip, which is used to ensure that the bracelet fit limbs with smaller circumference.
- Binding clips, whose purpose is constraining the length of connectors as described earlier to fit limbs of smaller circumference.

Because of the modular design, the number of sensors for each bracelet can be changed, and fine adjustments can be made as required in order to improve the fit on any individual user, either by using the binding clips, or by adding additional connectors and shells. The bracelet was manufactured via fused deposition modeling out of TPU material, with shore hardness 90A, which gives the outer surfaces a gritty texture making the friction between connectors and shell bodies such that no additional fasteners are required to keep the elements in place. The used force-sensing resistors are shown in Castellini and Ravindra (2014) and Connan et al. (2016) to have an extended linear region in the sensitivity curve. The bracelets were designed and tested to keep the sensor in this linear region.

The measurements from the FMG sensors were acquired and transmitted to a remote host via a data acquisition (DAQ) system shown in Figure 4. The DAQ board used here is an updated version of the one presented in Connan et al. (2016).

The DAQ board is designed around a low-power microcontroller (MSP430F5529, by Texas Instruments) running at 25 MHz. During normal operation, the system

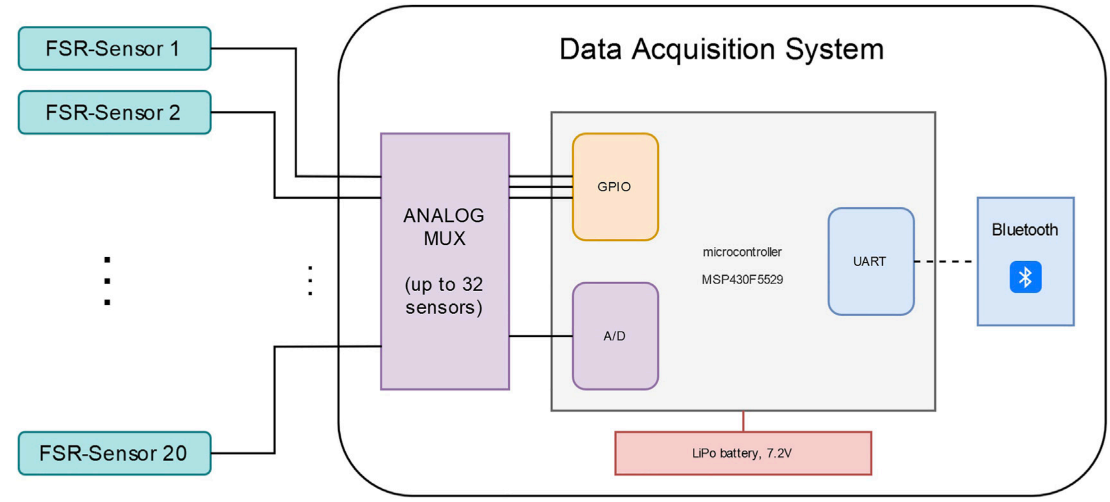

FIGURE 4
DAQ system for FMG: overview of the major components.

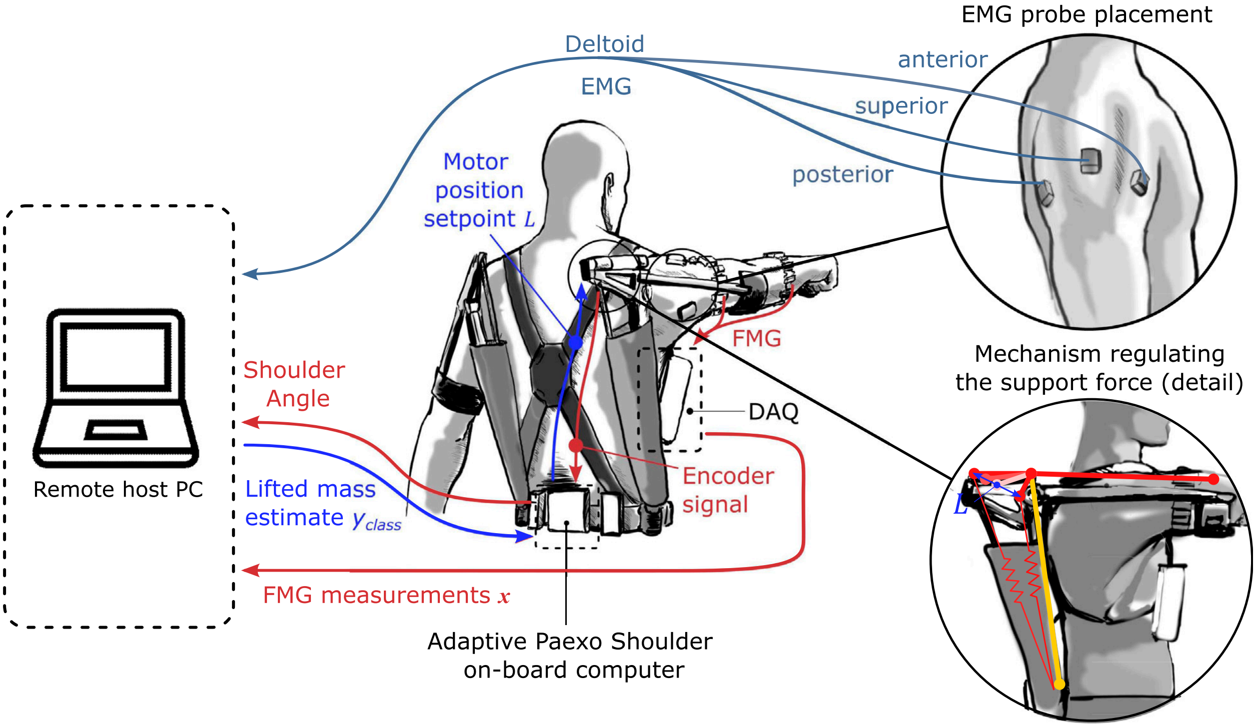

FIGURE 5
Block diagram of the control loop regulating the level of assistance and detail of EMG sensor placement.

draws approximately 80 mA, which translates to more than a day of continuous operation when powered by a 7.2 V 2400 mAh LiPo battery. The DAQ can acquire data on up to 32 hard-wired channels. The analog signal from these channels is converted to digital with 12 Bits resolution. In the setup presented here, only 20 FMG sensors are used. In order to facilitate the integration of remote hosts in the control loop, the adaptive Paexo Shoulder can be controlled through a wireless interface over a Bluetooth module (RN42 from Roving Networks). In the setup presented here, a remote host PC ran the prediction algorithm which estimated the mass lifted by the user (see *Estimation of the required support*) and translated it to a desired support level. The communication between the host computer and the adaptive Paexo Shoulder controller was based on a serial protocol and the out- and inbound messages were checked at a rate of 200 Hz. The control loop and the sensors used to monitor the muscular effort during the study are shown in Figure 5.

Estimation of the required support

To estimate the support desired by the participant in real time starting from the 20 FMG signals, we used standard ridge regression (Hoerl and Kennard, 1970). Let $\boldsymbol{x} \in \mathbb{R}^{20}$ denote the signal vector; then the output of the ridge regression estimator is $y = \boldsymbol{w}^T \boldsymbol{x}$, where $\boldsymbol{w} \in \mathbb{R}^{20}$ is obtained through regularized minimization of the mean-squared error, leading to the following closed form solution for $\boldsymbol{w}$

$$\boldsymbol{w} = \left(X^T X + \lambda I\right)^{-1} X^T \boldsymbol{y}, \tag{1}$$

where $X \in \mathbb{R}^{20 \times N}$ is the design matrix gathering N observed sensor measurements of the form $\boldsymbol{x}$, and $\boldsymbol{y} \in \mathbb{R}^N$ is a vector gathering the weight lifted in association with each observation $\boldsymbol{x}$ present in X. Although the weights in this vector were not in kilograms, the values were proportional and subsequently discretized and scaled as shown in Eq 2. X and $\boldsymbol{y}$ must be collected at the beginning of each experiment in order to create an appropriate training set for the calibration of the ridge regression model and provide a sensible estimation of the optimal $\boldsymbol{w}$. λ represents a regularization term, which keeps the parameters in $\boldsymbol{w}$ low in magnitude.

The FMG signals were sampled by the DAQ board at 192.5 Hz, and then wirelessly transmitted to a host computer where they were filtered with a first order Butterworth filter, with cut-off frequency of 1 Hz to extract slower dynamics. For the calibration procedure, the filtered signals were then fed to the ridge regression algorithm with $\lambda = 1$, which was trained once at the beginning of each experimental round (i.e. only once per subject), only allowing for initial re-calibrations if the prediction was visibly unstable. The reasons for instability of the prediction are most likely wrong sensor placement or an erroneous performance of the actions required for the calibration. During the calibration procedure, the FMG signals would be sampled for 10 s while the participant performed one of the following actions per sampling:

- Both arms relaxed and kept along the sides, hands unclenched.
- Right arm raised at 45° over the horizontal plane, no weight held.
- Right arm raised at 45° over the horizontal plane, holding a 1 kg weight.
- Right arm raised at 45° over the horizontal plane, holding a 2 kg weight.

These correspond, in turn, to the following labels: $y_{l,i} \in [0, 0.1, 0.5, 1.2]$. These values for the response variable were chosen based on previous tests. The dataset consisted, therefore, of approximately 1925 samples for each of the four labels. The training of the regression model takes under 1 s with this number of observations. The time efficiency in the training phase is the main reason why a ridge regression model was chosen for this application. Although no circumstances were observed during the course of the experiment where a model recalibration was necessary, the short duration of the procedure would make it possible to easily recalibrate the model, should the sensors need to be repositioned or re-instrumented ina real-world scenario. After training, the regression algorithm provided a 1-dimensional estimation y_{pred} of the user's effort based on signals filtered analogously to those used for calibration. The obtained prediction was then additionally low-pass filtered, clipped between 0 and 1, and subsequently discretized in three levels, according to the following criteria:

$$y_{class} = \begin{cases} 0 & \text{if } 0 \leq y_{pred} < 0.35 \\ 1 & \text{if } 0.35 \leq y_{pred} < 0.75 \\ 2 & \text{if } y_{pred} \geq 0.75 \end{cases}, \tag{2}$$

The prediction step of the regression model is instantaneous when compared to the latency due to the adaptive Paexo Shoulder's mechanism. The value of y_{class} was communicated to the adaptive Paexo Shoulder (Figure 5) in order to issue support levels for, respectively, 0 kg, 1 kg, or 2 kg weights. The exact amount of force provided to the user was computed on the adaptive Paexo Shoulder's internal controller, depending on each user's biometrics (specifically body weight and height, using the relations shown in Eqs 3–6). Although the FMG sensors used in the experiment have non-negligible hysteresis at high forces, as well as a non-linear transfer function, it was shown in Ravindra and Castellini (2014) that for moderately high forces (0–15N), like those that could be produced by muscle bulging, the behavior is fairly consistent and their transfer function is nearly linear. For this reason, it was not deemed necessary to make use of more advanced ML algorithms to account for non-linearity.

The conversion from the algorithm's estimate to lever arm length takes into account the estimated lifted weight y as well as the user's body mass m and arm's length l according to the following laws:

$$m_{lifted} = m\left(f_{ua} + f_{fa} + f_h\right) + y, \tag{3}$$

$$h_{COM} = \frac{m f_{ua} h_{ua} + m f_{uf} h_{fa} + (m f_h + y) h_h}{m_{lifted}}, \tag{4}$$

$$\tau = 0.7 g m h_{COM}, \tag{5}$$

$$L = 0.05523\tau + 3.007, \tag{6}$$

where f_{ua}, f_{fa}, and f_h represent the percentage of the bodyweight constituted by the upper-arm, forearm, and hand, respectively, h_{ua}, h_{fa}, and h_h represent the position of the centers of mass for the upper-arm, forearm, and hand, respectively, and g is the gravitational acceleration. All of the remaining constants were empirically determined during pre-tests in order to provide a good level of support without exerting too much pressure on the user. The bodyweight coefficients and the positions of the centers of mass are all based on anthropometric tables found in Drillis et al. (1964). The positions of the individual centers of mass are based on the length of the user's arm with the arm in a standard working position, which in this case was assumed to be constant across all tasks. Therefore, after the initial calibration and during the session, the level of assistance only changes as a function of the estimated lifted mass. The actual support force provided during the experiment depends on the characteristics of the user and on the shoulder anteversion angle, but for reference, the Paexo can provide a maximum support force of around 50 N.

Participants

Twelve participants (nine males, three females, 27.6 ± 2.9 years old, 71.9 ± 6.5 kg, 1.76 ± 0.07 m) were involved in a repetitive series of tasks, designed in order to require different levels of assistance at different times. The study design was within-subject: the participants were divided in two subgroups. Group A performed the tasks with the adaptive assistance on first, and then performed them again with the adaptive assistance off and the Paexo set to a mid-scale support force. Group B completed the tasks with the conditions inverted. This subdivision had the goal of counterbalancing the effects of fatigue over time on the outcome metrics. All users were thoroughly informed about the experiment before taking part in it, both orally and in writing, and then signed an informed consent form. The experiment was carried out in conformity with the WHO Helsinki Declaration and was authorized by the DLR internal committee for safety and data protection. Although the end-user group would presumably also consist of able-bodied individuals, no particular effort was put in assuring that the study population would match the end-user group in terms of age, gender, or BMI distribution.

Experimental setup

For the purposes of the experiment, in addition to the FMG sensor setup and the on-board sensors of the adaptive Paexo Shoulder described earlier, the participants were fitted with three *Trigno* EMG sensors by DelSys. These were placed on the anterior, superior, and posterior deltoid of the right arm, respectively, as shown in Figure 5. Although dorsal muscles are also involved in the overhead work, the EMG probes were placed exclusively on the deltoid muscles because the results presented in Maurice et al. (2019) suggested that the support force provided by the Paexo has the most significant effect on the activity of this muscle group, and does not significantly affect the activity of dorsal muscles. By extension, no significant differences could realistically be expected on dorsal muscle activity when comparing passive and adaptive assistance. The EMG measurements were bandpass filtered between 20 and 450 Hz. The feed from the sensors was sent to the host PC at a rate of 2000 Hz. For the purposes of the offline analysis, the absolute value of the EMG was extracted. The average and standard deviation of the EMG were extracted over the whole time during which the task was computed. The maximal value of the EMG measured for each participant was used as a normalizing factor.

The EMG measurements were used, among other things, to compute the muscular effort ratio r_d, defined as the ratio of the mean absolute value of the EMG on the deltoids (the index d indicates the deltoid group) when lifting 2 kg and when lifting 0 kg, in accordance with the following relation

$$r_d = \frac{\overline{|EMG_{m=2\text{ kg}}|}}{\overline{|EMG_{m=0\text{ kg}}|}}, d \in \{\text{ant.}, \text{sup.}\}. \tag{7}$$

This is indicative of the rate at which muscle activity increases as a consequence of increasing lifted mass. What we set out to demonstrate is that the adaptive assistance significantly decreases this rate when compared to the non-adaptive assistance.

The participants were asked to maintain their shoulders parallel to a screen placed in front of them, which showed them a GUI guiding them through the sequences by showing prompts and the remaining duration of each task. On the participant's right, a stack of shelves served to store the weights used throughout the session. Markings were drawn on the shelf in order to help the participants find the reference points for the two main angles at which they were required to hold their right arm. The experimental setup and GUI are shown in Figure 6. The stability of the shoulder angle as measured by the exoskeleton's internal encoder was also used as an evaluation metric. Specifically, the standard deviation on the shoulder angle is measured by the Paexo's on board shoulder encoder. This is indicative of the precision with which the user is able to maintain a position or a trajectory.

Experimental protocol

After providing their informed consent and general data, the participants were fitted with the exoskeleton and the sensor setup. The sensor density was sufficient to ensure that muscle activity caused by lifting a mass would be measurable independent of the bracelet's orientation around the body segment's longitudinal axis. The two bracelets were positioned in order to cover the region of largest diameter on both the right

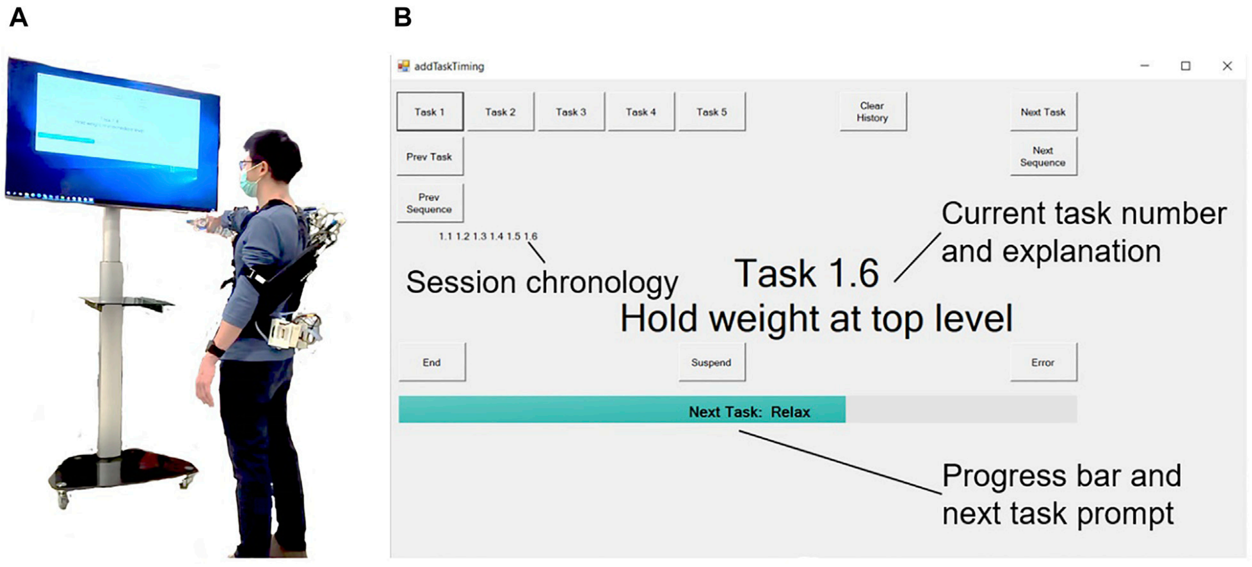

FIGURE 6
Experimental setup. **(A)** Participant performing the experiment. **(B)** GUI.

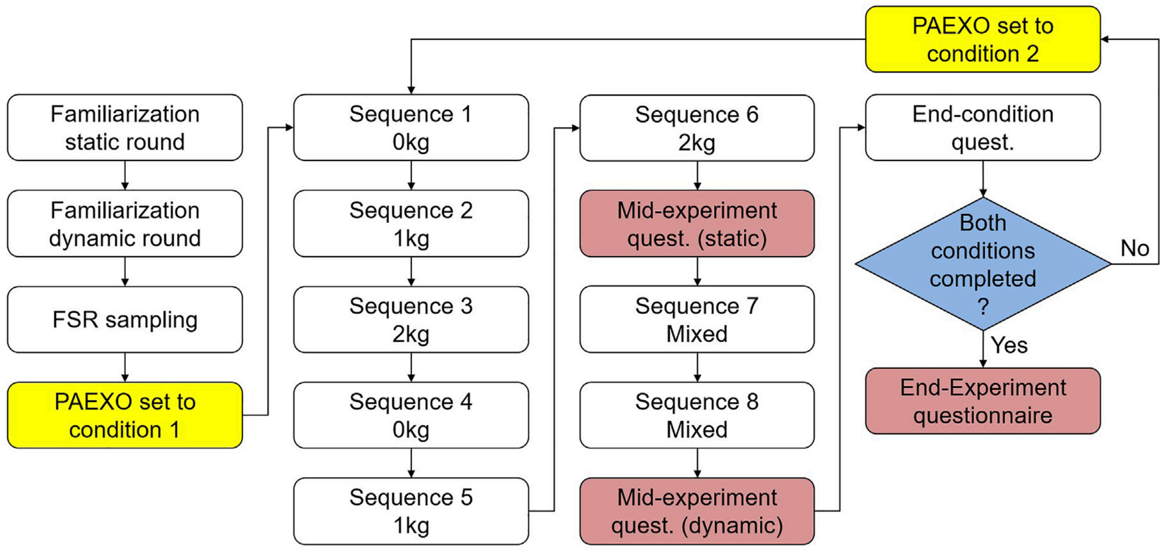

FIGURE 7
Flow-chart of the experimental protocol.

forearm and the right humerus, and the positioning of the sensors was never changed throughout the experimental session. After being fitted with the devices and after performing a familiarization round, the participants performed the calibration procedure described in the *estimation of the required support*. During the session proper, the participants were asked to perform a series of tasks involving holding either 0 kg, 1 kg, or 2 kg with the arm horizontal or at about 45° above the horizontal plane for 30 s. The weight was to be held either in an isometric contraction or moved in circles counter-clockwise at about one round per second. All of these tasks were to be repeated

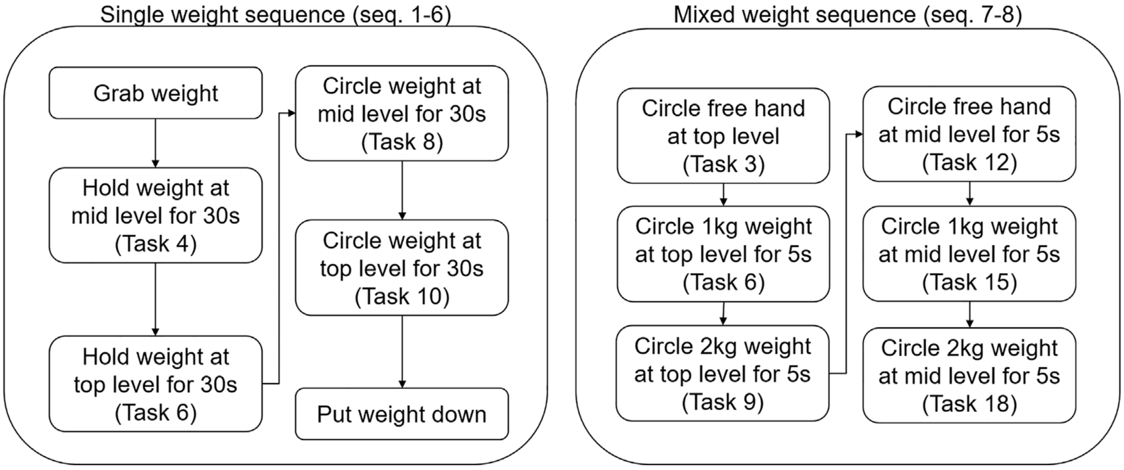

FIGURE 8
Detailed breakdown of each sequence.

twice. The combination of these factors gives sequences from 1 to 6 as shown in Figure 7. The relevant tasks for this sequence are shown on the left side of Figure 8. After completing these, the participants were asked to compile a mid-experiment questionnaire specific to these sequences. The participants were then asked to perform two further sequences. These required the participants to pick 0 kg, 1 kg, or 2 kg from a lower shelf, move them in circles close to a higher shelf, and then leave them there, and then repeat these tasks starting with the higher shelf. This sequence of tasks was to be repeated twice, and these two repetitions are shown as sequences seven and eight in Figure 7. The relevant tasks for these sequences are shown on the right side of Figure 8. The order in which the tasks were performed was not randomized, as the goal of the study was not to ascertain an effect of the task on the muscular activity, but only the effects of the adaptive assistance as opposed to the non-adaptive assistance. After this, the participants were asked to fill a mid-experiment questionnaire about sequences seven and eight, as well as a condition-specific mid-experiment questionnaire.

All participants completed all tasks and sequences with both adaptive and non-adaptive assistance. As the expected effect of the adaptive assistance was not to decrease the measured muscular activity overall, but rather to decrease the overall sensitivity of the muscular activity to the lifted mass, the level of support force set for the Paexo under the non-adaptive assistance condition is irrelevant. During the experiment, the Paexo was set to a mid-scale support force in order to drive the system at its average operating point. At the end of the session, the participants were asked to compile a post-experiment questionnaire. Here, as well as in the mid-experiment questionnaires, the participants were asked to assign a score from 0 to 20 to a set of task load metrics, in accordance with the NASA Task Load Index assessment Hart and Staveland, (1988). Furthermore, in the post-experiment questionnaire, the subjects were asked to assess the modified version of the adaptive Paexo Shoulder they used with a reduced version of the System Usability Score test (SUS, Brooke. (1996)). The SUS consists of a series of questions to be answered on a 5-level Likert scale. The questions are formulated in such a way that, when evaluating a maximally usable system, the answers should ideally alternate between the maximum and the minimum value on the Likert scale. This is to avoid response repetition bias. The particulars of the two experimental conditions were not explained to the participants. In spite of this, it was not possible to carry out the experiment with the participants completely blind to the current condition, as the adaptive assistance causes the Paexo's Shoulder motor to move and emit audible sounds, and moreover, one can easily detect changes in the level of assistance. This factor could influence the subjective evaluations, but it should not affect the other metrics. The alternating of groups starting with the non-adaptive and adaptive assistance should aid in counteracting possible biases in the subjective assessments.

Results

In order to analyze the effects of the different assistance types on the adopted metrics, a repeated measure analysis of variance (rmANOVA) on a multivariate model fitted to the data was performed. The model had the *mode of assistance* as the main independent variable, with value either adaptive or non-adaptive. Within the model, the variables *sequence*, *task*, and *mode of assistance* were all considered within-subject predictors, as all subjects completed all the tasks and sequences with both conditions. The rmANOVA analysis was performed using the Statistics and Machine Learning Toolbox within the Matlab environment (Matlab 2021a; MathWorks, Natick, Massachusetts MA, United States United States)

TABLE 1 Overview of the results for all experimental conditions and significant ANOVA effects were applicable. The metric values are indicated in format *mean (standard deviation)*.

Metric (condition) [Unit]	Non-adaptive assistance	Adaptive assistance	Significant ANOVA or t-test effects of assistance mode
r_{ant} (Single-weight tasks) [ ]	2.23 (0.69)	1.70 (0.41)	F (1, 11) = 13.02; $p < 0.005$
r_{ant} (Task 4) [ ]	2.34 (0.82)	1.86 (0.44)	F (1, 11) = 4.88; $p < 0.05$
r_{ant} (Task 6) [ ]	2.17 (0.56)	1.67 (0.28)	F (1, 11) = 16.19; $p < 0.005$
r_{ant} (Task 8) [ ]	2.25 (0.77)	1.78 (0.48)	F (1, 11) = 7.17; $p < 0.05$
r_{ant} (Task 10) [ ]	2.15 (0.61)	1.49 (0.36)	F (1, 11) = 18.39; $p < 0.005$
r_{sup} (Mixed-weights tasks)[ ]	2.26 (0.80)	1.85 (0.71)	F (1, 11) = 7.12; $p < .05$
SD on shoulder angle (single-weight seq.) [rad]	0.36 (0.12)	0.33 (0.13)	F (1, 11) = 50.88; $p < .001$
Subjective assessment of strain (single-weight sequences) [ ]	13.50 (3.40)	11.75 (3.36)	Paired T-test: $p < 0.1$
Weight estimation error (single-weight sequences) [%]	Does not apply	21.33 (24.72)	Does not apply
Weight estimation error (mixed-weight sequences) [%]	Does not apply	29.91 (32.02)	Does not apply
System usability scale assessment score [%]	Does not apply	74.23 (14.05)	Does not apply

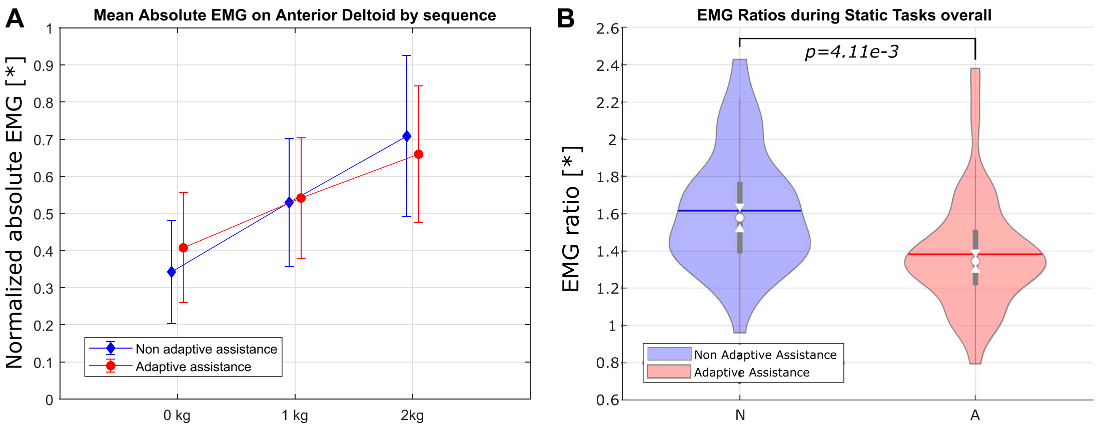

FIGURE 9
sEMG for single-weight sequences sorted by the assistance mode for the anterior deltoid. **(A)** Bar graph of sEMG measurements by lifted weight. **(B)** Violin plots of the sEMG ratios (sEMG when lifting 2 kg over sEMG when lifting no weight) by the assistance mode.

(MathWorks, 2021). The most significant results in terms of *p*-value are listed and explained in the discussion. All main results are reported in Table 1. The assessed metrics are indicated in the leftmost column. The average EMG on the most affected muscle groups and a comparison of the ratios r_d are shown in Figures 9, 10.

Table 1 also contains the result of a *post hoc* multiple comparison of estimated marginal means, which shows some of the relevant effects sorted by task. As the independent variable, which was the mode of assistance, only has two possible values, no adjustment was needed for the *post hoc* analysis. The subjective assessments (except the SUS) were evaluated on a discrete scale with 20 bins, where the participants had to express the perceived answer to a given question item, based on the NASA Task Load Index (TLX) test (Hart and Staveland, 1988). Figure 11 shows the measured standard deviation of the shoulder angle as measured by the Paexo's internal encoder. Finally, Table 1 reports the relative error in the estimation of the lifted weight, normalized by the maximum possible error value.

Discussion

The results presented earlier enable us to characterize many aspects of the presented setup, as well as to draw a few tentative conclusions on the overall effectiveness of the presented setup. Although many solutions involving passive or semi-passive exoskeletons have been presented in the literature in the past (Grazi et al., 2020; SuitX, 2021; Missiroli et al., 2022), intention-based

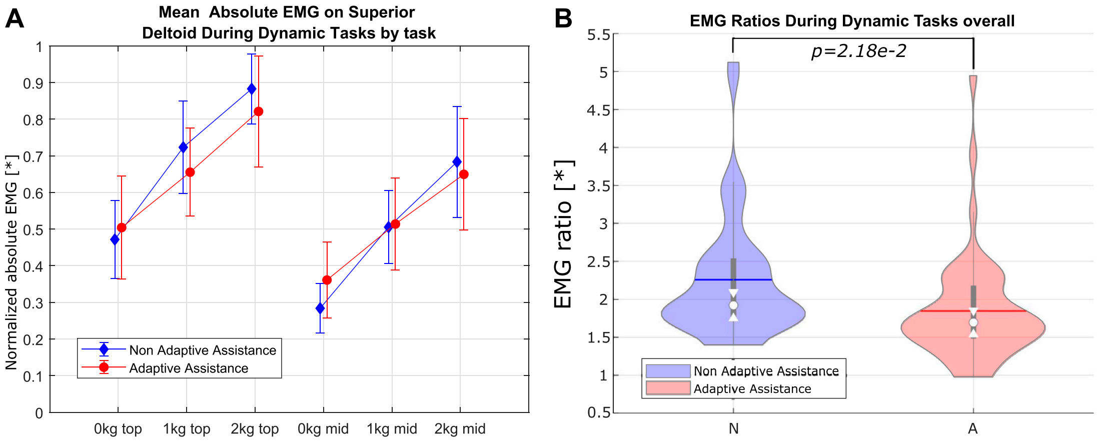

FIGURE 10
sEMG for mixed-weight sequences, color-coded by assistance mode for the superior deltoid. **(A)** Bar graph of sEMG measurements by lifted weight. **(B)** Violin plots of the sEMG ratios (sEMG when lifting 2 kg over sEMG when lifting no weight) by the assistance mode.

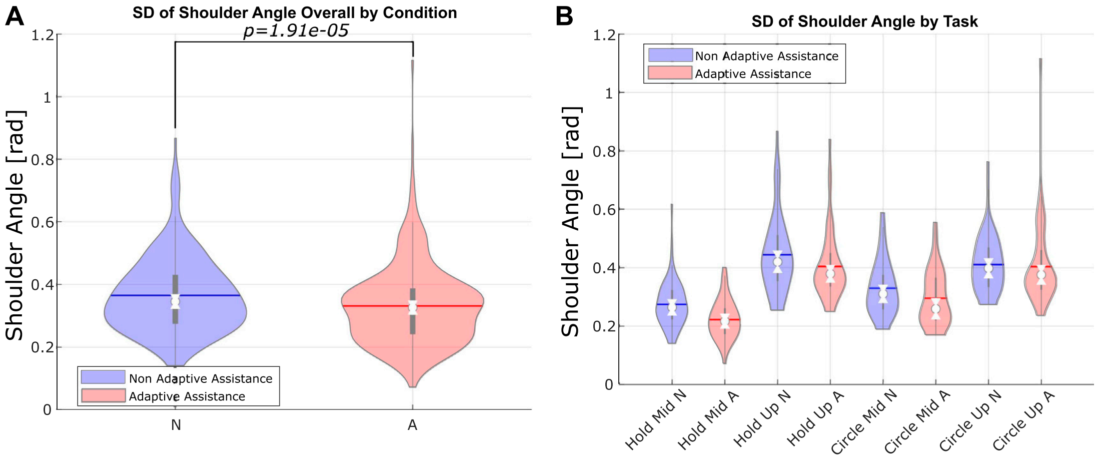

FIGURE 11
Angular encoder at the shoulder level **(A)** Violin plot of shoulder angle standard deviation by the assistance mode. **(B)** Violin plot of shoulder angle standard deviation by task.

control concepts for such systems are rarely investigated. The main hypothesis of this study is that an intention-based support level selector, used in real time, can effectively reduce the correlation of muscular effort to lifted mass by adjusting the torque and therefore the forces acting onto the user. This would have many potential advantages, and it minimizes the undesired interaction forces between the exoskeleton and the user, which is in general desirable (Ajayi et al., 2020). As the basis of the presented setup is a passive assistive exoskeleton whose main characteristics have been presented in the past (Maurice et al., 2019; Ottobock, 2021), this study does not focus on confirming the effects of the passive support as compared to the case unassisted condition, but rather focuses on identifying the effects of adaptive assistance as compared to a non-adaptive, mid-scale level of support provided by the Paexo.

Shoulder stability

The standard deviation on the shoulder angle as measured through the Paexo's encoder is significantly affected by the assistance modality, both in the tasks requiring the participant to hold the weight, as well as in those requiring circular movements. This effect was only detected in the sequences with single weight, most likely because the mixed-weight sequences involved faster movements over shorter times. This would reduce the effect of assistance mode on the shoulder angle stability. Conversely, in the case of single-weight sequences, the higher standard deviation detected under non-adaptive assistance seems to be due to the fact that the participants would slowly lower their arms because of fatigue over the required 30 s of contraction. Figure 11 shows violin plots of this metric overall as well as a breakdown of the tasks.

Subjective assessment

No effect of the assistance modality on the subjectively assessed metrics can be detected, with the remarkable exception of the *perceived strain* for the sequences involving one weight, which is positively affected by the adaptive modality ($p < 0.1$, Table 1). In the SUS test, the participants evaluated the system with an average score of 74.23 ± 14.05% (Table 1), which corresponds to a B according to the SUS score-grade curve.

Muscle activity

No significant effect of the mode of assistance on the mean EMG could be determined, when considering all tasks and all sequences. This is likely due to the fact that the adaptive Paexo Shoulder, when in the non-adaptive mode, was providing a mid-scale level of support, which is overall similar to the average level of support provided in the adaptive mode. However, the effect of adaptive assistance, as used within this user study, is statistically significant when one considers the difference in mean EMG activation when lifting no weight and when lifting 2 kg. In particular, the assistance mode shows a significant effect on the ratio between the mean EMG activity when lifting 2 kg and when lifting no weight (the ratios are shown in Figures 9, 10). The effects are most significant for the sEMG on the anterior deltoid during single-weight sequences and for the superior deltoid during mixed-weight sequences (Table 1). A possible reason for this is that the mixed-weight sequences entailed leaving and picking up weights from the shelves on the participant's right hand side. This would require the user to perform frequent horizontal arm abductions, in addition to the arm flexions and extensions needed in order to lift the weights and to return to the neutral position, which can be largely performed by the anterior deltoid. This could lead to an overall more noticeable recruitment of the superior deltoid, which is mainly used in horizontal arm abduction.

As stated earlier, this indicates that under adaptive assistance, the average muscle activity at the shoulder level does not increase as much when the mass to be lifted increases. If this trend were confirmed over a wider range of support forces, this would indicate that this type of adaptive control *can effectively scale the level of support as the weight to be lifted increases*. As the available support levels of the adaptive Paexo Shoulder increase with the future versions, the adaptive control could likely be used to reduce the amount of muscle fatigue even for higher weights, thereby easing the workload on the user, without increasing the amount of force necessary to lower the user's upper limbs. Actually, if the exoskeleton were able to provide higher support forces, conceivably even to such a degree that it would be difficult for the user to lower their arms without intention-based control, the adaptive assistance system would likely be able to further flatten the relation between mean sEMG and lifted mass, as shown in Figures 9, 10. There is an assumption underlying this claim, namely, that the adaptive assistance algorithm would then be able to decrease the provided support when needed. This has partially been shown by this study. An interesting fact is that the effect of assistance mode on the EMG ratio is more pronounced, with a p value of $1.105e-3$, when taking into consideration the second repetition performed by the participants, as opposed to the first one, where the effect has a p value of 0.022. This could indicate that the adaptive assistance leads to a slower onset of fatigue compared with the non-adaptive assistance.

Prediction accuracy

The muscle activity sensing system shown here and the associated prediction algorithm were accurate enough for practical uses. Remarkably, the user-exoskeleton system constitutes a closed-loop system, as the desired support is issued by the adaptive Paexo Shoulder, the muscle activity of the user naturally reduces, thereby reducing the amount of support provided. Evidently, each time the weight to be lifted changes, the user and the exoskeleton reach a new point of dynamical equilibrium in the provided support, balancing each other. In this work we have not explored this relationship, but it is a fascinating research issue and will be investigated in the future. We are especially interested in how modeling this relationship might render the device more ergonomic.

Study limitations

As is obviously the case, this study has limitations. First, the participants were instructed to only use one particular type of grasp, namely power grasping. Although many studies in prosthetics have shown that machine learning and FMG can easily be used to detect the intent of the users more precisely, the performance is naturally bound to change when allowing for different grasps. Second, we could not use any motion tracking system to determine the potential differences in the motor strategies of the participants, introduced by the adaptive support control. Third, the current range of support that the adaptive Paexo Shoulder is able to provide is rather limited and constitutes a simple case study, which needs to be broadened. These are some aspects which should be addressed by future research. The main goal of future work on this sort of device should focus on generalizing the estimation of the lifted mass to various kinds of grasp, and on the inclusion of posture data in the estimation of the needed assistance, as shown in Missiroli et al. (2022).

Conclusion

The Paexo has been conceived since its early design stage with non-obtrusiveness and simplicity in mind: it can be donned and doffed easily and quickly and guarantees the full range of motion of the user's shoulders while worn. The adaptive Paexo Shoulder follows the same design philosophy, and additionally provides adaptive support via a lightweight servo motor. Still, the question remains: *how* to let the user control it transparently, effectively, and in real time? Taking inspiration from the previous work in the field of upper-limb prosthetics, in this work, we have assessed the effectiveness of FMG to determine in real time the amount of support required by the user depending on the lifted mass, and consequently, to control the motor of the adaptive Paexo Shoulder, thereby determining the effects of an adaptive support offered by the device.

A substantial advantage provided by FMG is that it can be worn on the worker's clothing, as opposed to sEMG sensors, which is an unavoidable constraint in most industrial and commercial settings. Future work will also investigate the integration of further sensor modalities enabling the support force estimator to take into account also the user's posture, in addition to the estimation of the lifted mass.

Data availability statement

The raw data supporting the conclusion of this article will be made available by the authors, without undue reservation.

Author contributions

DB performed the initial experiment and part of the main user study, and built parts of the hardware; MS performed part of the main experiment and carried out the data analysis; BS performed the initial experiment; MC performed a preliminary experiment and built parts of the hardware; JB, JG-V, and CC supervised the work and provided the theoretical framework; all authors collectively wrote the manuscript. DB and MS share equal contribution to the manuscript.

Funding

This work was partially supported by the EU AnDy Project, receiving funding from the European Union's Horizon 2020 research and innovation programme under grant agreement No. 731540.

Conflict of interest

Authors BS, JB, and JG-V were employed by the Ottobock SE and Co. KGaA.

The remaining authors declare that the research was conducted in the absence of any commercial or financial relationships that could be construed as a potential conflict of interest.

Publisher's note

References

Ajayi, M. O., Djouani, K., and Hamam, Y. (2020). Interaction control for human-exoskeletons. *J. Control Sci. Eng.* 2020, 1–15. doi:10.1155/2020/8472510

Alabdulkarim, S., Kim, S., and Nussbaum, M. A. (2019). Effects of exoskeleton design and precision requirements on physical demands and quality in a simulated overhead drilling task. *Appl. Ergon.* 80, 136–145. doi:10.1016/j.apergo.2019.05.014

Anam, K., and Al-Jumaily, A. A. (2012). Active exoskeleton control systems: State of the art. *Procedia Eng.* 41, 988–994. doi:10.1016/j.proeng.2012.07.273

Bjelle, A., Hagberg, M., and Michaelsson, G. (1979). Clinical and ergonomic factors in prolonged shoulder pain among industrial workers. *Scand. J. Work. Health* 5, 205. doi:10.5271/sjweh.3094

Brooke, J. (1996). Sus-a quick and dirty usability scale. *Usability Eval. industry* 189, 4–7. doi:10.1201/9781498710411-35

Castellini, C., and Ravindra, V. (2014). "A wearable low-cost device based upon force-sensing resistors to detect single-finger forces," in 5th IEEE RAS/EMBS International Conference on Biomedical Robotics and Biomechatronics, 199–203. doi:10.1109/BIOROB.2014.6913776

Cho, E., Chen, R., Merhi, L.-K., Xiao, Z., Pousett, B., and Menon, C. (2016). Force myography to control robotic upper extremity prostheses: A feasibility study. *Front. Bioeng. Biotechnol.* 4, 18. doi:10.3389/fbioe.2016.00018

[Dataset] Comau (2021). Comau Mate exoskeleton home page. mate.

Connan, M., Ruiz Ramírez, E., Vodermayer, B., and Castellini, C. (2016). Assessment of a wearable force- and electromyography device and comparison of the related signals for myocontrol. *Front. Neurorobot.* 10, 17. doi:10.3389/fnbot.2016.00017

Curcie, D. J., Flint, J. A., and Craelius, W. (2001). Biomimetic finger control by filtering of distributed forelimb pressures. *IEEE Trans. Neural Syst. Rehabil. Eng.* 9, 69–75. doi:10.1109/7333.918278

[Dataset] MathWorks (2021). Statistics and machine learning toolbox: User's guide. Available at: https://de.mathworks.com/help/stats/repeatedmeasuresmodel.ranova.html (Accessed January 19, 2022).

Drillis, R., Contini, R., and Bluestein, M. (1964). Body segment parameters. *Artif. Limbs* 8, 44–66. doi:10.1177/001872086300500508

Ebrahimi, A., Gröninger, D., Singer, R., and Schneider, U. (2017). "Control parameter optimization of the actively powered upper body exoskeleton using subjective feedbacks," in 2017 3rd International Conference on Control, Automation and Robotics (ICCAR) (IEEE), 432–437.

[Dataset] Electronics, I. (2022). Fsr 400 short product page. Available at: https://www.interlinkelectronics.com/fsr-400-short (Accessed January 19, 2022).

Fritzsche, L., Galibarov, P. E., Gärtner, C., Bornmann, J., Damsgaard, M., Wall, R., et al. (2021). Assessing the efficiency of exoskeletons in physical strain reduction by biomechanical simulation with anybody modeling system. *Wearable Technol.* 2, e6. doi:10.1017/wtc.2021.5

Gopura, R. A. R. C., Kiguchi, K., and Li, Y. (2009). "Sueful-7: A 7dof upper-limb exoskeleton robot with muscle-model-oriented emg-based control," in 2009 IEEE/RSJ International Conference on Intelligent Robots and Systems, 1126–1131. doi:10.1109/IROS.2009.5353935

Grazi, L., Trigili, E., Proface, G., Giovacchini, F., Crea, S., and Vitiello, N. (2020). Design and experimental evaluation of a semi-passive upper-limb exoskeleton for workers with motorized tuning of assistance. *IEEE Trans. Neural Syst. Rehabil. Eng.* 28, 2276–2285. doi:10.1109/tnsre.2020.3014408

Hart, S. G., and Staveland, L. E. (1988). Development of nasa-tlx (task load index): Results of empirical and theoretical research. *Adv. Psychol.* 52, 139–183. doi:10.1016/S0166-4115(08)62386-9

Hoerl, A. E., and Kennard, R. W. (1970). Ridge regression: Biased estimation for nonorthogonal problems. *Technometrics* 12, 55–67. doi:10.1080/00401706.1970.10488634

Huang, J., Huo, W., Xu, W., Mohammed, S., and Amirat, Y. (2015). Control of upper-limb power-assist exoskeleton using a human-robot interface based on motion intention recognition. *IEEE Trans. Autom. Sci. Eng.* 12, 1257–1270. doi:10.1109/tase.2015.2466634

Huysamen, K., de Looze, M., Bosch, T., Ortiz, J., Toxiri, S., and O'Sullivan, L. W. (2018). Assessment of an active industrial exoskeleton to aid dynamic lifting and lowering manual handling tasks. *Appl. Ergon.* 68, 125–131. doi:10.1016/j.apergo.2017.11.004

Islam, M. R., and Bai, S. (2019). Payload estimation using forcemyography sensors for control of upper-body exoskeleton in load carrying assistance

Maurice, P., Čamernik, J., Gorjan, D., Schirrmeister, B., Bornmann, J., Tagliapietra, L., et al. (2019). Evaluation of paexo, a novel passive exoskeleton for overhead work. *Comput. Methods Biomechanics Biomed. Eng.* 22, S448–S450. doi:10.1080/10255842.2020.1714977

Merletti, R., Botter, A., Troiano, A., Merlo, E., and Minetto, M. (2009). Technology and instrumentation for detection and conditioning of the surface electromyographic signal: State of the art. *Clin. Biomech.* 24, 122–134. doi:10.1016/j.clinbiomech.2008.08.006

Miller, L. M., and Rosen, J. (2010). "Comparison of multi-sensor admittance control in joint space and task space for a seven degree of freedom upper limb exoskeleton," in 2010 3rd IEEE RAS & EMBS International Conference on Biomedical Robotics and Biomechatronics (IEEE), 70.

Missiroli, F., Lotti, N., Tricomi, E., Bokranz, C., Alicea, R., Xiloyannis, M., et al. (2022). Rigid, soft, passive, and active: A hybrid occupational exoskeleton for bimanual multijoint assistance. *IEEE Robot. Autom. Lett.* 7, 2557–2564. doi:10.1109/lra.2022.3142447

Nelson, A. J., Hall, P. T., Saul, K. R., and Crouch, D. L. (2020). Effect of mechanically passive, wearable shoulder exoskeletons on muscle output during dynamic upper extremity movements: A computational simulation study. *J. Appl. biomechanics* 36, 59–67. doi:10.1123/jab.2018-0369

[Dataset] Ottobock (2021). Paexo shoulder exoskeleton system description.

Radmand, A., Scheme, E., and Englehart, K. (2016). High-density force myography: A possible alternative for upper-limb prosthetic control. *J. Rehabil. Res. Dev.* 53, 443–456. doi:10.1682/jrrd.2015.03.0041

Ravindra, V., and Castellini, C. (2014). A comparative analysis of three non-invasive human-machine interfaces for the disabled. *Front. Neurorobot.* 8, 24. doi:10.3389/fnbot.2014.00024

Schmalz, T., Bornmann, J., Schirrmeister, B., Schändlinger, J., and Schuler, M. (2019). Principle study about the effect of an industrial exoskeleton on overhead work. *Verl. Orthopädie-technik, Dortm. Ger. Tech. Rep. Orthop. Tech.* 6, 19. doi:10.3390/ijerph16234792

Singh, R. M., Chatterji, S., and Kumar, A. (2012). Trends and challenges in emg based control scheme of exoskeleton robots-a review. *Int. J. Sci. Eng. Res.* 3, 933–940.

[Dataset] SuitX (2021). ShoulderX exoskeleton home page. Available at: www.suitx.com/shoulderx (accessed June 25, 2021).

Svendsen, S., Bonde, J., Mathiassen, S. E., Stengaard-Pedersen, K., and Frich, L. (2004). Work related shoulder disorders: Quantitative exposure-response relations with reference to arm posture. *Occup. Environ. Med.* 61, 844–853. doi:10.1136/oem.2003.010637

Wininger, M., Kim, N., and Craelius, W. (2008). Pressure signature of forearm as predictor of grip force. *J. Rehabilitation Res. Dev.* 45, 883–892. doi:10.1682/jrrd.2007.11.0187

Yamamoto, K., Hyodo, K., Ishii, M., and Matsuo, T. (2002). Development of power assisting suit for assisting nurse labor. *JSME Int. J. Ser. C* 45, 703–711. doi:10.1299/jsmec.45.703

Yang, C., Zhang, J., Chen, Y., Dong, Y., and Zhang, Y. (2008). "A review of exoskeleton-type systems and their key technologies," in Proceedings of the Institution of Mechanical Engineers, Part C: Journal of Mechanical Engineering Science, 1599–1612. doi:10.1243/09544062jmes936

A.4 Online and offline endpoint force control with the MyoCeption

Title: Omnidirectional endpoint force control through Functional Electrical Stimulation.

Authors: Marek Sierotowicz, and Claudio Castellini.

Journal: Biomedical Physics and Engineering Express.

Manuscript version: Published article.

Citation: M. Sierotowicz and C. Castellini. "Omnidirectional endpoint force control through functional electrical stimulation." In: *Biomedical Physics & Engineering Express* 9.6 (2023), p. 065008. DOI: `10.1088/2057-1976/acf04b`

Abstract: **Objective:** in recent years, Functional Electrical Stimulation has found many applications both within and outside the medical field. However, most available wearable FES devices are not easily adaptable to different users, and most setups rely on task-specific control schemes. **Approach:** in this article, we present a peripheral stimulation prototype featuring a compressive jacket which allows to easily modify the electrode arrangement to better fit any body frame. Coupled with a suitable control system, this device can induce the output of arbitrary forces at the end-effector, which is the basis to facilitate universal, task-independent impedance control of the human limbs. Here, the device is validated by having it provide stimulation currents that should induce a desired force output. The forces exerted by the user as a result of stimulation are measured through a 6-axis force-torque sensor, and compared to the desired forces. Furthermore, here we present the offline analysis of a regression algorithm, trained on the data acquired during the aforementioned validation, which is able to reliably predict the force output based on the stimulation currents. **Main results:** open-loop control of the output force is possible with correlation coefficients between commanded and measured force output direction up to 0.88. A twitch-based calibration procedure shows significant reduction of the RMS error in the online control. The regression algorithm trained offline is able to predict the force output given the injected stimulation with correlations up to 0.94, and average normalized errors of 0.12 RMS. **Significance:** A reliable force output control through FES is the first basis towards higher-level FES force controls. This could eventually provide full, general-purpose control of the human neuromuscular system, which would allow to induce any desired movement in the peri-personal space in individuals affected by e.g. spinal cord injury.

Author contributions: Conceptualization; Software Design; Hardware Design; Formal analysis; Writing-original draft; Writing-review and editing.

IOP Publishing *Biomed. Phys. Eng. Express* **9** (2023) 065008 https://doi.org/10.1088/2057-1976/acf04b

Biomedical Physics & Engineering Express

CrossMark

OPEN ACCESS

RECEIVED
4 April 2023

REVISED
3 August 2023

ACCEPTED FOR PUBLICATION
15 August 2023

PUBLISHED
13 September 2023

PAPER

Omnidirectional endpoint force control through functional electrical stimulation

Marek Sierotowicz[1,2,*] **and Claudio Castellini**[1,2]

[1] Assistive Intelligent Robotics, Friedrich-Alexander-Universität Erlangen-Nürnberg, Erlangen, Germany
[2] The Adaptive Bio-Interfaces Group, Institute of Robotics and Mechatronics, German Aerospace Center (DLR), Oberpfaffenhofen, Germany
[*] Author to whom any correspondence should be addressed.

E-mail: marek.sierotowicz@fau.de

Keywords: FES, Musculoskeletal model, Force control, Robot-inspired muscular control, Impedance control of human limbs, Assistive robotics

Supplementary material for this article is available online

Abstract

Objective. In recent years, Functional Electrical Stimulation has found many applications both within and outside the medical field. However, most available wearable FES devices are not easily adaptable to different users, and most setups rely on task-specific control schemes. *Approach.* In this article, we present a peripheral stimulation prototype featuring a compressive jacket which allows to easily modify the electrode arrangement to better fit any body frame. Coupled with a suitable control system, this device can induce the output of arbitrary forces at the end-effector, which is the basis to facilitate universal, task-independent impedance control of the human limbs. Here, the device is validated by having it provide stimulation currents that should induce a desired force output. The forces exerted by the user as a result of stimulation are measured through a 6-axis force-torque sensor, and compared to the desired forces. Furthermore, here we present the offline analysis of a regression algorithm, trained on the data acquired during the aforementioned validation, which is able to reliably predict the force output based on the stimulation currents. *Main results.* Open-loop control of the output force is possible with correlation coefficients between commanded and measured force output direction up to 0.88. A twitch-based calibration procedure shows significant reduction of the RMS error in the online control. The regression algorithm trained offline is able to predict the force output given the injected stimulation with correlations up to 0.94, and average normalized errors of 0.12 RMS. *Significance.* A reliable force output control through FES is the first basis towards higher-level FES force controls. This could eventually provide full, general-purpose control of the human neuromuscular system, which would allow to induce any desired movement in the peri-personal space in individuals affected by e.g. spinal cord injury.

1. Introduction

Functional electrical stimulation (FES) for artificial generation and support of movements through application of electrical currents represents a promising tool in the rehabilitation of certain neurological patients. Rehabilitation, at its root, has the purpose of forming new neural connections in lieu of damaged ones, typically between the central and the peripheral nervous system, by re-training the patient to perform movements or tasks. FES offers many advantages with respect to rehabilitation facilitated through externally exerted forces, mainly because the patient's muscles are stimulated and thus actively employed for task completion, thus avoiding secondary complications such as muscle atrophy. In the early phase of rehabilitation, FES can be used as an effective tool in a task-specific, restorative therapy program to foster neurological recovery [1]. In the chronic phase after a neurological disease or trauma, FES may still be used as a neuroprosthesis for compensation of completely lost or very weak motor functions. Particularly in individuals with spinal cord injury (SCI) and the associated functional impairments, FES has been successfully employed for assistance in activities of daily living (ADL), both using trans-cutaneous [2] and intramuscular electrodes [3]. Non-invasive FES applied through surface electrodes is also used in applications outside of the medical field, for example VR and AR [4].

Most control schemes focus on restoring functional, task relevant movements, such as reaching and grasping [2, 3], and focus on the identification of the dynamics relevant to these [5, 6]. Such parameters, however, are not guaranteed to generalize well over different postures. On the one hand, black box approaches typically have to sample the effects of muscle contractions in various postures [7, 8]. Musculoskeletal models, on the other hand, can inherently account for at least some effects of posture changes [9, 10]. In robotics, impedance-based controls can be used to impose a certain dynamic behaviour between a robot and its environment [11]. Impedance controls are robust in terms of kinematic singularities, and can be well integrated in wider motion-planning algorithms, but the main purpose of impedance control is to facilitate the interaction of a robot with an unpredictable environment with non-linear dynamics [11]. However, the characteristics of impedance control make it robust also with respect to actuators exhibiting these characteristics, as can be human muscles. A suitable impedance could facilitate conversion from a positional error into a desired force output, which is more directly correlated to muscular activity. FES-based force controls have been proposed, among others, in [7, 12, 13]. These works all present black box models of the endpoint force output as a consequence of FES. In the context of FES, a suitable impedance control could be used to assist movements towards any desired point in the user's peri-personal space, leading to a more general-purpose paradigm, which could be beneficial in rehabilitation, but especially in the case of FES used as a neuroprosthesis. Razavian *et al* present a demonstration of such a concept [7]. The compliant nature of the human body could allow for the safe inclusion of the positional error's integral over time in the impedance, which would lead to increased robustness with respect to modelling errors. Integrative terms are often excluded from impedance controls in conventional robotics, as they would cause an increase of force output over time, should the robot encounter an obstacle preventing it from reaching the desired pose. In such a scenario, the robot could cause damage to itself or its surroundings if its force output is not limited.

This paper should serve as a system description of the FES device, which consists of a wearable surface stimulation device designed to provide proportional force control through FES on the upper limb of a user on up to 10 channels with a resolution of 16 bits, and assess its capability to induce a desired force output in real time. Because of its practicality and versatility, surface FES is widely used in commercially available products, such as the Teslasuit® platform (VR Electronics Ltd., London, UK). This device has been successfully employed in user studies with able-bodied participants [14], and represents a good commercial benchmark, as it integrates various sensor modalities and gel-less surface stimulation electrodes. However, this system cannot adjust well to different body frames, and the electrode arrangement cannot be modified. The device proposed here, on the other hand, features a Velcro-lined compressive jacket which allows for easy modifications in electrode arrangement to fit any user frame. The jacket also increases repeatability of electrode placement once the ideal arrangement for an individual user has been established.

While this device proposes to be a general-purpose platform designed to test various control algorithms, here the system is driven by a musculoskeletal model presented and validated in [9]. Therein, the musculoskeletal model was tested against a third-party model introduced in [10], which was taken as baseline. The model associates a *line of action* to each stimulated muscle group, as exemplified in [15]. A core principle and fundamental goal in the design philosophy of this system is the adaptability to different users. In order to achieve this, the musculoskeletal model can be easily modified to better fit each individual without the need for much anatomical expertise. To this end, a calibration procedure able to adjust the model geometry is also introduced here. Canonically, a model based on line of action relies on a line running through the average centroid of the physiological cross section along the whole length of the stimulated muscle groups, as introduced in [16] and, more recently, in [17]. Many studies have demonstrated how inhomogeneities in muscle activation can lead to great effects on joint momenta. In the case of the musculoskeletal model used here, the reconstruction of the line of action is based on the observation of functional effects of muscle contraction on the musculoskeletal system in a given position, as introduced among others in [18]. Here, the model uses a fast and computationally efficient *Nearest Neighbour* recruitment strategy to calculate the stimulation currents necessary to cause a given endpoint force output.

The system is validated in an online experiment where the FES-induced force output of 3 able-bodied volunteers is compared to a desired force output. Part of these results were published in [19]. In addition, we evaluate the performance of an offline-trained predictor which is able to precisely predict the force output both in task space and in joint space based on the stimulation currents. Such a predictor could be trained based on data from a force-torque sensor prior to the normal operation of the device in a setup similar to the one used during the online system validation.

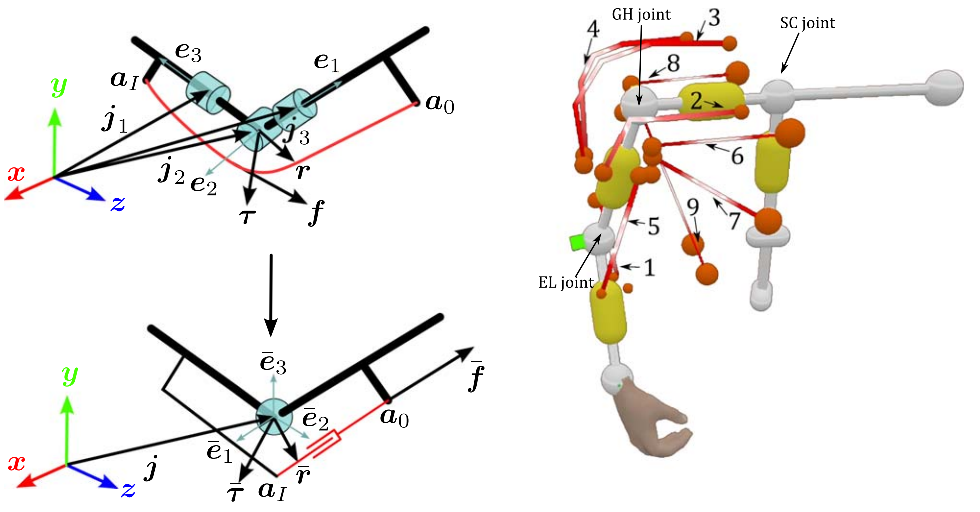

(a)   (b)

Figure 1. (a): Conceptual depiction of the process by which a muscle can be modeled as a continuous curve an then lumped into a single prismatic actuator able to exert a force by contracting along the direction of the vector $\bar{\boldsymbol f}$, and having an effective lever arm $\bar{\boldsymbol r}$, thus enabling the actuator to apply a torque $\bar{\boldsymbol \tau}$ about the joint $\boldsymbol j$. Every joint is modelled as having 3 revolute axes. (b): The musculoskeletal model. Each electrode pair is associated with a red line. The labels represent the channel numbers. The joints are also labeled.

2. Method

2.1. Musculoskeletal model

The line of action associated to every stimulated muscle group is routed through a series of points lying on a curve between an origin $\boldsymbol a_0 \in \mathbb{R}^3$ and an insertion point $\boldsymbol a_I \in \mathbb{R}^3$. In general, we can consider the line of action as a continuous curve in 3D space, with all intermediate positions $\boldsymbol a(l) \in \mathbb{R}^3$ between $\boldsymbol a_0$ and $\boldsymbol a_I$ defined by a scalar parameter $l \in [l_0, l_I] \subset \mathbb{R}$, so that $\boldsymbol a_0 = \boldsymbol a(l_0)$ and $\boldsymbol a_I = \boldsymbol a(l_I)$, as shown in figure 1(a).

The muscle groups stimulated by one electrode pair are considered as a string routed along the line of action's curve, with the muscle force being exerted homogeneously in a tangential direction, which is to say that the force along the line of action has constant module $f \in \mathbb{R}$. Given this, knowing the line of action's routing in 3-D space, we can compute the average force vector $\bar{\boldsymbol f} \in \mathbb{R}^3$ through

$$\bar{\boldsymbol f} = (l_I - l_0)^{-1}\int_{l_0}^{l_I} \boldsymbol f(l)dl \tag{1a}$$

$$= (l_I - l_0)^{-1}\int_{l_0}^{l_I} f\frac{d\boldsymbol a(l)}{dl}\left\|\frac{d\boldsymbol a(l)}{dl}\right\|^{-1} dl \tag{1b}$$

$$= f(l_I - l_0)^{-1}\int_{l_0}^{l_I} \frac{d\boldsymbol a(l)}{\|d\boldsymbol a(l)\|}dl. \tag{1c}$$

Following the same rationale, we can calculate an average torque vector $\bar{\boldsymbol\tau} \in \mathbb{R}^3$ exerted by the muscle group about the joint's position $\boldsymbol j \in \mathbb{R}^3$

$$\bar{\boldsymbol\tau} = f(l_I - l_0)^{-1}\int_{l_0}^{l_I} (\boldsymbol a(l) - \boldsymbol j) \times \frac{d\boldsymbol a(l)}{\|d\boldsymbol a(l)\|}dl. \tag{2}$$

Reducing the points on the curve to a finite set of $N + 1$ points $\boldsymbol a_i \in \{\boldsymbol a_0, \dots \boldsymbol a_i, \dots \boldsymbol a_N\} \subset \mathbb{R}^3$, equation (2) becomes a sum of the form

$$\bar{\boldsymbol\tau} = fN^{-1}\sum_{i=1}^{N}(\boldsymbol a_i - \boldsymbol j) \times [(\boldsymbol a_i - \boldsymbol a_{i-1})\|\boldsymbol a_i - \boldsymbol a_{i-1}\|^{-1}]. \tag{3}$$

The average force $\bar{\boldsymbol f}$ and average torque $\bar{\boldsymbol\tau}$ derived from the line of action characterize a lumped model of the muscle, which behaves like a prismatic joint able to exert a force f determined by the stimulation in the direction $\bar{\boldsymbol f} f^{-1}$ by contraction, with an average effective moment arm $\bar{\boldsymbol r}$, which results in a torque $\bar{\boldsymbol\tau}$ about the joint at position $\boldsymbol j$ with revolute axes $\bar{\boldsymbol e}_i$, as depicted in figure 1(a). Depending on which skeletal segments the muscle group originates from and inserts into, this prismatic actuator approximation of the stimulated muscle group can exert a torque around more than one of the skeleton's rotational axes. In particular, if the i-th degree of freedom is a revolute joint at position $\boldsymbol j$ with its axis pointing in a known direction $\bar{\boldsymbol e}_i \in \mathbb{R}^3$, if a muscle group is able to exert a torque about it, we can reduce the expected torque computed as shown in equations (2) and (3) to a scalar torque magnitude $\bar\tau_i \in \mathbb{R}$ by computing

$$\bar\tau_i = \bar{\boldsymbol\tau}^T\bar{\boldsymbol e}_i. \tag{4}$$

If the muscle group is not able to exert a torque about the i-th degree of freedom, on the other hand, the scalar projection of the expected torque onto joint space is 0. As depicted in figure 1(a), every joint in the musculoskeletal model is modelled as having 3 revolute axes. This is done due to the difficulty of reliably measuring the direction of the anatomically correct revolute axes. This makes every joint in the model as depicted in figure 1(b) defined by a single position $\boldsymbol j$ and 3 revolute axes.

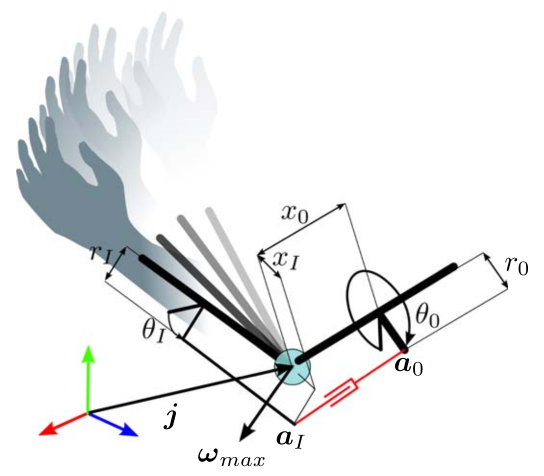

Figure 2. Depiction of the twitch calibration. A sharp muscle stimulation causes a twitch characterized by an angular velocity vector $\boldsymbol{\omega}_{\max}$.

2.2. Model calibration

The line of action's routing can be initially set based on cursory anatomical expertise and the known electrode placement, but can be further adjusted based on the measured response to stimulation pulses. Here, a simplified calibration procedure is implemented. This is based on the assumption that the average force vector $\bar{\boldsymbol{f}}$ should lie in the plane in which the limb moves when a stimulation pulse is applied. The calibration finds the points $\boldsymbol{a}_i$ for each line of action which minimize the difference between the expected and the measured torque output in joint space resulting from the stimulation pulse. Although this condition could be satisfied even if the line of action were not to lie entirely on this same plane, this is assumed for simplicity's sake. A stimulation pulse causes an average torque $\bar{\boldsymbol{\tau}}$ over the pulse time, which in turn causes the body segments distal to the affected joint at position $\boldsymbol{j}$ to accelerate at an angular acceleration rate $\bar{\boldsymbol{\tau}} \approx \bar{\boldsymbol{\alpha}} \boldsymbol{I}_{distal}$, where $\boldsymbol{I}_{distal} \in \mathbb{R}^{3\times 3}$ is the cumulative moment of inertia of the distal body segments, which is assumed to be constant throughout the stimulation, and $\bar{\boldsymbol{\alpha}} \in \mathbb{R}^3$ is the angular acceleration vector due to the twitch. In this study, the moment of inertia was calculated based on the user's mass and the anthropometric tables from [20]. Over the course of this study, the participants were directed to hold their arm in the starting position voluntarily, and therefore the influence of gravity was assumed to be compensated by volitional muscle contraction. Assuming, furthermore, a constant acceleration rate during the stimulation pulse, and an initial rest state of the joint, the distal body segments reach a maximum angular velocity $\boldsymbol{\omega}_{\max} \approx \bar{\boldsymbol{\alpha}}(t_{end} - t_0) \in \mathbb{R}^3$, where t_0 and t_{end} are the times at which the stimulation starts and ends, respectively. Therefore, we have an approximate proportionality between the maximal observed angular velocity and the expected torque of the stimulated muscle group, namely

$$\bar{\boldsymbol{\tau}} \approx \boldsymbol{\omega}_{\max} (t_{end} - t_0)^{-1} \boldsymbol{I}_{distal}. \tag{5}$$

The plane of movement for the limb is defined as passing through the joint's position $\boldsymbol{j}$ and being normal to the angular velocity vector $\boldsymbol{\omega}_{\max}$ of the twitch itself. As shown in figure 2, based on the observed twitch $\boldsymbol{\omega}_{\max}$, the position of the origin point $\boldsymbol{a}_0$ and the insertion point $\boldsymbol{a}_I$ are set over the $\theta_0 \in \mathbb{R}$ and $\theta_I \in \mathbb{R}$ coordinates, respectively, in order to minimize the distance of the two points from the twitch plane passing through $\boldsymbol{j}$ and normal to $\boldsymbol{\omega}_{\max}$. Here, θ_0 and θ_I are the azimuth of the origin and insertion point, respectively, expressed in a cylindrical coordinate frame the height axis of which corresponds to the longitudinal axis of the proximal body segment in the case of the origin point and the distal body segment for the insertion point, as shown in figure 2. The origin and insertion point positions are additionally defined by a radius $r_0 \in \mathbb{R}$ and $r_I \in \mathbb{R}$, respectively, and a height $x_0 \in \mathbb{R}$ and $x_I \in \mathbb{R}$. This optimization is usually done based on a series of K observed twitch vectors $\boldsymbol{\omega}_k \in \mathbb{R}^3$, $k \in \{1,\ldots, M\} \subset \mathbb{N}$. A cost function is minimized in order to find the cylindrical coordinate θ_I^* which minimizes the distance between the insertion point $\boldsymbol{a}_I$ and the plane in which the body segment moves during the twitch motion. The cost function is represented by the sum of all the observed distances of the line of action routing points from this plane, and it is minimized as follows

$$\theta_I^* = \underset{\theta_I}{\operatorname{argmin}} \left(\sum_{k=1}^{K} ((\boldsymbol{a}_I(\theta_I) - \boldsymbol{j})^T \boldsymbol{\omega}_k \cdot \|\boldsymbol{\omega}_k\|^{-1})^2 \right). \tag{6}$$

The cost function can be minimized through a gradient descent. All routing points with freely settable coordinates, such as the origin point $\boldsymbol{a}_0$, are adjusted analogously. In addition to routing point placement, the magnitude of the observed twitch angular velocity vector $\boldsymbol{\omega}_{\max}$ leads to an estimation of the proportionality constant g_i between the stimulation current s_i and the force f. In addition to that, the stimulation is offset by a constant q_i so that minimum current is at the edge at which force is exerted as a result of stimulation. This offset is set manually during an initial phase of comfort level setting occurring at the beginning of the experimental session, shown as *Comfort level setting* in figure 6. By setting these two coefficients, the stimulation currents delivered to the user can be assumed to be within a nearly linear region of the force to stimulation curve. The coefficients were determined by identifying a minimum and maximum threshold for each channel current. The minimum threshold is slightly below the lowest amount of current that the user is able to discern for a given stimulation channel. The maximum is around the highest non-painful stimulation current for which the force output stops rising. These thresholds were maintained throughout the experiment. The expected torque's magnitude $\bar{\tau}_i$ is computed as in equation (3) by plugging $f = (s_i + q_i)g_i$. While the present study was performed with the arm locked in a single posture, the calibration procedure had to be performed with

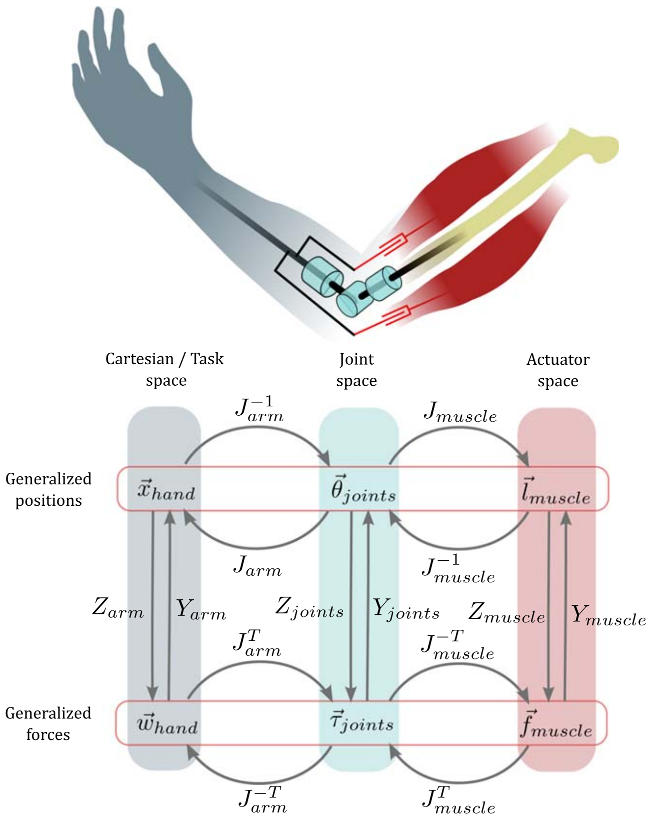

Figure 3. General overview of the coordinate spaces relevant for the control of the human musculoskeletal system. Muscles can be modeled as compliant, prismatic joints. In all spaces, a corresponding set of generalized forces can be defined. These forces are exerted on the musculoskeletal system by both its own actuators and the environment. The momentary positional state of the system and its time derivatives can be linked to a generalized force through an impedance $\boldsymbol{Z}$, whose inverse is the admittance $\boldsymbol{Y}$. Positions and forces in either space can be projected onto another space by using forward or inverse kinematics, or employing differential calculus, by the appropriate Jacobians $\boldsymbol{J}$. These can't always be inverted, and when this is the case, a fitting matrix pseudo-inverse should be put in place.

the arm free to move, as the twitch resulting from a sharp stimulation signal had to be observed. Since the calibration operates based on several stored twitch vectors, it could place the insertion and origin point in a position that should minimize the distance of the line of action from the twitch plane for all the postures in which the calibration is executed.

2.3 Projection matrices

For the purposes of movement control, it is necessary to calculate the projection matrices from the relevant coordinate systems shown in figure 3, which are the muscular Jacobian $\boldsymbol{J}_{\boldsymbol{mus}} := \frac{\partial \boldsymbol{l}_{mus}}{\partial \boldsymbol{\theta}_{joints}} \in \mathbb{R}^{M \times J}$, which can be computed by differentiating the elongation $\boldsymbol{l}_{mus}$ of M muscle groups over the revolute angular motion $\boldsymbol{\theta}_{joints}$ of J joints, and the arm Jacobian $\boldsymbol{J}_{arm} := \frac{\partial \boldsymbol{x}_{arm}}{\partial \boldsymbol{\theta}_{joints}} \in \mathbb{R}^{6 \times J}$, computed by differentiating the pose $\boldsymbol{x}_{arm}$ of the arm's end point, which comprises both 3 positional and 3 orientation coordinates, by the same rotational movements $\boldsymbol{\theta}_{joints}$. In both cases, due to energy conservation, the Jacobians can project velocities or differentially small shifts in position from the joint space to the Cartesian or muscular space, as well as generalized Cartesian wrenches $\boldsymbol{w}_{hand} \in \mathbb{R}^6$ and muscle forces $\boldsymbol{f}_{mus}$ onto the joint space.

The averaged torque from equation (4) can be used to approximate the muscular Jacobian $\boldsymbol{J}_{\boldsymbol{mus}}$ defined from the muscle space to the joint space, as shown in figure 3, as per

$$\boldsymbol{\tau}_{joints} = \begin{bmatrix} \frac{\overline{\tau}_{1,1}}{f_1} & \cdots & \frac{\overline{\tau}_{1,M}}{f_M} \\ \vdots & & \vdots \\ \frac{\overline{\tau}_{J,1}}{f_1} & \cdots & \frac{\overline{\tau}_{J,M}}{f_M} \end{bmatrix} \boldsymbol{f}_{mus} = \boldsymbol{J}_{mus}^{T} \boldsymbol{f}_{mus}, \qquad (7)$$

where $\boldsymbol{f}_{mus} \in \mathbb{R}^M$ is the vector of the forces acting on the M actuators, formed by the single scalar force components f_i, and $\overline{\tau}_{j,i}$ is the scalar projection of expected torque caused by the i-th muscle around the j-th revolute joint, as shown in equation (4).

The arm's Jacobian $\boldsymbol{J}_{arm}$ is similarly calculated and can also be used to project the Cartesian wrench $\boldsymbol{w}_{hand}$ onto the joint space, as per

$$\boldsymbol{\tau}_{joints} = \qquad (8a)$$

$$= \begin{bmatrix} \bar{\boldsymbol{e}}_1^T((\boldsymbol{x}_{hand} - \boldsymbol{j}_1) \times \boldsymbol{f}_{hand} + \boldsymbol{\tau}_{hand}) \\ \vdots \\ \bar{\boldsymbol{e}}_J^T((\boldsymbol{x}_{hand} - \boldsymbol{j}_J) \times \boldsymbol{f}_{hand} + \boldsymbol{\tau}_{hand}) \end{bmatrix} = \tag{8b}$$

$$= \begin{bmatrix} [\bar{\boldsymbol{e}}_1^T[\boldsymbol{x}_{hand} - \boldsymbol{j}_1]_\times, \bar{\boldsymbol{e}}_1^T] \\ \vdots \\ [\bar{\boldsymbol{e}}_J^T[\boldsymbol{x}_{hand} - \boldsymbol{j}_J]_\times, \bar{\boldsymbol{e}}_J^T] \end{bmatrix} \begin{bmatrix} \boldsymbol{f}_{hand} \\ \boldsymbol{\tau}_{hand} \end{bmatrix} = \tag{8c}$$

$$= \boldsymbol{J}_{arm}^T \boldsymbol{w}_{hand}. \tag{8d}$$

$[\boldsymbol{a}]_\times \in \mathbb{R}^{3\times3}$ is the so-called skew symmetric matrix of the vector $\boldsymbol{a}$, which satisfies $[\boldsymbol{a}]_\times \boldsymbol{b} = \boldsymbol{a} \times \boldsymbol{b}$,×being the vector cross product, $\bar{\boldsymbol{e}}_j \in \mathbb{R}^3$ represents the direction of the j-th joint's axis in the Cartesian coordinate frame, $\boldsymbol{f}_{hand} \in \mathbb{R}^3$ and $\boldsymbol{\tau}_{hand} \in \mathbb{R}^3$ are the desired force and the torque to be applied to the endpoint, which are concatenated in a wrench $\boldsymbol{w}_{hand}$ as shown above. These relations are summarized in figure 3. The control system uses a musculoskeletal model shown in figure 1(b), which works based on the principles discussed above. This model is used to compute the stimulation necessary to achieve a certain force output at the endpoint, and this is done by projecting the desired wrench $\boldsymbol{w}_{hand}$ onto the joint space using the transposed arm Jacobian $\boldsymbol{J}_{arm}$. In order to calculate the necessary muscle forces $\boldsymbol{f}_{mus}$, and consequently the stimulation currents $\boldsymbol{s}_{mus} \in \mathbb{R}^M$, the desired joint torques are approximately projected onto muscle force space using a *Nearest Neighbour* muscle recruitment strategy, by which only the single muscle group that would cause the torque closest in direction to the desired torque on a given joint are stimulated. Solving for the necessary muscle forces is often non-trivial, as muscle forces are not a conventional vector space, because of the fact that muscles can only actively contract, not expand. The pseudo-code in algorithm 1 explains how this strategy works.

Algorithm 1. The muscle force and stimulation solver iterates over all joints shown in figure 1(b). For each joint, only the muscle group which would elicit the torque closest in direction to the desired one is stimulated.

```
Require: $\boldsymbol{w}_{hand} \in \mathbb{R}^6$, which is the desired wrench at the endpoint
Require: $\boldsymbol{J}_{mus} = \frac{\partial \boldsymbol{l}_{mus}}{\partial \boldsymbol{\theta}_{joints}} := [\boldsymbol{c}_1, \ldots, \boldsymbol{c}_J] \in \mathbb{R}^{M\times J}$, $\boldsymbol{c}_i \in \mathbb{R}^M$
Require: $\boldsymbol{J}_{arm} = \frac{\partial \boldsymbol{x}_{arm}}{\partial \boldsymbol{\theta}_{joints}} \in \mathbb{R}^{6\times J}$
Require: $q_i, g_i, i \in \{1, \ldots, M\} \subset \mathbb{N}$, $g_i$ and $q_i$ as described in section 2.2
$\boldsymbol{\tau}_{target} := [\tau_{target,1}, \ldots, \tau_{target,J}] \in \mathbb{R}^J \leftarrow \boldsymbol{J}_{arm}^T \boldsymbol{w}_{hand}$, as per equation (8a)–(8d)
$\boldsymbol{f}_{mus} := [f_1, \ldots, f_M]^T \leftarrow \boldsymbol{0} \in \mathbb{R}^M$, $\boldsymbol{0}$ being a vector with all zero elements
$\boldsymbol{s}_{mus} := [s_1, \ldots, s_M]^T \leftarrow \boldsymbol{0} \in \mathbb{R}^M$
$k \leftarrow 1$
while $k \leqslant J - 2$ do
    $\boldsymbol{\tau}_{des} \leftarrow [\tau_{target,k}, \tau_{target,k+1}, \tau_{target,k+2}]^T \in \mathbb{R}^3$
    $\boldsymbol{J}_{mus,sub} := [\boldsymbol{d}_1, \ldots, \boldsymbol{d}_M]^T$, $\boldsymbol{d}_i \in \mathbb{R}^3 \leftarrow [\boldsymbol{c}_k, \boldsymbol{c}_{k+1}, \boldsymbol{c}_{k+2}]^T \in \mathbb{R}^{3\times M}$
    $\boldsymbol{J}_{mus,sub,normed} \leftarrow [\boldsymbol{d}_1 \cdot \|\boldsymbol{d}_1\|^{-1}, \ldots, \boldsymbol{d}_M \cdot \|\boldsymbol{d}_M\|^{-1}]^T \in \mathbb{R}^{3\times M}$
    $\boldsymbol{p} := [p_1, \ldots, p_M]^T \leftarrow \boldsymbol{J}_{mus,sub,normed}^T \boldsymbol{\tau}_{des} \in \mathbb{R}^M$
    $c \leftarrow \underset{1\leqslant i\leqslant M}{argmax}(p_i)$, $c$ is the index of the muscle torque closest in direction to $\boldsymbol{\tau}_{des}$
(Continued.)
    $f_c \leftarrow \boldsymbol{\tau}_{target}^T \boldsymbol{d}_c \cdot (\|\bar{\boldsymbol{r}}\| \cdot \|\boldsymbol{d}_c\|)^{-1}$, with $\bar{\boldsymbol{r}}$ as shown in figure 1(a)
    $s_c \leftarrow f_c g_c^{-1} - q_c$
    $k \leftarrow k + 3$, the increment being 3 because all joints have 3 revolute axes
end while
yield $\boldsymbol{f}_{mus}$, $\boldsymbol{s}_{mus}$
```

The algorithm iterates over all joints shown in figure 1(b), which are all modelled as having 3 revolute axes, as shown in figure 1(a). Because of this, both the required and the exerted torques for each joint are three-dimensional. This simplification was put in place because of the difficulty of reliably estimating the direction of certain anatomical musculoskeletal axes. The Nearest Neighbour recruitment strategy can be applied without this simplification, but it does require that every modeled muscle group only exerts a torque about one joint, and that each joint can be defined as having a central position $\boldsymbol{j}$ and up to three revolute axes. The Nearest Neighbour recruitment strategy is efficient in terms of computation and time, in comparison to iterative optimisation algorithms used, for example, in [12]. It also reduces the amount of current delivered to the user, thus improving comfort and minimizing metabolic costs.

2.4. Hardware and experimental setup

The FES device's wearable stimulation setup can inject stimulation currents through surface electrodes. The system can provide amplitude-modulated, rectangular current stimulation pulses with 16-bits resolution on up to 10 channels, with a pulse-width of 200 μs, frequency ranging from 0.5 Hz to 100 Hz, and a maximum current amplitude of 70 mA. In addition to the wearable stimulation device, the setup includes a posture tracking sensor system, which in the case of the experiment presented here was the BodyRig [21], an IMU-based posture tracker, visible in figure 4.

In order to generate the stimulation currents, the setup includes 3 FES devices (2 *TNS SM2 AKS* and 1 *TNS SM 2MF*, Pierenkemper GmbH, Am Geiersberg 6, 35 630 Ehringshausen, Germany). An intermediate wirelessly controlled modulation box built around the wireless Bluetooth module *ESP32 Wroom 32*, Espressif systems modulates the generated currents in amplitude from 0 A to the maximum amplitude set on the FES device. The channels are electrically insulated from each other, and are controlled by using analog optocouplers driven by operational amplifier-based driver circuits. The levels of stimulation for each channel are calculated by a remote host running the control model. Exact schematics of the control box are available on request.

The system was validated through an experiment. The setup consisted of the wearable stimulation device, the BodyRig posture tracker [21], as well as a

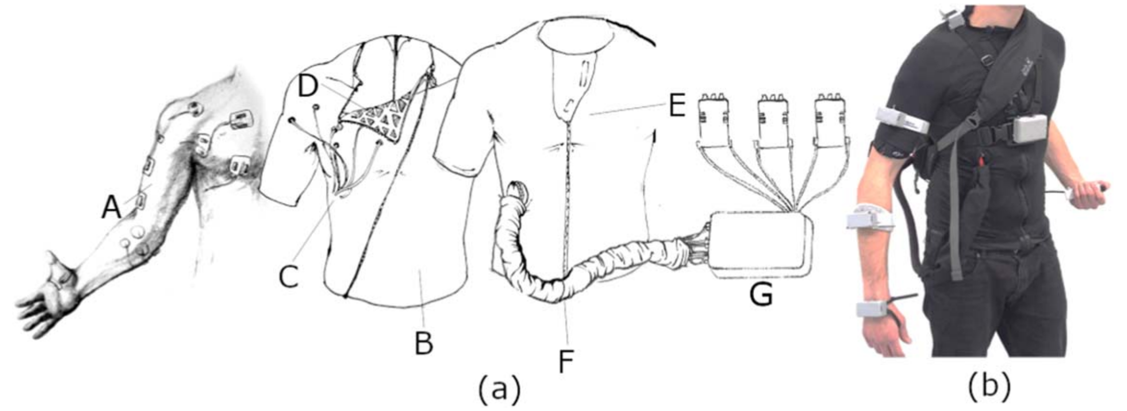

Figure 4. (a):. Main elements of the wearable stimulator. From left to right: adhesive electrodes applied to the user's skin, fitted with Velcro hooks on the outside (A). Inner compression jacket (B) featuring holes (C) to run the electrode cables through, fitted with Velcro loops on the inside (D). Outer jacket (E) grouping the cables in a single umbilical (F) connected to the control electronics (G), and providing further compression. b: the full setup worn by a user.

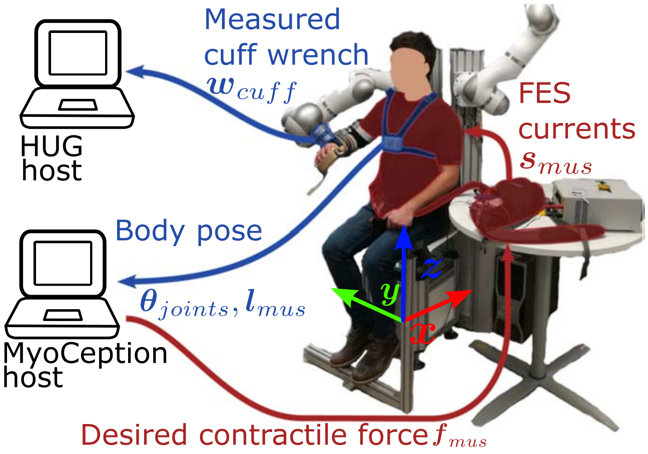

Figure 5. Experimental setup. The two hosts were working independently of each other during the experiment, and the measurements were manually synchronized during offline analysis. The stimulation device is highlighted in red, as is the actuation loop. The posture and force torque measurement devices and respective signals are highlighted in blue. The coordinate frame used in the experiment is also visible.

robotic arm [22], which was used here as a measurement device. The robotic arm streamed the measurements of its 6-DoF force-torque sensor, which is visible in figure 5 and served as coupling between the robot's end effector and the cuff holding the user's forearm, to its own host at a rate of 1kHz. The stimulation device's control loop was operating at a rate of 200 Hz on a separate host, as shown in figure 5. The signals to the single stimulation channels, however, were sub-sampled at 20 Hz. This rate for the controller was deemed sufficient for this scenario based on pre-tests, which showed that more than 99% of the force output signal power lies between 0 Hz and 2 Hz on the frequency spectrum. This is in line with observations published in [23]. The outcome metrics of this study are the measured force outputs compared with the commanded forces in terms of Pearson correlation coefficients. Furthermore, a regression model was trained and cross validated on the acquired data in order to test the feasibility of a machine learning-based controller of the force output via FES.

The surface electrodes were applied in order to stimulate the *biceps brachii*, the *triceps brachii*, *the deltoid superior, anterior, posterior*, the *clavicular* and the *sternocostal* head of the *pectoralis major*, the *trapezoid scapular*, and the *latissimus dorsi*.

2.5. Experimental protocol

The system is validated here through an experiment employing 3 able-bodied male volunteers (34.3 ± 12.7 years old, 1.76 ± 0.09 m, 77.3 ± 6.67 kg). The experiment was approved by the ethical commission of the university/institution to which the authors are affiliated. This research was conducted in accordance with the principles of the Declaration of Helsinki and in accordance with local statutory requirements. All participants were thoroughly informed about the experimental protocol, and all gave written informed

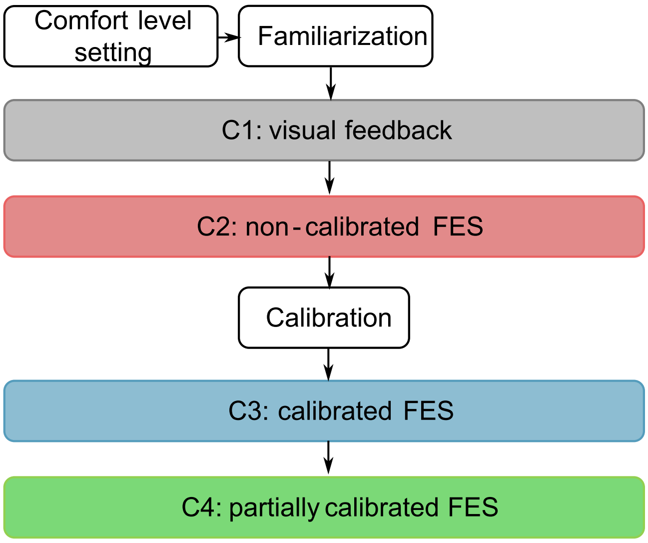

Figure 6. Breakdown of the experimental session.

consent to participate in the study. This research involves no identifiable human subjects, and does not rely on clinical trials. Participants sat in a predetermined position as shown in figure 5 with their right arm coupled to a force-torque sensor attached to a robotic manipulator [22]. Using a robot-mounted force-torque sensor allowed for easy realignment if the robot had to be re-positioned to better fit the size of the user, as the robot's arm made it possible to instantly know the absolute orientation of the force-torque sensor in space, and therefore to reconstruct the absolute direction of the measured forces and torques in the environment. The session breakdown is shown in figure 6. The participants were first asked to voluntarily exert forces along 6 directions, namely backward, forward, upward, downward, left and right, for 10 repetitions by following visual feedback (C1).

Thereafter, visual feedback was taken away. The device, without any calibration, was then fed desired force output vectors selected randomly among the 6 directions from condition C1 at 2 different magnitudes (namely 50% and 100% of the achievable force output, as determined by the threshold detection during the comfort level setting), over 5 repetitions, for a total of 60 commanded force outputs. All conditions employing FES used such a sequence of commanded forces. The FES device provided stimulation to induce a force output corresponding to the commanded force outputs (C2).

Following this, the calibration procedure described above was performed for all stimulation channels, and the experiment with no visual feedback was then repeated with the calibrated device (C3). Finally, one further condition was tested, where the parameters set through the device's calibration are maintained, except the proportionality constant g_i between the stimulation s_i and the muscle group's contraction force f_i. This proportionality constant is reset to its initial value. This condition has the goal of verifying that, if the calibration procedure improves the performance by correcting the musculoskeletal model or by virtue of increasing, even saturating the current flow through the stimulation channels (C4).

2.6. Signal conditioning and data analysis

During the experiment, each sequence consisted of a total of 12 target output forces (6 directions×2 magnitudes), corresponding to a set of stimulation currents delivered by the FES device in all experimental conditions except for the first one, where the participants were directed to exert a given force output through visual feedback. In either case, the contraction lasted 2 seconds, and was always followed by 2 seconds of inactivity before the next contraction. The force output measurement was given by the difference of the wrench measured by the 6-DoF force-torque sensor, minus the wrench measured immediately before the onset of the stimulation currents. The difference was averaged over the whole time of contraction. This was done in order to subtract out of the wrench measurement the effect of the arm's own weight and of the user's volitional actions immediately prior to the onset of stimulation. Because the robotic arm used for measurements and the FES device were using two different coordinate systems, the sets of measured and commanded forces were aligned using the Kabsch algorithm [24] through a rotation around the vertical axis. The reason why the rotation was limited to the vertical axis is that the two coordinate systems can be presumed to be aligned along the vertical direction, as the FES device's coordinate system is based on IMUs, which are able to measure the direction of the gravitational acceleration vector. The measured forces thus calculated were compared to the commanded forces in terms of the Pearson's correlation coefficients

Table 1. Table with squared Pearson's correlation coefficient and normalized root mean square error of the offline predictors trained on the Cartesian output wrench (left columns) and on the joint torques (right columns). All values are given in the format R^2/RMS. The RMSE is normalized by the maximum range of the regression target.

	Regression to		Regression to		
	Cartesian wrench		joint torques		
Subject/Condition	Force	Torque	SC-joint	GH-joint	EL-joint
S1/C2	0.92/0.10	0.86/0.10	0.92/0.13	0.86/0.14	0.93/0.14
S1/C3	0.91/0.11	0.93/0.08	0.73/0.17	0.87/0.17	0.84/0.13
S1/C4	0.91/0.11	0.94/0.09	0.70/0.17	0.88/0.12	0.92/0.10
S2/C2	0.94/0.09	0.83/0.12	0.94/0.06	0.92/0.07	0.91/0.07
S2/C3	0.92/0.09	0.89/0.10	0.93/0.06	0.92/0.07	0.95/0.08
S2/C4	0.86/0.09	0.84/0.09	0.92/0.08	0.92/0.08	0.95/0.09
S3/C2	0.82/0.15	0.74/0.21	0.77/0.18	0.83/0.15	0.76/0.16
S3/C3	0.74/0.17	0.67/0.26	0.85/0.16	0.77/0.17	0.72/0.18
S3/C4	0.87/0.14	0.80/0.14	0.88/0.13	0.84/0.14	0.83/0.14

of the commanded force direction with the measured force direction.

Besides the analysis of the online system performance, a regression algorithm was trained with the goal of predicting the output wrench $\boldsymbol{w}_{hand} \in \mathbb{R}^6$ based on the stimulation currents. This algorithm was based on ridge regression applied to a so-called Random Fourier Features kernel (RFF) [25]. The predictor was cross-validated over a 10-fold partition of the available data, which consisted of 60 data points for each subject and each of the 3 experimental conditions where the FES device was delivering stimulation currents. The regression's predicted wrench is evaluated in terms of squared Pearson correlation coefficient (R squared) of the prediction w.r.t. the ground truth represented by the measured forces and torques, as well as in terms of root mean square (RMS) error. An analogous predictor was trained to predict the estimated joint torques $\boldsymbol{\tau}_{joints} \in \mathbb{R}^J$ as a function of the stimulation currents $\boldsymbol{s} \in \mathbb{R}^M$. The joint torques were not directly measured, and had to be estimated by projecting all wrenches acting on the user's body onto the joint space, as shown in equation (8*a*)–(8*d*). The estimated joint torques are used as target labels to train the regression algorithm to predict the joint torques based on stimulation currents.

3. Results

The results are subdivided between the offline analysis of the force output predictor and the evaluation of the force output control in real time, hereafter referred to as online control.

For the offline analysis of the force output predictor, table 1 shows the root mean square error (RMSE) normalized by the maximum range of force or torque output for each subject and experimental condition, and the squared Pearson correlation coefficients (R^2) of the regression algorithm trained to predict the force output in Cartesian space and the joint torques based on the stimulation currents, respectively. The joints are as shown in figure 1(b). The predictor'performance achieved a grand average of 0.860 R^2 and 0.124 RMSE for the prediction of the joint torques, and 0.855 R^2 and 0.124 RMSE for the prediction of Cartesian output wrench.

Concerning the results of the online control, figure 7 shows the correlation matrices of the commanded force direction $\boldsymbol{f}_c = [f_{c,x}, f_{c,y}, f_{c,z}]^T \in \mathbb{R}^3$ w.r.t. the measured force direction $\boldsymbol{f}_m = [f_{m,x}, f_{m,y}, f_{m,z}]^T \in \mathbb{R}^3$ after the two have been aligned using the Kabsch algorithm. Each matrix element represents the Pearson's correlation coefficient between one of the components of $\boldsymbol{f}_m$ and one of the components of $\boldsymbol{f}_c$. Each row of matrices represents one experimental condition (C1 to C4, as shown in figure 6), and each column of matrices represents one experimental subject (S1 to S3). Within the correlation matrices, the asterisks represent the significance of the correlation coefficient in terms of its p-value, as ascertained through the right-tailed test. The diagonal elements in the correlation matrices were compared across condition 2 and 3 through a paired Wilcoxon signed-rank test, showing a statistically significant improvement in the correlation coefficient with $p < 0.05$. In condition 2, the diagonal elements of the matrices are 0.615 ± 0.204, and for condition 3 the diagonal coefficients are 0.709 ± 0.128 (mean ± 1SD)). Cohen's d is 0.552. Figure 8 shows the RMSE detected during the online experiment. The error is displayed in its components separately, as well as in its euclidean norm. Next to the RMSE is the achievable range also represented in its three components and its euclidean norm. Seen as the RMSE samples are not normally distributed, and that the individual measurements of the RMSE are assumed to be independent of each other, a non-parametric Mann-Whitney U-test was performed to detect potential effects of the experimental conditions on the euclidean norm of the RMSE across all test participants. Significant effects

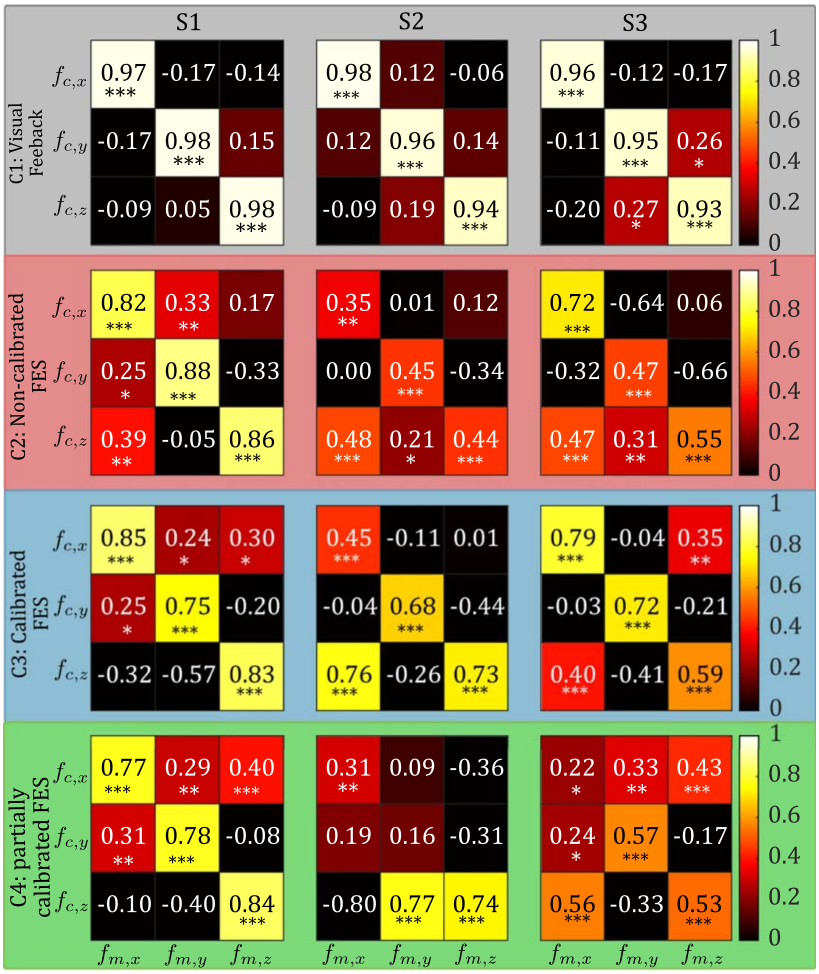

Figure 7. Correlation matrices between the commanded and measured output force direction at the user's end effector. Each row of matrices represents one experimental condition, and each column a participant. $^{***}p < 0.001$, $^{**}p < 0.01$, $^{*}p < 0.05$.

were detected between conditions C2 and C3 ($p < 0.01$). Among the directions of force, it seems that the most significant overall effect is on the x-axis ($p < 0.001$) which, as shown in figure 5, corresponds to the backward/forward direction. However, asignificant effect ($p < 0.05$) is also detectable on the y-axis between conditions C2 and C3, with a noticeable increase in this component of the RMSE. No significant effect is detectable on the vertical z-axis. Significant effects are also present between conditions C2 and C4 ($p < 0.05$). On a per-participant basis, the effects vary strongly. Participant S3 shows the strongest effect between conditions C2 and C3 ($p < 0.001$). In general, the calibration procedure in both C3 and C4 leads to a consistent decrease in variance between the RMSE components compared to C2. The RMSE for condition C1 can serve as qualitative comparison.

4. Discussion

The correlation between the commanded and measured force for online control, shown in figure 7, shows a high variation depending on the user. The fourth experimental condition, C4, is associated with significantly worse correlations compared to either C2 or C3. While the purpose of condition 4 is to verify whether any benefit deriving from the FES device's calibration are due to the geometrical adjustments of the musculoskeletal model or due to the adjustment to stimulation intensity, the expected outcome in the latter case would have been a better performance than using the non-calibrated FES device, but worse than the fully calibrated condition. The fact that the correlation is worse than both C2 and C3 would seem to indicate that the most likely cause of this decrease in performance is fatigue and other progressive effects, which are well documented in FES applications [26, 27]. In this regard, the study design could have benefited from randomizing the order of conditions C2-C4, or at the very least from allowing more resting time between trials.

The calibration procedure leads to a more consistent performance across different users (for this, compare for example the C2 and C3 row of matrices in figure 7) and to a significantly higher correlation of the commanded and measured force output, as well as to a lower overall RMSE. S1 does not show significant improvement between experimental condition 2 and

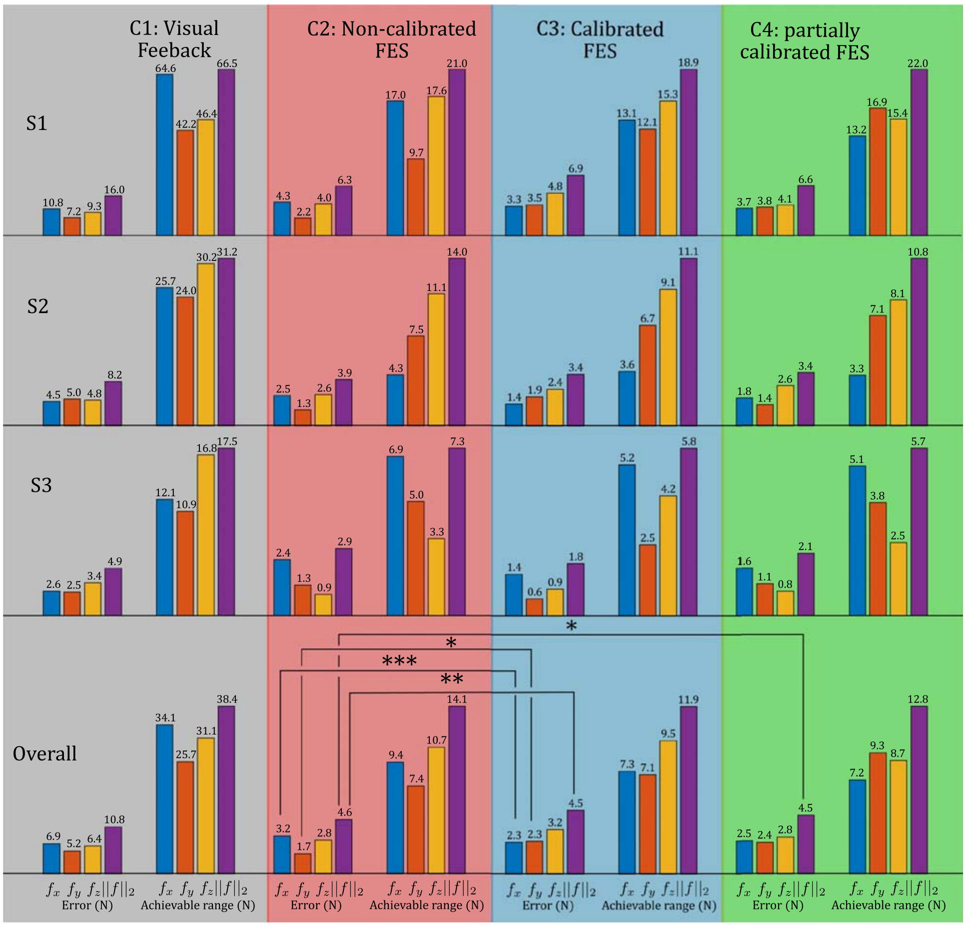

Figure 8. Root mean square error of force output next to the achievable range for each condition (C1—C4) and participant (S1—S3). The lowest row of graphs marked *Overall* shows the more statistically significant effects over all participants as determined by a non-parametric Mann-Whitney U-test. In this row, the maxima are derived by averaging over the per-subject maxima for each condition and RMSE component. $^{***}p < 0.001$, $^{**}p < 0.01$, $^{*}p < 0.05$.

3. This is likely due to the fact that the non-calibrated state of the system is based on S1's frame. The performance assumed as baseline is the one attained when working in the visual feedback condition C1, where the participants were voluntarily exerting force in the indicated direction. As expected, this condition shows the clearest correlation between commanded and measured force direction.

While the RMSE is relatively high in most cases in relation to the maximum achievable range, this is also true for the control condition C1. Participant 2 shows the highest RMSE relative to the maximum force output across the experimental conditions. This is likely due to the difficulties in stimulating the anterior deltoid group of this specific participant. Calibration seems to sensibly reduce the RMSE along the x direction. However, since the muscle groups available for stimulation cannot adequately cover the needed torque output space, the cumulative RMSE remains high, even though the variance between error components is strongly reduced. Overall, calibration seems to lead to an overall reduction in RMSE in both condition 3 and 4 compared to condition 2. The results of this validation show that an open-loop force control enacted through transcutaneous FES can enable qualitatively good directional control of the endpoint force output. This is significant, as the ability to induce a desired force output is paramount for the implementation of any control, even in position.

The performance of the regression algorithm that was trained and validated to predict the output force, on the other hand, shows better precision and accuracy when compared to the real-time correlation coefficients, as shown in table 1, at least when the arm is static, to the point that the correlation coefficients seem to rival those attained in C1. The prediction of the joint torque output should generalize better over different arm postures, which is an aspect worth investigating in future work. Looking at possible implementations using such a regression machine in order to control a FES setup, the results reported in the works by Schearer *et al* [12] and Friedrich *et al* [28] can be helpful, mainly because of their finding that muscle stimulation can be modelled as combining linearly in the force output space. As demonstrated in [27], this fact can be employed to design ridge regression-based FES controllers which can facilitate movement with a time-effective calibration procedure, once the electrodes are in place. The work by Schearer *et al.*, in particular, presents an experiment which employs a setup in many ways identical to that adopted in the present study. Crucially, however, both Schearer and Friedrich focus on subjects with implanted electrodes, which are in many ways less challenging from a control point of view, as they allow for a far higher selectivity in muscle stimulation, causing only the firing of the nerve cells in the nerve bundle they are implanted onto, as noted also in [13].

Based on the findings of the offline analysis, it should be possible to use a setup such as the one used in this experiment in order to calibrate the system before normal operation. Such a procedure could entail either the training of a regression algorithm similar to the one used in the offline analysis, or simply using the measured joint torques instead of the maximal angular twitch velocity $\boldsymbol{\omega}_{\max}$ in the calibration used in this study. Either way, the results of the offline analysis clearly indicate that it would be preferable to include torque measurements in the calibration of the system, as this would bypass any error deriving from erroneous modelling of the body's dynamic parameters, which did play a major role in the online calibration used in this experiment.

This study presents some limitations. First and foremost, while many works rely on data from a limited amount of participants [7, 8, 12, 29], future work should focus on including a wider base of participants, including spinal cord injury patients. Furthermore, the presented musculoskeletal model, while being computationally efficient, relies on several simplifying assumptions, and currently does not model biarticular muscle groups. The Nearest Neighbour recruitment strategy can also lead to sudden switches in stimulated muscles with changes in posture or desired wrench. Additionally, as the calibration procedure used in this study does not call for direct measurement of the force output at the endpoint, the calibrated musculoskeletal model only allows for qualitative control of the force output.

Overall, the evidence seems to point to some benefits offered by the proposed calibration procedure. However, this study could not determine definitively whether these improvements in performance stem from the calibration's adjustments in the geometry of the musculoskeletal model or from the adjustments in stimulation intensity, as fatigue is likely to have rendered some effects between condition C4 and others harder to detect. Enlarging the pool of subjects and adjusting for time-dependent effects will hopefully clarify this aspect.

5. Conclusion

In this study, we described a portable, wearable FES device which, coupled with an appropriate posture tracking system and control architecture, can facilitate qualitatively precise endpoint force output control in three dimensions. We also demonstrated a computationally efficient calibration procedure which can adapt the geometry of the musculoskeletal model and the magnitude of the stimulation currents delivered to the user through simple observation of the twitch, with no need for additional sensors beside the posture tracker.

Future work should focus on investigating the inclusion of force measurement systems for the purpose of calibration as done in [12], and potentially also in order to close the control loop in terms of force during normal operation as done in [7]. In particular, the perspective of using an Exosuit in order to both provide further assistance to the user, as introduced in [30], and to measure the joint torques directly would be worth investigating. The addition of an impedance on top of the force control presented here would allow for general purpose movement control, and should be the focus of future research. In such a case, even if we were to adopt a regression model for the computation of the muscular Jacobian, a model such as the one presented here would still be required to project the desired endpoint force output and the interaction forces measured by the exosuit onto joint torque space.

The precise performance observed during the offline analysis clearly indicates that inclusion of force and torque data in the calibration of the system would improve motion control through FES. The described RFF-based ridge regression algorithm could be able to generalize over non-linearities in the force-stimulation curve. However, including posture in the input vector to the regression could be a challenge, and whether RFF regression will be able to generalize over different body postures remains an open question. As the experiment was conducted in a single posture, the system's adaptability to different limb poses is still theoretical, and not definitively proven by this study.

Future work should also entail user studies involving a larger population of both able-bodied participants and patients suffering from neurological ailments that could benefit from FES-facilitated rehabilitation.

Funding

This work was partially supported by the German Research Society individual research grant *HIT-Reha – Human Impedance control for Tailored Rehabilitation*, DFG Sachbeihilfe CA1389/3-1, project #505327336.

Acknowledgments

The authors wish to thank Dr Thomas Hulin and Dr Michael Panzirsch for the valuable assistance provided.

Data availability statement

The data that support the findings of this study are available at the address https://zenodo.org/record/8228596 and have DOI https://doi.org/10.5281/zenodo.8228596 [31]. Data will be available from 1 June 2024.

ORCID iDs

Marek Sierotowicz https://orcid.org/0000-0001-8040-6438
Claudio Castellini https://orcid.org/0000-0002-7346-2180

References

[1] Kapadia N, Moineau B and Popovic M R 2020 *Frontiers in Neuroscience* **14** 718

[2] Rupp R, Rohm M, Schneiders M, Kreilinger A and Müller-Putz G R 2015 *Proc. IEEE* **103** 954–68

[3] Ajiboye A B *et al* 2017 *Lancet (London, England)* **389** 1821

[4] Lopes P, You S, Ion A and Baudisch P 2018 Adding force feedback to mixed reality experiences and games using electrical muscle stimulation *Proceedings of the 2018 chi conference on human factors in computing systems* pp 1–13

[5] Freeman C, Hughes A, Burridge J, Chappell P, Lewin P and Rogers E 2009 *J. Biomech. Eng.* **131** 031011

[6] Freeman C, Exell T, Meadmore K, Hallewell E and Hughes A M 2015 *Biomedical Engineering/Biomedizinische Technik* **60** 179–91

[7] Sharif Razavian R, Ghannadi B, Mehrabi N, Charlet M and McPhee J 2018 *IEEE Trans. Neural Syst. Rehabil. Eng.* **26** 2033–43

[8] Schearer E M, Liao Y W, Perreault E J, Tresch M C, Memberg W D, Kirsch R F and Lynch K M 2016 *IEEE Trans. Neural Syst. Rehabil. Eng.* **24** 1405–15

[9] Sierotowicz M, Lotti N, Rupp R, Masia L and Castellini C 2022 A comprehensive framework for the modelling of cartesian force output in human limbs *2022 International Conference on Rehabilitation Robotics (ICORR) (IEEE)* pp 1–6

[10] Chadwick E K, Blana D, Kirsch R F and Van Den Bogert A J 2014 *IEEE Trans. Biomed. Eng.* **61** 1947–56

[11] Hogan N 1984 Impedance control: an approach to manipulation *1984 American Control Conference* pp 304–13

[12] Schearer E M, Liao Y W, Perreault E J, Tresch M C, Memberg W D, Kirsch R F and Lynch K M 2014 *IEEE Trans. Neural Syst. Rehabil. Eng.* **22** 654–63

[13] Westerveld A J, Schouten A C, Veltink P H and van der Kooij H 2013 *Journal of neuroengineering and rehabilitation* **10** 1–12

[14] Galofaro E, D'Antonio E, Lotti N and Masia L 2022 *Sensors* **22** 5069

[15] Maurel W 1999 3d modeling of the human upper limb including the biomechanics of joints, muscles and soft tissues *Tech. Rep. EPFL* EPFL (https://doi.org/10.5075/epfl-thesis-1906)

[16] Jensen R H and Davy D T 1975 *J. Biomech.* **8** 103–10

[17] Hainisch R, Gfoehler M, Zubayer-Ul-Karim M and Pandy M G 2012 *Multibody Sys.Dyn.* **28** 143–56

[18] Van der Helm F C and Veenbaas R 1991 *J. Biomech.* **24** 1151–63

[19] Sierotowicz M and Castellini C 2022 *Artif. Organs* **46** e323–7

[20] Drillis R, Contini R and Bluestein M 1964 *Artificial Limbs* **8** 44–66

[21] Sierotowicz M, Connan M and Castellini C 2020 *Sensors* **20** 890

[22] Hulin T, Hertkorn K, Kremer P, Schätzle S, Artigas J, Sagardia M, Zacharias F and Preusche C 2011 The dlr bimanual haptic device with optimized workspace *2011 IEEE International Conference on Robotics and Automation (IEEE)* pp 3441–2

[23] Baratta R, Solomonow M and Zhou B H 1998 *Journal of Electromyography and Kinesiology* **8** 79–91

[24] Kabsch W 1978 *Acta Crystallographica Section A: Crystal Physics, Diffraction, Theoretical and General Crystallography* **34** 827–8

[25] Gijsberts A, Bohra R, Sierra González D, Werner A, Nowak M, Caputo B, Roa M A and Castellini C 2014 *Frontiers in Neurorobotics* **8**

[26] Xia T and Law L A F 2008 *J. Biomech.* **41** 3046–52

[27] Sierotowicz M and Castellini C 2023 Robot-inspired human impedance control through functional electrical stimulation *2023 International Conference on Rehabilitation Robotics (ICORR) (IEEE)* in print

[28] Friederich A R, Audu M L and Triolo R J 2020 *IEEE Trans. Biomed. Eng.* **68** 2389–99

[29] Schearer E M and Wolf D N 2020 *J. Neural Eng.* **17** 016051

[30] Burchielli D, Lotti N, Missiroli F, Bokranz C, Pedrocchi A, Ambrosini E and Masia L 2022 Adaptive hybrid fes-force controller for arm exosuit *2022 International Conference on Rehabilitation Robotics (ICORR) (IEEE)* pp 1–6

[31] Sierotowicz M and Castellini C 2023 Dataset to the article 'Omnidirectional endpoint force control through Functional Electrical Stimulation' by Marek Sierotowicz and Claudio Castellini *Zenodo* (https://doi.org/10.5281/zenodo.8228596)

A.5 The MyoCeption musculoskeletal model

Title: A Comprehensive Framework for the Modelling of Cartesian force Output in Human Limbs.

Authors: Marek Sierotowicz, Nicola Lotti, Rüdiger Rupp, Lorenzo Masia and Claudio Castellini.

Journal: Proceedings of 2022 International Conference on Rehabilitation Robotics (ICORR).

Manuscript version: Accepted article.

Citation: M. Sierotowicz, N. Lotti, R. Rupp, et al. "A Comprehensive Framework for the Modelling of Cartesian Force Output in Human Limbs." In: *2022 International Conference on Rehabilitation Robotics (ICORR)*. 2022, pp. 1–6. ISBN: 1-66548-829-8. DOI: `10.1109/ICORR55369.2022.9896547`

Abstract: Neuromuscular functional electrical stimulation represents a valid technique for functional rehabilitation or, in the form of a neuroprosthesis, for the assistance of neurological patients. However, the selected stimulation of single muscles through surface electrodes remains challenging particularly for the upper extremity. In this paper, we present the MyoCeption, a comprehensive setup, which enables intuitive modeling of the user's musculoskeletal system, as well as proportional stimulation of the muscles with 16-bit resolution through up to 10 channels. The system can be used to provide open-loop force control, which, if coupled with an adequate body tracking system, can be used to implement an impedance control where the control loop is closed around the body posture. The system is completely self-contained and can be used in a wide array of scenarios, from rehabilitation to VR to teleoperation. Here, the MyoCeption's control environment has been experimentally validated through comparison with a third-party simulation suite. The results indicate that the musculoskeletal model used for the MyoCeption provides muscle geometries that are qualitatively similar to those computed in the baseline model.

Author contributions: Conceptualization; Software Design; Formal analysis; Writing-original draft; Writing-review and editing.

A Comprehensive Framework for the Modelling of Cartesian Force Output in Human Limbs

Marek Sierotowicz^{1,2}, Nicola Lotti^{3}, Rüdiger Rupp^{4}, Lorenzo Masia^{3} and Claudio Castellini^{1,2}

Abstract— **Neuromuscular functional electrical stimulation represents a valid technique for functional rehabilitation or, in the form of a neuroprosthesis, for the assistance of neurological patients. However, the selected stimulation of single muscles through surface electrodes remains challenging particularly for the upper extremity. In this paper, we present the MyoCeption, a comprehensive setup, which enables intuitive modeling of the user's musculoskeletal system, as well as proportional stimulation of the muscles with 16-bit resolution through up to 10 channels. The system can be used to provide open-loop force control, which, if coupled with an adequate body tracking system, can be used to implement an impedance control where the control loop is closed around the body posture. The system is completely self-contained and can be used in a wide array of scenarios, from rehabilitation to VR to teleoperation. Here, the MyoCeption's control environment has been experimentally validated through comparison with a third-party simulation suite. The results indicate that the musculoskeletal model used for the MyoCeption provides muscle geometries that are qualitatively similar to those computed in the baseline model.**

I. INTRODUCTION

Functional electrical stimulation (FES) for artificial generation and support of movements through application of electrical currents represents an integral part in the rehabilitation of neurological patients. In the early phase of rehabilitation, FES is an effective tool in a task-specific, restorative therapy program to foster neurological recovery [1]. In the chronic phase after a neurological disease or trauma, FES may be used as a neuroprosthesis for compensation of completely lost or very weak motor functions. Particularly in individuals with cervical spinal cord injury (SCI) and the associated impairments of the reaching and grasping function, FES has been successfully employed for assistance in activities of daily living (ADL), both using trans-cutaneous [2] and intramuscular electrodes [3].

Non-invasive ES applied through surface electrodes is also used in applications outside the medical field, for example VR and AR [4] [5].

The context of rehabilitation can offer some advantages, as the repetitive, task-specific nature of the movements typically performed during a therapy session allows to implement iterative learning, which allows, among other things, to calibrate inertial parameters and to differentiate the user's own volitional efforts from electrical stimulation [6] [7]. However, many of this sort of setup rely heavily on the assumption of repeated movements, and are ill-fitted to aid movements that do not fulfill this assumption. Furthermore, currently available FES systems, both in the medical field and beyond, use static stimulation schemes, which are open-loop in terms of force, in order to generate predefined multi-joint movements. While most setups available can successfully induce specific movements requiring the stimulation of muscle groups directly associated to them in a bijective fashion (see for example [8]), a general-purpose framework able to associate arbitrary movements or force outputs to more than a few stimulated muscle groups, in particular without relying on the assumption of repeated actions, seems to be still missing.

In this paper, we present a musculoskeletal model which enables to intuitively simulate most kinds of muscle groups, and a prototype designed to use this model in order to provide proportional force control through FES on the upper limb of a user on up to 10 channels with a resolution of 16 bits.

A core principle and fundamental goal in the design philosophy of this system is the adaptability to different users. In order to achieve this, the musculoskeletal model should be easily modifiable to better fit each individual, ideally without the need for much anatomical expertise, and if possible even automatically. In this paper, we describe the entirety of the MyoCeption system, with a particular emphasis on the musculoskeletal model which lies at the basis of its control architecture. This model is experimentally validated by comparing it to a third-party OpenSim model of the right upper limb.

II. SYSTEM DESCRIPTION

The MyoCeption's main purpose is to compute the stimulation currents to be injected through each electrode pair so as to induce a generalized force defined in Cartesian terms at a point which is considered to be the user's end-effector. The hardware, as shown in Fig. 1, consists of a wearable stimulation device and compressive jacket, which presses the surface electrodes onto the user's skin. The stimulation currents (pulse width $200\,\mu s$, frequency settable from $0.5\,Hz$ to $100\,Hz$, maximum amplitude up to $70\,mA$) are generated by three FES devices (2 *TNS SM2 AKS* and 1 *TNS SM 2MF*, Pierenkemper GmbH, Am Geiersberg 6, 35630 Ehringshausen, Germany). An intermediate wirelessly controlled block (the wireless bluetooth module is an *ESP32*

---

*This work was not supported by any organization

[1] Marek Sierotowicz and Claudio Castellini are with the Institute of Medical Robotics, Friedrich-Alexander Universität Erlangen-Nürnberg, 91052 Erlangen, Germany `marek.sierotowicz@fau.de`

[2] Marek Sierotowicz and Claudio Castellini are also with the Institute of Robotics and Mechatronics, German Aerospace Center, 82234 Wessling, Germany

[3] Nicola Lotti and Lorenzo Masia are with the Institute for Technical Informatics (ZITI), Heidelberg University, 69120 Heidelberg, Germany.

[4] Rüdiger Rupp is with the Spinal Cord Injury Center, Heidelberg University Hospital, 69118 Heidelberg, Germany

Wroom 32, Espressif systems) modulates the generated currents in amplitude from 0 A to the maximum amplitude set on the FES device. The levels of stimulation for each channel are calculated by a remote host computer running an interface software and the MyoCeption Control Environment (MCE). Additionally, the BodyRig [9], a wireless IMU-based body tracking system, is employed. The BodyRig allows to track the body pose with high precision, aligning the musculoskeletal model to the user's posture. Thus, the MCE is provided with the approximated geometry of the user's muscle groups.

Within the MCE, each stimulated muscle group is represented by a line of action going through 4 points ($\vec{p}_1$ to $\vec{p}_4$) plus the origin ($\vec{p}_0$), as shown in Fig. 2.

It is important to notice that, as FES applied through adhesive electrodes typically can not selectively target single muscle groups, there is no bijective mapping from a given line of action in the MCE to a muscle group in the anatomical sense. Rather, each line of action in the MCE is supposed to represent the combined action of all muscle groups stimulated by an electrode pair, and can therefore be seen as a weighted average of the lines of action of the anatomical stimulated muscle groups. The main aim of the analysis presented here, besides comparing different routing methods for the lines of action around different joints, is to confirm this claim. This simplification makes the muscle geometry less computationally expensive, and should ideally make the model easier to fit to an individual user. To this end, future work will focus on perfecting a calibration procedure which should adjust the routing points of each line of action based on recorded twitch movements or torques originating from stimulation of each individual muscle group.

The cumulative moment arm $\vec{r}$ over the entire line of action about the joint $\vec{j}$ is computed according to the following relation

$$\vec{r} = \frac{1}{4}\sum_{i=1}^{4}(\vec{p}_i - \vec{j}) \times \left(\frac{\vec{p}_i - \vec{p}_{i-1}}{||\vec{p}_i - \vec{p}_{i-1}||}\right). \tag{1}$$

This model works under the assumption that the pulling force of the muscle f_m is homogeneous along the whole line of action, which is the case in static conditions. Under this assumption, the force can be considered a scalar, and the torque generated by the muscle is simply the moment arm vector as defined in equation 1 multiplied by f_m. Therefore, overall magnitude of the torque $\vec{\tau}_m$ generated at the joint level by the muscle group m itself can be computed as a function of the moment arm length and of the magnitude of the force f_m pulling along the line of action according to

$$||\vec{\tau}_m|| = ||\vec{r} f_m|| = ||\vec{r}|| f_m, \tag{2}$$

where $\vec{r}$ indicates the moment arm vector of a muscle group acting on the joint j as described in equation 1. The moment arm is therefore of high importance for the smooth control of the force output at the user's end-effector over different postures.

The muscle geometry is used to calculate the muscle force needed in order to output an arbitrary generalized force in Cartesian terms. In particular, from a desired wrench at the end-effector $\vec{w}_{ee}$, the system calculates the corresponding torques at each joint $\vec{\tau}_j$ through the arm's Jacobian to that joint J_{arm}^{j} according to the following equation

$$\vec{\tau}_j = J_{arm}^{jT} \vec{w}_{ee}. \tag{3}$$

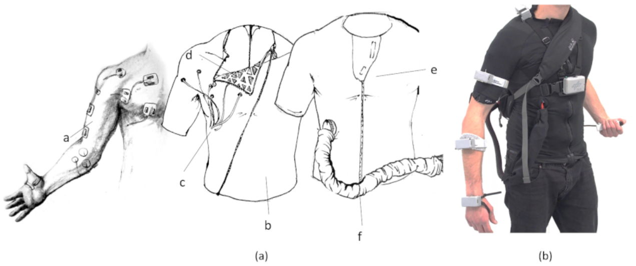

(a) (b)

Fig. 1. **a:** MyoCeption system elements. In the picture, from left to right, one can see the surface electrodes applied to the user's skin, which are fitted with Velcro hooks on the outside (a). The inner compression jacket (b) features holes (c) to run the electrode cables through, and is fitted with Velcro loops on the inside, so as to ease electrode application (d). The outer jacket (e) groups the cables in a single umbilical (f) connected to the control electronics, and provides further compression. **b:** Picture of the full setup as worn by a user.

The single stimulation currents are then computed in order to generate the linear combination of muscular joint outputs $\vec{\tau}_m$ acting on the joint j that best approximates the desired joint torque $\vec{\tau}_j$. The kind of linear combination depends on the selected muscle recruitment strategy. For instance, in the case of a nearest neighbour recruitment strategy, only the muscle group with the torque output $\vec{\tau}_m$ closest in direction to the desired joint torque $\vec{\tau}_j$ is stimulated. Other strategies could employ a suitable pseudo-inverse of the muscular Jacobian, or its transpose in the case of an admittance controller. The intensity of the stimulation also depends on the expected effect of the stimulation current on the muscular force f_m.

Different routings of the lines of action are possible. In particular, here we examine a simple line-of-sight routing, a routing similar to the one presented in [10], and a third one. From this point on, these routings will be referred to as *line of sight*, *sphere projection* and *shifted sphere projection*, respectively.

The line of sight routing, shown in Fig. 2 left, simply connects the origin point $\vec{p}_0$ (the most proximal point of the line of action) to the insertion point $\vec{p}_4$ (the most distal point of the line of action) with a straight line. The line of action of many muscle groups can be well approximated through such a routing, and because of its simplicity, it is used within the MCE any time a line of sight exists between the origin and the insertion point. However, this routing can not accurately model any line of action going around a joint, as is the case, e.g., for the triceps in most postures.

The sphere projection routing, shown at the center in Fig. 2, routes the line of action through via points co-planar to the joint and the line of action's origin and insertion (shown in the figure as $\vec{p_1}$ and $\vec{p_3}$). The routing connects the two

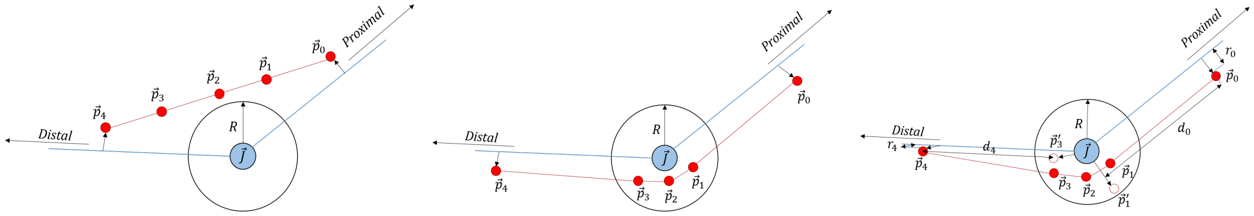

Fig. 2. Illustration of the line of sight routing (left), the sphere projection routing (center), and the shifted sphere projection routing (right).

via points closest to the joint with a straight line if said line does not enter a sphere of radius R with the joint lying at its center. If, on the other hand, the line of sight does intersect the sphere, then the line of action is routed through a point $\vec{p}_2$, which is the point on the line of sight that is closest to the joint projected onto the sphere in the radial direction.

In the MCE, this method can lead to problems if the $\vec{p}_0$ and $\vec{p}_4$ points lie far away from the joint relative to the sphere's radius R. An example of this problem is shown in Fig. 3. The figure shows the difference in orientation of the expected torque output from the line of action corresponding to the elbow extenders when the line is routed through the shifted sphere projection and when it is routed through sphere projection. Ideally, the torque output should be aligned with the elbow axis $\vec{e}$, but as shown in the figure, this can sometimes not be the case when using sphere projection routing. In [10], this problem presumably doesn't present itself because the via points are based on MRI imaging, and can therefore be precisely placed with high spatial accuracy even in close proximity of the joint. In [11], where a routing similar to sphere projection is used to predict the kinematics of a tendon-actuated tremor-suppressing glove, this is not an issue, as the tendons pass through guides which are very close to the user's joints. If the joint is modeled as having a single rotational degree of freedom, a possible solution would be to then project the torque onto the joint's axis, or even use a cylinder of radius R with its axis aligned with that of the joint instead of a sphere. However, if the direction of the axis is itself not known with certainty, this solution is not viable.

The shifted sphere projection routing, shown in Fig. 2 on the right, consists of the following steps.

- Compute the points $\vec{p}'_1$ and $\vec{p}'_3$. These are points obtained by shifting $\vec{p}_0$ and $\vec{p}_4$ along the respective link towards the joint $\vec{j}$ until they are closest to it, and by then projecting them in the radial direction onto the sphere of radius R with the joint lying at its center.
- The point $\vec{p}_2$ is the closest point on the sphere from $\vec{p}' = \frac{(\vec{p}'_1 + \vec{p}'_3)}{2}$.
- Finally, the points $\vec{p}_1$ and $\vec{p}_3$ are the point on the sphere closest to the projections of $\vec{p}'_1$ and $\vec{p}'_2$ on the planes defined by $\left\langle \vec{p}_0, \vec{j}, \vec{p}_2 \right\rangle$ and $\left\langle \vec{p}_4, \vec{j}, \vec{p}_2 \right\rangle$, respectively.

As shown in Fig. 3, shifted sphere projection can give a more consistent torque direction than the sphere projection routing for lines of action whose origin and insertion points lie far from the joint relative to the sphere's radius R. However, shifted sphere projection cannot transition to line of sight without discontinuities, which is possible using the sphere projection routing. Such discontinuities are shown in Fig. 5.

III. EXPERIMENTAL PROTOCOL

In order to validate the MCE, a comparison was drawn between the MyoCeption's musculoskeletal model and an OpenSim Dynamic Arm Simulator model (DAS) [12] shown on the right in Fig. 4, which simulates the musculature responsible for the movements of the right upper limb in detail. OpenSim is widely used as a modelling tool in bio-mechanics, and can boast a vast community creating simulations and models for a diverse range of applications.

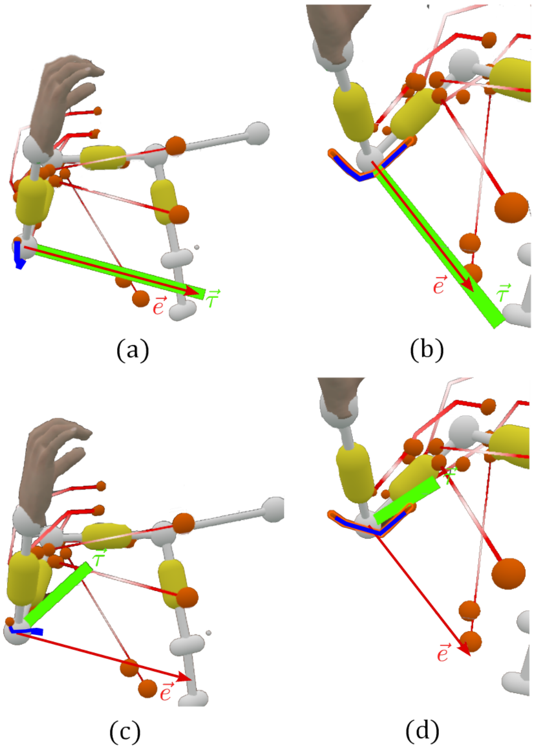

(a) (b)

(c) (d)

Fig. 3. Issue with the sphere projection routing. In this example, a line of action within the MCE close in position to the *triceps brachii*, highlighted in blue, is shown with the direction of the torque it can exert on the elbow joint (shown as a green line and labeled as $\vec{\tau}$). **a** and **b:** the action line is routed using shifted sphere projection. The expected torque is aligned with the elbow's axis (red arrow marked $\vec{e}$). **c** and **d:** the sphere projection routing is used instead. Notice how the action line passes on the side, and this causes the expected torque direction $\vec{\tau}$ to deviate from the elbow's axis $\vec{e}$.

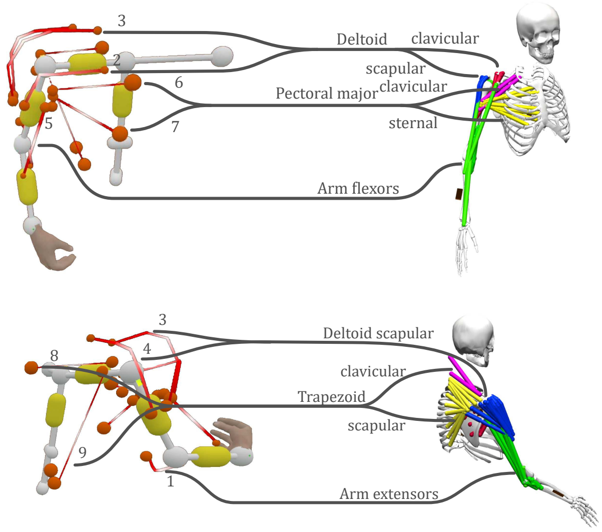

Fig. 4. The two musculoskeletal models to be compared. On the left is the MyoCeption Control Environment, on the right the Dynamic Arm Simulator implemented in OpenSim. The action lines of the MCE are designated by channel number, while the DAS muscle groups are designated by name and differentiated by color. The grey lines represent the assumed correspondences between the DAS muscle groups and the MCE stimulation channels based on positional proximity and on the joint about which each line of action operates.

The data set for the comparison was recorded with the body tracking system from [9]. One able-bodied user (age 27, 1.87m, 85kg) performed elbow flexion/extension, shoulder flexion/extension, and shoulder adduction/abduction over 4 repetitions in real time. The postures during these movements were used to align both the MCE and the DAS kinematics. The moment arm of the involved muscle groups were compared across the recorded movements between the two. The moment arm length $||\vec{r}||$ of the lines of action is the effective moment arm of the muscle group.

In order to test the claim that each line of action in the MCE could be seen as a weighed average of all muscle groups stimulated by an electrode pair, here we executed a multivariate regression from the moment arms in the DAS to the moment arms of the MCE assumed to correspond to them. Here we focus on demonstrating a qualitative similarity between the two models. Therefore, we would expect high correlation between the moment arm length corresponding to the lines of action in the MCE and the muscle groups that are closest in position in the DAS. The assumed correspondences between the DAS muscle groups and the MCE lines of action are shown in Fig. 4. This analysis is also used to evaluate which routing method would provide the better qualitative correlation of the muscle's lever arm between the MCE and the OpenSim DAS model.

IV. RESULTS

The evaluated metrics from the multivariate regression performed from the moment arm lengths of the DAS muscle groups onto the moment arm lengths of the MCE lines of action are the squared Pearson's correlation coefficient R^2 and the root mean square error (RMS) normalized by the maximum difference of the moment arm from its mean. This normalization has the purpose of representing the RMS as a fraction of the maximum range of the regression target. Table I gathers the result of the multivariate regression analysis from each DAS muscle group involved in the movements performed during the experiment to the MCE stimulation channels assumed to correspond to them, according to Fig. 4. The results are sorted by the movements performed during the experiment. In Fig. 5, the moment arm on the MCE stimulation channel 2, routed using shifted sphere projection, is shown and compared to the moment arm of the DAS deltoid clavicular. Fig. 6 shows the moment arm length of the MCE line of action closest to the biceps brachii in the DAS over the elbow flexion angle, as well as the moment arm length of the DAS biceps brachii itself. For ease of comparison, the curve shown in Fig. 6 is not obtained aligning the DAS to the IMU data, but rather shows a sweep of the moment arm length over the full range of the elbow flexion angle, which in the OpenSim model can be freely set.

TABLE I
MULTIVARIATE REGRESSION RESULTS.

MCE	DAS	Movement	R^2	RMS
5	Elbow flexors	Elbow flex/ext	0.917	0.152
1	Elbow extenders	Elbow flex/ext	0.96	0.100
2	delt clav	Sh. add/abd	0.940	0.152
2	delt scap	Sh. add/abd	0.960	0.124
3	delt clav	Sh. add/abd	0.879	0.190
3	delt scap	Sh. add/abd	0.910	0.164
4	delt scap	Sh. add/abd	0.917	0.103
2	delt clav	Sh. flex/ext	0.904	0.140
3	delt clav	Sh. flex/ext	0.906	0.140
4	delt clav	Sh. flex/ext	0.967	0.100
2	delt scap	Sh. flex/ext	0.906	0.139
3	delt scap	Sh. flex/ext	0.969	0.081
4	delt scap	Sh. flex/ext	0.971	0.094
6	pect maj c	Sh. flex/ext	0.736	0.147
7	pect maj c	Sh. flex/ext	0.783	0.219
6	pect maj t	Sh. flex/ext	0.886	0.097
7	pect maj t	Sh. flex/ext	0.836	0.190
8	trap clav	Sh. flex/ext	0.879	0.131
9	trap clav	Sh. flex/ext	0.534	0.228
8	trap scap	Sh. flex/ext	0.868	0.077
9	trap scap	Sh. flex/ext	0.971	0.121

V. DISCUSSION

While the shifted sphere projection routing seems to more robustly model line of action torque output where the origin and the insertion points are far away from the joint relative to the joint's sphere diameter R, it is unable to transition to a line-of-sight routing without discontinuities when the line of action does not go around a joint. This effect is shown in Fig. 5. The discontinuities in the moment arm length from the MCE are clearly visible. These happen due to the transition of the routing from shifted sphere to line of sight. This leads to generally poor correlations between the two models for all muscle groups where such a transition occurs during movement. This, in particular, is the case for the lines of action corresponding to the deltoids, for which it happens that the line of sight from the origin and the insertion point can run outside of the joint sphere during shoulder abduction or shoulder flexion.

Using the sphere projection routing on the lines of action corresponding to the deltoids in the MCE leads to high correlation coefficients on the moment arm lengths both during shoulder adduction/abduction and shoulder flexion/extension, as shown in Table I.

Finally, Fig. 6 shows the moment arm length of the biceps brachii of the DAS, as well as the moment arm length of the closest action line in the MCE, which is routed using line-of-sight. The moment arm length of the two muscle groups are normalized by the respective maximum to ease the comparison. As shown in Table I, the moment arm of the MCE lines of action going over the elbow joint are well represented by a weighed sum of the moment arms of the DAS elbow flexors and extensors. Looking at this comparison between two specific lines of action, it seems that the curves look qualitatively very similar, showing only a discrepancy in the angle for which the curve's maximum occurs. By adjusting only a few parameters through a suitable calibration procedure, the similarity could be improved. In general, the multivariate regression shows a good fit of the moment arms as computed by the MCE with the regression model based on the DAS muscle groups, with the main exception of action line 9, which shows a poor fit with the linear model with the trapezoid clavicular group from the DAS. This could perhaps be explained by the relative distance in position between the two muscle groups in the models, as shown in Fig. 4.

The good fit of the multivariate regression indicates that the moment arm length of the lines of action in the MCE can be well explained by the moment arm lengths in the DAS. This confirms that the MCE is able to compute qualitatively similar moment arms over the motions examined in this experiment as those computed in the DAS. As the moment arms are fundamental in the estimation of the torque output associated to each line of action, this is a indispensable validation for the MCE. Furthermore, the results shown here suggest that shifting the origin and insertion points of the lines of action in the MCE could account for stimulation currents hitting different muscle groups than the anticipated ones. This can be inferred by looking, e.g., to the better fit between the trapezoid clavicular group from the DAS and the MCE line of action 8, as opposed to the MCE line of action 9, as shown in Table I. In a hypothetical scenario where the stimulation current associated with the MCE line of action 9 exclusively hits the trapezoid clavicular, shifting the line of action 9 to be closer to the line of action 8 would ensure a more accurate calculation of the torque output deriving from this stimulation. Future work will focus on calibration procedures able to accomplish such an adjustment automatically based on data acquired on human users.

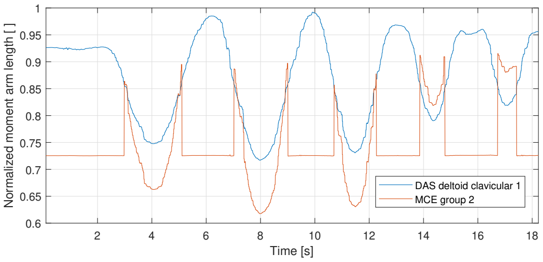

Fig. 5. Moment arm length of the MCE muscle group 2 and the deltoid clavicular group 1 from the DAS using the shifted sphere projection routing.

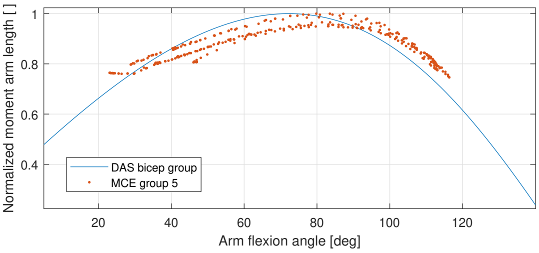

Fig. 6. Comparison of the moment arm of the bicep group 1 from the DAS and the MCE line of action 5, which is modeled using line of sight routing, over the elbow flexion angle.

VI. CONCLUSIONS

The present article serves as a presentation of the MyoCeption system, and as a validation of the system's control environment. A comparison with a third-party, detailed model of the human upper limb shows that the musculoskeletal model governing the MyoCeption's control system, while being simpler and not requiring almost any anatomical expertise to be set up, is able to compute the salient characteristics of the muscle geometry to a comparable degree.

Furthermore, the comparison between MCE and DAS allowed to evaluate the advantages and disadvantages of the three proposed line of action routings. In particular, the line-of-sight routing is very simple, and could be easily adjusted to fit the effective moment arm length of an arbitrary user's muscle measured over the range of motion of a given joint. However, the line of action of most muscles can not be approximated as a straight line, especially if the line of action passes around a joint. The sphere projection routing does allow for transition without discontinuities in the moment arm's length between a state where the line of action goes around a joint and a state where a line of sight exists between origin and insertion point. However, the sphere projection routing seems to not be particularly robust to inaccuracies in the placement of the via points $\vec{p}_1$ and $\vec{p}_3$. The shifted sphere projection does not allow for continuous transition to a line of sight state, which leads to discontinuities that could be extremely problematic when this routing is used to compute the amount of stimulation current to be injected into a user. However, this routing seems more robust with respect to the placement of the origin and insertion point of the line of action. It would therefore be advisable to use this routing for lines of action which are not expected to have a line-of sight between their origin and their insertion, independent of the user's posture.

This test suffers from a few limitations. In particular, here we showed only a qualitative correlation between the moment arm lengths of the two musculoskeletal models. No effort was put into verifying whether the MyoCeption's control environment provides values close in value to those that would be measured in reality for a given user. The results presented by Hainisch et Al. in [10] show that, even when fitting the muscular lines of action to MRI data in an OpenSim model, the torque output computed by the calibrated model can show noticeable discrepancies with data acquired directly on humans over joint movements. Therefore, a model such as the DAS is not necessarily the best possible ground truth, and future work should focus on the comparison of the MCE model with data gathered *in vivo*, and on improving the fitness of the model in a quantitative sense as well. Furthermore, here the MCE has been verified just for single-joint movements and not for movements involving more than one joint. In such cases, the geometry of biarticular muscles in particular could change noticeably, and lead to discrepancies between the ground truth and the MCE model.

Besides the offline comparison of the MCE with other models or data gathered *in vivo*, future work will also focus on closing the real-time control loop in force. In order to do so, a few possibilities exist. In particular, the integration of further sensor modalities in the system, such as force and torque, would allow to monitor the applied forces on each joint during movements, and optimize the model's parameters accordingly. Such measurement modalities could be added to the system by fitting it with a passive or even an active sensor-fitted exoskeleton or exosuit. Therefore, the interaction of the MyoCeption's FES setup and such rehabilitative robotic systems shall be investigated.

In [13], Anaya et al. present many examples of hybrid FES-robotic gait rehabilitation technologies, mostly based on rigid exoskeletons used in conjunction with electrical stimulation. The MCE could be employed in such setups also on upper limbs: the pulling vector estimation could be used to generate force fields in rehabilitation robotics that mimic the effect of a single musculutendon unit or a muscle group [14].

In the context of soft wearable exosuit control, on the other hand, the MCE could be used to extend the so called *Myoprocessor* presented in [15] to multiple degrees of freedom in order to assist both the elbow and the shoulder. In conjunction with FES, an exosuit controlled through the MCE could be more effective in restoring motor function in the presence of chronic neuromuscular diseases. Future steps will test the presented approach in exosuit control both in clinical and industrial settings [16].

Regarding the MCE's use in VR and AR, future studies will involve a bimanual rigid exoskeleton [17] with MyoCeption-driven haptic rendering in order to improve immersiveness of a simulation.

REFERENCES

[1] N. Kapadia, B. Moineau, and M. R. Popovic, "Functional electrical stimulation therapy for retraining reaching and grasping after spinal cord injury and stroke," *Frontiers in Neuroscience*, p. 718, 2020.

[2] R. Rupp, M. Rohm, M. Schneiders, A. Kreilinger, and G. R. Müller-Putz, "Functional rehabilitation of the paralyzed upper extremity after spinal cord injury by noninvasive hybrid neuroprostheses," *Proceedings of the IEEE*, vol. 103, no. 6, pp. 954–968, 2015.

[3] A. B. Ajiboye, F. R. Willett, D. R. Young, W. D. Memberg, B. A. Murphy, J. P. Miller, B. L. Walter, J. A. Sweet, H. A. Hoyen, M. W. Keith, *et al.*, "Restoration of reaching and grasping in a person with tetraplegia through brain-controlled muscle stimulation: a proof-of-concept demonstration," *Lancet (London, England)*, vol. 389, no. 10081, p. 1821, 2017.

[4] P. Lopes and P. Baudisch, "Interactive systems based on electrical muscle stimulation," *Computer*, vol. 50, no. 10, pp. 28–35, 2017.

[5] P. Lopes, S. You, A. Ion, and P. Baudisch, "Adding force feedback to mixed reality experiences and games using electrical muscle stimulation," in *Proceedings of the 2018 chi conference on human factors in computing systems*, 2018, pp. 1–13.

[6] K. L. Meadmore, A.-M. Hughes, C. T. Freeman, Z. Cai, D. Tong, J. H. Burridge, and E. Rogers, "Functional electrical stimulation mediated by iterative learning control and 3d robotics reduces motor impairment in chronic stroke," *Journal of neuroengineering and rehabilitation*, vol. 9, no. 1, pp. 1–11, 2012.

[7] C. Freeman, T. Exell, K. Meadmore, E. Hallewell, and A.-M. Hughes, "Computational models of upper-limb motion during functional reaching tasks for application in fes-based stroke rehabilitation," *Biomedical Engineering/Biomedizinische Technik*, vol. 60, no. 3, pp. 179–191, 2015.

[8] C. Freeman, A. Hughes, J. Burridge, P. Chappell, P. Lewin, and E. Rogers, "A model of the upper extremity using fes for stroke rehabilitation," *Journal of Biomechanical Engineering*, vol. 131, no. 3, 2009.

[9] M. Sierotowicz, M. Connan, and C. Castellini, "Human-in-the-loop assessment of an ultralight, low-cost body posture tracking device," *Sensors*, vol. 20, no. 3, p. 890, 2020.

[10] R. Hainisch, M. Gfoehler, M. Zubayer-Ul-Karim, and M. G. Pandy, "Method for determining musculotendon parameters in subject-specific musculoskeletal models of children developed from mri data," *Multibody System Dynamics*, vol. 28, no. 1, pp. 143–156, 2012.

[11] P. Daemi, Y. Zhou, K. Inzunza, M. D. Naish, A. D. Price, and A. L. Trejos, "Kinematic modeling and characterization of a wearable tremor suppression device for pathological tremor reduction," in *2020 8th IEEE RAS/EMBS International Conference for Biomedical Robotics and Biomechatronics (BioRob)*. IEEE, 2020, pp. 1236–1241.

[12] E. K. Chadwick, D. Blana, R. F. Kirsch, and A. J. Van Den Bogert, "Real-time simulation of three-dimensional shoulder girdle and arm dynamics," *IEEE Transactions on Biomedical Engineering*, vol. 61, no. 7, pp. 1947–1956, 2014.

[13] F. Anaya, P. Thangavel, and H. Yu, "Hybrid fes–robotic gait rehabilitation technologies: a review on mechanical design, actuation, and control strategies," *International journal of intelligent robotics and applications*, vol. 2, no. 1, pp. 1–28, 2018.

[14] N. Lotti and V. Sanguineti, "Emg-driven force fields: Toward a myoprocessor for virtual biomechanics," in *International Conference on NeuroRehabilitation*. Springer, 2018, pp. 1161–1165.

[15] N. Lotti, M. Xiloyannis, F. Missiroli, C. Bokranz, D. Chiaradia, A. Frisoli, R. Riener, and L. Masia, "Myoelectric or force control? a comparative study on a soft arm exosuit," *IEEE Transactions on Robotics*, 2022.

[16] F. Missiroli, N. Lotti, E. Tricomi, C. Bokranz, R. Alicea, M. Xiloyannis, J. Krzywinski, S. Crea, N. Vitiello, and L. Masia, "Rigid, soft, passive, and active: a hybrid occupational exoskeleton for bimanual multijoint assistance," *IEEE Robotics and Automation Letters*, 2022.

[17] E. D'Antonio, E. Galofaro, F. Patané, M. Casadio, and L. Masia, "A dual arm haptic exoskeleton for dynamical coupled manipulation," in *2021 IEEE/ASME International Conference on Advanced Intelligent Mechatronics (AIM)*. IEEE, 2021, pp. 1237–1242.

A.6 MyoCeption impedance control

Title: Robot-inspired human impedance control through functional electrical stimulation.

Authors: Marek Sierotowicz, and Claudio Castellini.

Conference: Proceedings of 2023 International Conference on Rehabilitation Robotics (ICORR).

Manuscript version: Accepted article.

Citation: M. Sierotowicz and C. Castellini. "Robot-Inspired Human Impedance Control Through Functional Electrical Stimulation." In: *2023 International Conference on Rehabilitation Robotics (ICORR)*. 2023, pp. 1–6. DOI: `10.1109/ICORR58425.2023.10304750`

Abstract: Functional Electrical Stimulation is an effective tool to foster rehabilitation of neurological patients suffering from impaired motor functions. It can also serve as an assistive device to compensate for compromised motor functions in the chronic phase occurring after a disease or trauma. In all cases, the dominant paradigm in FES applications is that of aiding specialized, task-specific movements, such as reaching or grasping. Usually this is achieved by targeting specific muscle groups which are associated to the targeted motion by experts. A general purpose, FES-based control theory capable of enabling neurological patients to achieve a wide range of positional goals in their peri-personal space is still missing. In this paper, we present an early analysis of the performance achievable through a muscular impedance control loop employing FES to actuate force and movement. The control is evaluated in a test where the user's upper limb is moved by means of an exonerve to a series of target positions on a plane without providing visual feedback nor requiring volitional effort. The results allow to characterize the performance of such a setup over time and to assess how well can it generalize over different target positions in the user's peri-personal space. The current study population also allows to evaluate the effects of user's experience with FES systems on the overall performance during the test. The results indicate that the proposed control loop can generalize well over different arm poses.

Author contributions: Conceptualization; Software Design; Hardware Design; Formal analysis; Writing-original draft; Writing-review and editing.

Robot-inspired human impedance control through functional electrical stimulation

Marek Sierotowicz[1], and Claudio Castellini[1]

Abstract— **Functional Electrical Stimulation is an effective tool to foster rehabilitation of neurological patients suffering from impaired motor functions. It can also serve as an assistive device to compensate for compromised motor functions in the chronic phase occurring after a disease or trauma. In all cases, the dominant paradigm in FES applications is that of aiding specialized, task-specific movements, such as reaching or grasping. Usually this is achieved by targeting specific muscle groups which are associated to the targeted motion by experts. A general purpose, FES-based control theory capable of enabling neurological patients to achieve a wide range of positional goals in their peri-personal space is still missing. In this paper, we present an early analysis of the performance achievable through a muscular impedance control loop employing FES to actuate force and movement. The control is evaluated in a test where the user's upper limb is moved by means of an *exonerve* to a series of target positions on a plane without providing visual feedback nor requiring volitional effort. The results allow to characterize the performance of such a setup over time and to assess how well can it generalize over different target positions in the user's peri-personal space. The current study population also allows to evaluate the effects of user's experience with FES systems on the overall performance during the test. The results indicate that the proposed control loop can generalize well over different arm poses.**

I. INTRODUCTION

Functional electrical stimulation (FES) for artificial generation and support of movements represents an integral part in the rehabilitation of certain neurological patients. In the early phase of rehabilitation, FES can be an effective tool in a task-specific, restorative therapy program to foster neurological recovery [1]. In the chronic phase after a neurological disease or trauma, FES may be used as a neuroprosthesis for compensation of lost or weakened motor functions. Particularly in individuals with cervical spinal cord injury (SCI) and the associated impairments of the reaching and grasping function, FES has been successfully employed for assistance in activities of daily living (ADL), both using trans-cutaneous [2] and intramuscular electrodes [3]. Outside of the medical field, FES-based interfaces have also been used to provide force feedback in virtual and augmented reality applications [4][5].

The context of rehabilitation in particular can offer some advantages, as the repetitive nature of the movements typically performed during a therapy session allows to implement iterative learning, which allows, among other things, to calibrate inertial parameters and to differentiate the user's own volitional efforts from movements caused by FES [6] [7]. However, such setups are usually meant to address specialized, functionally relevant movements, such as reaching and grasping in a specific arm pose, and are therefore optimized towards facilitating these motions. In such setups, FES is often used to target specific muscle groups which are associated to the targeted motion by experts (e.g. the triceps is often stimulated to facilitate reaching). While this sort of approach has been proven effective in various studies, it is also very specific to the targeted motions, and would not generalize well to other movements. A multi-joint control in force, mediated by a proper mechanical impedance, on the other hand, could theoretically facilitate movements to any desired pose in the peri-personal space. A few possibilities exist to implement such a control in force. Musculoskeletal models, such as that presented in [8] for instance, offer the advantages that they can inherently account, at least to some extent, for changes in muscle geometry due to kinematics, if the stimulated muscle groups are modeled with sufficient accuracy. In previous studies [9], we determined the attainable precision of a musculoskeletal model adjusted to the anatomy of the user [10] in achieving an arbitrary endpoint force output direction by means of FES. However such models applied to FES require some anatomical expertise to be set up, as the routing of the stimulated muscle groups has to be pre-set within certain boundaries. In [9], a calibration procedure was proposed, which allowed partial automatic adjustments of the musculoskeletal geometry to any particular user. However, this calibration can only operate relatively small adjustments.

On the other hand, robot-inspired machine learning (ML)-based controls have been shown in [11], among others, to have high precision and accuracy in producing force output at the endpoint through FES. ML models have the advantage to not require expert knowledge of the muscle routing, nor the explicit connection of a muscle group to individual joints. However, they can not inherently generalize over different arm poses, and usually are trained with the limb in various positions, as was done in [12] and [13]. In this paper, we describe the early results of a pilot study were a machine learning model is employed to create an impedance control of the human upper limb, which is then used in a Target Achievement Control (TAC) test [14] where the user's hand is drawn to a set of randomized locations on

---

[1] Marek Sierotowicz and Claudio Castellini are with the Institute of Assistive Intelligent Robotics, Friedrich-Alexander Universität Erlangen-Nürnberg, 91052 Erlangen, Germany `marek.sierotowicz@fau.de` The authors are also affiliated with the Institute of Robotics and Mechatronics, German Aerospace Center, 82234 Wessling, Germany.

This work was partially supported by the German Research Society individual research grant HIT-Reha – Human impedance control for Tailored Rehabilitation, DFG Sachbeihilfe CA1389/3-1, project No. 505327336.

a plane spanning the whole of the user's workspace using FES without visual feedback and no volitional effort on the user's side. Differently from [13] and [12], we posit that the model employed in this study can generalize over different arm poses because of its being formulated in the joint space (see Fig. 1). This formulation enables the model to account for the user's skeletal geometry, but without the need to establish muscle routing, which is effectively learned through model calibration. Because of this characteristic, the model calibration procedure is only executed with the arm in one posture. Such FES controls are closely related to the control of wearable robotics. Because of this, the MyoCeption, which is the device employed for this experiment, could be considered as being to the efferent nerves what an exoskeleton is to the musculoskeletal system. The MyoCeption could therefore be construed to be an *exonerve*.

While the study is eventually going to be expanded to include also paretic patients, the initial able-bodied population should provide normative data to characterise the performance of the human impedance control. It is expected that the able-bodied population should show less inter-individual variance than the idiosyncratic manifestation of individual ailments would cause in a patient population.

II. METHODS

A. Setup

In this experiment, the MyoCeption FES device [10] is used together with the BodyRig body pose tracker [15] to perform a positional Target Achievement Control (TAC) test on a planar surface. In this test, the MyoCeption is tasked with providing stimulation currents such that the user's wrist is brought within 10 cm of a target, which is randomly drawn out of a set of 5 points in the peri-personal space. For the target to be considered reached, the wrist has to stay within range for 1 s, and the target has to be reached within 20 s. The test setup and the render of the avatar and targets to be reached are shown in Fig. 2.

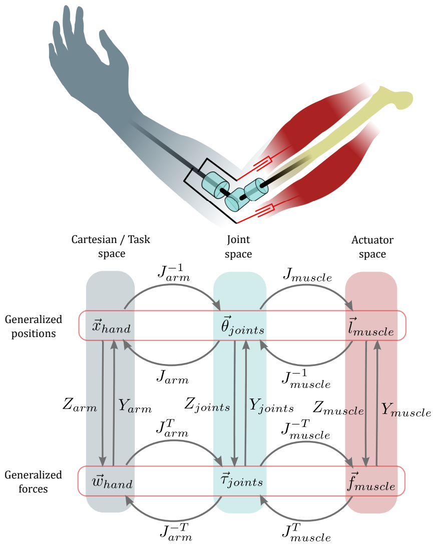

Fig. 1. Depiction of the relevant projections between Cartesian, joint and muscular spaces of generalized positions and forces. In each coordinate space, the positions and their time derivatives can be converted into the corresponding forces through an impedance $\boldsymbol{Z}$, and the reverse conversion can be operated through an admittance $\boldsymbol{Y}$. The projection of velocities and forces from one coordinate space and the other can be performed through the proper Jacobians and their transposed and inverse forms.

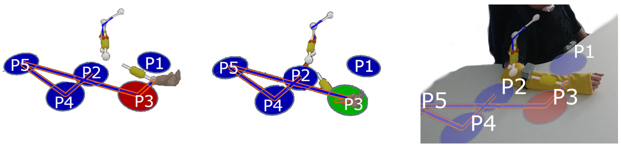

Fig. 2. Dynamic TAC test layout. **Above:** Visualisation of the arm posture with the wrist outside of the target point P3 (left) and within the target point P3 (right). **Below:** Overlay of the visualised task space and arm render over the actual test setup for the positional TAC test.

The MyoCeption is controlled by means of a ridge regression model which is trained to predict the joint torque output $\boldsymbol{\tau}_{joints} = [\boldsymbol{\tau}_{GH}, \boldsymbol{\tau}_{EL}] \in \mathbb{R}^6$, which is the concatenation of the elbow and glenohumeral joint torques $\boldsymbol{\tau}_{GH}, \boldsymbol{\tau}_{EL} \in \mathbb{R}^3$, based on the provided stimulation currents $\boldsymbol{s}_{act} \in \mathbb{R}^8$. The regression is trained sampling the stimulation $\boldsymbol{s}_{act}$ during calibration and projecting it onto the endpoint wrench output $\boldsymbol{w}_{cuff} = \left[\boldsymbol{f}_{cuff}, \boldsymbol{\tau}_{cuff}\right] \in \mathbb{R}^6$ measured by a 6-axes force torque sensor coupled to the user's forearm and projected onto the joint space using the arm Jacobian $J_{arm} \in \mathbb{R}^{6\times6}$ as per

$$\boldsymbol{\tau}_{joints} = J_{arm}^T \boldsymbol{w}_{cuff}. \tag{1}$$

The linear predictor trained in this manner is effectively learning the muscular Jacobian $J_{muscle} \in \mathbb{R}^{8\times6}$ multiplied by the diagonal stimulation transmission matrix $\boldsymbol{\Sigma} \in \mathbb{R}^{8\times8}$, so that

$$\boldsymbol{\tau}_{joints} = J_{muscle}^T \boldsymbol{f}_{muscle} = J_{muscle}^T \Sigma \boldsymbol{s}_{act} = W \boldsymbol{s}_{act}, \tag{2}$$

where $W \in \mathbb{R}^{6\times8}$ is the matrix enclosing the linear model's weights. While the mapping of stimulation to force is non-linear, in this experiment the control is assumed to operate in a quasi-linear region of the curve.

The calibration setup is shown in Fig. 4, together with the vectors relevant for the projection from the cuff's coordinate frame to the joint coordinate frame. In particular, the joints and cuff positions, which are inferred from the orientations of the Inertial Measurement Units (IMUs) 1 and 2, are used to calculate the arm Jacobian J_{arm} from eq. 1.

The impedance control is realized by inverting the prediction of the linear regression algorithm, thus finding the values of stimulation that best approximate a desired joint torque output. This inversion has to keep some further factors into consideration, namely the fact that the provided stimulation can only be positive and within a maximum. Furthermore, in this problem the null-space of the stimulation vector corresponding to a given joint torque has dimensionality 2, as there are 8 input channels and 6 output channels. This means that the stimulation vectors which would cause a given force

TABLE I

IMPEDANCE COEFFICIENT VALUES

Coefficient [Unit]	Value
K_d $[Nm^{-1}]$	80
K_q $[Nm^{-2}]$	80
D $[Nm^{-1}]$	15
$I_{max}[Nm^{-1}s^{-1}]$	0.07
I_d $[m^{-1}]$	0.05

output exist anywhere on a two-dimensional manifold. This can be intuitively understood if one thinks that a state of co-contraction in the musculature would lead to a net zero force and torque output. This means that for any solution vector of muscle contraction forces corresponding to a desired joint torque output, any muscle force vector equal to this solution plus a force vector that would lead to an arbitrary isometric co-contraction state would give the same result in terms of torque output. Because of this redundancy, we can impose further constraints on the solution by projecting the proper gradient onto the null space multiplying it by the matrix $(I_{8\times8} - W^{\#}W)$, where the symbol $\#$ indicates the pseudo-inverse and $I_{8\times8} \in \mathbb{R}^{8\times8}$ is an 8×8 unit matrix. In this experiment, the null-space projection was used to minimize the magnitude of the stimulation vector.

The complete control loop, once the predictive algorithm is trained, is shown in Fig. 3. This shows the conversion of the positional error in Cartesian space $\boldsymbol{e} = \boldsymbol{p}_{target} - \boldsymbol{p}_{hand}$ into a desired Cartesian force $\boldsymbol{f}_{des} \in \mathbb{R}^3$ through a mechanical impedance $\boldsymbol{Z} : \mathbb{R}^3 \rightarrow \mathbb{R}^3$, so that

$$\begin{aligned} \boldsymbol{f}_{des} &= \boldsymbol{Z}(\boldsymbol{e}) = \\ &= K_d\boldsymbol{e} + K_q\boldsymbol{e}^2 - D\dot{\boldsymbol{e}} + (I_{max} - exp(I_d\boldsymbol{e}))\int \boldsymbol{e}dt. \end{aligned} \quad (3)$$

The impedance coefficients were set as shown in Table I. The inclusion of quadratic terms and the fact that the integrative gain changes with the distance from the target position make it so that the impedance is more sensible to the momentary value of the error if the target is far away, and more to the integration of the error over time if the target is closer. This leads to a temporal increase in the desired force in time if, for example, the user's hand happens to stop in proximity of the target.

The MyoCeption was controlled at a rate of 300 Hz, and provided pulsed stimulation currents with a pulse rate of 30 Hz, pulse width 1 µs, amplitude modulated between 0 A and a maximum based on the comfort threshold, but at any rate never above 70 mA. The BodyRig tracker provided posture at a rate of 600 Hz. During calibration, the load cell was sampled at 200 Hz. The relative position of the user's hands and targets were sampled at 100 Hz. Where necessary, signals with different rates were re-sampled in the control loop. The model inversion block, in particular, was run at 600 Hz, in order to provide a faster convergence of the solution.

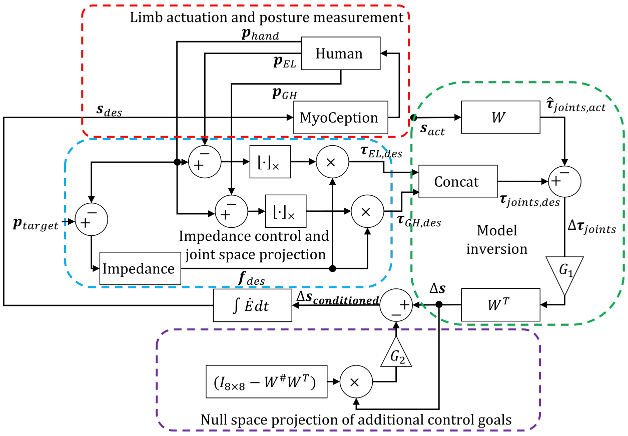

Fig. 3. Block diagram for the controller employing the linear regression algorithm calibrated through the force-torque sensor with weights W. The block diagram is divided in a few main sub-blocks, namely the conversion from positional error to a desired force through an impedance $\boldsymbol{Z}$ and the projection of said force onto joint space, the inversion of the previously trained regression model, the addition of the null-space projected stimulation vector in order to minimize the solution's magnitude, and finally the closing of the loop through the FES-actuated human limb.

B. Participants

In this analysis, we present results gathered from 6 able-bodied participants (5 males 1 female, Age 31 ± 9 years, weight 74±12kg, height 181±9cm). 3 of these had previous experience with FES ranging from a few to tens of hours of use, while 3 reported no prior experience, and were therefore considered naive. All participants signed an informed consent form. The experiment was approved by the ethical committee of the Friedrich-Alexander Universität Erlangen-Nürnberg (ID 22-304-S).

C. Experimental protocol

The participants sat at a table wearing the MyoCeption stimulation jacket and the BodyRig posture tracker. The stimulation electrodes were placed above *biceps*, *triceps*, *pectoralis clavicularis*, *pectoralis sternocostalis*, *deltoid anterior*, *superior* and *posterior*, and *trapezius*. The participants were harnessed to a seat, in order to eliminate any influence of chest movements. During calibration, the participants had their hand immobilized in a 6-Axis force torque sensor, as shown in Fig. 4.

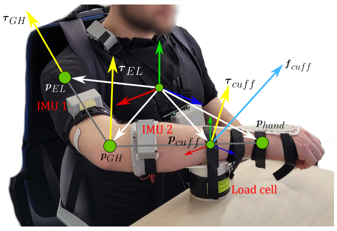

Fig. 4. Calibration setup with a harnessed user with a forearm locked in a splint coupled to a 6-DoF force-torque sensor. The IMUs are used to determine the joints positions, which in turn are used to project the wrench measured at the splint's center to the joint space.

After the identification of the comfort threshold of the participants for each channel's current, the calibration was performed by observing the wrench at the cuff through the force torque sensor. The trained regression model was then loaded in the control loop.

The TAC test, which is described above, consisted in driving the user's hand on a trajectory formed by 5 points, shown in Fig. 2. 4 of the 5 points were chosen by prompting the user to position their arm in each of the 4 postures resulting from combining full flexion/extension of the elbow and full horizontal adduction/abduction of the shoulder on the table. The 5th point was then computed as the mean of the two postures with extended elbow. The 5 points, therefore, spanned the whole of the user's functional workspace on the plane. The TAC test over these 5 points in random order was performed over 10 repetitions, forming an uninterrupted trajectory of 48 segments (5×10 points connected by 49 segments minus 1, as the start point was indicated to the participants, and therefore excluded from the TAC). This same experiment was then performed again with expert-performed adjustments of the impedance control coefficients shown in Table I, based on the observation of the performance in the first run, to assess the effect of expert intervention on the performance and correct any functional issues, such as certain channels not providing enough current to facilitate movement.

The evaluated metrics were overall and fatigue-corrected success rate, which is to say the highest success rate over a 15-points window, which in the case of naive subjects seems to comprise the average success rate after familiarization but before the onset of fatigue. Additionally, the metrics included time to completion and accuracy in expressed as the lowest distance error from the target over a time window of $1\,\mathrm{s}$, in accordance with the parameters of the TAC test. To ascertain the effects of experience on the main TAC metrics, a repeated measure ANOVA was performed with the experience of the participants with FES as a between-subject independent variable, and run number (first or second run), targeted point (out of the possible 5) and segment number (out of the possible 48) as within-subject independent variables.

III. RESULTS

Table II shows the main metrics and effects for the TAC test. The only statistically significant effect that could be found is a significantly lower time to completion for experienced participants in the second run (with $p < 0.01$ according to a post-hoc Tukey analysis).

Fig. 6 shows the average success rate over a moving window 15 points wide, corresponding to the longest apparent stretch for which familiarization and fatigue appear to balance out for naive participants, filtered additionally over a moving window of width 5, corresponding to the total number of points. The figures show also a best-fit line (in red) from a polynomial model of various order. The order of the polynomial model was chosen based on the condition that the regression coefficients of the model all have to satisfy $p < 0.05$. Based on how the data is subdivided, more or less complex dynamics can be shown through this method. For experienced participants, only a monotonic decrease in success rate over time can be shown. For naive participants, on the other hand, a more complex dynamic over time can be shown to occur (it is possible to fit a 6-th degree polynomial regression model to the success rate over time with $p < 0.05$ for all polynomial coefficients). Similarly, a 3rd-degree polynomial fits well to the success rate over time for the naive subjects during the first (expert-set) run of the experiment.

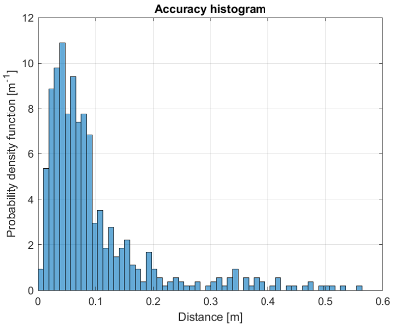

Fig. 5. Normalized histogram of the lowest distance from each target over a time window of $1\,\mathrm{s}$.

Figure 5 shows a normalized histogram of the accuracy normalized as a probability density function. 72% of the samples fall below the $10\,\mathrm{cm}$ threshold.

IV. DISCUSSION

The user's experience does seem to affect some outcome metrics, and this is likely due to the fact that the naive users have to familiarize themselves with the sensation of FES, and not work against it. It is also possible that experienced participants are able identify the target and actively move towards more consistently. If this were the case, however, we would expect to see a significant effect of experience on the overall or fatigue-corrected success rate, which we do not see. The outcome metrics vary greatly between individuals, but the fatigue-corrected success rates in particular indicate that the proposed system shows much promise.

Regression analysis of the success rate over trajectory segment for all participants shows a significant decrease

TABLE II

TAC PERFORMANCE METRICS. ALL VALUES IN FORMAT MEAN(STANDARD DEVIATION).

Metric[Unit]	Experienced	Naive	Effects
Success rate [%]	67.4(25.5)	46.5(8.5)	None
Best success rate over 15 segments [%]	81.2(20.2)	69.4(12.7)	None
Accuracy [cm]	9.77(9.73)	9.38(9.24)	None
Time to completion (ttc) [s]	9.97(5.20)	12.38(3.35)	Significantly lower ttc on run 2 for experienced subjects $F(1, 12) = 12.5$ $p < 0.05$

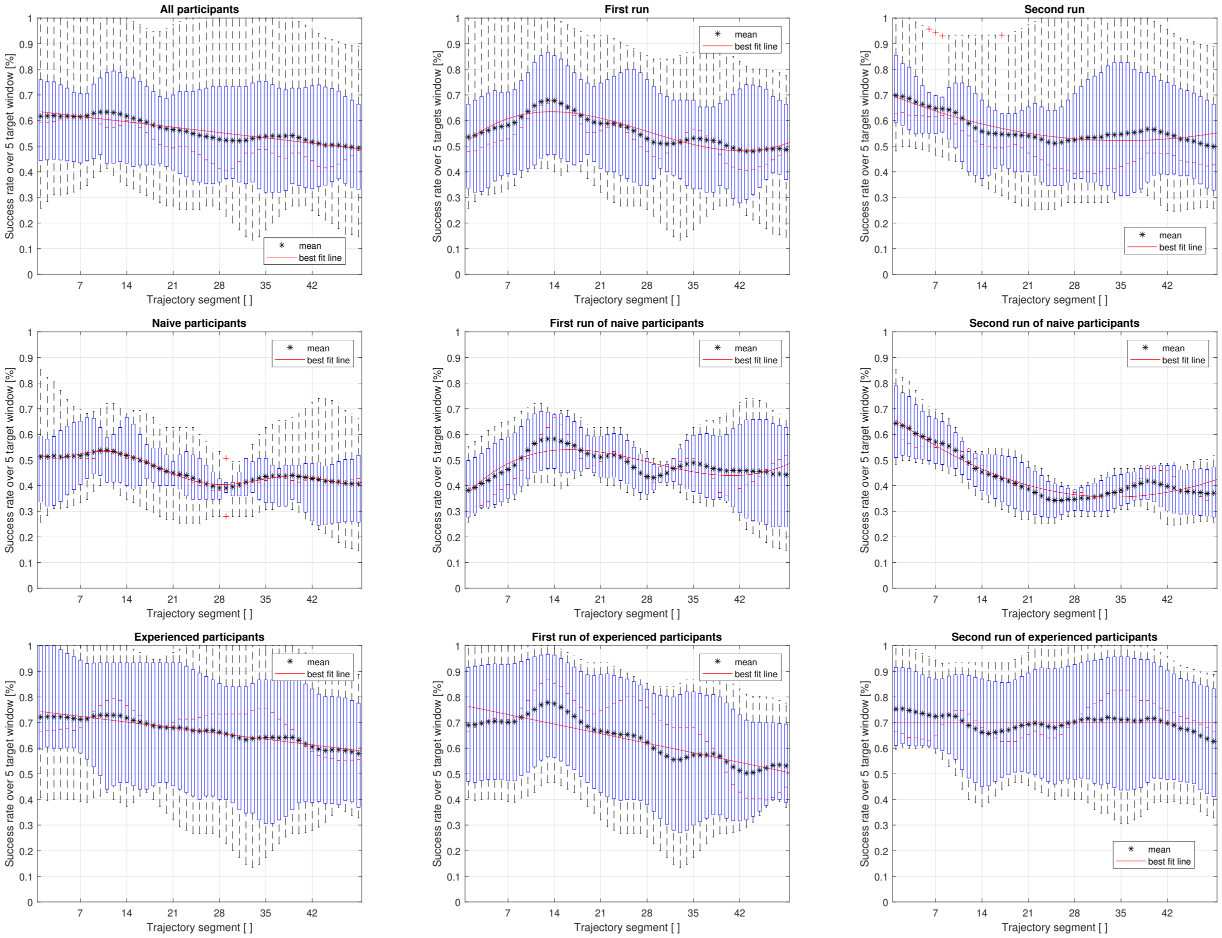

Fig. 6. Success rate over trajectory segments with best-fit lines. In all cases, the best-fit line is a polynomial model of varying order with $p < 0.05$ for all polynomial coefficients. The black stars indicate the mean, while the red lines within the individual boxes indicate the median.

of performance over time. This is likely due to the onset of muscular fatigue, which diminishes the force output of the musculature under stimulation [16]. Sorting the data by the experience of the participants, and by first and second run, some of the constituent dynamics can be identified, as shown in Fig. 6. If we assume that the main cause for deterioration of success rate over time is fatigue, and that, conversely, familiarization can lead to an increase in performance over time, we can expect familiarization to play a qualitatively bigger role for inexperienced subjects, especially during the first run. Looking at the best-fit lines, an initial increase in performance during the first run seems indeed more evident for naive subjects (although it is not completely absent for experienced subjects). The fact that the success rate for experienced subjects during the second run is nearly constant, by comparison, could be determined by the fact that experienced subjects spend shorter times under stimulation on average (even though the effect is not statistically significant for the first run). This would lead to a lessened impact of fatigue during the second run leading to a more pronounced difference.

The compounding effect of fatigue in performance over time is confirmed by the fact that a statistically significant effect of user experience on time to completion could be determined for the second run, but not for the first, with the experienced subjects requiring significantly less time to reach the target.

Overall, the main causes for bad performance seem to be time-dependent muscle response, which was very pronounced in some cases, as well as the convergence of the model inverter to local minima if the force vector $\boldsymbol{f}_{des}$ passed through the joints, which sometimes happened if, for example, the target to be reached was under the forearm and the arm was in an outstretched position. One inherent flaw of the proposed controller which became evident in some cases was a certain instability due to lags, both due to the equipment, the model inversion taking some time to converge, as well as the inherent compliance of the muscular system. This lag could cause situations where the user's arm oscillated around the target position, and without a proper inertial compensation, the system would not become stable.

The rmANOVA could not detect any overall effect of the target position on the success rate nor on the accuracy. This is to be expected, as potential functional difficulties of the subjects in reaching a given point seemed to be idiosyncratic, and would therefore not figure as a statistically significant effect when looking at the global data. Only when looking at individual subjects significant effects of the target's location on TAC success rate can be identified for 3 out of the 12 runs. Based on the recorded observations, however, the reason for this is rather an incapability of the MyoCeption to provide enough currents to facilitate a movement towards specific targets, rather than an inherent flaw of the impedance control. This finding marks the potential problems that could arise should this system be applied to chronic patients with reduced muscle tone. The effect of target position on the time to completion is on the edge of significance, and an effect could be found once the test population is enlarged, since ttc seems to be a sensitive indicator. The fact that no effect of target position on TAC performance can consistently be identified across all participants and runs speaks to the fact that the impedance controller proposed in this paper can indeed induce movements towards arbitrary points in the user's peri-personal space with consistent precision and accuracy even though the calibration is executed with the limb in a single posture, as opposed to [13] and [12], where the ML system is trained in various arm postures. Impedance-based, FES-actuated control of the upper limb could therefore prove a versatile tool in non movement-specific FES-facilitated rehabilitation techniques. The proposed system could also be employed in a hybrid solution involving also external aids to facilitate movements and measure the exerted force in real time, such as an exosuit, as was demonstrated, among others, by Burchielli et Al. in [17]. This would allow, among other things, to close the loop in force during normal operation, thus eliminating the need for the estimation of joint torques in the loop shown in Fig. 3, in favour of a direct measurement of the force output.

Coupled with a suitable intent prediction setup, this system could also be employed to assist chronic patients in activities of daily living, provided that muscle atrophy has not set in.

V. CONCLUSIONS

In this paper we presented an early analysis of a trial involving a FES-mediated impedance control concept for the human upper limb. The results make it possible to characterise the performance attainable by such a controller in facilitating movements towards arbitrary points in the peri-personal space. Furthermore, the effect of the user's experience can also be evaluated from a qualitative standpoint based on these early findings. Future work should focus on increasing the test population, even to include SCI patients. The long-term assessment of a single user's performance could also be the focus of upcoming research. The proposed force control could be improved by compensating for inertial and gravitational effects, which were not addressed in this experiment. Furthermore, the known lag between the onset of stimulation and the actual muscle contraction could also be accounted for.

REFERENCES

[1] N. Kapadia, B. Moineau, and M. R. Popovic, "Functional electrical stimulation therapy for retraining reaching and grasping after spinal cord injury and stroke," *Frontiers in Neuroscience*, p. 718, 2020.

[2] R. Rupp, M. Rohm, M. Schneiders, A. Kreilinger, and G. R. Müller-Putz, "Functional rehabilitation of the paralyzed upper extremity after spinal cord injury by noninvasive hybrid neuroprostheses," *Proceedings of the IEEE*, vol. 103, no. 6, pp. 954–968, 2015.

[3] A. B. Ajiboye, F. R. Willett, D. R. Young, W. D. Memberg, B. A. Murphy, J. P. Miller, B. L. Walter, J. A. Sweet, H. A. Hoyen, M. W. Keith, *et al.*, "Restoration of reaching and grasping in a person with tetraplegia through brain-controlled muscle stimulation: a proof-of-concept demonstration," *Lancet (London, England)*, vol. 389, no. 10081, p. 1821, 2017.

[4] P. Lopes and P. Baudisch, "Interactive systems based on electrical muscle stimulation," *Computer*, vol. 50, no. 10, pp. 28–35, 2017.

[5] E. Galofaro, E. D'Antonio, N. Lotti, and L. Masia, "Rendering immersive haptic force feedback via neuromuscular electrical stimulation," *Sensors*, vol. 22, no. 14, p. 5069, 2022.

[6] K. L. Meadmore, A.-M. Hughes, C. T. Freeman, Z. Cai, D. Tong, J. H. Burridge, and E. Rogers, "Functional electrical stimulation mediated by iterative learning control and 3d robotics reduces motor impairment in chronic stroke," *Journal of neuroengineering and rehabilitation*, vol. 9, no. 1, pp. 1–11, 2012.

[7] C. Freeman, T. Exell, K. Meadmore, E. Hallewell, and A.-M. Hughes, "Computational models of upper-limb motion during functional reaching tasks for application in fes-based stroke rehabilitation," *Biomedical Engineering/Biomedizinische Technik*, vol. 60, no. 3, pp. 179–191, 2015.

[8] E. K. Chadwick, D. Blana, R. F. Kirsch, and A. J. Van Den Bogert, "Real-time simulation of three-dimensional shoulder girdle and arm dynamics," *IEEE Transactions on Biomedical Engineering*, vol. 61, no. 7, pp. 1947–1956, 2014.

[9] M. Sierotowicz and C. Castellini, "A surface neuromuscular electrical stimulation device for universal cartesian force control in humans," *Artificial Organs*, vol. 46, no. 11, pp. e323–e327, 2022. [Online]. Available: https://onlinelibrary.wiley.com/doi/pdf/10.1111/aor.14408

[10] M. Sierotowicz, N. Lotti, R. Rupp, L. Masia, and C. Castellini, "A comprehensive framework for the modelling of cartesian force output in human limbs," in *2022 International Conference on Rehabilitation Robotics (ICORR)*. IEEE, 2022, pp. 1–6.

[11] E. M. Schearer, Y.-W. Liao, E. J. Perreault, M. C. Tresch, W. D. Memberg, R. F. Kirsch, and K. M. Lynch, "Multi-muscle fes force control of the human arm for arbitrary goals," *IEEE Transactions on Neural Systems and Rehabilitation Engineering*, vol. 22, no. 3, pp. 654–663, 2014.

[12] ——, "Semiparametric identification of human arm dynamics for flexible control of a functional electrical stimulation neuroprosthesis," *IEEE Transactions on Neural Systems and Rehabilitation Engineering*, vol. 24, no. 12, pp. 1405–1415, 2016.

[13] R. S. Razavian, B. Ghannadi, N. Mehrabi, M. Charlet, and J. McPhee, "Feedback control of functional electrical stimulation for 2-d arm reaching movements," *IEEE Transactions on Neural Systems and Rehabilitation Engineering*, vol. 26, no. 10, pp. 2033–2043, 2018.

[14] A. M. Simon, L. J. Hargrove, B. A. Lock, and T. A. Kuiken, "The target achievement control test: Evaluating real-time myoelectric pattern recognition control of a multifunctional upper-limb prosthesis," *Journal of rehabilitation research and development*, vol. 48, no. 6, p. 619, 2011.

[15] M. Sierotowicz, M. Connan, and C. Castellini, "Human-in-the-loop assessment of an ultralight, low-cost body posture tracking device," *Sensors*, vol. 20, no. 3, p. 890, 2020.

[16] M. Bergstrom and E. Hultman, "Energy cost and fatigue during intermittent electrical stimulation of human skeletal muscle," *Journal of applied physiology*, vol. 65, no. 4, pp. 1500–1505, 1988.

[17] D. Burchielli, N. Lotti, F. Missiroli, C. Bokranz, A. Pedrocchi, E. Ambrosini, and L. Masia, "Adaptive hybrid fes-force controller for arm exosuit," in *2022 International Conference on Rehabilitation Robotics (ICORR)*. IEEE, 2022, pp. 1–6.

Appendix B Additional publications

B.1 Force feedback for rover navigation

Title: Investigating the Influence of Haptic Feedback in Rover Navigation with Communication Delay

Authors: Marek Sierotowicz, Bernhard Weber, Rico Belder, Kristin Bussmann, Harsimran Singh and Michael Panzirsch

Conference: Haptics: Science, Technology, Applications

Publisher: Springer

Review: Peer-reviewed

Citation: M. Sierotowicz, B. Weber, R. Belder, et al. “Investigating the influence of haptic feedback in rover navigation with communication delay.” In: *International Conference on Human Haptic Sensing and Touch Enabled Computer Applications*. Springer. 2020, pp. 527–535. ISBN: 3-030-58146-2. DOI: `10.1007/978-3-030-58147-3_58`

Abstract: Safe navigation on rough terrain in the presence of unforeseen obstacles is an indispensable element of many robotic applications. In such conditions, autonomous navigation is often not a viable option within certain safety margins. Yet, a human-in-the-loop can also be arduous to include in the system, especially in scenarios where a communication delay is present. Haptic force feedback has been shown to provide benefits in rover navigation, also when confronted with higher communication delays. Therefore, in this paper we present the results of a user study comparing various performance metrics when controlling a rover with a car-like interface with and without fictitious force feedback, both with no communication delay and with a delay of 800 ms. The results indicate that with force feedback the navigation is slower, but task performance in the proximity of obstacles is improved.

Author contributions: Software Design; Study execution; Formal analysis; Writing-original draft; Writing-review and editing.

B.2 IMU-based teleoperation of a humanoid robot: an early analysis

Title: Learning teleoperation of an assistive humanoid platform by intact and upper-limb disabled users

Authors: Mathilde Connan, Marek Sierotowicz, Bernd Henze, Oliver Porges, Alin Albu-Schäffer, Máximo A. Roa and Claudio Castellini

Conference: Proceedings of the 5th International Conference on Neurorehabilitation (ICNR2020)

Publisher: Springer

Review: Peer-reviewed

Citation: M. Connan, M. Sierotowicz, B. Henze, et al. "Learning teleoperation of an assistive humanoid platform by intact and upper-limb disabled users." In: *International Conference on NeuroRehabilitation*. Springer. 2020, pp. 165–169. DOI: `10.1007/978-3-030-70316-5_27`

Abstract: With the advent of highly dexterous robotic arms, assistive platforms for home healthcare are gaining increasing attention from the research community. Control of the many degrees of freedom of such platforms, however, must be ensured uniformly, both for non-disabled and disabled users, in order to give them as much autonomy as possible. Nine users, including two upper-limb disabled, were asked to complete highly complex bimanual tasks by teleoperating a humanoid robot with biosignals. The users were equipped with a light and wearable interface consisting of a body tracking device for guiding the torso and arms and two electromyography armbands for controlling the hands by means of interactive machine learning. All users were able to complete the required tasks, and learning curves are visible in completion time metric.

Author contributions: Conceptualization; Software Design; Hardware Design; Formal analysis.

B.3 IMU-based teleoperation of a humanoid robot

Title: Learning to teleoperate an upper-limb assistive humanoid robot for bimanual daily-living tasks

Authors: Mathilde Connan, Marek Sierotowicz, Bernd Henze, Oliver Porges, Alin Albu-Schäffer, Máximo A Roa and Claudio Castellini

Journal: Biomedical Physics & Engineering Express

Publisher: IOP Publishing

Review: Peer-reviewed

Citation: M. Connan, M. Sierotowicz, B. Henze, et al. "Learning teleoperation of an assistive humanoid platform by intact and upper-limb disabled users." In: *International Conference on NeuroRehabilitation*. Springer. 2020, pp. 165–169. DOI: `10.1007/978-3-030-70316-5_27`

Abstract: **Objective.** Bimanual humanoid platforms for home assistance are nowadays available, both as academic prototypes and commercially. Although they are usually thought of as daily helpers for non-disabled users, their ability to move around, together with their dexterity, makes them ideal assistive devices for upper-limb disabled persons, too. Indeed, teleoperating a bimanual robotic platform via muscle activation could revolutionize the way stroke survivors, amputees and patients with spinal injuries solve their daily home chores. Moreover, with respect to direct prosthetic control, teleoperation has the advantage of freeing the user from the burden of the prosthesis itself, overpassing several limitations regarding size, weight, or integration, and thus enables a much higher level of functionality. **Approach.** In this study, nine participants, two of whom suffer from severe upper-limb disabilities, teleoperated a humanoid assistive platform, performing complex bimanual tasks requiring high precision and bilateral arm/hand coordination, simulating home/office chores. A wearable body posture tracker was used for position control of the robotic torso and arms, while interactive machine learning applied to electromyography of the forearms helped the robot to build an increasingly accurate model of the participant's intent over time. **Main results.** All participants, irrespective of their disability, were uniformly able to perform the demanded tasks. Completion times, subjective evaluation scores, as well as energy- and time- efficiency show improvement over time on short and long term. **Significance.** This is the first time a hybrid setup, involving myoelectric and inertial measurements, is used by disabled people to teleoperate a bimanual humanoid robot. The proposed setup, taking advantage of interactive machine learning, is simple, non-invasive, and offers a new assistive solution for disabled people in their home environment. Additionally, it has the potential of being used in several other applications in which fine humanoid robot control is required.

Author contributions: Software Design; Hardware Design; Formal analysis.

B.4 Teleimpedance through random Fourier features

Title: Deflection-Domain Passivity Control of Variable Stiffnesses Based on Potential Energy Reference

Authors: Michael Panzirsch, Marek Sierotowicz, Revanth Prakash, Harsimran Singh and Christian Ott

Journal: Robotics and Automation Letters

Publisher: IEEE

Review: Peer-reviewed

Citation: M. Panzirsch, M. Sierotowicz, R. Prakash, et al. "Deflection-Domain Passivity Control of Variable Stiffnesses Based on Potential Energy Reference." In: *IEEE Robotics and Automation Letters* 7.2 (2022), pp. 4440–4447. ISSN: 2377-3766. DOI: `10.1109/LRA.2022.3147566`

Abstract: With emerging capabilities, robots will advance gradually into human environments in the near future. Thereby, safety and robustness is currently tackled through intrinsically soft robotics or variable impedances, mainly stiffnesses. In tele-operation, for instance, the control stiffness can be adapted to a measured arm impedance of the operator to stiffen the robot only when required for a manipulation task. Thus, humans or moving objects in the robot's environment are protected from hard collisions. Independent from its realization through hardware or software, the stability of the variation needs to be ensured through control strategies since energy is potentially introduced into the robotic system. This work presents a novel gradient-based passivity control concept for variable stiffnesses. In contrast to state-of-the-art methods, the approach is based on a potential energy storage reference and prevents phases of zero stiffness through deflection-domain control. I.e., according to the energy storage, the stiffness variation over the spring deflection is controlled to ensure passivity. Experiments confirm the functionality of the approach and its robustness against delayed communication and active environments.

Author contributions: Software Design; Writing-review and editing.

B.5 Early analysis on static force control using the Nearest-Neighbor recruitment strategy

Title: A surface neuromuscular electrical stimulation device for universal Cartesian force control in humans

Authors: Marek Sierotowicz and Claudio Castellini

Conference: Abstracts From the IFESS 2022 Conferences, published in Journal of Artificial Organs

Publisher: John Wiley & Sons, Ltd

Review: Peer-reviewed

Citation: M. Sierotowicz and C. Castellini. "A surface neuromuscular electrical stimulation device for universal cartesian force control in humans." In: *JOURNAL OF ARTIFICIAL ORGANS* 46.11 (2022), e323–e327. ISSN: 1525-1594

Abstract: In recent years, neuromuscular electrical stimulation (NMES) has found many applications both within the medical field and outside. While this technology has been widely recognized as a valid tool for rehabilitative and assistive applications, most solutions presented in the literature seem to focus on highly specific cases and facilitate very selective movements. In this article, we present a novel surface stimulation-based prototype which, coupled with an internally designed musculoskeletal model, allows to induce the output of generalized forces at the human end-effector in Cartesian coordinates. The control has been validated here through a 6-axis force-torque sensor coupled with a robotic manipulator. Thus, the measured forces at the user's end-effector were compared to the commanded forces. The results confirm that open-loop control of the output force is possible with an average correlation coefficient between commanded and measured force output direction >0.7. This could eventually provide full, general-purpose impedance control of the human neuromuscular system, which would allow to induce arbitrary movements in the peri-personal space.

Author contributions: Conceptualization; Software Design; Formal analysis; Writing-original draft; Writing-review and editing.

B.6 Adaptive filter for sEMG-based force output estimation

Title: Adaptive filter for biosignal-driven force controls preserves predictive powers of sEMG

Authors: Marek Sierotowicz, Marc-Anton Scheidl and Claudio Castellini

Conference: Proceedings of 2023 International Conference on Rehabilitation Robotics (ICORR)

Publisher: IEEE

Review: Peer-reviewed

Citation: M. Sierotowicz, M.-A. Scheidl, and C. Castellini. "Adaptive Filter for Biosignal-Driven Force Controls Preserves Predictive Powers of sEMG." in: *2023 International Conference on Rehabilitation Robotics (ICORR)*. 2023, pp. 1–6. DOI: `10.1109/ICORR58425.2023.10304772`

Abstract: Electromyographic controls based on machine learning rely on the stability and repeatability of signals related to muscular activity. However, such algorithms are prone to several issues, making them non-viable in certain applications with low tolerances for delays and signal instability, such as exoskeleton control or teleimpedance. These issues can become dramatic whenever, e.g., muscular activity is present not only when the user is trying to move but also for mere gravity compensation, which generally becomes more prominent the more proximal a muscle is. A substantial part of this instability is attributed to electromyography's inherent heteroscedasticity. In this study, we introduce and characterize an adaptive filter for sEMG features in such applications, which automatically adjusts its own cutoff frequency to suit the current movement intention. The adaptive filter is tested offline and online on a regression-based joint torque predictor. Both the offline and the online test show that the adaptive filter leads to more accurate prediction in terms of root mean square error when compared to the unfiltered prediction and higher responsiveness of the signal in terms of lag when compared to the output of a conventional low-pass filter.

Author contributions: Conceptualization; Software Design; Formal analysis; Writing-original draft; Writing-review and editing.

B.7 Fusion of posture and muscular activity data to improve robot control

Title: Fusion of IMU and Muscular Information in Order to Solve the Limb Position Effect

Authors: Marek Sierotowicz

Institution: Technical University of Munich

Review: Approved by a Master's thesis commission

Citation: M. Sierotowicz. "Fusion of IMU and Muscular Information in Order to Solve the Limb Position Effect." Technical University of Munich, 2019

Abstract: The main goal of the work hereafter presented is to integrate data about a subject's body pose with data regarding the muscular activity in the forearm in order to improve the prediction of hand movement intention, particularly with respect to the limb position effect. The efforts to this end were articulated in three fundamental phases. Firstly, a portable and lightweight upper body tracking system was designed, implemented and characterized, particularly with respect to drift. Secondly, offline and online analyses about possible approaches to integrate the data from the body tracking system with different kinds of data measuring muscular activity in the forearm were conducted. Finally, a user study involving telemanipulation using a humanoid platform was conducted with the main goal of evaluating the learning curve of a subject using the upper body tracking system and in order to test some of the offline test results in terms of performance in the execution of daily tasks. Furthermore, this user study allowed to test an alternative control scheme especially suited for transradial amputees, with the main goal to estimate wrist rotation intention without the need to rely on muscular activity information.

Appendix C Copyrights

All figures in the main text, which are not attributed to other publications by citing the sources in the caption, are the author’s original work. Occasionally, original figures are the result of compositing images by a third party. Wherever applicable, the sources of the composited images are indicated in the caption.

C.1 Frontiers copyright statement

Frontiers publishes its own journals (referred to here as Frontiers Journals) and journals owned by third parties (referred to here as Hosted Journals). When we refer to Journals, we include both Frontiers Journals and Hosted Journals.

In this Copyright Statement, Websites (with a capitalised W) refers to all Frontiers websites, including those of Hosted Journals. An Owner means Frontiers as owner of all Frontiers Journals, or the respective owner of a Hosted Journal.

All content included on these Websites (including Loop), such as text, graphics, logos, button icons, images, video/audio clips, downloads, data compilations and software, is the property of the person or entity who or which owned it prior to submission to Frontiers or to a Hosted Journal. If not owned by Frontiers or an Owner of a Hosted Journal, it is licensed to Frontiers Media SA ("Frontiers"), such Owner or its or their licensees and/or subcontractors.

The ownership of copyright in the text of individual articles (including research articles, opinion articles, book reviews, conference proceedings and abstracts) is not affected by its submission to or publication by Frontiers, whether for itself or for a Hosted Journal. Frontiers benefits from a general licence over all content submitted. Hosted Journal Owners benefit from a general licence over all content submitted to their respective Hosted Journals. Frontiers, Hosted Journal Owners and all their users benefit from a Creative Commons CC-BY licence over all content, as specified below.

Images and graphics not forming part of user-contributed materials are the property of or are licensed to Frontiers and may not be downloaded or copied without Frontiers' explicit and specific permission or in accordance with any specific copyright notice attached to that material.

The combination of all content on Frontiers websites, and the look and feel of the Frontiers websites, is the property of Frontiers Media SA.

As an author or contributor you grant permission to others to reproduce your articles, including any graphics and third-party materials supplied by you, in accordance with the Frontiers Terms and Conditions. The licence granted to third parties over all contents of each article, including third-party elements, is a Creative Commons Attribution ("CC BY") licence. The current version is CC-BY, version 4.0 (http://creativecommons.org/licenses/by/4.0/), and the licence will automatically be updated as and when updated by the Creative Commons organisation.

You may include a requirement to reproduce copyright notices but you may not restrict the right to reproduce the entire article, including third-party graphics. This means that you must obtain any necessary third-party consents and permissions to reproduce third-party materials in your articles submitted to Frontiers.

E-books are subject to the same licensing conditions as the articles within them.

Articles published prior to 25th May 2018: Please note that reproduction of third-party graphics and other third-party materials contained in articles published prior to 25th May 2018 may be subject to third-party notices prohibiting their reproduction without permission. You must comply with those notices.

Articles published prior to July 2012: The licence granted for these articles may be different and you should check the pdf version of any article to establish what licence was granted. If an article carries only a non-commercial

C.2 IOP Publishing copyright statement

These special terms and conditions are in addition to the standard terms and conditions for CCC's Republication Service and, together with those standard terms and conditions, govern the use of the Works. As the User you will make all reasonable efforts to contact the author(s) of the article which the Work is to be reused from, to seek consent for your intended use. Contacting one author who is acting expressly as authorised agent for their coauthor(s) is acceptable. User will reproduce the following wording prominently alongside the Work: the source of the Work, including author, article title, title of journal, volume number, issue number (if relevant), page range (or 1rst page if this is the only information available) and date of 1rst publication; and a link back to the article (via DOI); and if practicable, and IN ALL CASES for new works published under any of the Creative Commons licences, the words "© IOP Publishing. Reproduced with permission. All rights reserved" Without the express permission of the author(s) and the Rightsholder of the article from which the Work is to be reused, User shall not use it in any way which, in the opinion of the Rightsholder, could: (i) distort or alter the author(s)' original intention(s) and meaning; (ii) be prejudicial to the honour or reputation of the author(s); and/or (iii) imply endorsement by the author(s) and/or the Rightsholder. This licence does not apply to any article which is credited to another source and which does not have the copyright line '© IOP Publishing Ltd'. User must check the copyright line of the article from which the Work is to be reused to check that IOP Publishing Ltd has all the necessary rights to be able to grant permission. User is solely responsible for identifying and obtaining separate licences and permissions from the copyright owner for reuse of any such third party material/Figures which the Rightsholder is not the copyright owner of. The Rightsholder shall not reimburse any fees which User pays for a republication license for such third party content. This licence does not apply to any material/Figure which is credited to another source in the Rightsholder's publication or has been obtained from a third party. User must check the Version of Record of the article from which the Work is to be reused, to check whether any of the material in the Work is third party material. Third party citations and/or copyright notices and/or permissions statements may not be included in any other version of the article from which the Work is to be reused and so cannot be relied upon by the User. User is solely responsible for identifying and obtaining separate licences and permissions from the copyright owner for reuse of any such third party material/Figures where the Rightsholder is not the copyright owner. The Rightsholder shall not reimburse any fees which User pays for a republication license for such third party content. User and CCC acknowledge that the Rightsholder may, from time to time, make changes or additions to these special terms and conditions without express notification, provided that these shall not apply to permissions already secured and paid for by User prior to such change or addition. User acknowledges that the Rightsholder (which includes companies within its group and third parties for whom it publishes its titles) may make use of personal data collected through the service in the course of their business. If User is the author of the Work, User may automatically have the right to reuse it under the rights granted back when User transferred the copyright in the article to the Rightsholder. User should check the copyright form and the relevant author rights policy to check whether permission is required. If User is the author of the Work and does require permission for proposed reuse of the Work, User should select 'Author of requested content' as the Requestor Type. The Rightsholder shall not reimburse any fees which User pays for a republication license. If User is the author of the article which User wishes to reuse in User's thesis or dissertation, the republication licence covers the right to include the Version of Record of the article, provided it is not then shared or deposited online. User must include citation details. Where User wishes to share their thesis or dissertation online, they should remove the Version of Record before uploading it. User may include a Preprint or the Accepted Manuscript (after the embargo period) in the online version of the thesis or dissertation, provided they do so in accordance with the Rightsholder's policies on sharing Preprints or Accepted Manuscripts. User may need to obtain separate permission for any third party content included within the article. User must check this with the copyright owner of such third party content. Any online or commercial use of User's thesis or dissertation containing the article, including publication via ProQuest, would need to be expressly notified in writing to the Rightsholder at the time of request and would require separate written permission from the Rightsholder. As well as CCC, the Rightsholder shall have the right to bring any legal action that it deems necessary to enforce its rights should it consider that the Work infringes those rights in any way. For content reuse requests that qualify for permission under the STM Permissions Guidelines, which may be updated from time to time, the STM Permissions Guidelines supplement the terms and conditions contained in this license.

C.3 IEEE copyright statement

Thesis / Dissertation Reuse

The IEEE does not require individuals working on a thesis to obtain a formal reuse license, however, you may print out this statement to be used as a permission grant:

Requirements to be followed when using any portion (e.g., figure, graph, table, or textual material) of an IEEE copyrighted paper in a thesis:

1) In the case of textual material (e.g., using short quotes or referring to the work within these papers) users must give full credit to the original source (author, paper, publication) followed by the IEEE copyright line © 2011 IEEE. 2) In the case of illustrations or tabular material, we require that the copyright line © [Year of original publication] IEEE appear prominently with each reprinted figure and/or table. 3) If a substantial portion of the original paper is to be used, and if you are not the senior author, also obtain the senior author's approval.

Requirements to be followed when using an entire IEEE copyrighted paper in a thesis:

1) The following IEEE copyright/ credit notice should be placed prominently in the references: © [year of original publication] IEEE. Reprinted, with permission, from [author names, paper title, IEEE publication title, and month/year of publication]

2) Only the accepted version of an IEEE copyrighted paper can be used when posting the paper or your thesis on-line.

3) In placing the thesis on the author's university website, please display the following message in a prominent place on the website: In reference to IEEE copyrighted material which is used with permission in this thesis, the IEEE does not endorse any of [university/educational entity's name goes here]'s products or services. Internal or personal use of this material is permitted. If interested in reprinting/republishing IEEE copyrighted material for advertising or promotional purposes or for creating new collective works for resale or redistribution, please go to http://www.ieee.org/publications_standards/publications/rights/rights_link.html to learn how to obtain a License from RightsLink.

If applicable, University Microfilms and/or ProQuest Library, or the Archives of Canada may supply single copies of the dissertation.

C.4 MDPI copyright statement